Synthesis of Multi-modal Metallodrugs as Anti-cancer Agents

Synthesis of Multi-modal Metallodrugs as Anti-cancer Agents

A Thesis Submitted for the Degree of

Doctor of Philosophy

Clara Adele von Randow

Magdalen College

University of Oxford

April 2024

Per aspera ad astra

Statutory Declaration

The present thesis is based on my personal work from October 2019 (Michaelmas Term) to April 2024 (Hilary Term) at the University of Oxford. Research was performed in the workgroup of Dr N. J. Farrer from April 2020 until February 2022 and subsequently continued in the workgroup of Prof S. Faulkner.

I herewith confirm that I have composed this thesis independently and without the help of any impermissible resources. All contents from external sources are explicitly marked as such and are acknowledged by citation. References are listed in Chapter 9.

Cytotoxicity studies were conducted in collaboration with the research group of Prof G. Higgins in the Department of Oncology at the University of Oxford.

Clara von Randow

Oxford, 12th April 2024

Gratitude

Many of you know what a rollercoaster the last 4.5 years have been for me. Coming to Oxford, I was ready to do Science – finally let go of the breaks, take off, indulge in Chemistry and do what I love. However, a rollercoaster includes both surging ups and deathly falls (and apparently a pandemic). Such is life. My DPhil held a myriad of challenges for me, many of which were not merely the Science not doing as I wanted it to. It has included blood, sweat and (many) tears. But it has also been so much more, cut deep and been greatly formative. It has included connecting with inspiring and brilliant people, kindling profound friendships, paired with an overwhelming portion of fun, opportunities, laughter, love and banter. In absence of the lab being my Happy Place, I indulged in the tantalising Oxford bubble, and I am so much richer for this experience. I have dwelled on the pitfalls of this degree many a time, but here, I would like to relish the aspects – the people – who have contributed in so many ways to my time in Oxford and helped me complete this degree.

I would like to extend a huge thank you to Prof Stephen Faulkner for his incredible fortitude throughout the ups and downs. Steve – you are the kindest person I have met in this department and your sense of people and helpfulness are a blessing and gift to all of those around you. – Thank you.

Thank you, Dr Nicola Farrer for introducing me to the field of platinum-based anti-cancer research and to Prof Stephen Faulkner, Prof Simon Aldridge and Prof Jose Goicoechea for taking on supervision when the going got tough. Thank you to the EPSRC Centre for Doctoral Training OxICFM for financial support throughout this degree. I would like to extend gratitude to the members of the Higgins Group at the department of Oncology who conducted the cytotoxicity studies, in particular to Rathi Puliyadi.

Thank you to the members of the Chemistry department at the Freie Universität Berlin who welcomed me back at any time of day for support – be it of crystallographic nature, companionship with other doctorate students or offering me a safe space to do Chemistry.

As in most workplaces, the day-to-day routine in the lab is shaped immensely by the people around you. Thank you to the Faulkner group throughout the years and to the dedicated members of the material stores and workshops who are invaluable in keeping research going. To the remaining “Platinum-people” among S9: you’ve got this! Marie – completing this together has made us stronger. Thank you for speaking up when it mattered the most. Sharing our love for Oxford, daytrips and the little things in life has been amazing. Debs – I have missed having you as an evening and weekend buddy and really value all of your support. Rachel and Gabi – I will miss the walks and chats, the lab vents. Rachel, thank you so much for your friendship. Knowing you were always just a message away for an impromptu walk or coffee after the next inevitable mental breakdown means more to me than you know. Kelly – your friendly smile and wave goes such a long way. I am so glad I have got to know you better, you are an amazing person.

Magdalen – you have become my home and I am eternally grateful for that. The last years would not have been the same without you. I have learned so much from working with College, have thoroughly enjoyed my time with you and feel incredibly lucky. I have had the privilege of connecting with extraordinary people on my path here and will not be able to do all of them just. Ilse – you have been my rock since the Wine & Cheese in Freshers’ Week MT2019. I cannot imagine having pursued this path without you as my friend. I savour all of the squares we have sewn together in my memory quilt. My gratitude for all of the hugs, the smiles, the mischief – for you – goes beyond “thank you”. Matthew, Grace, Sally, Lucas, Will, Róbert, Hamish, Seb, Dan and so many others: I feel overwhelmed and humbled to call you my friends and to have shared this time with you.

Mathias – thank you for the long nights in the lab, the even longer walks, for talking Chemistry with me, for seeing me, for your friendship. I will never forget the support you gave me in dire times.

Günther – “thank you” does not even begin to cut it. I am so grateful for your unfaltering belief in me. Thank you for your mentorship, your supervision and your friendship through all of the “character building” I have experienced here.

Ulrike and Katharina – your constant support over the last years has been invaluable to me. You helped get me to Oxford and have continued to be a safe harbour I can turn to at any time. – Thank you for helping me find my way.

To my family, near and far. My mother, my brother, my dear cousin Dan, all of my wonderful family in the land of the long white cloud. To my father – this is the only thesis of mine you will not have read. You are all a part of me and contribute to who I am today, to who I would like to be. Thank you.

And to all the friends outside this Oxford bubble who never fail to believe in me – Miri, Katharina, Pia, Giulia, Juli, Mirjana – I am deeply grateful for you all. Thank you for all the years that have been and all the years to come.

Oxford – you are an amazing place I feel honoured to have called home. With your beauty, your impressive architecture, the nature around you, a wafting gown always in sight. Thank you for letting me partake in your journey.

I have grown. I have nurtured my resilience. I have fostered my backbone. Stood up, spoke up, stumbled. Repeat. Perhaps I did not learn a myriad of new techniques, or cure cancer. But I have taken so much more from this time than textbooks could ever teach me, and isn't that what a DPhil is really about?

Table of Contents

Abstract

Since the serendipitous discovery of Cisplatin in 1965, innumerable platinum-based derivatives have been explored as alternative anti-cancer agents. In the scope of this research, [2+3]-cycloaddition reactions between diazidoplatinum(II) complexes and gold(I) alkynes were utilised for the synthesis of functionalised multi-modal platinum(II)-gold(I) complexes. The rationale of ligand design was based on literature reports as well as theoretical investigations of the frontier orbitals of potential candidates. With the aim of expanding the historic focus on *N*-donor ligands, *P*-donor ligands in the form of substituted phosphines were chosen on the platinum centre. In addition, complexes with both *N*- and *P*-functionalities within the ligands were pursued in order to identify electronic trends. The readiness of the diazidoplatinum(II) complexes towards the cycloaddition reaction was correlated to the electronic configuration of the platinum centres *via* ^{195}Pt NMR spectroscopy. The complexes were characterised *via* NMR, IR and UV-visible spectroscopy, along with mass spectrometry. Various molecular structures in the solid state were confirmed by means of X-ray diffractometry. Attempted development of the platinum(II) complexes as candidates for platinum(IV) prodrugs *via* oxidation were unsuccessful.

Four of the synthesised complexes were investigated regarding their photosensitising and radiosensitising properties following the irradiation with blue or green light, and X-rays. In most cases, irradiation of the bimetallic complexes led to bond cleavage and breakdown of the compounds. Cytotoxicity studies were performed on three cancer cell lines with and without irradiation under X-

rays and the results were compared to those of Cisplatin. No clear indication of radiosensitising properties were observed, however, cytotoxicity was enhanced by the combination of the two metal complexes. Further in-depth investigations are required in order to draw final conclusions on the reproducibility and the activation of the cytotoxic properties of the complexes following irradiation.

List of Abbreviations

B2-PLYP	Becke, Lee-Yang-Paar Double Hybrid Functional with Perturbation Correction
B3-LYP	Becke, 3-parameter, Lee-Yang-Paar Functional
BP-86	Becke 1988 Exchange Functional and Perdew 86 Correlation Functional
COSMO	Conductor-like Screening Model
CuAAC	Copper-catalysed Azide-Alkyne Cycloaddition
DACH	(1*R*,2*R*)-Diaminocyclohexane
DFT	Density Functional Theory
DMF	Dimethylformamide
DMSO	Dimethyl Sulfoxide
ESI	Electron Spray Ionisation
FDA	Food and Drug Administration
HOMO	Highest Occupied Molecular Orbital
iClick	Inorganic Click
IR	Infrared
LC-MS	Liquid-Chromatography Mass Spectrometry
LED	Light-emitting Diode
LMCT	Ligand-to-Metal-Charge-Transfer
LUMO	Lowest Unoccupied Molecular Orbital
MAAC	Metal-catalysed Azide-Alkyne Cycloaddition
NCS	*N*-Chlorosuccinimide
NIR	Near-Infrared Light

NMR	Nuclear Magnetic Resonance
PACT	Photoactivatable Chemotherapy
PBE	Perdew-Burke-Ernzerhof
RI	Resolution-of-Identity
ROS	Reactive Oxygen Species
SPAAC	Strain-promoted Azide-Alkyne Cycloadditions
THF	Tetrahydrofuran
TLC	Thin Layer Chromatography
TZVP	Valence Triple-Zeta Polarisation
UV-Vis	Ultraviolet-visible
X-PDT	X-ray Photodynamic Therapy
XRD	X-ray Diffraction

1. Introduction

1.1 Platinum(II) Anti-Cancer Agents

The medicinal properties of transition metal compounds were observed as early as 2500 BC.[1] The application of metallic complexes as potential anti-cancer agents in particular was already reported in the sixteenth century, and numerous gold, ruthenium as well as gallium compounds have entered clinical evaluations.[1–3] To date, platinum complexes are amongst the most prominent anti-cancer agents with 50% of chemotherapy patients being administered a platinum-based drug.[2] The serendipitous discovery of Cisplatin (*cis*-diamminedichloridoplatinum(II)) in the 1960s revolutionised the treatment of cancer and significantly promoted research in the field of metal-organic compounds for medical applications.[4–6] The compound was first synthesised by M. Peyrone as early as 1844 and known as Peyrone's salt.[7–10] Structural elucidation of the complex followed by A. Werner in 1893. In 1965 B. Rosenberg observed the cells of *Escherichia coli* bacteria seizing cell division and instead increasing 300 times in their average size when applying an electric field using platinum electrodes and a solution of ammonium chloride as electrolyte. Upon turning the field off, cell division resumed. Under the electric field, the platinum had reacted with the electrolyte to form Cisplatin causing cell inhibition. Four years later, Rosenberg demonstrated controlled cytotoxicity of the complex towards tumour cells in animals. In 1971 the first patients were tested with Cisplatin in a trial commenced by the National Cancer Institute and only seven years later, Cisplatin was approved by the US Food and Drug Administration

(FDA) for testicular and ovarian cancer.[7,8]

The mode of action of Cisplatin is well-understood and can be divided into four steps: cellular uptake, activation of the compound *via* aquation, formation of DNA cross-links, and follow-up processes leading to apoptosis (Figure 1). Cellular uptake is obtained through a combination of passive diffusion and active transport by membrane proteins. Due to a substantially lower concentration of chloride within the cell, the chlorido ligands are substituted by water molecules, resulting in positively charged platinum species. The aquated Cisplatin enters the nucleus and binds to the negatively charged DNA. Platination of the DNA occurs at the nucleophilic nitrogen atoms mainly on the purine residues adenine and guanine. The aqua ligands are eliminated and the Cisplatin derivative forms cross-links in the form of 1,2-intrastrand links to predominantly adjacent DNA bases, which leads to a substantial distortion of the helical DNA structure. If the nucleotide excision repair mechanisms cannot reach the DNA lesion due to shielding by bound proteins, cell death is initiated. If, however, the Cisplatin is sequestered by sulphur-rich metallothioneins such as glutathione, the complex is removed from the cytoplasm before reaching the DNA.[2,11] More recently, Cisplatin has additionally been reported to form adducts with cellular proteins, as well as causing endoplasmic reticulum and mitochondrial stress as further modes of action.[12]

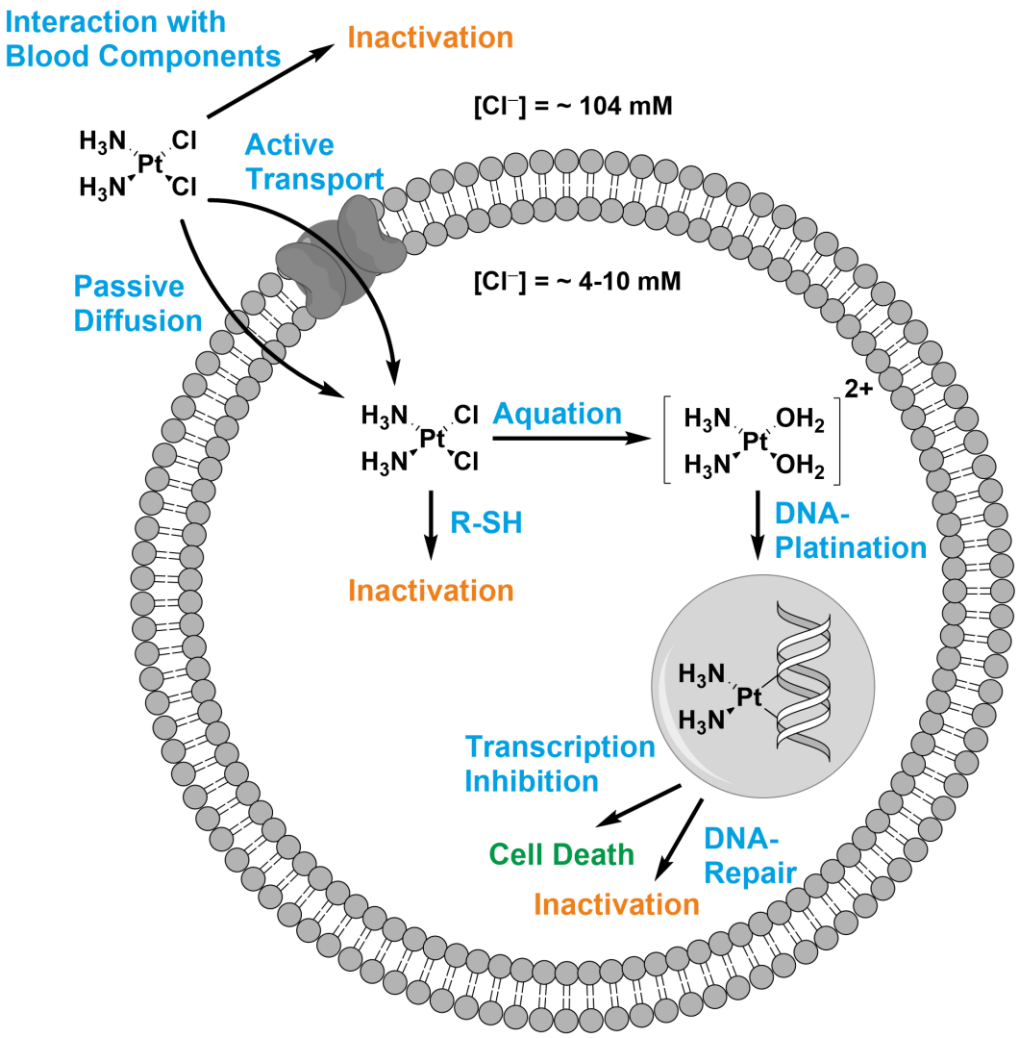

Figure 1: Extra- and intracellular activity of Cisplatin leading to either inactivation of the drug or cell death.

Cisplatin does not differentiate between cancerous and healthy cells with regards to its cytotoxicity, leading to dire side-effects among which are neurotoxicity, ototoxicity and nephrotoxicity.[1,7,13,14] Resistance and acute toxicity have prompted the investigation into a myriad of Cisplatin derivatives and the development of analogous square-planar neutral *cis*-platinum(II) complexes with two (chelating) anionic leaving groups, next to two inert non-leaving group ligands such as amines.[2,7] Currently, two further analogous platinum-based anti-cancer

agents have been approved for admission in the clinic worldwide, with three more reaching regional approval (Scheme 1).[1,7,11] Cisplatin is particularly effective in the treatment of testicular cancer while Carboplatin is primarily administered for ovarian cancer, and Oxaliplatin finds application for colorectal and gastrointestinal cancers.[11,13,15] Platinum-based chemotherapeutics are used for treating the vast majorities of cancers, including bladder, lung, melanoma, lymphoma, myeloma, head and neck cancer.[11,15]

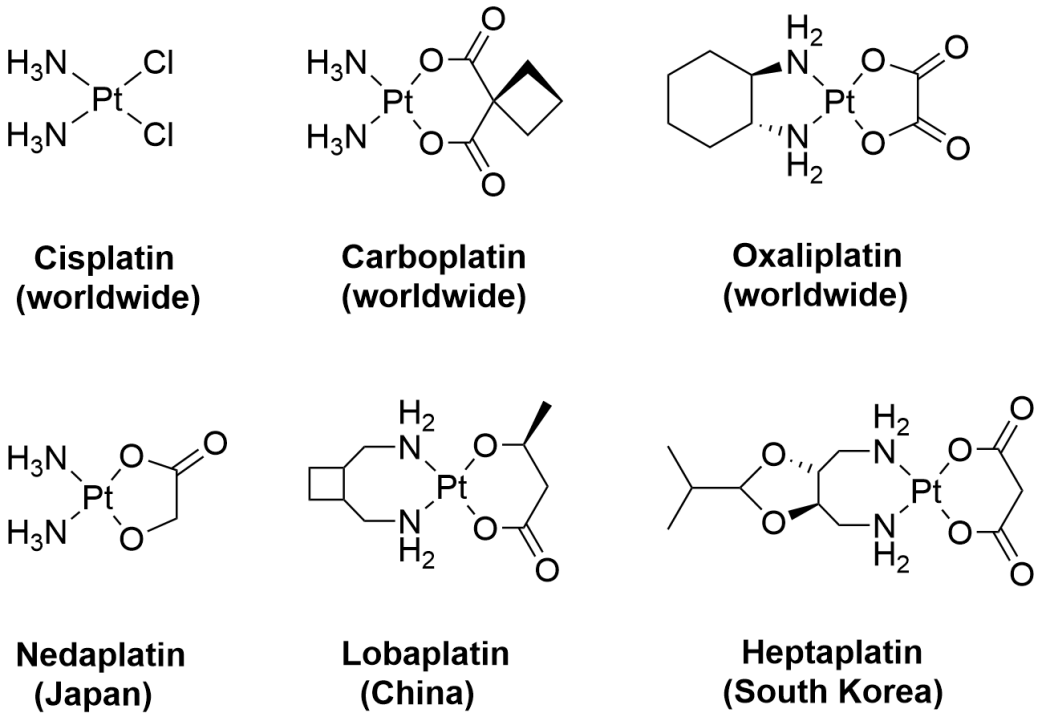

Scheme 1: Current platinum-based chemotherapeutics and their region of approved admission.[1,11]

While Cisplatin is considered a first generation platinum-based anti-cancer drug, further developments aimed at increasing the safety of the treatment and at

overcoming intrinsic or acquired resistance.[8] Second generation drugs display a variation in the leaving or the ammine groups on the platinum centre. Carboplatin includes the chelating 1,1-cyclobutyldicarboxylic anion in place of two chlorido ligands. The mechanism of action within the cell is similar to that of Cisplatin, however, due to the bidentate anionic ligand, ligand exchange with water molecules occurs at a slower rate. Toxicity leads to the formation of analogous DNA adducts with guanine, inhibiting the replication of the cell and leading to apoptosis. The slower kinetics of Carboplatin result in reduced neurotoxicity and ototoxicity after treatment whilst being similarly effective as Cisplatin, and may increase tolerance of the drug by patients rendering it more suitable for a more aggressive high-dose chemotherapy.[8,16–18] Nedaplatin is a further example of a second generation platinum-based anti-cancer drug in which the chlorido ligands have been replaced by a chelating glycolate ligand. The compound received regional approval in Japan and is used for treatment against ovarian and cervical cancers.[7,19] As treatment of each Cis- and Carboplatin led to the development of resistance, the third generation of platinum-based anti-cancer agents was developed. Oxaliplatin includes two chelating ligands: a (1*R*,2*R*)-diaminocyclohexane (DACH) ligand in place of the ammine ligands with an oxalato ligand in place of the chlorido ligands. While the oxalato ligand reduces the reactivity of the complex, the more lipophilic DACH ligand increases passive uptake into the cells. In addition to forming DNA adducts, Oxaliplatin induces immunogenic cell death by causing a T-cell dependent immune response alongside ribosome biogenesis. This additional mode of cytotoxicity in comparison with Cisplatin might explain its potency in Cisplatin-resistant cell lines.[20] Oxaliplatin is usually administered in combination with other

chemotherapeutic compounds for higher efficacy of the treatment.[16–18] Lobaplatin and Heptaplatin are further examples of third generation platinum-based anti-cancer agents, both of which received regional approval for the clinic: Lobaplatin in China, and Heptaplatin in South Korea.[7,17]

The nature of the ligands contributes to the overall lipophilicity of the drug, which is critical for its distribution, cellular uptake, and metabolism. Depending on the method of cell penetration, *i.e.* passive diffusion *vs* active transport mechanisms, the modification of the lipophilicity of the complex and thus its path of interaction could have a significant impact on the rationale behind drug design.[21]

The chemotherapeutic activity of metal complexes is greatly influenced by features such as the oxidation state of the metal centre, geometry and the type of ligand. An alteration of these properties can lead to a drastic change in potency. *Trans*-diamminedichloridoplatinum(II) (Transplatin) expresses a different kinetic profile to its *cis*-isomer and historically appeared to be significantly less cytotoxic towards cancer cells. This led to the false belief of *cis*-standing ligand groups being imperative for effective platinum-based anti-cancer agents.[8,11,15,17,22] The geometry of *trans*-isomers of platinum-based anti-cancer agents prevents them from forming 1,2-intrastrand cross-links within the DNA helix, however, they do in fact form 1,3-interstrand adducts, which cannot be repaired by the nuclear excision repair system explaining cytotoxicity towards Cisplatin-resistant cells.[7,16] Since the 1990s, extensive research has been performed on *trans*-isomers of cytotoxic platinum-based anti-cancer agents which suggests that the historically low observed potency of the isomers is actually due to a higher reactivity of the complexes resulting in faster deactivation

of them by sulphur-containing compounds such as glutathione within the cell. Exchanging the ammine ligands for sterically more demanding ligands decreased the rate of ligand substitution of the chlorido ligands within the cell and with that the rate of activity of the complex. *Trans*-platinum(II) anti-cancer agents can be divided into three groups depending on the type of *N*-donor ligands: planar aromatic bases (pyridine, quinoline, thiazole, imidazole), iminoethers and aliphatic amines (piperidine, piperazine). These structural modifications improved the cytotoxicity significantly, compared to that of Transplatin, including towards Cisplatin-resistant cell lines.[7,16,19,23] *Trans*-platinum(II) complexes form monofunctional interstrand DNA products instead of intrastrand links, as mainly is the case for *cis*-isomers. This observation implies that pursuing anti-cancer agents with mechanisms distinct from those of Cisplatin are more promising. Further methods include targeted systems with ligands that respond to particular cellular targets within the cancer cell, however, poor solubility and lack of stability remain major obstacles in complexes reaching clinical trials.[14,19,20]

1.2 Platinum(IV) Anti-Cancer Agents

As previously discussed, all platinum-based anti-cancer agents which currently find application in cancer treatment are composed of square-planar *cis*-platinum(II) complexes with two inert amine donors and semi-labile chlorido or oxygen donors. Albeit this structure-activity relationship for platinum anti-cancer agents was first discussed by M. J. Cleare and J. D. Hoeschele in 1973 – based on a distinctly limited database at the time – it appears that the conclusions drawn still hold more than half a century later.[24,25] The challenges of both intrinsic and

acquired resistance along with the severe dose-limiting side-effects of the chemotherapeutics demand further research into alternative approaches to platinum anti-cancer agents. Delivery strategies including encapsulation of the compounds into liposomes, micelles or nanoparticles have been explored. New advances comprise the synthesis of so-called prodrugs: kinetically more inert six-coordinate octahedral platinum(IV) complexes which are reduced *in vitro* to yield the active, cytotoxic square-planar platinum(II) species (Scheme 2).[26,27] The application of platinum(IV) prodrugs was pioneered by J. Matthey in 1995.[24,28] The ligands on the prodrugs can be classified into two neutral non-leaving groups, two anionic leaving groups and two axial ligands.

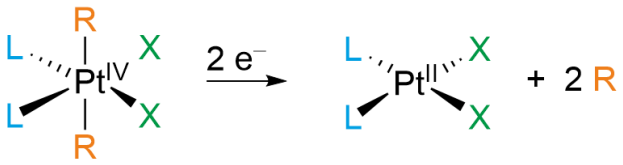

Scheme 2: Schematic reduction of the octahedral platinum(IV) prodrug yielding the square-planar platinum(II) complex with non-leaving group ligands (L) in blue, leaving group ligands (X) in green and axial ligands (R) in orange.

The two additional axial ligands pose as molecular handles for tuning the prodrug's chemical and biological properties. In addition to functional groups, the attachment of targeting moieties, reactive organic functionalities, or even nanoparticles and carrier systems, can be realised.[11,29] Axial ligands can include bioactive or non-bioactive functionalities, *e.g.* compounds such as phenylbutyrate or dichloroacetate, the former facilitating exposure of DNA to

platination, and the latter promoting conditions for cell death.[26,30] Targeting moieties in the axial ligands could include peptide receptors, enzyme inhibitors, hormones or even a molecule which blocks the nucleotide excision repair mechanism, hence preventing DNA repair of formed cross-links.[30] All six ligands can affect the water solubility of the complex, while enhancing its lipophilicity can improve its cellular uptake significantly.[11,26,29,31]

N-donors typically constitute the non-leaving group ligands and directly influence the properties of the platinum-DNA adduct.[11,29] The leaving group ligands modify the reaction and thus the aquation kinetics. A fine balance between the lability of these ligands, which is somewhat labile but not too susceptible to substitution reactions, is essential for the compound's anti-cancer activity.[31] Recent investigations have revealed that the variation in kinetic inertness of platinum(IV) prodrugs is greater than was initially thought. The equatorial core of the compound greatly influences the rate of hydrolysis, which in turn impacts their rate of reduction. Of the three platinum(II) anti-cancer agents approved worldwide, the equatorial core of Carboplatin has been reported to exhibit the highest hydrolytic stability.[32]

One approach to minimising acquired resistance of platinum-based anti-cancer agents is through combination therapy with other chemotherapeutic drugs with different modes of action and cellular targets, administered for synergistic attack. Major challenges with administrating multiple drugs include disparities in the pharmacokinetic properties of the compounds. Further development of platinum(IV) prodrugs to multi-modal dual-action prodrugs presents a platform for co-treatment with multiple agents, ensuring the simultaneous release through

reduction of the prodrug. Further anti-cancer agents can be conjugated to the platinum(II) chemotherapeutic drug *via* the axial ligands resulting in multiple anti-proliferative agents within the cell with different targets acting synergistically towards cell death.[24,33] The released axial ligands demonstrate their own cytotoxicity unconnected to the core platinum(II) species.[26,30] The likelihood for a cross-resistance with the DNA-targeting platinum(II) compound is reduced if the chosen biologically active moiety acts independently of the DNA, exhibiting a contrasting mode of activity and triggering distinct cellular responses.[11,29] Examples of dinuclear quadruple action platinum(IV) prodrugs have proven substantially more cytotoxic than their single components. An increase of the therapeutic potential seems particularly promising when combining more than one clinically approved anti-cancer agent.[31]

Scheme 3 shows a multi-modal compound with quadruple action. The dinuclear platinum(IV) complex contains four active entities which are linked together. Dichloroacetate (red) and phenylbutyrate (green) both inhibit specific cellular enzymes whilst pursuing different paths of action, essentially promoting apoptosis. Cleavage of these moieties and their links results in the release of two platinum(II) anti-cancer agents. The quadruple drug displayed distinctly higher cytotoxicity compared to its dual congener or the single platinum(II) complexes, indicating a substantial contribution of the attached bioactive functionalities.[26] Exploiting the rational design of axial ligands on platinum(IV) prodrugs bears the potential for development of multi-active compounds incorporating chemo-, immuno-, phototherapeutic and/or diagnostic properties.[33]

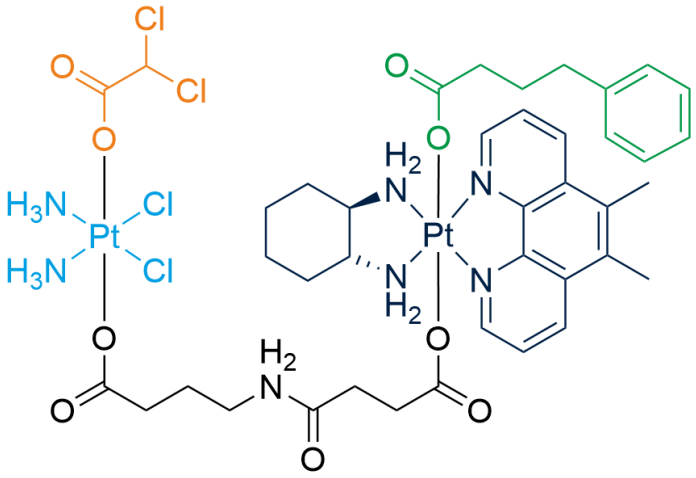

Scheme 3: Dinuclear quadruple-action platinum (IV) prodrug with entities of the multi-modal compound highlighted in different colours.

Scheme 4 depicts a selection of platinum(IV) complexes which have entered clinical trials as anti-cancer prodrug candidates. Tetraplatin, Iproplatin and Satraplatin are among promising prodrug candidates without bioactive moieties, though none of them succeeded in becoming approved for admission.[7,34] Tetraplatin caused severe cumulative neurotoxicity, while Iproplatin did not display significantly higher potency compared to Cisplatin or Carboplatin. The most promising candidate, Satraplatin, was developed in 1992 as the first platinum(IV) prodrug suitable for oral administration. In comparison to Cisplatin, the complex includes two acetato ligands and a cyclohexyl group on the amine ligand which increases the overall lipophilicity of the drug. Satraplatin forms various DNA-adducts that are not recognised by DNA repair proteins.[35] The complex displays relevant levels of concentration in cell lines resistant to Cisplatin, however, the prodrug was observed to reduce prematurely in the

bloodstream, resulting in several products and in poor overall improvement of cytotoxicity compared to platinum(II) anti-cancer agents.[16,36]

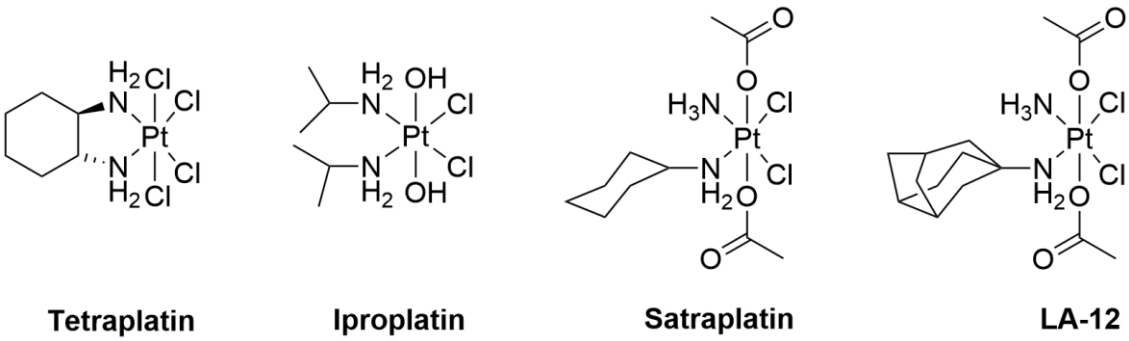

Scheme 4: Selection of platinum(IV) prodrug candidates that have entered clinical trials.

While platinum(IV) prodrugs appear to be better tolerated by patients compared to direct administration of the cytotoxic compound, the drugs are typically discontinued for reasons such as non-conclusive increase in activity or unpredictable side-effects, which at present do not render these compounds viable.[30,33] All platinum(IV) prodrugs that have entered clinical trials in the past did not include bioactive moieties in the axial position and relied on delivery of the cytotoxic platinum(II) anti-cancer agent to the tumour cell. More recent investigations have focused on including axial ligands on the complexes which enhance mitochondrial recognition, over-expressed receptors on cancer cells, or inhibition of cellular processes leading to cell proliferation.[20,24]

Platinum(IV) compounds are commonly accessed *via* oxidation of the corresponding platinum(II) complex. Typical synthetic routes include hydrogen

peroxide or chlorine, carboxylation of the platinum(II) species, or in rarer approaches ligand substitution of a platinum(IV) compound, though, as discussed earlier, the latter is kinetically hindered.[29] The oxidant commonly formerly removes two electrons from the platinum centre and occupies one axial position. The second anion usually is obtained either from the oxidant or the solvent, and takes the position of the second axial ligand. Oxidations with hydrogen peroxide will yield one hydroxido ligand. Depending on the solvent, the second ligand could vary between a second hydroxido ligand for water, to a methoxido ligand for methanol or an acetato ligand for acetic acid. Neat halogens as oxidation agents typically lead to symmetrical products with two halogenido ligands in the axial positions. *N*-chlorosuccinimide and analogues with heavier halogens act as electrophilic halogenation agents displaying “positive halides” which acquire two electrons from the platinum centre. In analogous manner to oxidation with peroxides, the second anion usually is provided by the solvent.[37]

In addition to being coordinatively saturated, the low-spin 5d^6-platinum(IV) centres are more reluctant to undergo undesired side-reactions, display lower interactions with plasma proteins in the blood circulation and reduce the likelihood for systemic toxicity.[16,20,29] Due to steric constraints in the platinum(IV) compounds, DNA lesions *via* ligand substitution appear on the scale of weeks.[11] For this reason, the prodrugs require reduction to their cytotoxic platinum(II) congener before binding to the DNA in the cell.[29] Activation can occur by means of a two-electron reduction forming for instance through molecules such as ascorbate or glutathione, which in many cases are readily expressed in tumour

cells.[11,30] Further reports include reduction of platinum(IV) prodrugs by cellular proteins such as metallothionein or serum albumin.[16,37]

Obtaining remote spatial and temporal control of the drug concentration through the controlled activation at a specific time in a certain region could yield significant improvements in the shortcomings of anti-cancer agents. There are a number of exogenous and endogenous stimuli for the activation of prodrugs. Endogenous stimuli rely on properties connected to the pathological features of the tumour, including a variation in the redox properties, the p*H*-value, or the concentration of certain biomolecules, such as enzymes or hormones. Contrary to this, exogenous stimuli are applied from outside the physiological environment, such as light, temperature, magnetic fields, ultrasound or high energy radiation (Scheme 5).[30,38]

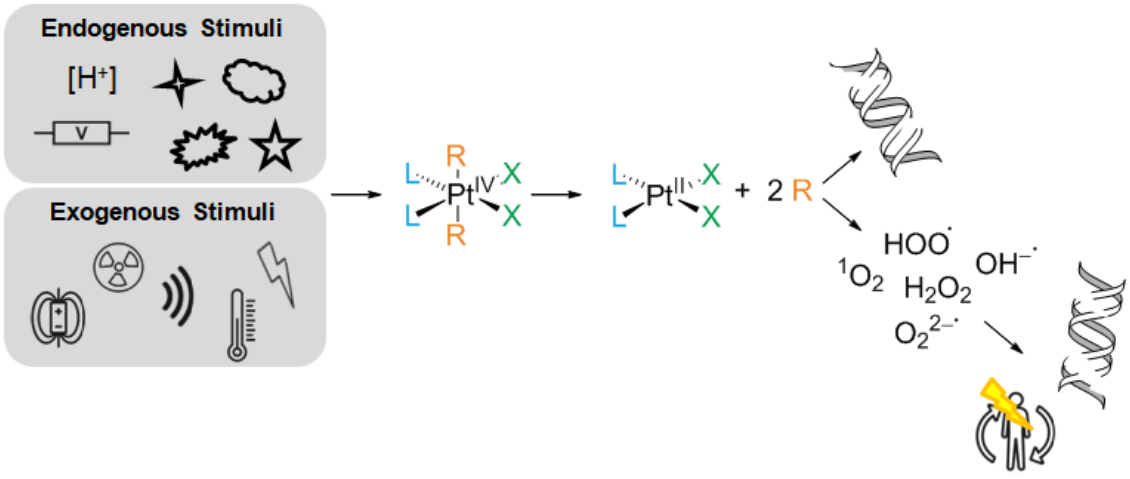

Scheme 5: Schematic overview of the exo- (*e.g.* light, temperature, magnetic fields) and endogenous (*e.g.* p*H*-value, enzymes, hormones) stimuli applied for the activation of platinum(IV) prodrugs and their path of action.

When tuning drugs to become more targeted for tumour cells, applying stimuli that respond to the (metabolic) abnormalities of cancerous tissue can prove fruitful. As a result of proliferation, the extracellular p*H*-value of tumour cells (6.5–6.9) tends to be slightly lower compared to that of healthy tissue (7.4). Due to the up-regulation, the concentration of certain enzymes like protease or glycosidase, or other biomolecules contributing to the redox properties, can be higher in cancer cells. One of the over-expressed reductants is glutathione, which can be found at a fourfold concentration in tumour tissue and accounts significantly for the highly reducing conditions. The redox potential in the cells is pivotal for the evaluation of the activation of redox-sensitive prodrugs.[38]

A change in temperature as an exogenous stimulus is mainly applied to induce changes in drug-carrier systems, *e.g.* the structural transformation of a thermosensitive polymer resulting in the release of the anti-cancer agent.

The application of light as a further exogenous stimulus has received a substantial amount of attention. This is mainly attributed to its non-invasive and highly spatio-temporal properties, realised through the wavelength, the intensity, or the time of exposure. Approaches include the photoinduced structural change of prodrugs, yielding bioactive compounds, or the generation of toxic reactive oxygen species (ROS) resulting from the irradiation of photosensitisers, and will be further discussed in Chapter 1.4.[38]

In successful drug design, all the above-mentioned exogenous and endogenous characteristics could contribute to the selectivity of the compounds by chemical bonds becoming more labile for intended cleavage. The discrepancy between healthy and cancerous tissue typically is marginal, so that the scope for targeted

response is remarkably narrow. Establishing highly stimuli-selective drugs can lead to the differential activation of individual agents incorporated into multi-modal drugs. Next to exo- and endo-stimuli-responsive compounds, a further class are dual-stimuli-responsive drugs. Multiple stimuli attuned in a synergistic manner could overcome challenges regarding targeted delivery and activation, thus improving drug efficacy whilst reducing side-effects. Common combinations are redox- and p*H*-, redox- and light-, p*H*- and light- or biomolecule- and light-responsiveness. To date, no stimuli-responsive metallodrugs have been approved for treatment, as mechanisms relating to their absorption, distribution and metabolism remain to be fully understood.[38] The ideal platinum(IV) prodrug candidate should demonstrate no cytotoxicity, be resistant to hydrolysis or other ligand substitution reactions under physiological conditions, inert to being reduced by biological agents, with its reduction being specifically initiated with a controlled stimulus yielding the release of active agents with synergistic anti-proliferative effects. However, despite the immense advances in this field, further research is necessary to render suitable complexes.[37]

1.3 Phosphine Ligands in Anti-Cancer Agents

Following the serendipitous discovery of Cisplatin, the main focus of metal-based anti-cancer agents has been on complexes with *N*-donor ligands and the variation of monodentate or bidentate amine derivatives. Platinum-phosphine complexes have gained substantial attention in coordination chemistry due to the stability of the Pt–P bond stemming from the high affinity of platinum for

phosphorus. ^{31}P NMR spectroscopy poses a useful analytical handle and characterisation technique for metal-phosphine complexes. Compared to platinum complexes with *N*-donor ligands, studies screening the biological and pharmaceutical activity of analogous compounds incorporating their heavier analogues are limited.[39] However, the properties which render metal-phosphine complexes appealing for catalysis, further qualify them for medicinal applications, including anti-inflammatory, antibacterial and anti-cancer activities.[40] Auranofin is the first example of a metal-phosphine complex to demonstrate anti-cancer activity (Scheme 6). The gold(I)-phosphine prodrug was clinically approved in 1985 for the treatment of rheumatoid arthritis. Since its initial clinical profile, it has been applied for the treatment of multiple other diseases including tuberculosis, acute respiratory syndrome in the coronavirus disease Covid-19 as well as in cancer therapy. In particular its interaction with the thioredoxin reductase system within cells has made it a viable candidate as an anti-cancer agent. The antioxidant enzymes are both found in the cytoplasm and mitochondria and regulate the levels of reactive oxygen species within the cell. The enzymes are commonly over-expressed in cancerous tissue, preventing anti-cancer agents from inducing apoptosis which is directly related to a poor prognosis for the patients' survival. Auranofin acts as an inhibitor to thioredoxin reductases consequently leading to a cellular concentration of reactive oxygen species inducing cell death.[41,42] The complex has demonstrated acute potency towards leukaemia and ovarian malignancies. The high activity of Auranofin has led to the development of further gold(I) complexes with medicinal applications. Examples include triphenylphosphinegold(I) compounds with cytotoxic properties twentyfold those of Cisplatin for certain cell lines.[43] After discovering its mode of

action, a focus on gold(I)-phosphine complexes with an effective inhibition of thioredoxin reductase, particularly in mitochondria, has emerged.[44,45]

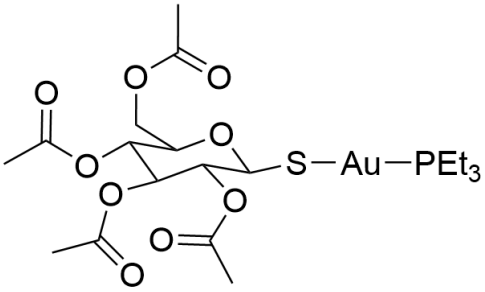

Auranofin
(worldwide)

Scheme 6: First metal-phosphine complex to demonstrate anti-cancer activity approved worldwide for the treatment of rheumatoid arthritis.

Building on the success of Auranofin, several metal phosphine complexes have been investigated for cancer treatment. Since platinum phosphine compounds have also displayed restraining effects on thioredoxin reductase, the phosphine ligands themselves appear to play a critical role in the blockage of these antioxidant enzymes.[40] Whilst the hydrophilicity of a compound is directly related to its solubility in water and its ability to be administered into the blood stream, the lipophilicity of a compound is decisive in terms of the accumulation of anti-cancer agents in cells. Phosphine ligands with non-polar substituents can modify the lipophilic character of a complex and influence its bioavailability and cytotoxicity. Incorporating sterically more demanding ligands of hydrophobic character could lead to enhanced drug uptake into the cell. The choice of tertiary

phosphines greatly affects the biological activity of the metal complex.[46,47] Investigations of the structure-activity relationship of complexes including diphosphine and phosphinopyridyl ligands indicated selectivity for uptake of the agent into cancerous *vs* healthy cells could be influenced by adjusting the lipophilic properties of the compound.[48]

Reports of platinum(II) complexes with phosphine ligands being investigated as anti-cancer agents have been steadily increasing.[39,49–54] Examples include ligand substitution of amine ligands with triphenylphosphine on a platinum(II) complex leading to enhanced cytotoxicity,[47] chloridosaccharinateplatinum(II) complexes with diphenylbenzylphosphine ligands demonstrating extremely high potency surpassing that of Cisplatin attributed to the increased cellular uptake due to the increased lipophilicity of the complex,[46] or a dithiocarbazate triphenylphosphineplatinum(II) compound displaying cytotoxicity on four human cell lines.[55]

1.4 Irradiation of Anti-Cancer Agents

O. Raab was the first to report the cytotoxic effect of chemicals under the irradiation of light in 1900.[56,57] Following from this, the term “photodynamic” was introduced in 1907 by H. von Tappeiner, referring to photosensitisation after irradiating the dye eosin in cancer cells with visible light. Cell death occurred due to an interplay of the three main components of photodynamic therapy (PDT): a photosensitiser, light of a wavelength corresponding to the photosensitiser and molecular oxygen. Despite extensive research, it was not until 88 years later that

a hematoporphyrin derivative commercially known under the name Photofrin, was released for clinical application as the first FDA-approved photosensitive drug.[57] Absorption of light leads to a singlet excited state of the photosensitiser with multiple possibilities for dissipation of this energy back to the ground state (Figure 2). One possibility is the direct radiative decay from the S^1 to the S^0 state releasing a photon of lower energy than the incident photon as fluorescence. An alternative pathway is a non-radiative vibration in which the relaxation is mediated by the collision with further molecules generating heat. Another option is intersystem crossing resulting in excited triplet states T^1 of the photosensitiser. Subsequent reactions of the triplet state with water or molecular oxygen form reactive oxygen species (ROS), either through the direct transfer of electrons (Type I PDT), or through the sensitisation of triplet oxygen to form singlet oxygen $^1O_2$ (Type II PDT).[57–61] The high reactivity of ROS towards the oxidation of biomolecules in cells such as nucleic acids, proteins or lipids illustrate the mode of toxicity, causing severe damage to cancer cells due to necrosis, apoptosis, autophagy or ferroptosis.[57,59]

PDT is discussed as one of the most effective available cancer treatments due to high therapeutic efficiency and selectivity, whilst being minimally invasive and displaying low side-effects. However, its dependence on oxygen and light exhibits a severe disadvantage. Due to malignant proliferation and the rapid growth of tumour cells, the poor microvasculature leads to a lack of oxygen supply in the cancer tissue. In addition, although the effectiveness of PDT heavily relies on molecular oxygen levels, its toxicity destroys blood vessels resulting in

even lower concentrations of oxygen, creating an intrinsic limitation to the treatment.[56–58]

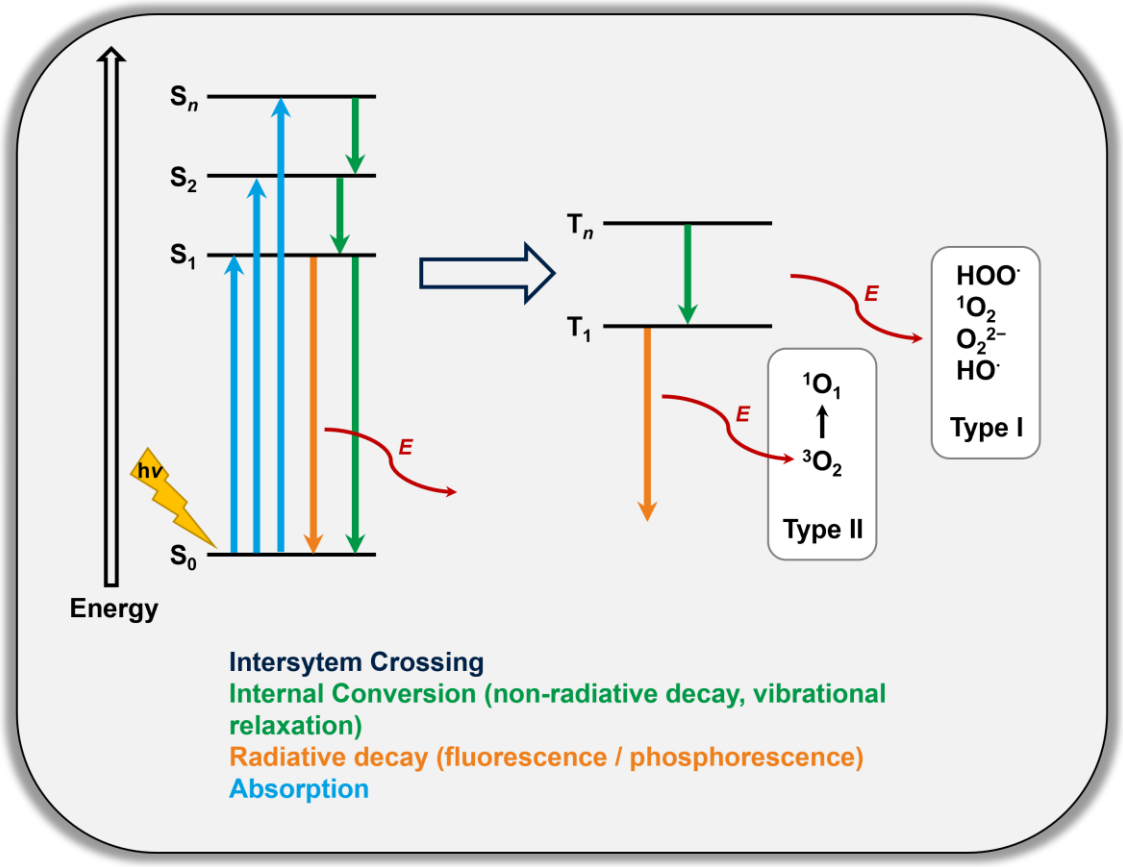

Figure 2: Schematic representation of the mechanism of photosensitisation describing Type I and Type II PDT.[59,61,62]

The application of light as an essential component of PDT poses a further constraint on the treatment. Photoresponsive anti-cancer agents are hampered by the limitations imposed by the radiation. Shorter wavelengths (300–500 nm) can penetrate skin up to 3 mm and are hindered by absorption of chromophores such as melanin and haemoglobin, or by scattering processes. Wavelengths

longer than 950 nm are strongly absorbed by water, leading to the optimal wavelengths for tissue penetration being 650–950 nm. While wavelengths shorter than 450 nm can inflict biological damage due to photolysis, wavelengths in the range of 650–750 nm, although energetically much weaker, can penetrate tissue up to 5 mm (Figure 3). The photobiological effects of wavelengths longer than 1000 nm have yet to be investigated more extensively.[63–65] The processes initiated by the radiation depend on both the energy, *i.e*. the wavelength, and the intensity of the light applied. Selective photolysis of certain compounds at the site of illumination can result in interference with intercellular metabolic pathways. Photoresponsive compounds can be prepared by modifying a biologically relevant functional group with a photocleavable moiety. Upon radiation, the dormant inactive molecule is activated through cleavage of the added moiety yielding full restoration of the bioactive functionality.[64] The addition of a common fluorophore responsive to longer wavelengths could improve the activation of compounds in deeper tissue.[65]

Commonly, light sources with wavelengths of >620 nm are applied in PDT and green light is used for more superficial tumours.[57,58,60] The spot size of the radiation source influences the penetration and dispersion of the light in the tissue, with an increasing spot size inducing less lateral scattering and deeper penetration.[63] Technological advances have helped to increase the penetration depth of irradiation of shorter wavelengths. Lasers and optical fibres within transparent needles for endoscopic procedures or specific LEDs enable the delivery of light to deeper regions of the body through administration.[57,58,60]

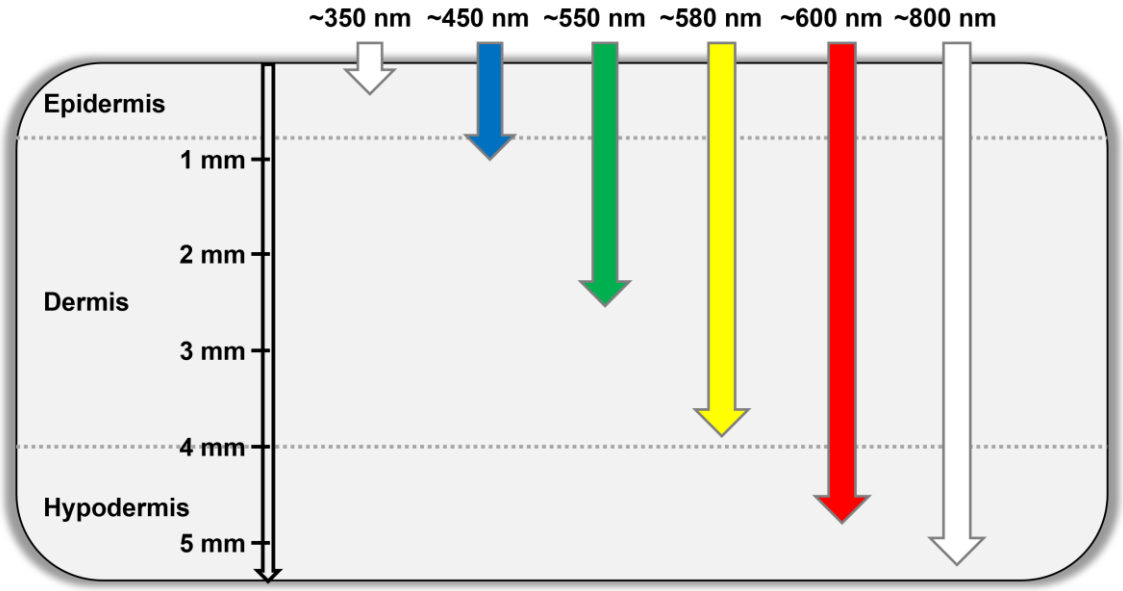

Figure 3: Schematic visualisation of the penetration depth of light into skin according to its wavelength.[57,63]

The compound class of porphyrins has been extensively studied as photosensitisers for PDT, due to their inherent properties in light absorption which is converted to energy and heat in cancerous tissue. The first generation of photosensitisers for PDT were based on hematoporphyrins, however, they were restricted by challenges regarding their chemical purity. Second generation photosensitisers aimed at overcoming these limitations by designing well-defined structures with high chemical purity. Benzoporphyrin derivatives and phthalocyanines were explored, which demonstrated poor water solubility, leading to difficulties in intravenous administration. Finally, the third generation of photosensitisers incorporated targeting and delivery moieties, such as antibodies, nucleic acids or vitamins, with the goal of increasing the selectivity of the compounds.

The ideal photosensitiser for PDT can be administered easily and demonstrates properties promoting tumour-specific accumulation, absorption at longer wavelengths, such as red or the near-infrared light to facilitate treatment of cancer in deeper tissue, with low toxicity in the dark. The solubility of hydrophobic compounds could be enhanced through the addition of hydrophilic substituents or incorporation of the drug in liposomes or nanocarriers. Despite the efforts and research regarding photosensitisers, only three photosensitisers have, to date, been approved worldwide (Scheme 7), with Photofrin remaining the dominant candidate for PDT albeit displaying low red-light absorption and poor cancer selectivity. [56,59,60,66]

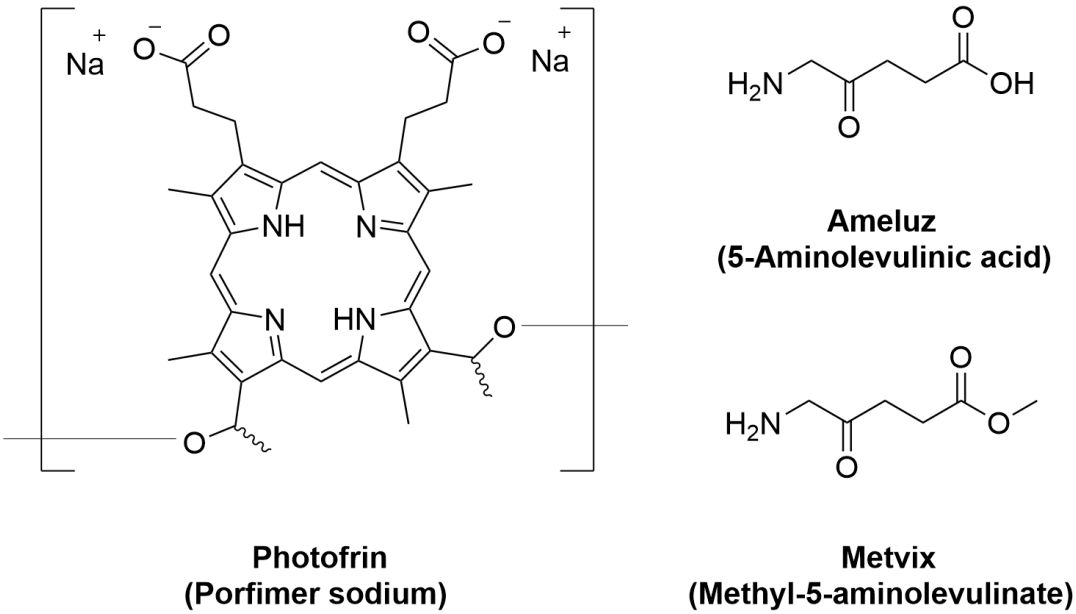

Scheme 7: Current photosensitisers that have been approved worldwide for admission.

Due to the ready modification of photophysical properties *via* ligand choice, a number of coordination compounds have been investigated as suitable photosensitisers. Phorbiplatin (Scheme 8) was the first platinum(IV) prodrug functionalising an electron transfer process from a reductant to the metal centre upon irradiation with red light. The reduction and activity of the multi-modal prodrug releases the chemotherapeutic Oxaliplatin as well as pyropheophorbide-*a* (PPA). Phorbiplatin shows superior cellular accumulation and cytotoxicity in comparison to Oxaliplatin.[67]

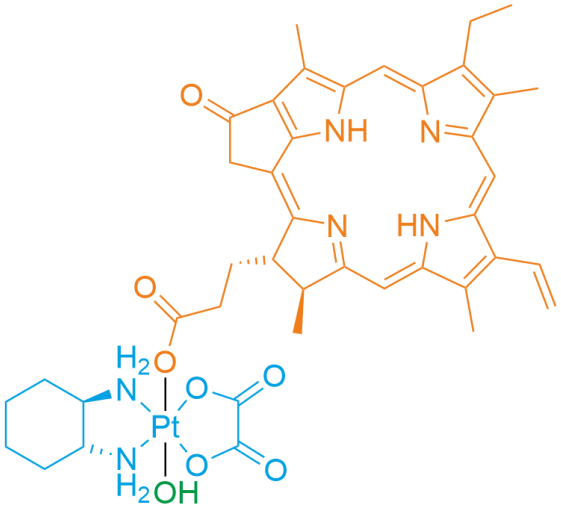

Scheme 8: Dual-action platinum (IV) prodrug Phorbiplatin with Oxaliplatin in blue, pyropheophorbide-*a* in orange and the hydroxy group in green.

Irradiation with significantly shorter wavelength and higher energy, such as X-rays in radiotherapy, allows for deeper penetration into the tissue. With penetration depths of >10 cm, all regions in the body can be targeted.[12,61] The X-rays can either cause direct lesion of the DNA or induce indirect toxicity through the interaction with water resulting in the generation of ROS. Materials with heavy

atoms, such as platinum or gold, exhibit large X-ray attenuation coefficients, presenting a synthetic strategy of minimising excessive radiation doses. Both Carboplatin and Oxaliplatin have shown activity as radiosensitisers. The combination of photosensitisers activated following the irradiation with X-rays (radiosensitisers) in X-ray photodynamic therapy (X-PDT), allows the treatment of deep-seated cancers with lower radiation doses compared to radiotherapy alone.[12] After the effects of X-rays on porphyrin were first investigated in 1955, X-PDT utilising porphyrin-based compounds as sensitisers commenced in 2006. With penetration depths of 1–40 cm, X-PDT builds on the advantage of low-invasiveness whilst overcoming the challenge of accessing deeper tissue in regular PDT.[68] However, it must be noted that the X-rays will cause an adverse affect on healthy tissue as well. While irradiation of surrounding tissue of the target region should be minimised, it usually cannot be prevented entirely.[12,57,61,69]

Applying metal complexes as sensitisers can improve the stability and photocytotoxic response, in particular following irradiation with X-rays.[60] The possibility of multi-functionality in metal complexes bears a lot of potential for the combination of moieties of different activity. Examples include triphenylphosphine ligands demonstrating targetability of mitochondria as an alternative route of toxicity. Gold(I) compounds with triphenylphosphine or triethylphosphine ligands have displayed high modes of cytotoxicity. Similarly, terpyridylplatinum(II) with a triphenylphosphine ligand has exhibited cytotoxicity towards Cisplatin-resistant ovarian cancer cells.[12,14]

The youngest prominent development in the evolution of light-responsive anti-cancer agents responding to irradiation is the class of photoactivatable chemotherapy (PACT). Interaction of light with the chemotherapeutic compound generates short-lived excited states inducing changes in the molecular formula, which subsequently results in an alteration of the physical and biological activity of the complex. Ideally, the compound will display no biological activity in the non-radiated form and strong biological activity upon irradiation, enabling spatial and temporal control of the cytotoxic activity of the chemotherapeutic agent and allowing targeted site-activation at the tumour to minimise side-effects.[12,62,70,71] Metal compounds have been explored extensively as candidates for PACT. In particular, heavy metals have been of interest due to their strong spin-orbit coupling which promotes intersystem crossing of excited states. The photophysical and chemical properties of noble metal photosensitisers can be readily modified through the ligands. More specifically, the choice of ligands can help navigate challenges regarding solubility, lipophilicity, absorption bands and targetability.[59]

The concept was introduced in the early 1990s by H. Morrison who reported on a rhodium(III) compound which required UV-light for activation. In 1996, P. J. Bednarski demonstrated pioneering research on photoactivatable platinum(IV) complexes with iodido and amine ligands. The complexes exhibited photoreductive elimination by ligand-to-metal-charge-transfer (LMCT) upon irradiation around 400 nm. After undergoing structural changes, the resulting compound could bind to DNA in cancer cells.[70] The term “photoactivated chemotherapy” was proposed by P. J. Sadler in 2009.[62]

Typical modes of activation of complexes for PACT can be divided into three classes. The first group includes platinum(IV) or similar centres which are reduced upon irradiation within the cell to produce the corresponding cytotoxic platinum(II) analogues. Another class describes the activation of d^6-metal centres. Absorption of light induces an excited metal-to-ligand-charge-transfer ^{3}MLCT, leading to an energetically lower triplet metal centre state displaying a strong dissociative character through the population of σ-antibonding orbitals along a metal-ligand bond. The oxidation states of neither the metal, nor the ligand are changed and commonly, the ligand is substituted by a solvent molecule. The third group of activation describes a C–C bond cleavage *via* photoabsorption by the heavy metal. While LMCT excitations account for a large portion of the photochemistry of platinum(IV) complexes, energetically lower *d*–*d*-transitions are also feasible.

A distinct difference between PDT and PACT lies in the photochemical properties of the photosensitisers. In PDT the photosensitiser in principle is photostable and energy transfer of the excited states results in generation of the active species. However, in PACT, the photosensitisers themselves are the photoactive compounds which decompose under light producing the bioactive entities. Since the photochemical activation of the platinum(IV) compound is irreversible, the photoproducts are required to display high toxicity. Either the released ligand, or the structurally altered metal-complex – or both – can act as the source of biological activation. The combination of multiple active moieties on the prodrug poses as a great opportunity for the development of more efficient drugs.[71,72] Whilst the absorption spectrum of a complex can provide valuable insight into a suitable excitation wavelength, there have been reports in literature illustrating

photoactivity of platinum(IV) complexes due to energetically low-lying LMCT states, although no absorption was recorded in the UV-visible spectra for the respective wavelengths.[62]

Platinum(IV) and platinum(II) complexes have both been investigated for PACT. Platinum(IV) compounds are prodrugs and require a reduction to platinum(II) to yield the bioactive species. With platinum(II) complexes, photoactivation commonly results in the removal of a pre-blocking activity. Nitrophenyl groups have been reported to block the biological activity of biomolecules until exposure to light induces cleavage of the group in the ligand backbone, resulting in a cytotoxic platinum(II) species. Similarly, Carboplatin has demonstrated enhanced DNA interaction under irradiation, which is suspected to be a result of photolysis of the platinum-oxygen bond.[70]

Azidoplatinum(IV) complexes were reported to undergo reductive elimination of the azido ligand following irradiation by A. Vogler in 1980. Building from this, P. J. Sadler performed in-depth research on the photoreduction of diazidoplatinum(IV) complexes yielding cytotoxic platinum(II) compounds. Complexes of the general formula [Pt(N_1)(N_2)(L_1)(L_2)(A_1)(A_2)] with N_1 and N_2 as non-leaving ligands, L_1 and L_2 as leaving ligands and A_1 and A_2 as axial ligands were investigated. The leaving ligand dissociates from the platinum centre following irradiation, yielding it a key component in PACT. A broad range of amines including aliphatic and aromatic groups have been explored as non-leaving ligands. Axial modifications span targeting moieties or functionalities aiding delivery strategies. Applying azides as the leaving ligands appeared to be highly beneficial: the electronic properties of the metal complex are modified to a

small LMCT ($N_3 \rightarrow Pt$) transition energy, causing facile reduction following irradiation. Reductive elimination results in the release of toxic azidyl radicals as well as the platinum(II) species which continue to form DNA-cross-links. Sadler and co-workers inspected the structure-activity relationship of diazidoplatinum(IV) compounds moving from ammine ligands to *N*-heterocycles as the non-leaving group ligands. Complexes with pyridine exhibited strong cytotoxicity following absorption in the blue region. The results were attributed to LMCT and inter-ligand transitions inducing the cleavage of azidyl radicals with a dipyridylplatinum(II) complex binding to the DNA. Incorporating arene-derivatives as the non-leaving ligand promotes interaction with DNA due to *π*-stacking. When comparing the cytotoxicity of both *cis*- and *trans*-isomers of the complexes, the *trans*-isomers usually are more potent, presumably due to the formation of multiple DNA cross-links in the cells. It was further observed that conjugated ligands promote photoactivity and resulting cytotoxicity of the platinum complexes significantly. Overall, the investigations showed that besides diazidoplatinum(IV) derivatives of Cisplatin and Oxaliplatin, exploring complexes of a general formula *trans*-$[Pt(N_3)_2(py)_2(OR^1)(OR^2)]$ tend to display photoactivation with blue or green light and are highly cytotoxic. While a selection of platinum(IV) prodrugs have entered clinical trials in the past, no photoactivatable platinum(IV) prodrug has been suitable for clinical trials thus far.[73,74]

The high stability of diazidoplatinum(IV) in the dark paired with the readiness for decomposition following irradiation with visible light into cytotoxic azidyl radicals as well as a DNA-binding species, renders this group of compounds promising

candidates for PACT. High versatility in ligand choice affords scope for targeting strategies, as well as possible modification of the absorption profile.[60] With the photoreduction of platinum(IV) prodrugs, spontaneous cellular reduction is replaced by radiation-induced reduction enabling control over the activation.[70] While PDT finds clinical application, thus far no PACT compounds have reached the clinic. Exploiting the crucial differences between PDT and PACT can help promote PACT as an approach to cancer therapy. As discussed previously, the effectiveness of PDT heavily relies on the supply of molecular oxygen in the tumour tissue, albeit, cancer cells often are hypoxic. As the mode of action in PACT does not require oxygen and is independent of redox stress within the cells, hypoxic tumours could be a promising target for PACT. However, as the lack of oxygen often is a consequence from poor tumour vasculature, efficient delivery of the compounds to the cancerous tissue remains a serious challenge and future development of complexes for PACT will have to address strategies. Efforts in overcoming difficulties with respect to penetration depth of light in PDT are applicable to PACT. A majority of explored photoactivatable platinum(IV) prodrugs can be activated by UV- and blue light which both display poor tissue penetration, creating a demand for candidates responding to longer wavelengths.[37,71]

1.5 [2+3]-Cycloaddition Reactions of Platinum Complexes

The concept of [2+3]-cycloaddition reactions between azides and alkynes were first described in the scope of 1,3-dipolar cycloaddition reactions by R. Huisgen

in 1963. The generalised conception included two reagents forming a cyclic compound under the expense of two *π*-bonds and the creation of two new *σ*-bonds.[75,76] The products are regio-isomers of aromatic heterocycles, more specifically, a mixture of 1,4- and 1,5-triazoles. It was not until 2001, that K. B. Sharpless coined the term “Click reaction” for the description of facile stereospecific [2+3]-cycloaddition reactions with high yields and negligible side-products. The key difference to Huisgen’s approach was the utilisation of *in situ* generated copper(I) salts catalysing the reaction between the azide and alkyne. Applying copper(I) increases the reaction rate significantly and enables the formation of regioselective 1,4-disubstituted 1,2,3-triazoles at mild temperatures.[77–81] Copper-catalysed azide-alkyne cycloadditions (CuAAC) revolutionised the synthetic linkage of C–C and C–N bonds whilst exhibiting excellent functional group tolerance, high selectivity and atom efficiency. The key step in the synthesis is the deprotonation of the alkyne leading to a copper(I)-acetylido complex with additional *π*-complexation of another copper centre reducing the electron-density of the *sp*-hybridsised carbon atoms, and with that increasing its reactivity. Identifying the core step to the mechanism simultaneously reveals the main restriction of CuAAC: a limitation to terminal alkynes.[77,78] Additionally, due to the toxicity of copper(I) species, the synthetic systems described by Sharpless could not be applied in a biological context.[80,82] A more generalised approach to metal-catalysed azide-alkyne cycloaddition (MAAC) reactions include the addition of other metals such as silver-, iridium- or tin-based compounds, as well as gold nanoparticles.[77] Realising that the activation of the alkyne was the breakthrough in Click reactions, it was C. R. Bertozzi who noticed reports from G. Wittig and A. Krebs dating back as far as

1961 informing on compounds with ringstrain significantly promoting reactivities in cycloaddition reactions.[79,80,83] This observation lead to the discovery of strain-promoted azide-alkyne cycloadditions (SPAAC) in 2004 by Bertozzi and co-workers. Cyclooctyne and its derivatives have been thoroughly explored for selective Click reactions without the necessity of a catalyst, rendering them suitable under physiological conditions.[79,80] Further modifications of the strained ring such as the addition of electron-withdrawing atoms or groups, *e.g*. fluorides, can increase the C–C–C bond angle further, adding to the strain and the reactivity of the ring.[84] However, the versatility of the substituents to the triple bond appears to be somewhat restricted to synthetically accessible alterations of cyclooctyne.[82]

The term “iClick” as a short-hand for inorganic Click reactions was introduced by A. S. Veige and co-workers in 2011 who completed the [2+3]-cycloaddition reaction between a diazidoplatinum(II) complex and a gold(I) alkyne leading to a bimetallic complex. This was the first example of two metal compounds undergoing a Click reaction. Compared to promoting the reactivity of the alkyne with help of a catalyst or ringstrain, the addition of an electron-poor metal centre effectively withdrawing electron-density from the C–C triple bond activates the alkyne. In contrast to the products of CuAAC reactions, iClick reactions result in the selective formation of trisubstituted 1,4,5-triazoles.[82,85] With the cycloaddition reaction occurring in the inner coordination sphere of the metal centres, the choice of additional ligands plays a substantial role in their reactivity. Successful cycloaddition reactions of diazidoplatinum(II) complexes have been demonstrated with a range of functional groups incorporating triple bonds, such as acetylides, isocyanides or nitriles. The main limitation to iClick reactions is the

requirement for disubstituted alkynes. Applying terminal alkynes can lead to unintended side-products such as ligand substitution of the azido ligands and end-on binding of the alkyne to the platinum centre. In comparison to diazidoplatinum(II), the more electron-deficient platinum(IV) complexes have displayed significantly lower reactivity towards Click reactions with electron-deficient alkynes.[82]

Figure 4 depicts a schematic overview of the variations of the [2+3]-cycloaddition reaction.

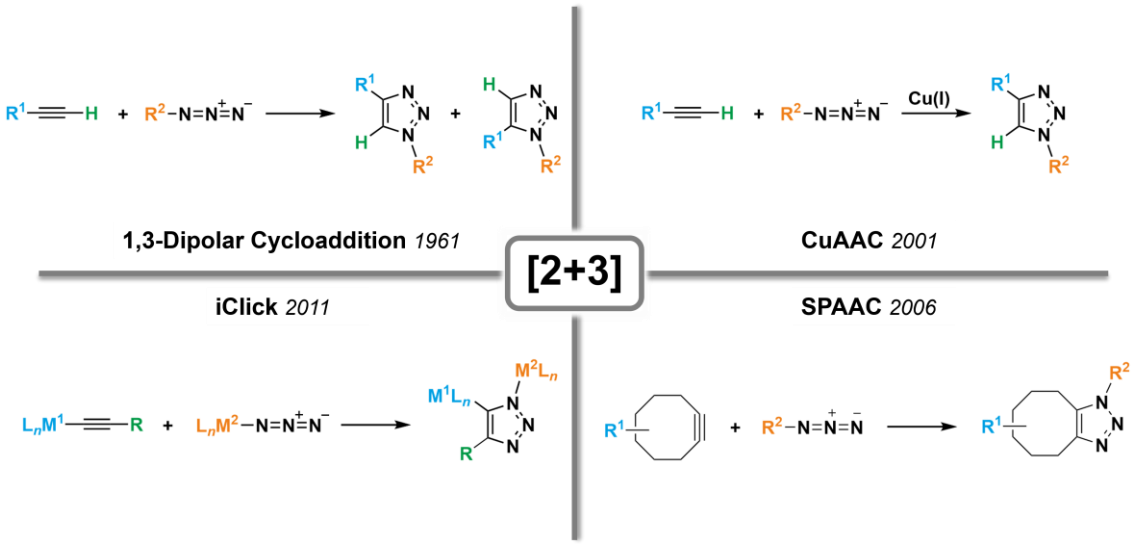

Figure 4: Schematic overview of 1,3-dipolar cycloadditions, CuAAC, SPAAC and iClick reactions as variations to the [2+3]-cycloaddition reaction.

Overall, the evolution of [2+3]-cycloaddition reactions since being first described 61 years ago has enabled simple and straightforward strategies for the design of metal complexes which has had a crucial impact in the field of drug discovery,

imaging and biomedical engineering.[78,80] Click reactions facilitate the functionalisation of platinum-based drugs amongst which are targeting moieties, delivery systems or fluorescent reporters for theranostics. In addition, they can be exploited as a platform in the preparation of platinum(IV) prodrugs through the modification with secondary chemotherapeutics, yielding multi-modal drugs.[11,82]

1.6 ^{195}Pt NMR Spectroscopy

Of the 32 known isotopes of the noble transition metal platinum, merely the three ^{194}Pt, ^{195}Pt and ^{196}Pt display noteworthy natural abundances of 32.9%, 33.8% and 25.3%, respectively. With a nuclear spin of one half, ^{195}Pt is the only NMR-active isotope.[86,87] The combination of its abundance and its gyromagnetic ratio ($5.768 \cdot 10^7$ rad$\cdot$s$^{-1}\cdot$T^{-1}), results in NMR spectra of low signal-to-noise ratio and a receptivity of 0.0034 relative to ^{1}H. The frequency range in which resonances appear for ^{195}Pt nuclei spans an extensive width of 15 000 ppm, compared to 300 ppm for ^{13}C and 15 ppm for ^{1}H (for diamagnetic compounds).[88] As the chemical shift of platinum nuclei is highly influenced by the nature of the ligands in the coordination sphere of the complex, each platinum species will provide a unique resonance dependent on its environment. Upon applying an external magnetic field, the electrons within the compound create an opposing magnetic field, shielding the external field. Closer nuclei are affected more strongly by the shielding effect.[86] The chemical shift tensor can be described as a sum of paramagnetic, diamagnetic and extraneous components under consideration of spin-orbit relativistic effects. The diamagnetic term is the most dominant

component and describes the local spherical electron density around the nucleus, which increases with heavier elements but is identical for all platinum(II) nuclei. In contrast, the paramagnetic contribution is a correction term and considers the non-spherical charge distribution around the nuclei causing displacement to a lower field. The extraneous component accounts for various anisotropic contributions such as substituents, ring currents originating from aromatic components or intermolecular forces like hydrogen bonding. The chemical shift of a nucleus is an anisotropic value which is averaged in solution NMR spectroscopy due to rapid motion of the compounds.[86,88]

The frequency of the chemical shift is highly susceptible to changes in the oxidation state of the metal centre, ligand substitution and the geometry of the complex. All contributions leading to a reduction in electron density around the platinum nucleus, create deshielding and induce a shift of the signals to higher frequencies (downfield). Oxidising platinum(0) centres to platinum(II) and further to platinum(IV) compounds, removes electron density from the metal centre incurring a downfield shift. Conversely, the coordination of polar solvent molecules, such as water, on a platinum(II) ion can increase the electron density close to the ^{195}Pt nucleus, resulting in higher shielding and an upfield shift (lower frequencies) of the signal. Complexes with sterically demanding ligands often reduce intermolecular effects such as the coordination of solvents, and lead to deshielding of the platinum centre. Shielding effects due to the geometry of the ligands are determined by the extent of the σ- and π-bonding between the donor atom and the metal. A strong σ-donor shifts electron density from the ligand to the platinum, however, in the event of π-back bonding, electron density is

reduced on the platinum and increased on the ligand, often under shortening of the platinum-ligand bond.[87,88] The resonances for platinum(II) complexes with triethylphosphine, tripropylphosphine and tributylphosphine ligands shift to lower frequencies in that order due to an increase in their strength as σ-donors.[89] In contrast, sterically more demanding and weaker σ-donating triphenylphosphine ligands display a lengthening of the platinum-phosphorus bond and deshielding of the platinum centre.[87,90] Chemical shifts of *cis*-isomers appear at lower frequencies than those of the corresponding *trans*-isomers. In addition, the values usually shift upfield when progressing down to heavier analogues of an element. Group 15 poses an exception to this observation and resonances appear at lower frequencies along the following series: N < Sb < As <P.
The chemical shift recedes in the example of $[PtX_2L_2]$ (X = halido ligands, L = ligand) as a result of the influence of the ligand geometry when X and L exhibit similar electron donating properties.[91]

With a natural abundance of 32.9% and 25.3%, respectively, signals corresponding to NMR-silent ^{194}Pt and ^{196}Pt nuclei appear unchanged in NMR spectra. However, in 33.8% of the compounds in a sample, coupling to ^{195}Pt centres will occur as Pt-satellites. If the main resonance appears as a singlet, the spectrum will display a singlet together with a doublet of significantly lower intensity. The strength of the satellites depends on the frequency of the spectrometer. Due to the chemical shift anisotropy, an increase of the applied magnetic field results in a decrease of the intensities.[88] Spin-spin coupling between two nuclei in a complex is composed of three main terms: the interactions of orbital electronic currents with nuclear magnetic moments leading

to secondary magnetic fields which influence other nuclei in the compound; dipole-dipole interactions describing the interaction between the magnetic moments of the nuclei with those of the electrons; and finally the Fermi contact term, which considers the magnetic moments of electrons in binding orbitals.[92] The latter poses the dominant contribution to the coupling. As a result of this, the magnitude of the coupling constant can be directly related to the level of *s*-components with a finite electron probability density within the binding orbitals.[86,93,94] Ligands with stronger *π*-acceptor properties display larger coupling constants, compared to strong *σ*-donors. As an example, $^{1}J(^{31}P, ^{195}Pt)$ coupling constants increase for both *cis*- and *trans*-isomers when changing from alkyl to phenyl substituted phosphine ligands in platinum complexes.[89]

With $^{1}J(^{1}H, ^{195}Pt) > 1000$ Hz and $^{1}J(^{31}P, ^{195}Pt) > 2000$ Hz, spin-spin interactions in platinum complexes vary over several orders of magnitude depending on the involved nuclei.[87] Platinum complexes in the higher oxidation state +IV exhibit a smaller *s*-component along the platinum-ligand bond. The *s*-character of the involved orbitals along the bond is directly proportional to its covalency, which can diverge significantly by the nature of the ligand as well as the geometry of the complex.[93] The magnitude of ^{1}J-coupling constants in phosphine platinum complexes is larger for *cis*-configuration of the ligands compared to the corresponding *trans*-isomers, indicating an increase of *s*-character along the metal-ligand bond in *cis*-isomers. It was further observed that the platinum-phosphorus bond often is longer for *cis*-configuration, suggesting that an increase in bond energy might result from an increase in the *s*-component. The variation of selected anionic ligands with different donor and acceptor properties within analogous compounds leads to a change in the coupling constant in the

following order Cl > Br > NCS > I > CN, suggesting that the ligands display less overlap with the σ-orbitals of the platinum centre, effectively reducing the covalent character of the metal-ligand bond.[94] Thus, the magnitude of ^{1}J-couping provides diagnostic value for the geometry of the compounds and can be applied to estimate hybridisation and the nature of bonding within the platinum complexes.[88,92]

With the advancement of the applicable magnetic fields for NMR spectrometers, the prominence of ^{195}Pt NMR spectroscopy in pharmaceutical chemistry and industrial applications has grown substantially. In particular, its significance in determining kinetics and mechanistic details of ligand displacement in drug binding studies has hugely contributed to the field of unprecedented biological and chemical processes of platinum-based anti-cancer agents. Explorations with ^{195}Pt NMR spectroscopy have been applied to investigate the mechanism of Cisplatin and Transplatin binding to the DNA, leading to the identification of multiple platinum-DNA adducts. Upon displacement of the chlorido ligands and binding of the platinum-backbone to N7 of the purine base guanine, monofunctional and bifunctional platinum-DNA adducts can be determined due to new resonances appearing at lower frequencies from the signal corresponding to Cisplatin. Considering the supposed difference in cytotoxicity of *cis*- and *trans*-isomers of platinum(II) anti-cancer agents, ligand substitution of Transplatin in solution has been thoroughly studied *via* NMR spectroscopy with a selection of ligands, including aqua, chlorido, nitrato, sulfato, acetato and phosphato ligands.[87,88,95]

Figure 5 provides a schematic overview of some of the influences on the magnitudes of the chemical shift as well as on the $^{1}J(^{31}P, ^{195}Pt)$ coupling constant in phosphine platinum complexes.

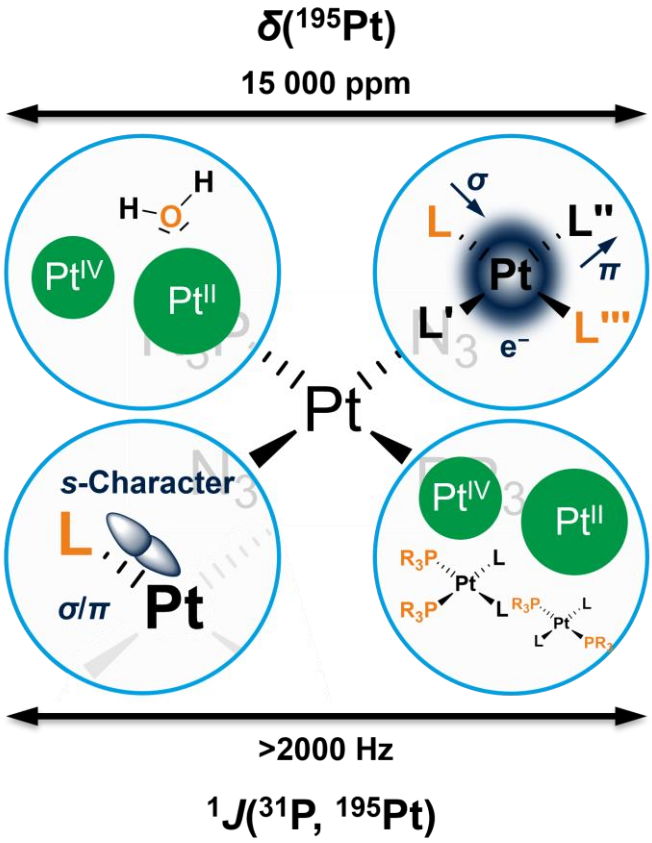

Figure 5: Schematic overview of the main influences on the magnitudes of the chemical shift $\delta(^{195}Pt)$ and the $^{1}J(^{31}P, ^{195}Pt)$ coupling constant in ^{195}Pt NMR spectroscopy of phosphine platinum complexes.

1.7 Aims and Objectives

The rationale behind this research is the synthesis and isolation of phosphine-based platinum(II)-gold(I) complexes with potential for applications as multi-modal anti-cancer agents. To this end, suitable diazidodiphosphineplatinum(II)

complexes and gold(I) alkynes will be identified for [2+3]-cycloaddition reactions. Oxidation of the compounds to less reactive platinum(IV) complexes will be pursued in order to explore their future as anti-cancer prodrugs. ^{31}P and ^{195}Pt NMR spectroscopy will provide a strong experimental handle for monitoring the reactivity and properties of the respective complexes.

After isolating successful candidates, the compounds' properties as photosensitisers with visible light, as well as their responsiveness to X-rays and their aptitude as radiosensitisers will be probed. Cytotoxicity studies will be carried out in collaboration with the research group of Prof G. Higgins in the Department of Oncology of the University of Oxford.

While the platinum (II) and gold (I) complexes will be notated in their sum formula such as *cis*-$[Pt(N_3)_2(PR_3)_2]$ with R = Et, Ph or $[Au(PPh_3)(CC(C_6H_4)X]$ with X = NO_2, Br, CN, the cycloaddition reaction products of the diazidoplatinum(II) complexes and the gold(I) alkynes will be referred to as **Pt,R[2+3]Au,X** with R = Et, Ph and X = NO_2, Br, CN throughout the thesis.

2. Determining Synthetic Objectives *via* Density Functional Theory

[2+3]-cycloaddition reactions of azido ligands and alkynes have proven a convenient path to functionalised platinum(II/IV) compounds.[96,97] As a rationale for planning the first syntheses, resolution-of-identity density functional theory (RI-DFT) calculations were performed to correlate experimentally observed reactivities of previously isolated and targeted compounds with theoretical investigations. When considering diazidoplatinum complexes and alkynes viable for cycloaddition reactions, the oxidation state of the platinum centre, as well as the electron-donating or -withdrawing nature of the ligands, can be expected to directly influence the energetic levels and the localisation of the respective molecular orbitals. Based on this, theoretical investigations of the energies and spatial orientation of the frontier orbitals could reveal trends in reactivities. The electronic influence of a variety of ligands, their configurational isomerism, and the addition of substituents were evaluated. The calculations comprised the assessment of four types of compounds for [2+3]-cycloaddition reactions: a range of each, alkynes, platinum(II) complexes and platinum(IV) complexes, as well as a comparison of *cis*- and *trans*-isomers. To ensure the calculations did not converge in transition states, minima on the potential energy surface were verified by harmonic vibrational frequency analysis.

2.1 Choice of Functional

In order to determine an appropriate choice of basis set and functional for investigation of the respective compounds, initial calculations were performed on a selection of azidoplatinum complexes which have been observed to successfully undergo [2+3]-cycloaddition reactions. Figure 6 shows a schematic overview of the steps which were applied for determining an appropriate functional for the theoretical investigations.

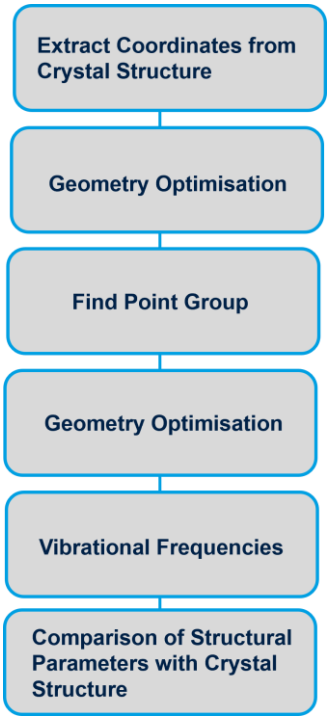

Figure 6: Schematic overview of the procedural steps for determining an appropriate functional for the theoretical investigations.

A selection of five literature-known platinum(II/IV) complexes were chosen for investigation of an appropriate functional (Scheme 9). The starting coordinates

for the geometry optimisation of the compounds were taken from the molecular structures in the solid state.[98–100] RI-DFT calculations of the five complexes **A**-**E** were performed with *Turbomole 7.3* using the basis set def2-TZVP and the functionals B3-LYP, BP-86, PBE and B2-PLYP (COSMO $\varepsilon = \infty$).

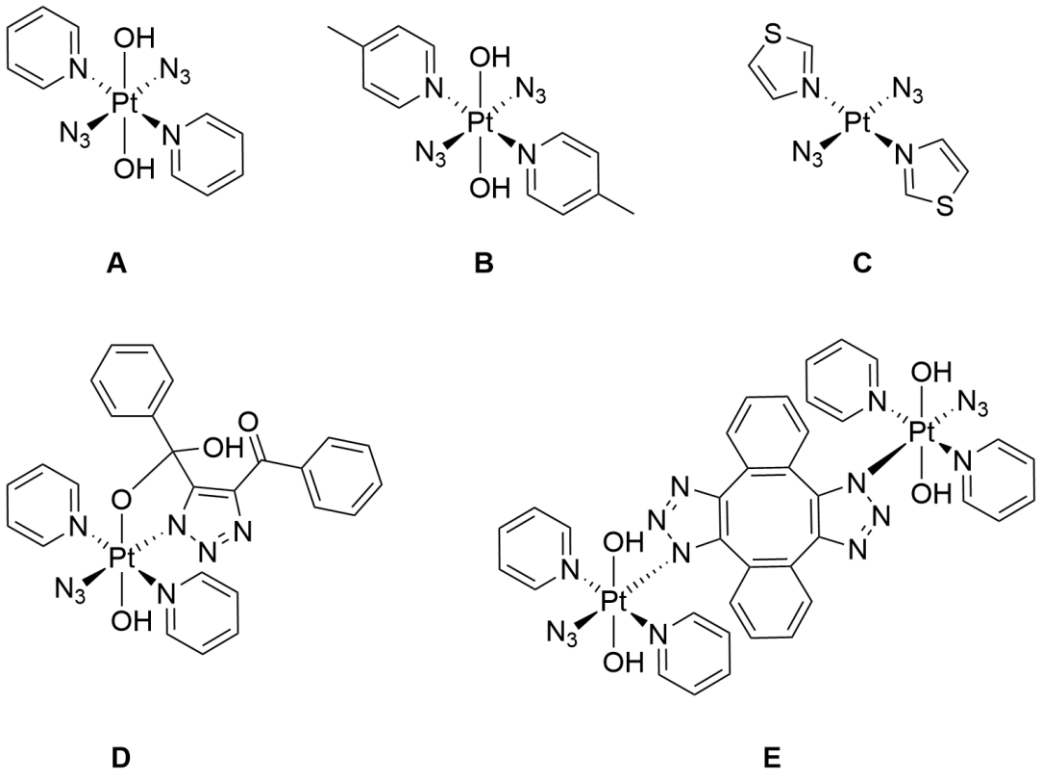

Scheme 9: Platinum(II/IV) complexes with varying ligand systems selected for theoretical investigations to determine an appropriate functional.

Table 1 and Table 2 display a comparison of experimentally and theoretically obtained selected bond lengths and angles, for exemplarily two of the five compounds (**A** and **D**) after the geometry optimisation. Figure 7 provides labels for the atoms and respective angles of the complexes.

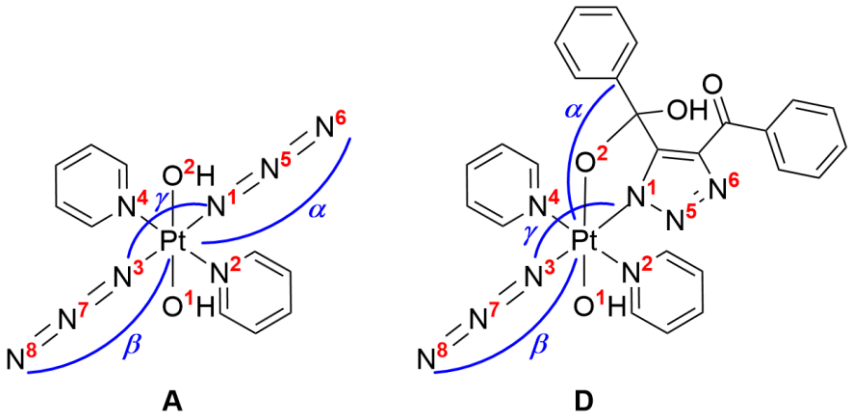

Figure 7: Labelling of atoms and angles of compound **A** (left) and **D** (right) for discussion of the experimentally and theoretically determined bond lengths and bond angles.

Table 1: Selected bond lengths and angles of compound **A** (Figure 7) determined experimentally and theoretically for varying functionals.[98] Theoretical investigations were performed with *Turbomole 7.3*, the basis set def2-TZVP and the functional B2-PLYP, B3-LYP, BP-86 or PBE (COSMO $\varepsilon = \infty$)

	Experimental	**B2-PLYP**	**B3-LYP**	**BP-86**	**PBE**
Pt–N1	2.046 Å	2.062 Å	2.080 Å	2.080 Å	2.077 Å
Pt–N2	2.046 Å	2.060 Å	2.071 Å	2.069 Å	2.058 Å
Pt–N3	2.043 Å	2.062 Å	2.080 Å	2.080 Å	2.077 Å
Pt–N4	2.047 Å	2.060 Å	2.071 Å	2.060 Å	2.058 Å
Pt–O1	2.027 Å	1.997 Å	2.026 Å	2.039 Å	2.037 Å
Pt–O2	1.990 Å	1.997 Å	2.026 Å	2.039 Å	2.037 Å
N1–N5	1.215 Å	1.198 Å	1.206 Å	1.215 Å	1.215 Å
N5–N6	1.140 Å	1.122 Å	1.143 Å	1.158 Å	1.158 Å
N3–N7	1.218 Å	1.198 Å	1.206 Å	1.215 Å	1.215 Å
N7–N8	1.146 Å	1.122 Å	1.143 Å	1.158 Å	1.158 Å
α	175.7°	180.0°	180.0°	180.0°	180.0°
β	177.9°	180.0°	180.0°	180.0°	180.0°
γ	176.8°	180.0°	180.0°	179.2°	180.0°

Table 2: Selected bond lengths and angles of compound **D** (Figure 7) determined experimentally and theoretically for varying functionals.[96] Theoretical investigations were performed with Turbomole 7.3, the basis set def2-TZVP and the functional B2-PLYP, B3-LYP, BP-86 or PBE (COSMO ε = ∞)

	Experimental	**B2-PLYP**	**B3-LYP**	**BP-86**	**PBE**
Pt–N1	1.997 Å	2.022 Å	2.033 Å	2.030 Å	2.026 Å
Pt–N2	2.032 Å	2.052 Å	2.064 Å	2.058 Å	2.055 Å
Pt–N3	2.035 Å	2.045 Å	2.063 Å	2.064 Å	2.062 Å
Pt–N4	2.033 Å	2.053 Å	2.064 Å	2.058 Å	2.055 Å
Pt–O1	1.982 Å	1.984 Å	2.015 Å	2.029 Å	2.027 Å
Pt–O2	2.017 Å	2.015 Å	2.045 Å	2.059 Å	2.058 Å
N1–N5	1.361 Å	1.326 Å	1.343 Å	1.357 Å	1.354 Å
N5–N6	1.314 Å	1.288 Å	1.306 Å	1.318 Å	1.316 Å
N3–N7	1.218 Å	1.201 Å	1.209 Å	1.217 Å	1.217 Å
N7–N8	1.142 Å	1.121 Å	1.121 Å	1.157 Å	1.157 Å
α	125.6°	130.5°	131.4°	131.3°	131.0°
β	173.0°	176.6°	177.2°	177.9°	176.3°
γ	172.2°	171.2°	171.1°	171.0°	171.6°

Comparison of the values for selected bond lengths and angles of the converged geometry optimisations for **A** and **D** for the five functionals with the experimental data show similar magnitudes with a tolerance of ± 0.05 Å. The theoretical investigations appear to overestimate the Pt–L (L = N, O) bond lengths, whereas the N–N bond lengths are underestimated. The largest deviations, of up to 4.62%, are observed for the calculated angles in comparison to the experimentally found data. This is likely to be attributed predominantly to packing effects leading to thermodynamically favoured arrangements in the solid state, *i.e*. *π*-stacking, *vs* the isolated complex in the gas phase, as it is modelled in DFT

calculations. Overall, the values obtained from the hybrid functional B2-PLYP show slightly less variance towards the experimental data. Moving forward, the main interest lies in calculating the energetic levels of the frontier orbitals of complexes. As the double hybrid functional B2-PLYP has been developed for more accurate calculation of in particular imaginary orbitals,[101,102] it was decided to apply this functional for the subsequent calculations.

2.2 Theory *vs* Experiment

As discussed in Chapter 2.1, geometry optimisations were performed for a range of platinum complexes with a variation of ligands. Correlating the resulting bond lengths and angles with experimental data in the solid state led to the choice of the functional B2-PLYP as an appropriate functional for the investigations at hand. The frontier orbitals of selected diazidoplatinum(II) complexes and gold(I) alkynes (Scheme 10) with potential for [2+3]-cycloaddition reactions were calculated. The distinction between *cis*- and *trans*-platinum complexes will influence the electronic properties of the compound: readiness to undergo cycloaddition reactions, solubility of the complex and reactivity towards oxidation and activation processes. Based on previous results, strained and electron-deficient alkynes are more likely to yield successful cycloaddition reactions. This consideration has led to gold(I) alkynes incorporating electron-withdrawing groups as viable candidates.[82] RI-DFT calculations on prospective compounds were performed with *Turbomole 7.3*, the basis set def2-TZVP and the functional B2-PLYP (COSMO $\varepsilon = \infty$).

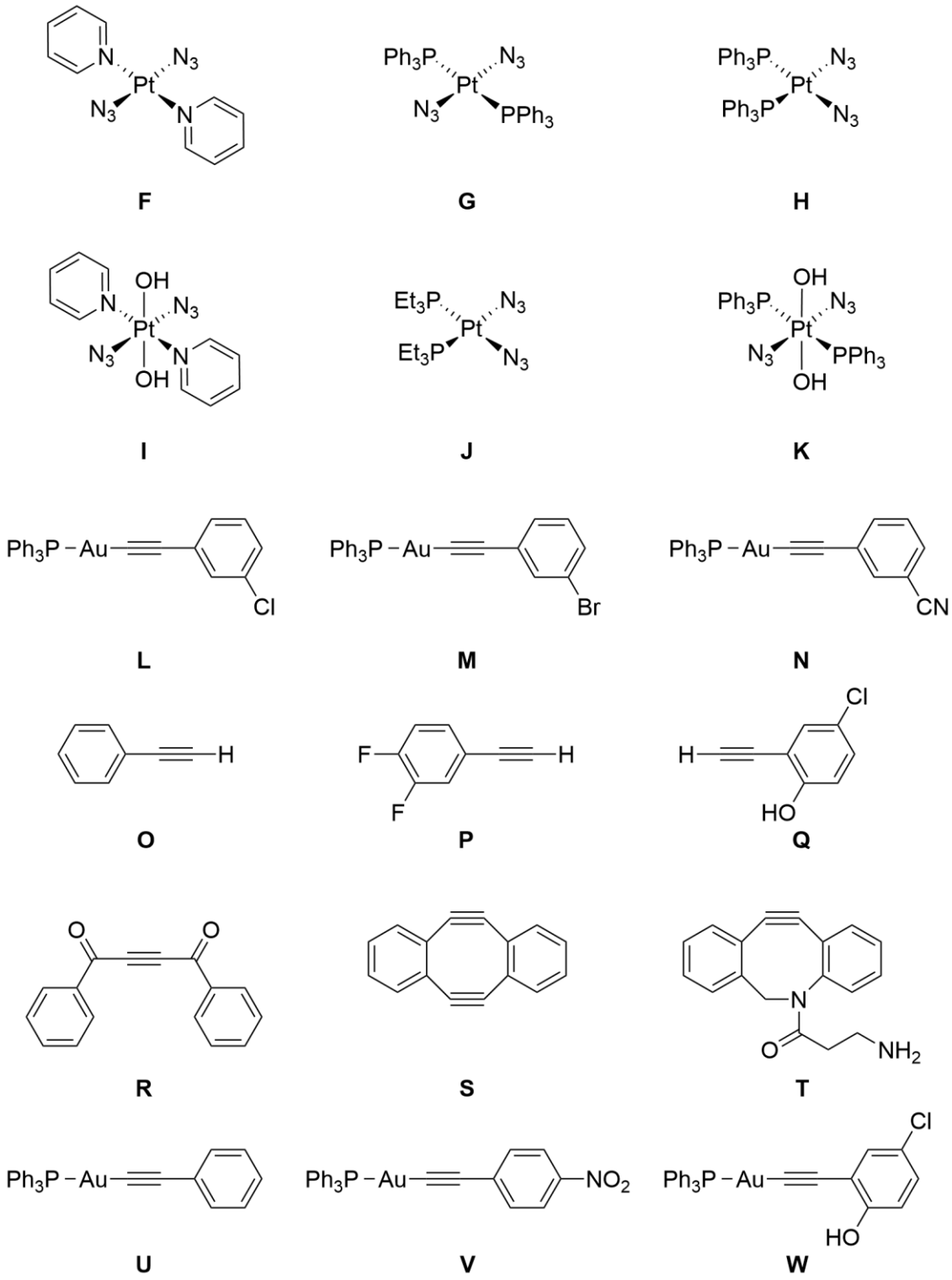

Scheme 10: Diazidoplatinum(II/IV) complexes with varying ligand systems and alkynes selected for theoretical investigation towards [2+3]-cycloaddition reactions.

By way of example, Figure 8 displays a schematic illustration of the spatial orientation and energetic levels of the frontier orbitals of the gold(I) alkynes **U**, **V** and **W**. The addition of electron withdrawing groups on the phenyl ring of the acetylido ligand causes a decrease in energy of the LUMO. In particular, an electron-withdrawing substituent in *para*-position causes a distinct reduction of 1.315 eV (Table 3). The largest energy difference between the frontier orbitals was detected at 7.105 eV for complex **U**. In contrast to that, gold(I) complex **V** displays the energetically lowest lying LUMO with −1.362 eV and the highest lying HOMO with −7.562 eV, leading to the smallest energy gap between the frontier orbitals of 6.2 eV of the three alkynes. The spatial orientation of the orbitals confirms significant localisation of the HOMO along the C–C triple bond as well as on the aromatic ring of the acetylido ligand.

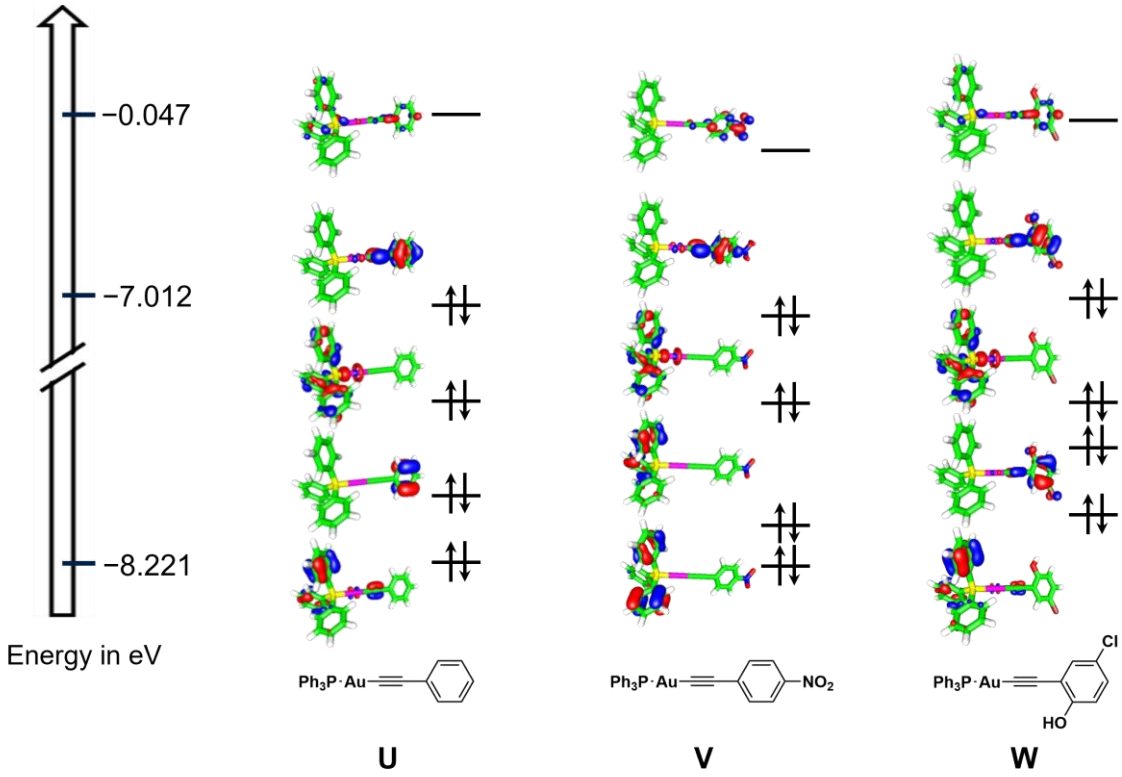

Figure 8: Schematic overview of the energetic levels and spatial orientation of the LUMO, HOMO, HOMO−1, HOMO−2 and HOMO−3 of gold(I) alkynes **U**, **V** and **W**. Orbitals are depicted with a threshold of 0.05 e/Å^3.

Table 3: Calculated energies of the LUMO (E_{LUMO}), the HOMO (E_{HOMO}) and the energy gap (ΔE_{L-H}) between these of gold(I) alkynes **U**, **V** and **W**.

	Complex U	**Complex V**	**Complex W**
$\boldsymbol{E_{LUMO}}$	−0.047 eV	−1.362 eV	−0.110 eV
$\boldsymbol{E_{HOMO}}$	−7.152 eV	−7.562 eV	−7.012 eV
$\boldsymbol{\Delta E_{L-H}}$	7.105 eV	6.2 eV	6.902 eV

Comparison of the calculations for a selection of *trans*-diazidoplatinum(II) complexes demonstrate that ligand substitution of the pyridyl ligands to triphenylphosphine ligands, leads to a decrease in the energetic gap between the

frontier orbitals of 0.223 eV: the energy of the LUMO is lowered, whilst the energy of the HOMO increases (Figure 9, Table 4). In addition, the energetic levels of the LUMO and HOMO between the *cis*- and *trans*-isomers of diazidobis(triphenylphosphine)platinum(II) suggests that the *cis*-configuration of these ligands leads to frontier orbitals of lower energy, with a decrease of energy of 0.136 eV for the LUMO and of 0.315 eV for the HOMO compared to the *trans*-isomer. Interestingly, for *trans*-diazidodipyridylplatinum(II), the LUMO appears to be solely located on the pyridyl ligands, whereas for the *cis*- and *trans*-diazidobis(triphenylphosphine)platinum(II) there is a significant contribution of the azido groups to the LUMO. This indicates that any reactions involving a donation of electron density to the LUMO are less likely to involve the azido groups for *trans*-diazidodipyridylplatinum(II). In contrast to this, the strong concentration of the spatial orientation of the HOMOs on the azido ligands of all three diazidoplatinum(II) compounds reveal a significant involvement of these atoms in reactions in which electron density is donated from the complexes.

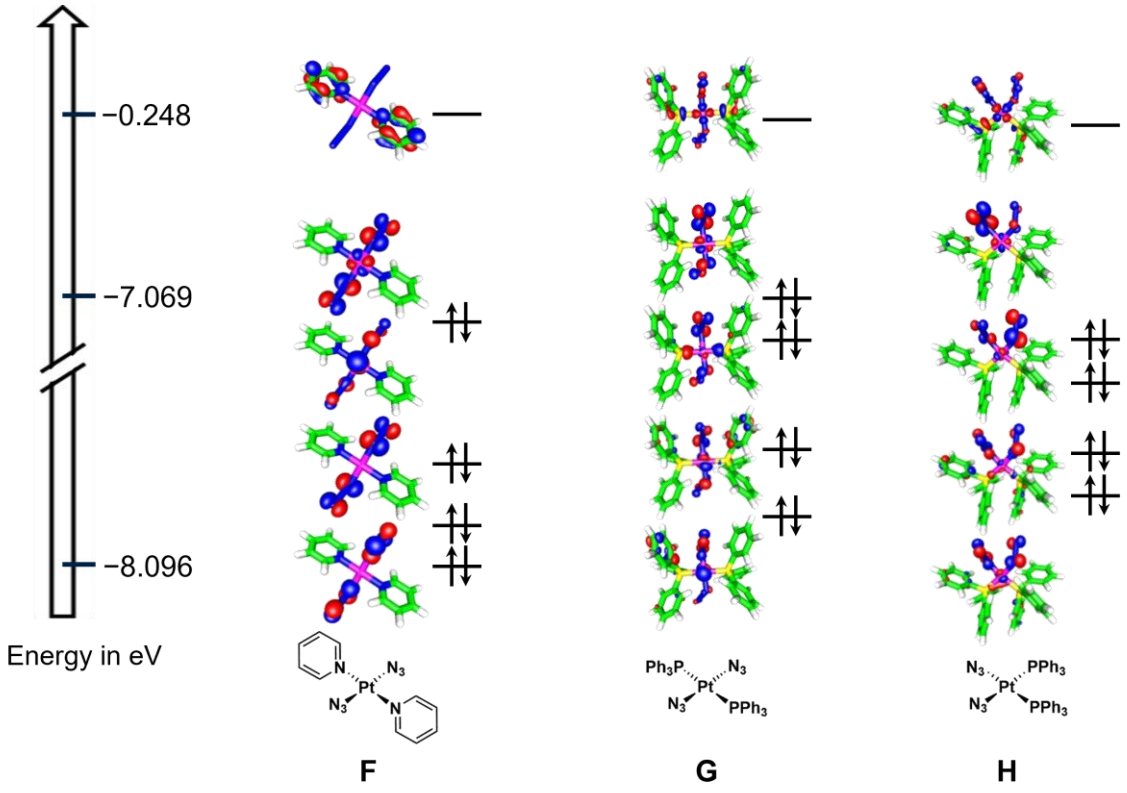

Figure 9: Schematic overview of the energetic levels and spatial orientation of the LUMO, HOMO, HOMO−1, HOMO−2 and HOMO−3 of diazidoplatinum(II) complexes **F**, **G** and **H**. Orbitals are depicted with a threshold of 0.05 e/Å^3.

Table 4: Calculated energies of the LUMO (E_{LUMO}), the HOMO (E_{HOMO}) and the energy gap (ΔE_{L-H}) of platinum(II) azido complexes **F**, **G** and **H**.

	Complex F	**Complex G**	**Complex H**
$\boldsymbol{E_{LUMO}}$	−0.248 eV	−0.312 eV	−0.448 eV
$\boldsymbol{E_{HOMO}}$	−7.228 eV	−7.069 eV	−7.384 eV
$\boldsymbol{\Delta E_{L-H}}$	6.98 eV	6.757 eV	6.936 eV

In order to evaluate the viability of using the calculated energetic levels of the frontier orbitals as an indicator for successful [2+3]-cycloaddition reactions, the values of diazidoplatinum complex **I** and those of a selection of alkynes were

compared with experimentally observed reactivities. During a cycloaddition reaction, electron density is commonly passed between two entities: the three-atom component and the diatomic multiple bond system. Depending on the mechanism at hand, the initial step is the reaction between the HOMO of the nucleophilic end of the dipolic three-atom component, in this case the azido groups, and the LUMO of the electrophile, the dipolarophile, here the alkynes.[103] Exemplarily, the energy of the HOMO of *trans*,*trans*-diazidodipyridyl dihydroxidoplatinum(IV) (**I**) was compared to the energy of the LUMOs of alkynes **O**, **P**, **S** and **T** (Figure 10).

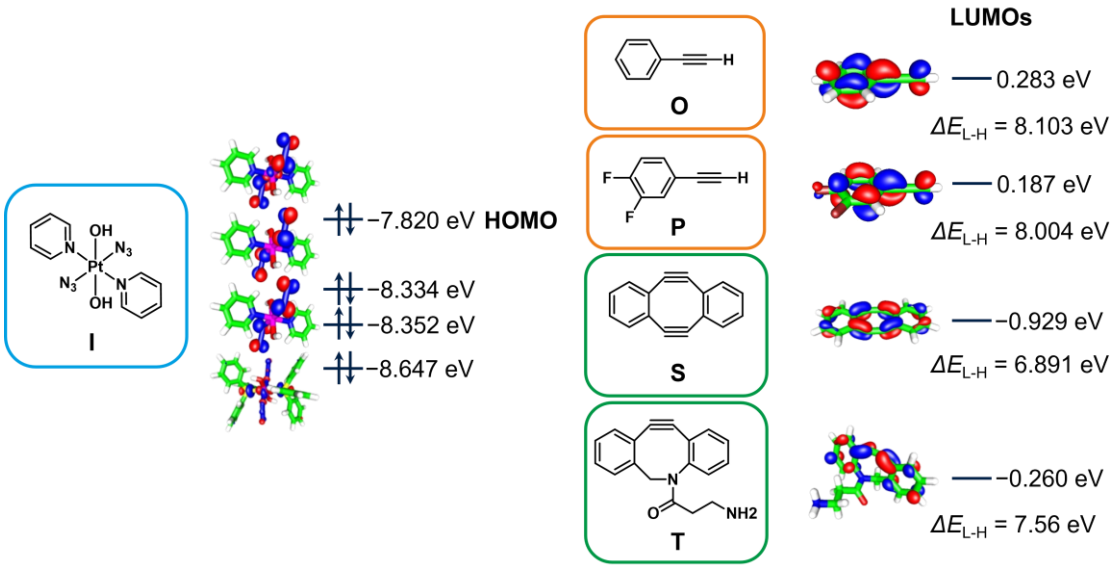

Figure 10: Schematic overview of the energetic levels and spatial orientation of the frontier orbitals of diazidoplatinum(II) complex **I** and alkynes **O**, **P**, **S** and **T**. Orbitals are depicted with a threshold of 0.05 e/Å^3.

Complex **I** successfully undergoes [2+3]-cycloaddition reactions with the strain-promoted alkynes **S** and **T**, however, no reactivity towards alkynes **O** and **P** was reported.[97,100] The energetic gap between compound **S** and **I** was calculated to be 6.891 eV, with 7.56 eV between **T** and **I**, respectively. In comparison to these values, the LUMO-HOMO gap (ΔE_{L-H}) between each alkynes **O** and **P**, and complex **I** in both cases exceeds 8 eV. The energetic differences of the frontier orbitals correlate with the experimental reactivities: Formation of a cycloaddition product for the compounds with a smaller LUMO-HOMO gap (compounds **S** and **T** with respect to **I**), and no successful cycloaddition reaction for larger LUMO-HOMO gaps of >8 eV (compounds **O** and **P** with respect to **I**). Confirming this correlation on multiple examples within the scope of this work, suggests that theoretical investigations can be applied as a tool for indicating viable reactants for [2+3]-cycloaddition reactions between diazidoplatinum(II) complexes and activated alkynes. However, it must be considered that this approach is purely based on thermodynamics of isolated compounds in the gas phase with neglect of kinetics.

Building on these conclusions, further platinum complexes and alkynes were examined theoretically. The aim was to identify trends which would help with optimising prospective synthetic approaches. Figure 11 displays a schematic overview of the energetic trends of the HOMOs of a selection of platinum(II/IV) complexes and of the LUMOs of a range of alkynes. The comparison indicates that the HOMO is energetically higher for platinum(II) *vs* platinum(IV) complexes, suggesting that platinum(II) complexes are more likely to undergo cycloaddition reactions under mild reactions. In an attempt to identify trends of the selected

compounds, no clear correlation between the energetic level of the HOMO of *cis*- *vs* *trans*-isomers of the platinum(II) complexes was identified. *cis*-diazidobis(triethylphosphine)platinum(II) displays the highest HOMO with an energy of −6.754 eV. The energetic levels of the LUMOs of the alkynes demonstrate that the addition of an electron-deficient gold(I) centre lowers the energy of the LUMO of the alkynes by 0.167 eV. With a substantially energetically low-lying LUMO of −1.362 eV, alkyne **V** was detected to be the most promising gold(I) alkyne for the [2+3]-cycloaddition reactions under the investigation at hand.

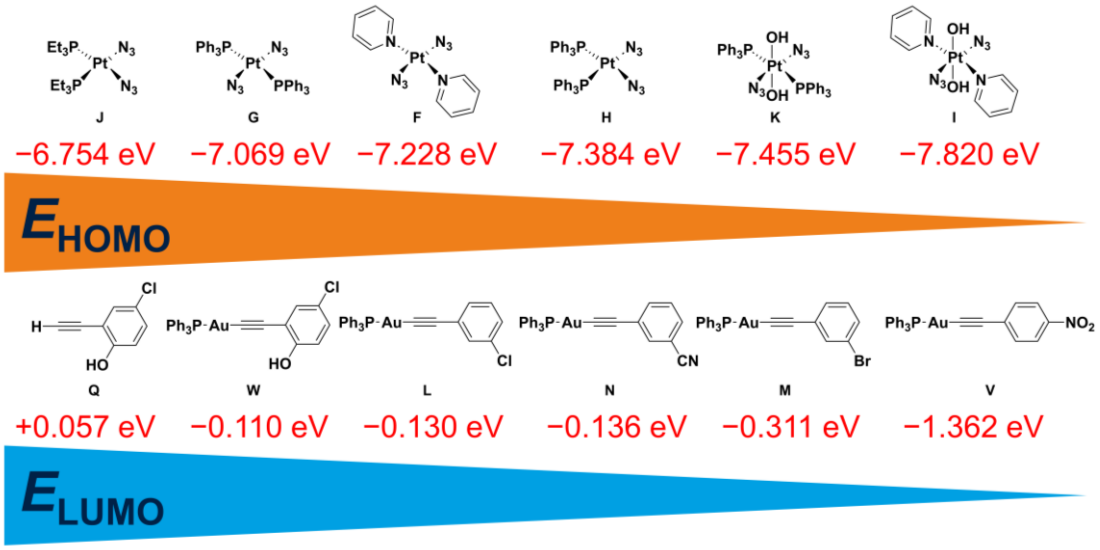

Figure 11: Schematic overview of the energetic trends of the frontier orbitals of a selection of platinum(II/IV) complexes and alkynes.

2.3 Target Compounds

Based on the results from the RI-DFT calculations, a selection of target compounds was identified for investigation of the [2+3]-cycloaddition reaction between diazidoplatinum(II) complexes and gold(I) alkynes. Since the HOMOs of the diphosphineplatinum(II) complexes are calculated to be higher in energy compared to those of the dipyridylplatinum(II) complexes, synthesis and investigation of the diphosphineplatinum(II) congeners is targeted as the first objective. Following on from that, investigations will include diazidodipyridylplatinum(II), as well as complexes with mixed ligand systems incorporating one phosphine and one pyridyl ligand attached to the platinum(II) centre. In all cases, the aim is to examine the readiness for these compounds to undergo cycloaddition reactions with gold(I) alkynes under mild conditions, in dependence of the respective ligand system as well as their isomerism. Scheme 11 shows an overview of the target compounds within the scope of this research. The selection comprises eight platinum(II) complexes and three gold(I) alkynes with substituted phenyl rings. Successful functionalisation of the platinum(II) complexes with these explicit gold(I) species *via* cycloaddition will lead to phenyl substituted triazoles. This particular structural feature allows targeting indoleamine 2,3-dioxygenase 1 (IDO1), a commonly overexpressed enzyme in tumour cells. Depending on the substitution patterns and the size of the substituent on the derivatives, these compounds have been reported to reduce the IDO1 inhibitory activity.[104] Realisation of these multi-modal platinum(II) complexes could yield active platinum, gold and organic entities within the

biological system – all of which potentially exhibit distinct cytotoxicity towards cancer cells.

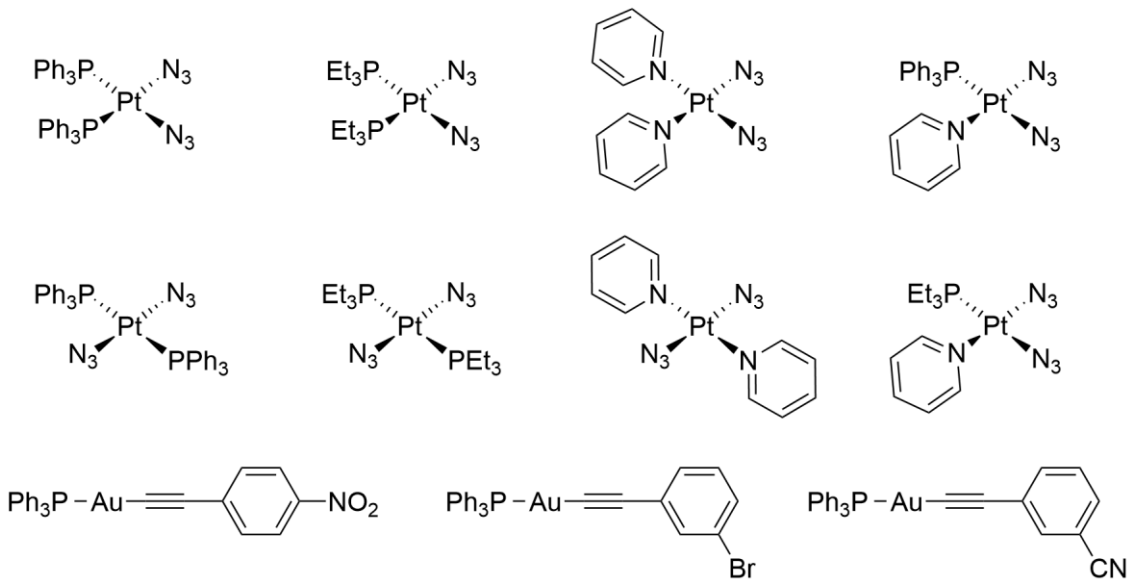

Scheme 11: Selection of targeted *cis*- and *trans*-diazidoplatinum(II) complexes and gold(I) alkynes for the synthesis of functionalised multi-modal platinum(II) compounds.

3. Synthesis of Platinum(II)-Gold(I) Complexes

The synthesis of the diazidodiphosphineplatinum(II) complexes was adapted from literature. Reports on *cis*- and *trans*-[Pt(N_3)$_2$(PR_3)$_2$] (R = Et, Ph) suggest that accessing the complex *via* the tetraazidoplatinate(II),[105,106] however, due to the safety risks associated with azido-platinum compounds,[107,108] a path *via* the synthesis of the corresponding dichloridodiphosphineplatinum(II) complexes starting from potassium tetrachloridoplatinate(II) was chosen. As discussed in Chapter 1.6, $^{31}P\{^{1}H\}$ NMR spectroscopy provides an effective handle for differentiating between the formation of the *cis*- and *trans*-isomers. In particular the $^{1}J(^{31}P, ^{195}Pt)$ coupling constant is extremely indicative of the distinction between isomers and is expected to be larger for *cis*-diphosphineplatinum(II) complexes compared to *trans*-diphosphineplatinum(II) complexes.[93,109,110]

3.1 Synthesis of Dichloridodiphosphineplatinum(II) Complexes

Various synthetic pathways involving potassium tetrachloridoplatinate(II) and the phosphines were explored.[105,110–112] The reaction of triphenylphosphine with the platinate(II) in ethanol at elevated temperatures (Scheme 12) led to a mixture of the *cis*- and *trans*-isomer in a ratio of 1:0.10, as determined by $^{31}P\{^{1}H\}$ NMR spectroscopy (Figure 12). Reacting the tetrachloridoplatinate with acetonitrile first and exchanging the acetonitrile ligands for triphenylphosphine in nitromethane

subsequently, leads to the selective formation of *trans*-[$PtCl_2(PPh_3)_2$] when the reaction is performed at 0 °C and to a mixture of the *cis*- and the *trans*-isomer in a ratio of 1:0.94 for a reaction temperature of 50 °C. Interestingly, combining potassium tetrachloridoplatinate(II) with triphenylphosphine in acetonitrile at 50 °C for 16 h results in the pure synthesis of *cis*-[$PtCl_2(PPh_3)_2$]. These observations suggest that the *cis*-isomer is the thermodynamic product, whereas the *trans*-isomer appears to be the kinetic product which can be accessed through more controlled reaction conditions such as lower temperature.

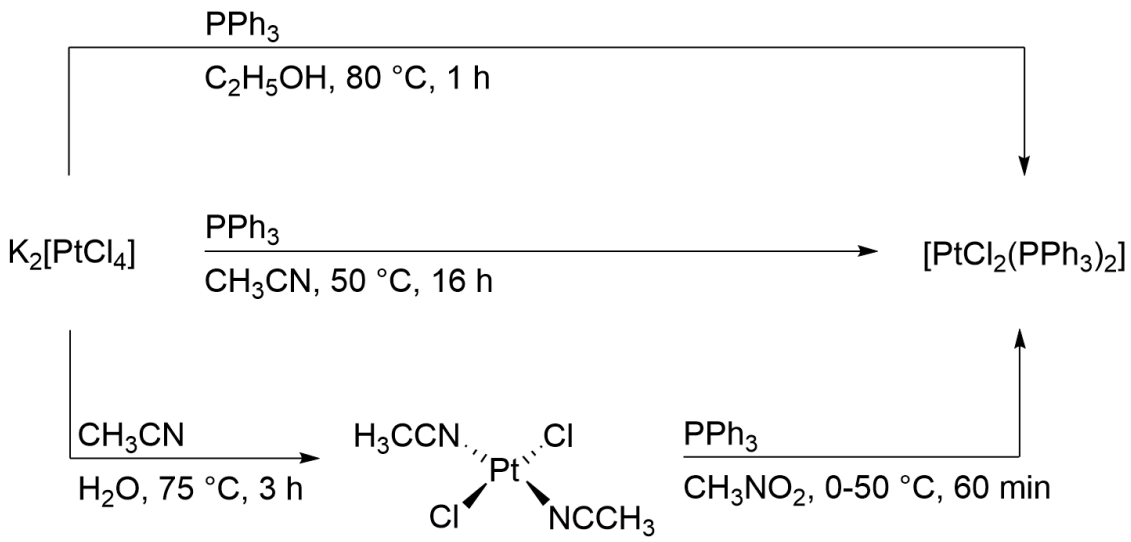

Scheme 12: Synthetic approaches to *cis*- and *trans*-[$PtCl_2(PPh_3)_2$].[105,110–112]

The resonance for *cis*-[$PtCl_2(PPh_3)_2$] appears as a singlet at 14.3 ppm in the $^{31}P\{^1H\}$ NMR spectrum, compared to the signal at 20.2 ppm for the corresponding *trans*-isomer (Figure 12). With 3675 Hz for *cis*-[$PtCl_2(PPh_3)_2$] and 2633 Hz for *trans*-[$PtCl_2(PPh_3)_2$], the $^1J(^{31}P, ^{195}Pt)$ coupling constants enable clear distinction

between the isomers. The experimental data are in good agreement with the literature.[110,111]

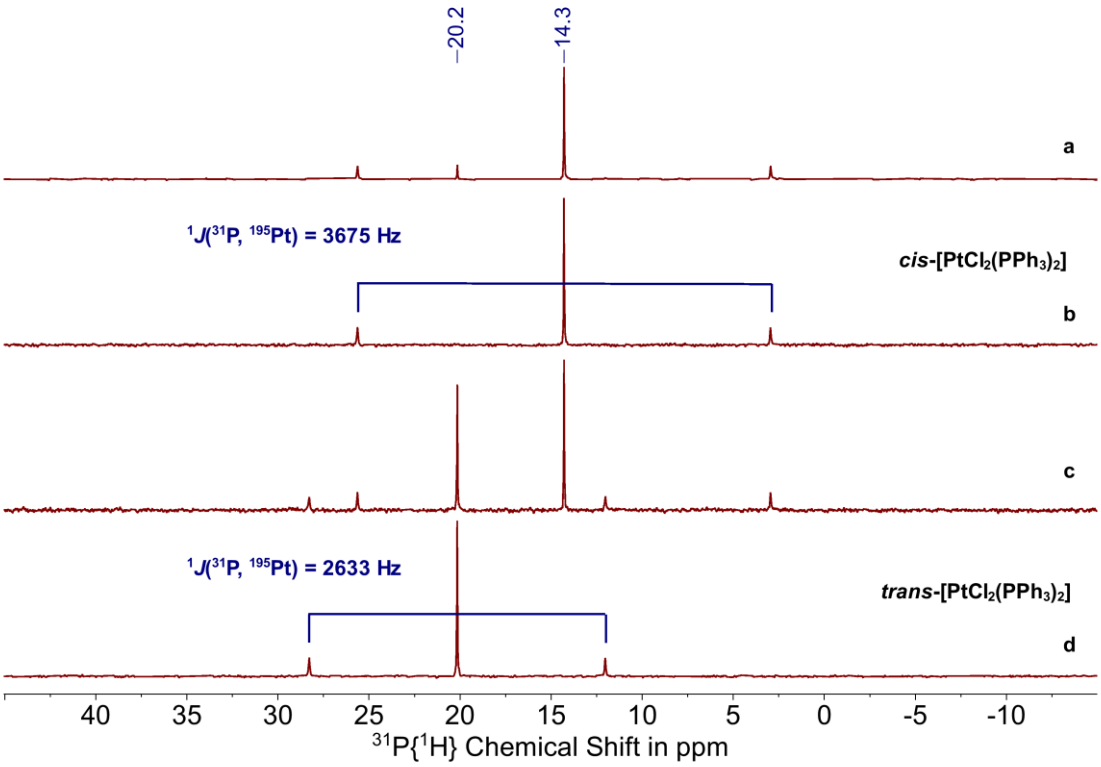

Figure 12: $^{31}P\{^1H\}$ NMR spectra (162 MHz, $CDCl_3$, 25 °C) of the reaction mixtures of the synthetic approaches to *cis*- and *trans*-[$PtCl_2(PPh_3)_2$] as outlined in Scheme 12. $K_2[PtCl_4]$ was reacted with triphenylphosphine in ethanol at 80 °C (a), acetonitrile at 50 °C (b) or *via* an acetonitrile complex in nitromethane at 50 °C (c) or at 0 °C (d).

The balance between the synthesis of *cis*- and *trans*-[$PtCl_2(PEt_3)_2$] can be controlled through the stoichiometry of the addition of triethylphosphine in tetrahydrofuran to a solution of potassium tetrachloridoplatinate(II) in water at 23 °C (Scheme 13).[113] The addition of four equivalents of phosphine to the platinate leads to the formation of the *cis*-isomer as the thermodynamic product,

whilst the reaction of one equivalent of phosphine allows for kinetic control and results in *trans*-[$PtCl_2(PEt_3)_2$], as determined by $^{31}P\{^1H\}$ NMR spectroscopy. The $^{31}P\{^1H\}$ NMR spectrum displays a clear singlet at 9.1 ppm for the *cis*-isomer with a $^1J(^{31}P, ^{195}Pt)$ coupling constant of 3515 Hz (Figure 13). The singlet is shifted slightly downfield for the *trans*-isomer with a distinctly smaller $^1J(^{31}P, ^{195}Pt)$ coupling constant of 2420 Hz, which is in good agreement with the literature.[93] To prevent the oxidation of the phosphine, the reaction is performed under nitrogen.

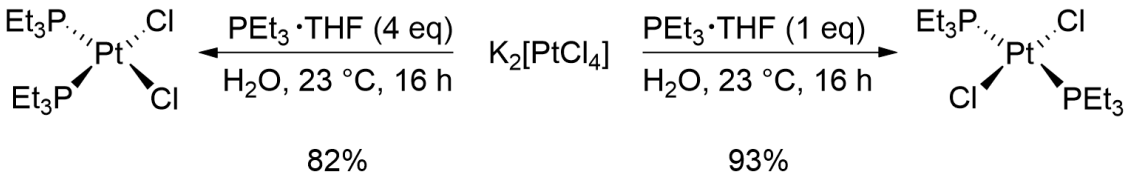

Scheme 13: Synthetic approaches to *cis*- and *trans*-[$PtCl_2(PEt_3)_2$].

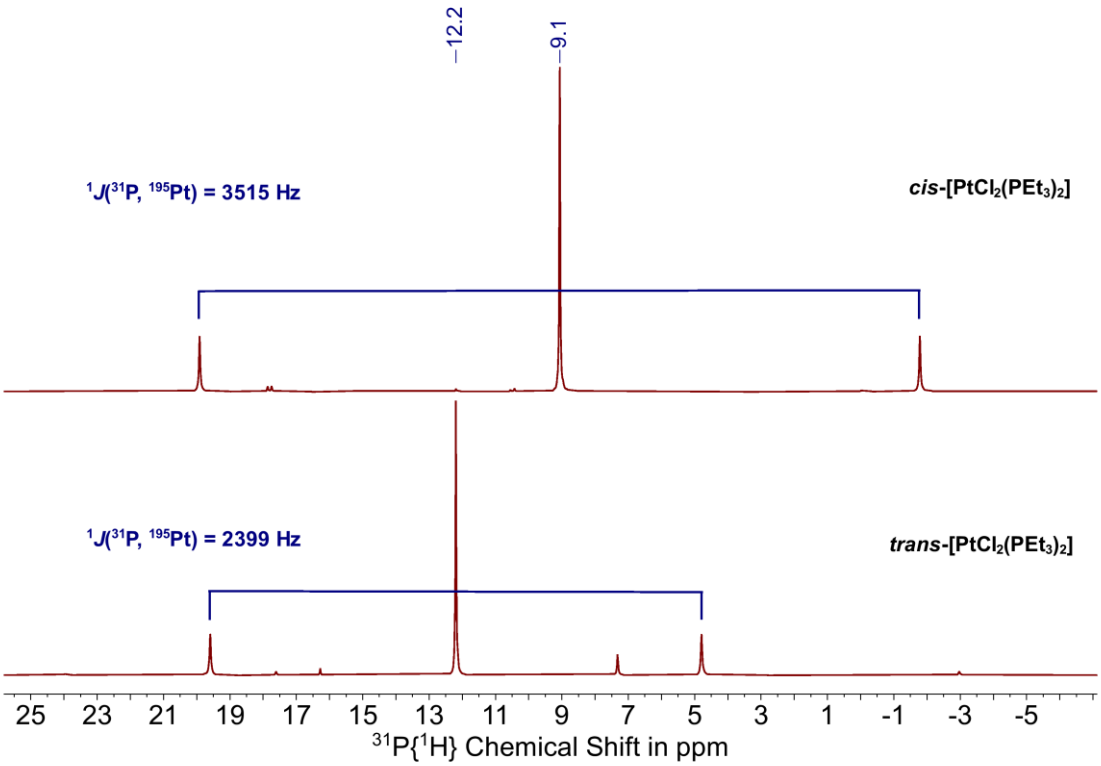

Figure 13: $^{31}P\{^{1}H\}$ NMR spectra (162 MHz, $CDCl_3$, 25 °C) of compounds *cis*- and *trans*-$[Pt(Cl)_2(PEt_3)_2]$.

3.2 Synthesis of *cis*-Diazidodiphosphineplatinum(II) Complexes

Various routes for the reaction of the dichloridodiphosphineplatinum(II) complexes to the diazidodiphosphineplatinum(II) compounds were explored. Analogous reactions of platinum(II) complexes with *N*-donor ligands choose the reaction path with silver nitrate and sodium azide in water,[114] however, all reaction paths with water as the main solvent yielded unreacted starting material, or oxidised phosphines. The difference in solubility of the less polar platinum(II) complexes and the sodium azide salt posed a challenge for the reaction. Ligand substitution utilising the lattice energy from the formation of sodium chloride in

organic solvents as a driving force provided access to the *cis*-diazidodiphosphineplatinum(II) compounds. The addition of an aqueous solution of sodium azide to an organic solvent which is miscible with water, allows for a reduced reaction time from 30 hours to 4 hours. Scheme 14 shows an overview of the synthetic approaches to *cis*-$[Pt(N_3)_2(PR_3)_2]$ (R = Et, Ph).

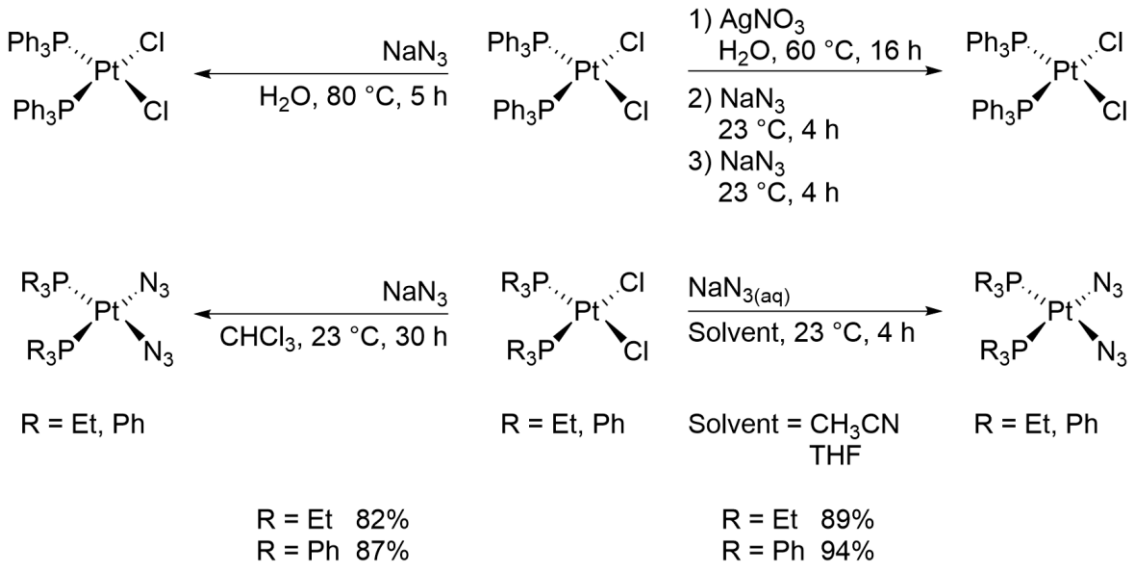

Scheme 14: Synthetic approaches to *cis*-$[Pt(N_3)_2(PR_3)_2]$ (R = Et, Ph).

Figure 14 shows the $^{31}P\{^1H\}$ NMR spectra of the reactions of *cis*-$[PtCl_2(PR_3)_2]$ (R = Et, Ph) and sodium azide in organic solvents. The $^{31}P\{^1H\}$ NMR spectrum displays a singlet at 12.0 ppm with platinum satellites and a $^1J(^{31}P, ^{195}Pt)$ coupling constant of 3507 Hz for *cis*-$[Pt(N_3)_2(PPh_3)_2]$ compared to a resonance at 7.3 ppm and platinum satellites with a $^1J(^{31}P, ^{195}Pt)$ coupling constant of 3338 Hz for *cis*-$[Pt(N_3)_2(PEt_3)_2]$. The ^{195}Pt NMR spectra show corresponding triplets with matching coupling constants at −4261 ppm for compound *cis*-$[Pt(N_3)_2(PPh_3)_2]$

and at −4335 ppm for the triethylphosphine analogue, respectively. The detection of triplets in the ^{195}Pt NMR spectra confirms the formation of symmetrical complexes including two phosphine ligands.

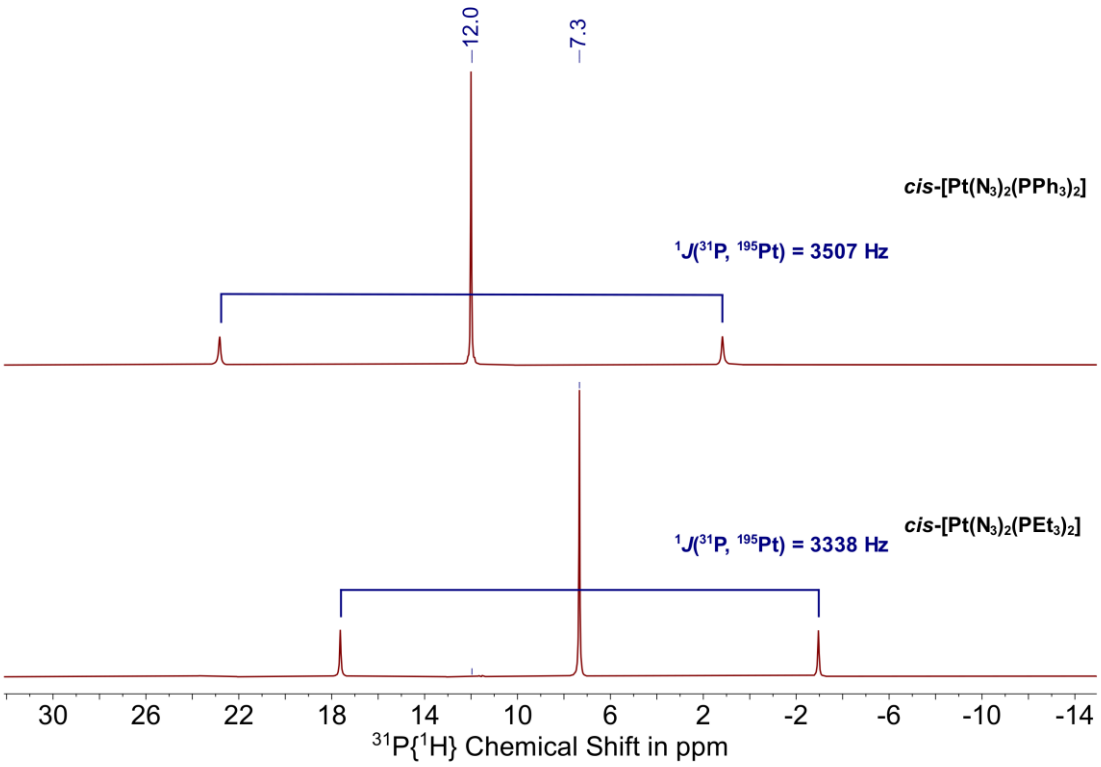

Figure 14: $^{31}P\{^{1}H\}$ NMR spectra (162 MHz, $CDCl_3$, 25 °C) of compounds *cis*-$[Pt(N_3)_2(PR_3)_2]$ (R = Et, Ph).

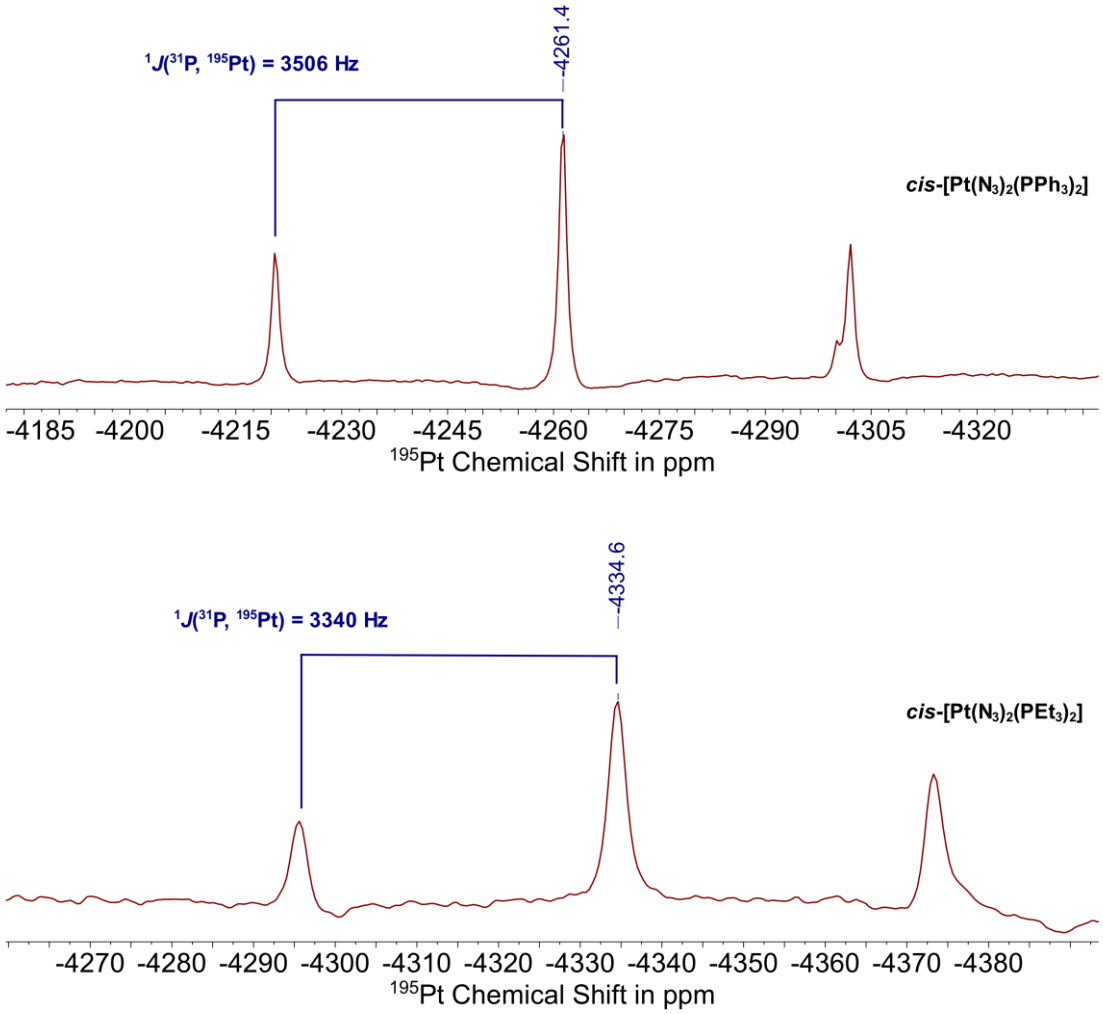

Figure 15: ^{195}Pt NMR spectra (86 MHz, $CDCl_3$, 25 °C) of compounds *cis*-[Pt(N3)2(PR3)2] (R = Et, Ph).

Infrared (IR) spectra of *cis*-[Pt(N3)2(PR3)2] (R = Et, Ph) display a strong band at 2060 cm^{-1}, corresponding to the asymmetric stretching vibration of the azido ligands which is in good agreement with the literature (Figure 16).[105] Neither the symmetric stretching frequency nor the deformation frequency of the azido group could be assigned unambiguously.

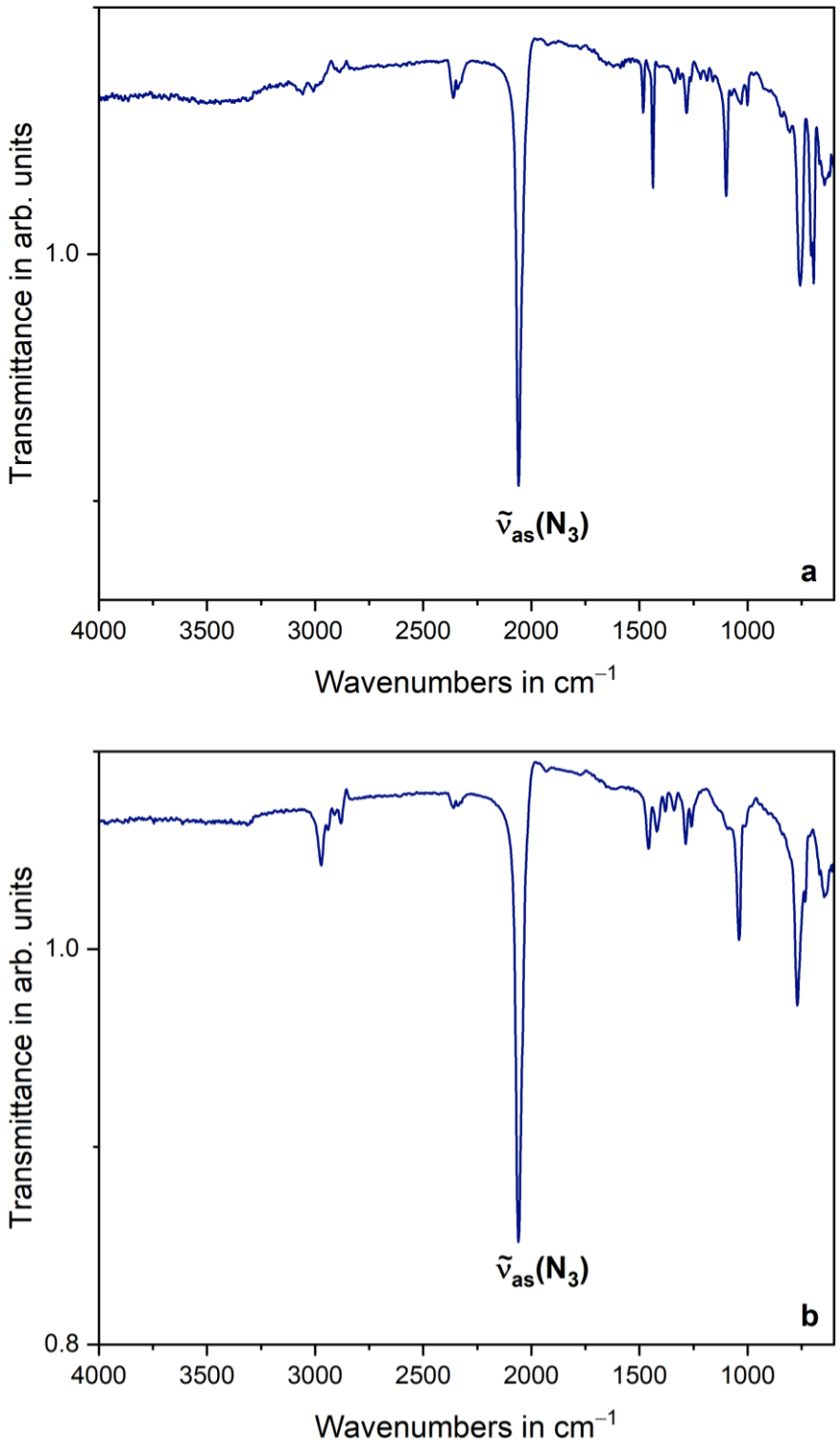

Figure 16: IR spectra (23 °C) of compounds *cis*-[Pt(N_3)$_2$(PPh_3)$_2$] (a) and *cis*-[Pt(N_3)$_2$(PEt_3)$_2$] (b).

The UV-visible spectra of diazidodiphosphineplatinum(II) complexes *cis*-$[Pt(N_3)_2(PR_3)_2]$ (R = Et, Ph) were recorded at room temperature in the range of 200-800 nm in solutions in tetrahydrofuran with a concentration of 23.4 µM. Compounds *cis*-$[Pt(N_3)_2(PR_3)_2]$ (R = Et, Ph) exhibit absorbances in the UV-region and the beginning of the visible light spectrum (Figure 17), which is in line with them both being isolated as pale yellow solids. The UV-visible spectrum for complex *cis*-$[Pt(N_3)_2(PPh_3)_2]$ displays a strong absorbance at 233 nm due to the phenyl groups on the phosphine ligands. The ligand-to-metal charge transfer bands ($N_3 \rightarrow Pt$) for the transition metal complexes appear at 269 nm for compound *cis*-$[Pt(N_3)_2(PPh_3)_2]$ and 248 nm for *cis*-$[Pt(N_3)_2(PEt_3)_2]$, respectively. With molar extinction coefficients of 24311 $L \cdot mol^{-1} \cdot cm^{-1}$ for *cis*-$[Pt(N_3)_2(PPh_3)_2]$ and 21834 $L \cdot mol^{-1} \cdot cm^{-1}$ for *cis*-$[Pt(N_3)_2(PEt_3)_2]$ (Table 5), the triphenylphosphine analogue is a stronger absorber than the triethylphosphine congener.

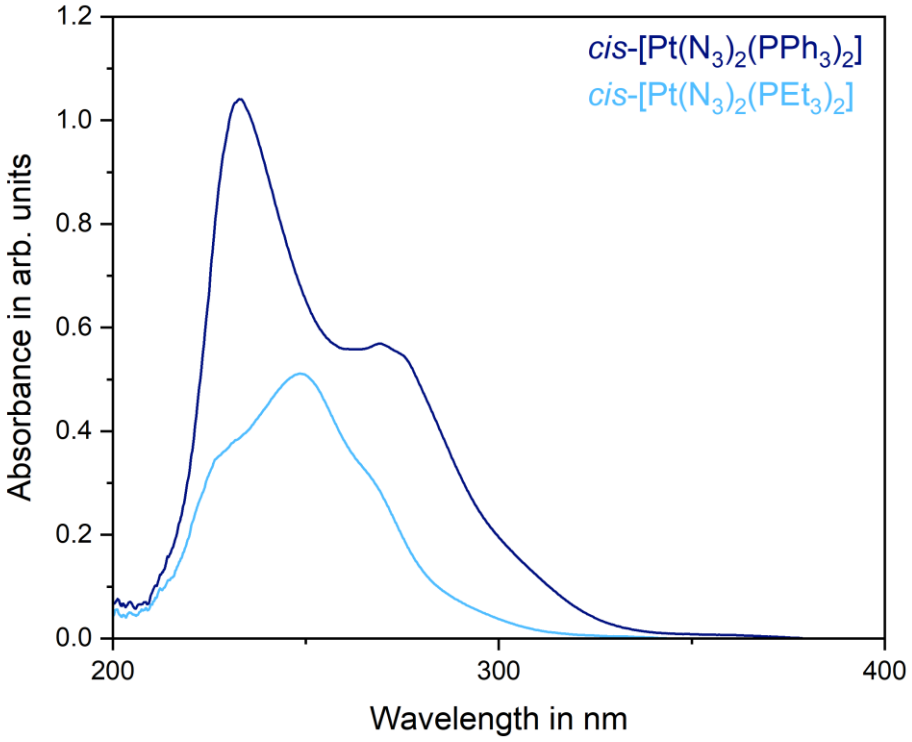

Figure 17: UV-visible spectra (THF, 23 °C) of compounds *cis*-$[Pt(N_3)_2(PR_3)_2]$ (R = Et, Ph).

Table 5: Wavelength of local maximal absorbance λ and molar extinction coefficient ε of UV-visible spectra (THF, 23 °C) of compounds *cis*-$[Pt(N_3)_2(PR_3)_2]$ (R = Et, Ph).

	λ	Molar Extinction Coefficient ε
***cis*-$[Pt(N_3)_2(PPh_3)_2]$**	233 nm	44486 $L \cdot mol^{-1} \cdot cm^{-1}$
***cis*-$[Pt(N_3)_2(PPh_3)_2]$**	269 nm	24311 $L \cdot mol^{-1} \cdot cm^{-1}$
***cis*-$[Pt(N_3)_2(PEt_3)_2]$**	248 nm	21834 $L \cdot mol^{-1} \cdot cm^{-1}$

Crystals of compounds *cis*-$[Pt(N_3)_2(PR_3)_2]$ (R = Et, Ph) suitable for X-ray diffraction analysis were grown from concentrated solutions in chloroform. The diazidoplatinum(II) complex *cis*-$[Pt(N_3)_2(PPh_3)_2]$ crystallises with one molecule of chloroform as yellow blocks in the orthorhombic space group *Pbca* with eight

formula units in the unit cell (R_1 = 1.98%, wR_2 = 4.65%, R_{int} = 4.12%, *GooF* = 1.087, $e_{min/max}$ = −0.74/0.68 Å^{-3}). The molecular structure in the solid state of *cis*-[Pt(N$_3$)$_2$(PPh$_3$)$_2$] is displayed in Figure 18. Two of the chlorine atoms in the solvent molecule are disordered by 31%. The anisotropic displacement parameters of the nitrogen atoms indicate a further disorder for the azido ligands. However, with a heavy element such as platinum in close proximity to these, it was not possible to fully resolve this disorder in the model.

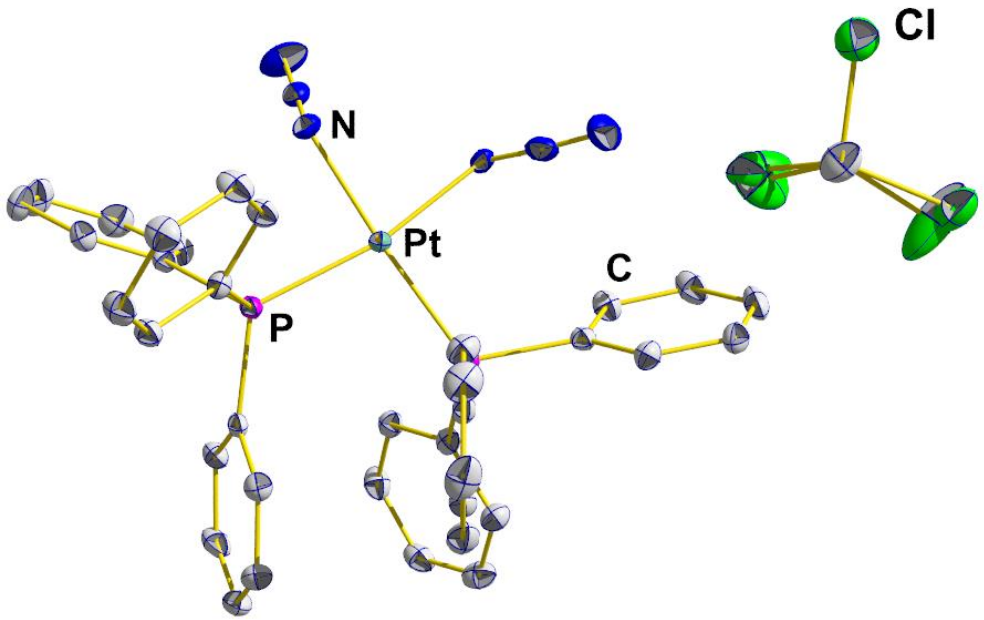

Figure 18: Molecular structure of *cis*-[Pt(N$_3$)$_2$(PPh$_3$)$_2$] · CHCl$_3$ in the solid state. Hydrogen atoms are omitted for clarity. Displacement ellipsoids are shown at the 50% probability level.

The triethylphosphine analogue *cis*-[Pt(N$_3$)$_2$(PEt$_3$)$_2$] crystallises as yellow blocks in the monoclinic space group $P2_1/c$ with four formula units in the unit cell (Figure 19) (R_1 = 2.59%, wR_2 = 6.87%, R_{int} = 3.79%, *GooF* = 1.240,

$e_{min/max}$ = −1.95/2.41 Å^{-3}). Whilst the majority of the quality factors of the structure solution and refinement support a model which is in good agreement with the experimental data (Table A2), residual electron density of 2.36 e·Å^{-3} is detected in between the ethyl groups of the triethylphosphine ligands. The location of the electron density is too close to be attributed to a solvent molecule and could not be resolved *via* the refinement of disordered ethyl groups. These observations might be due to a more significant error with the structure solution. The dataset was investigated for various Bravais lattices and space groups, twinning, a superstructure and whole-molecule disorder. It was not possible to resolve the residual electron density, suggesting that it might be an artefact and will likely require a measurement of a new crystal.

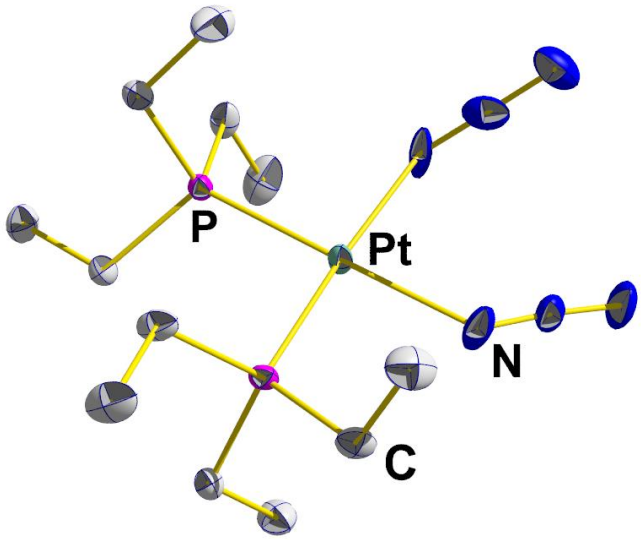

Figure 19: Molecular structure of *cis*-[Pt(N$_3$)$_2$(PEt$_3$)$_2$] in the solid state. Hydrogen atoms are omitted for clarity. Displacement ellipsoids are shown at the 50% probability level.

Comparison of selected bond lengths and angles of compounds *cis*-$[Pt(N_3)_2(PR_3)_2]$ (R = Et, Ph) confirms the structural similarity of the two complexes (Table 6).

Table 6: Selected bond lengths and angles of the molecular structures of complexes *cis*-$[Pt(N_3)_2(PPh_3)_2]\cdot CHCl_3$ and *cis*-$[Pt(N_3)_2(PEt_3)_2]$ in the solid state

	***cis*-$[Pt(N_3)_2(PPh_3)_2]\cdot CHCl_3$**	***cis*-$[Pt(N_3)_2(PEt_3)_2]$**
Pt1–N1	2.091(2) Å	2.092(4) Å
Pt1–N4	2.098(2) Å	2.121(4) Å
Pt1–P1	2.2755(7) Å	2.2483(11) Å
Pt1–P2	2.2593(7) Å	2.2561(10) Å
N1–N2	1.180(4) Å	1.183(6) Å
N2–N3	1.169(4) Å	1.161(6) Å
N4–N5	1.192(4) Å	1.147(6) Å
N5–N6	1.164(4) Å	1.165(7) Å
N1–Pt1–N4	84.66(9)°	87.93(16)°
N1–Pt1–P1	84.43(7)°	87.35(12)°
P1–Pt1–P2	97.92(3)°	96.19(4)°
P2–Pt1–N4	93.04(6)°	88.79(11)°
N1–Pt1–P2	174.03(7)°	175.02(14)°
P1–Pt1–N4	169.04(6)°	173.66(12)°

In both cases, the Pt–N bonds are distinctly shorter than the Pt–P bonds. The difference between the Pt–P and the Pt–N bond lengths of 0.1273–0.1845 Å could be a result of the stronger *trans*-influence displayed by the azido groups. With the azido as well as the phosphine ligands displaying strong properties as

σ-donors and *π*-acceptors, the bond lengths suggest that the azido ligands are in fact stronger *π*-acceptor ligands and experiencing *π*-back bonding from the platinum(II) centre, which is strengthening the Pt–N bond.[115] This is supported by the lengthened N1–N2 and N4–N5 bond lengths in *cis*-[Pt$(N_3)_2(PPh_3)_2$]: the electron density from the metal is donated *via* *π*-back bonding into the *π**-antibonding molecular orbitals of the azido ligand.[116]

3.3 Synthesis of *trans*-Diazidodiphosphineplatinum(II) Complexes

For the synthesis of the analogous *trans*-isomers of the diazidodiphosphineplatinum(II) complexes, *trans*-[$PtCl_2(PR_3)_2$] (R = Et, Ph) was reacted with sodium azide both in aqueous solution or as a solid in organic solvents such as tetrahydrofuran, acetonitrile and chloroform, at temperatures varying from 23–65 °C (Scheme 15). In all cases, the reaction led to unreacted starting material, decomposition products or a mixture of various new products as determined by $^{31}P\{^1H\}$ NMR spectroscopy. Heating the reaction mixture at elevated temperatures resulted in a mixture of both the *cis*- and the *trans*-isomer of the starting material, supporting the previous observation that *cis*-[$PtCl_2(PR_3)_2$] (R = Et, Ph) is the thermodynamically more stable isomer.

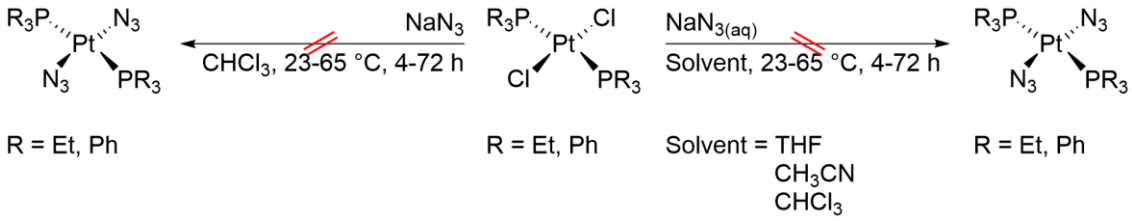

Scheme 15: Synthetic approaches to *trans*-$[Pt(N_3)_2(PR_3)_2]$ (R = Et, Ph).

Heating the reaction of *trans*-$[PtCl_2(PPh_3)_2]$ with sodium azide in chloroform under reflux for 16 hours resulted in the formation of two new resonances with ^{195}Pt-satellites in the $^{31}P\{^1H\}$ NMR spectrum in a ratio of 1.00:0.87 (Figure 20). The singlet at 12.0 ppm with a $^1J(^{31}P, ^{195}Pt)$ coupling constant of 3507 Hz was demonstrated to correspond to *cis*-$[Pt(N_3)_2(PPh_3)_2]$, however, the second singlet at 17.1 ppm exhibits a smaller $^1J(^{31}P, ^{195}Pt)$ coupling constant of 2851 Hz, indicating the formation of a *trans*-isomer. The corresponding triplet in the ^{195}Pt NMR spectrum was recorded at −3706 ppm and confirms a symmetrical complex with two phosphine groups.

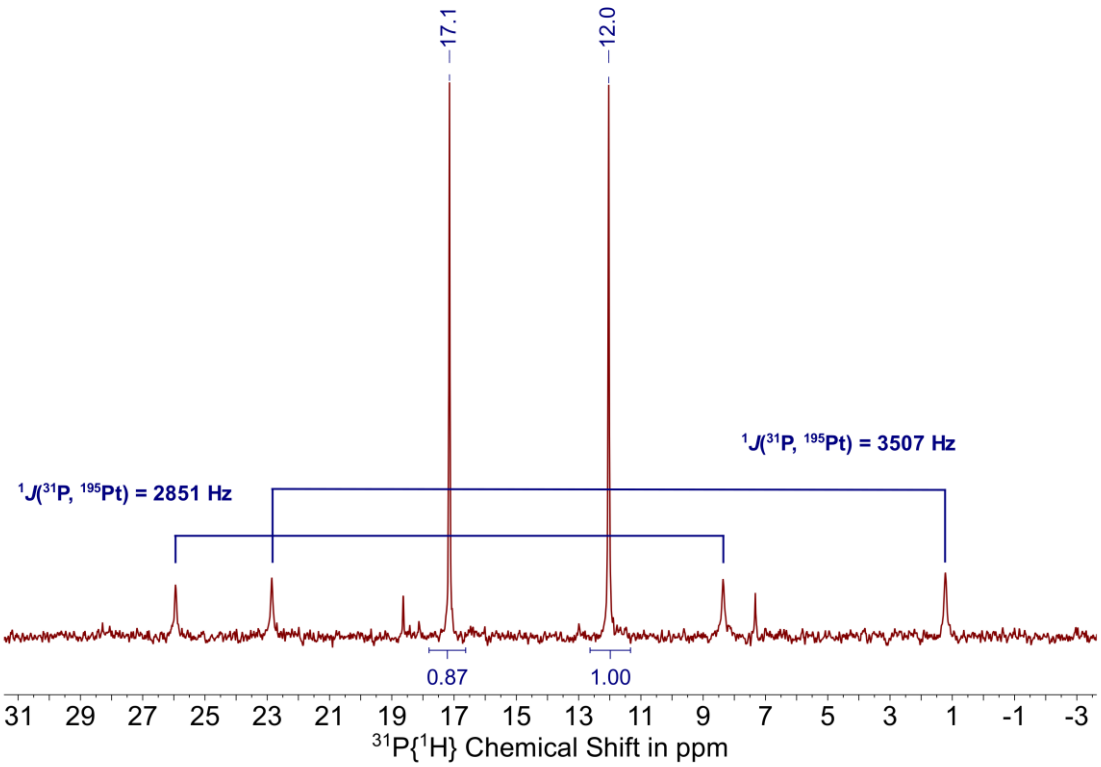

Figure 20: $^{31}P\{^1H\}$ NMR spectrum (162 MHz, $CDCl_3$, 25 °C) of the reaction mixture following the reaction of *trans*-$[PtCl_2(PPh_3)_2]$ with sodium azide in chloroform under reflux for 16 hours.

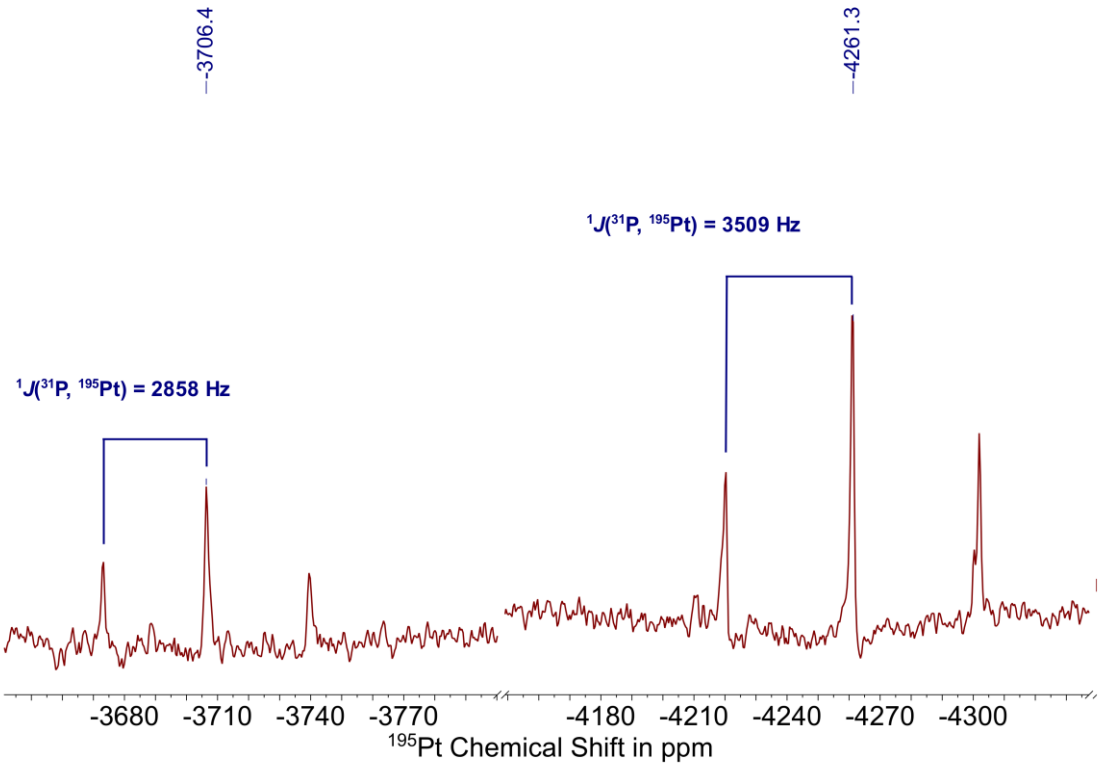

Figure 21: ^{195}Pt NMR spectrum (86 MHz, $CDCl_3$, 25 °C) of the reaction mixture following the reaction of *trans*-$[PtCl_2(PPh_3)_2]$ with sodium azide in chloroform under reflux for 16 hours.

As it was not possible to remove all *cis*-$[Pt(N_3)_2(PPh_3)_2]$ from the reaction mixture, recording an IR spectrum would not be indicative in determining the formation of *trans*-$[Pt(N_3)_2(PPh_3)_2]$ unambigously. However, considering in particular the $^1J(^{31}P, ^{195}Pt)$ coupling constant of 2633 Hz for *trans*-$[PtCl_2(PPh_3)_2]$ as discussed in Chapter 3.1, the experimental data at hand suggests that the resonance at 17.1 ppm indeed orginates from *trans*-$[Pt(N_3)_2(PPh_3)_2]$, though no definite assignment is possible without isolation of the pure complex.

Most synthetic efforts in affording *trans*-[Pt(N_3)$_2$(PEt_3)$_2$] resulted in the oxidation of the triethylphosphine ligands or the formation of the *cis*-isomer. The most promising synthetic route was the reaction of *trans*-[$PtCl_2$(PEt_3)$_2$] with sodium azide in chloroform under reflux for 72 hours. The $^{31}P\{^1H\}$ NMR spectrum confirms the formation of *cis*-[Pt(N_3)$_2$(PEt_3)$_2$] alongside another species in a ratio of 0.43:1.00 (Figure 22). The singlet at 18.4 ppm displays clear ^{195}Pt-satellites with a $^1J(^{31}P, ^{195}Pt)$ coupling constant of 2580 Hz. As no isolation of this complex was successful, it was not possible to assign the structure conclusively.

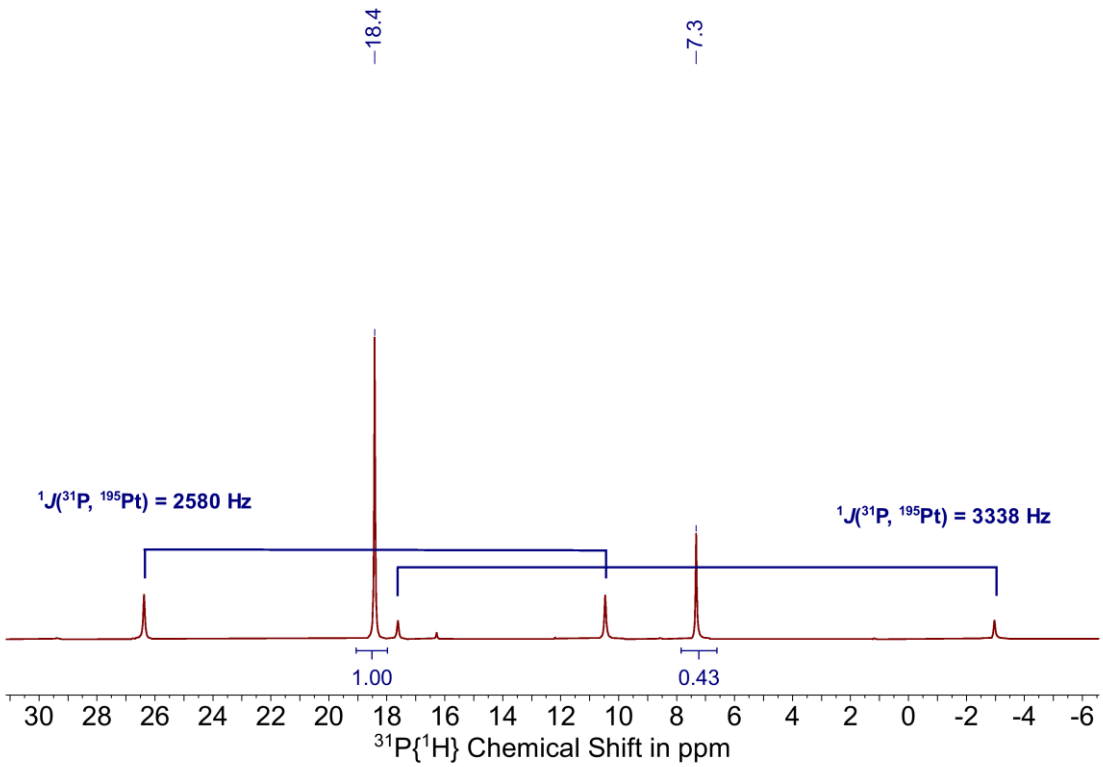

Figure 22: $^{31}P\{^1H\}$ NMR spectrum (162 MHz, $CDCl_3$, 25 °C) of the reaction mixture following the reaction of *trans*-[$PtCl_2$(PEt_3)$_2$] with sodium azide in chloroform under reflux for 72 hours.

3.4 Synthesis of *cis*-Diazidodipyridylplatinum(II) Complexes

Since previous work has focused on [2+3]-cycloaddition reactions of diazidodipyridylplatinum(II) complexes with strain-promoted or electron-deficient organic alkynes,[96,100] the platinum(II) complex *cis*-[Pt(N_3)$_2$(*py*)$_2$] was chosen as a benchmark compound for cycloaddition reactions with activated alkynes under mild conditions. Changing from a *N*-donor to a *P*-donor ligand will have an effect on the electron density on the platinum centre as well as the energetic levels of the frontier orbitals (see Chapter 2.1).

The selective synthesis of *cis*-diazidoplatinum(II) complexes has been established previously and is realised *via* the iodido complex rather than the chlorido complex due to the similarity in *trans*-effect between pyridyl and chlorido ligands (Scheme 16).[114]

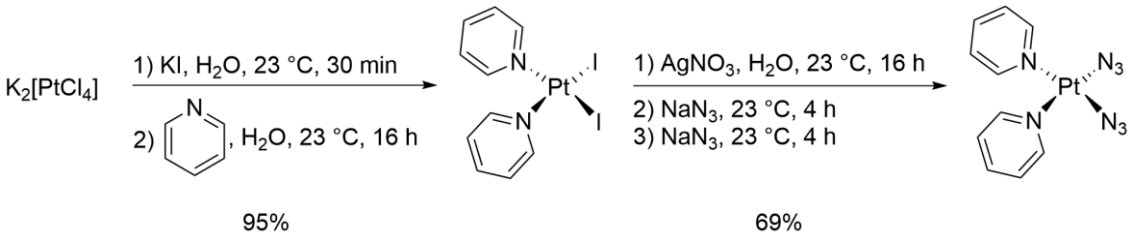

Scheme 16: Synthetic approach to *cis*-[Pt(N_3)$_2$(*py*)$_2$].

Starting with potassium tetrachloridoplatinate(II) the chlorido ligands are exchanged to iodido ligands through the addition of potassium iodide in water. The subsequent addition of pyridine leads to the isolation of *cis*-[PtI_2(*py*)$_2$]. The chemical shift of the proton in *ortho*-position on the pyridyl ligand as well as its

$^{3}J(^{195}Pt, ^{1}H)$ coupling constant of 42 Hz is indicative for the formation of the *cis*-isomer.[117] The reaction of the diiodidoplatinum(II) complex with silver nitrate and sodium azide in water proceeds in analogous manner to its established *trans*-isomer and results in the formation of *cis*-$[Pt(N_3)_2(py)_2]$, selectively. The complex was characterised *via* ^{1}H NMR and IR spectroscopy and the data is in accordance with that of diazidodipyridylplatinum(II) in literature.[98]

3.5 Synthesis of *cis*-Diiodidopyridylphosphineplatinum(II) Complexes

In order to determine a trend between the reactivity of the diazidoplatinum(II) complexes towards gold(I) alkynes in dependence of the *N*/*P*-donor ligand, next to the dipyridyl and the diphosphine compounds, synthesis of the complexes with a mixed ligand system comprising one pyridyl and one phosphine ligand was attempted.

When targeting mixed ligand systems, both the kinetic *trans*-effect as well as the thermodynamically more stable isomer can be utilised in the synthetic approach. Dihalidoplatinum(II) compounds act as the starting point for further substitution of the ligands. Whilst the synthesis for *trans*-$[PtCl_2(L)(L')]$ with L, L' = amine can be achieved through the addition of the second amine ligand to *cis*-$[PtCl_2L_2]$ under elevated temperatures, *cis*-$[PtCl_2(L)(L')]$ is accessed *via* an iodido-bridged dimer formed from *cis*-$[PtI_2L_2]$ (Scheme 17). Due to the stronger *trans*-effect of the iodido compared to the amine ligands, the Pt–I bonds in *trans*-position to the

terminal iodido ligand are cleaved, hence resulting in formation of the *cis*-isomers.[107,118,119]

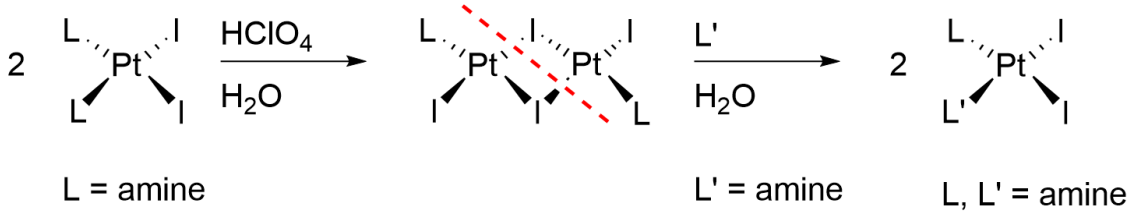

Scheme 17: Synthetic approach to *cis*-[PtI$_2$(L)(L')] with mixed amine ligands.[118,119]

Analogous compounds with mixed ligand systems incorporating one *N*- and one *P*-donor have as of yet not been established. The procedure was adapted from the route to mixed amine-ligand systems (Scheme 18).

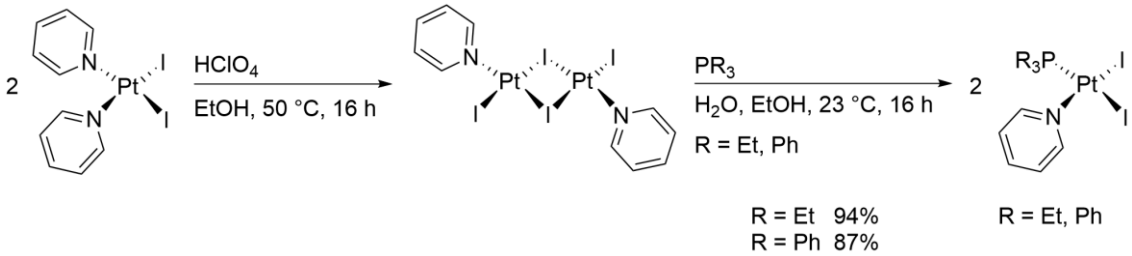

Scheme 18: Synthetic approaches to *cis*-[PtI$_2$(*py*)(PR$_3$)] (R = Et, Ph).

The reaction of two equivalents of *cis*-[PtI$_2$(*py*)$_2$] with perchloric acid results in the protonation of pyridine. The equilibrium shifts to an iodido-bridged dimer with the precipitation of the red-brown solid being the driving force to the reaction. As the

platinum-iodide stretching frequency is observed at wavenumbers below 200 cm^{-1},[118] it was not possible to determine this experimentally with the available equipment. ^{1}H NMR spectroscopy was performed on the dimer for characterisation which displayed signals in the aromatic region corresponding to the pyridyl ligands. However, due to poor solubility and resulting insufficient resolution of the spectrum, assigning the resonances unambiguously was not feasible. Since the literature procedures suggest quantitative formation of the dimer and continuing without further purification, in a next step the respective phosphine was dissolved in ethanol and added to a suspension of the dimer in water at room temperature. Solvent choice was based on facilitating the solubility of the phosphine in a form which is miscible with water.

The solid which was isolated from the reaction mixture of reacting *trans*-$[PtI_2(py)]_2$ with triphenylphosphine displays one clear resonance at 12.4 ppm in the $^{31}P\{^{1}H\}$ NMR spectrum (Figure 23). The resonance confirms coupling of the phosphorus nuclei to a platinum centre with a $^{1}J(^{31}P, ^{195}Pt)$ coupling constant of 2512 Hz. The magnitude of this coupling constant suggests the formation of a *trans*-isomer rather than the target compound *cis*-$[PtI_2(py)(PPh_3)]$. The ^{1}H NMR spectrum reveals several resonances within the aromatic region (Figure 24). The signal at 8.9 ppm corresponds to the protons in *ortho*-position to the nitrogen atom in the pyridyl ligand. The coupling constant of 42 Hz confirms a $^{3}J(^{1}H, ^{195}Pt)$ coupling of the protons to the platinum centre, suggesting the formation of a complex including both the triphenylphosphine and pyridyl ligand.

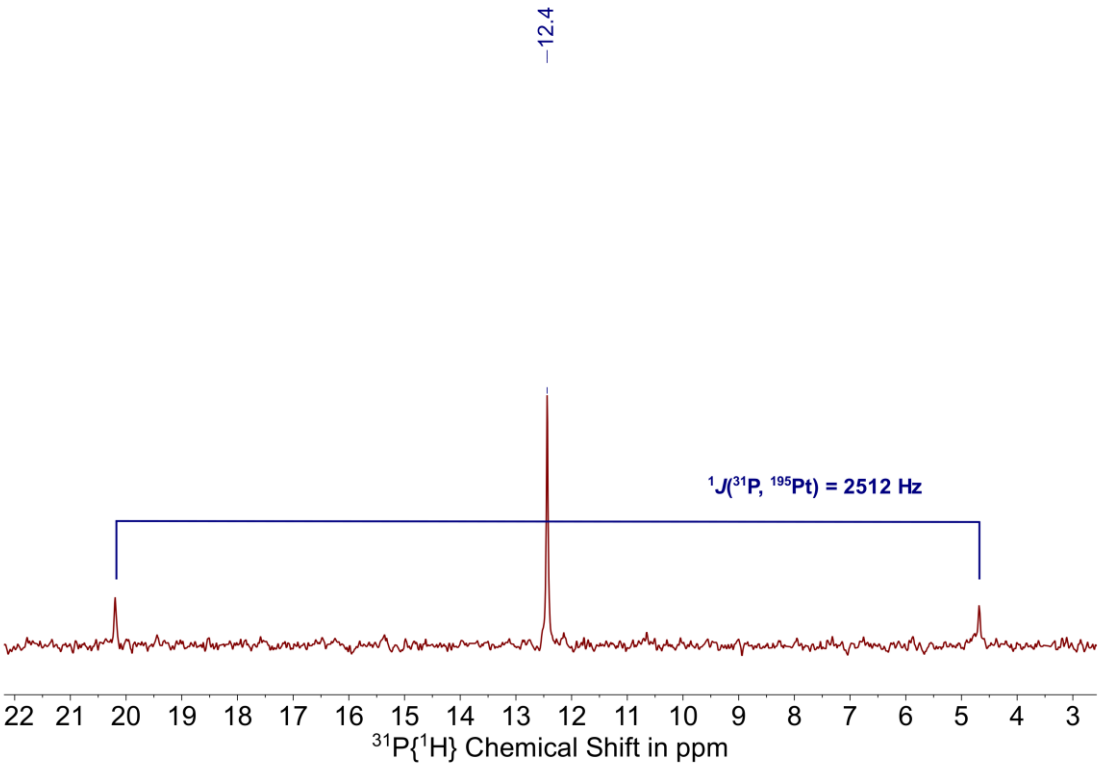

Figure 23: $^{31}P\{^{1}H\}$ NMR spectrum (162 MHz, C_4D_8O, 25 °C) of the reaction mixture following the reaction of *cis*-$[PtI_2(py)]_2$ and triphenylphosphine.

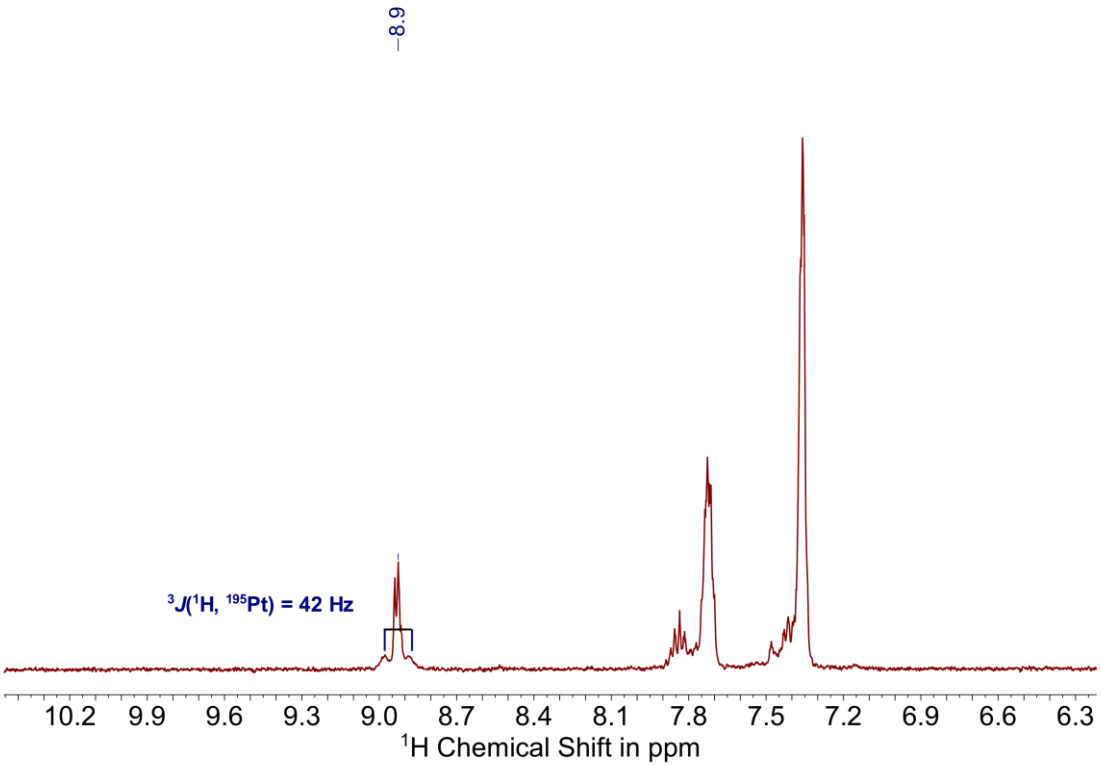

Figure 24: ^{1}H NMR spectrum (400 MHz, C_4D_8O, 25 °C) of the reaction mixture following the reaction of *cis*-[PtI_2(*py*)]$_2$ and triphenylphosphine.

The $^{31}P\{^1H\}$ and ^{1}H NMR spectra for the reaction product isolated from the reaction of *cis*-[PtI_2(*py*)]$_2$ with triethylphosphine show similar results. One clear singlet with coupling to a platinum centre is recorded in the $^{31}P\{^1H\}$ spectrum at 0.6 ppm (Figure 25). The $^1J(^{31}P, ^{195}Pt)$ coupling constant of 2263 Hz indicates the formation of a *trans*-isomer, analogously to the reaction with triphenylphosphine. The ^{1}H NMR spectrum displays three groups of resonances corresponding to the protons on the pyridyl ligand in the aromatic region (Figure 26). The signal at 9.0 ppm displays the coupling of the protons in *ortho*-position on the pyridyl ligand to the platinum centre. At 2.3 ppm a multiplet is observed, which can be assigned to an overlapping triplet and quartet from the aliphatic

protons of the triethylphosphine ligands. Comparison of the integrals of these resonances in the ^{1}H NMR spectrum suggest the formation of one complex with both a pyridyl and a triethylphosphine ligand.

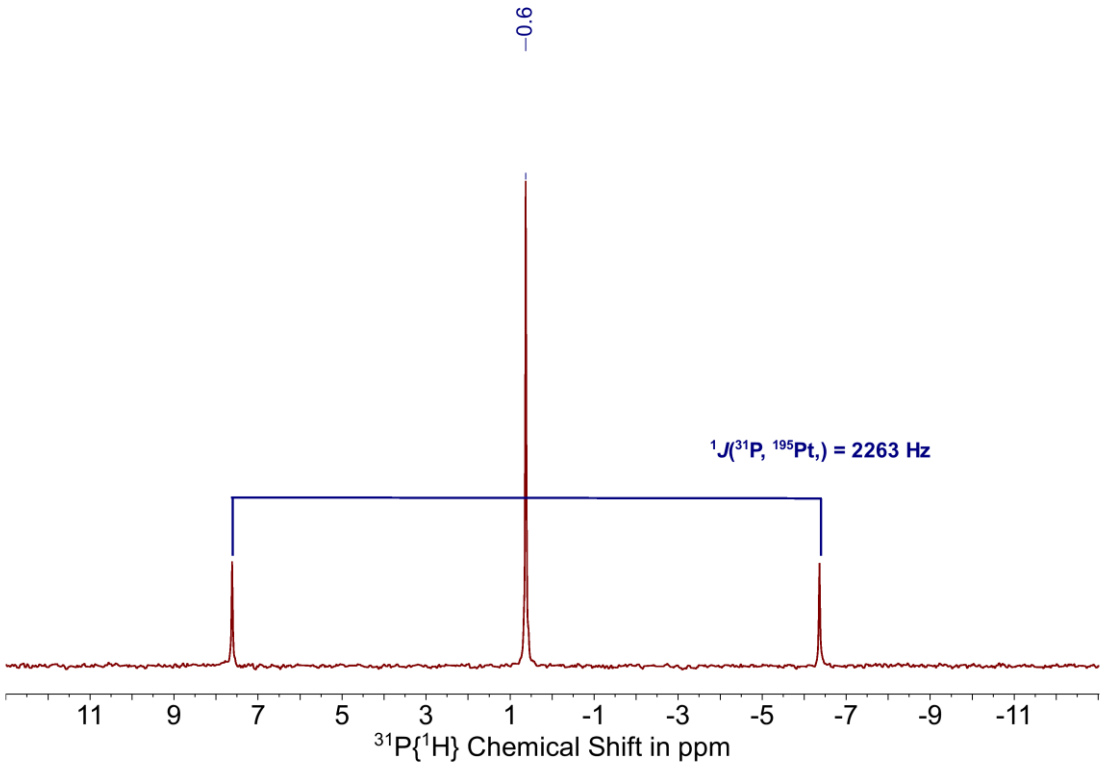

Figure 25: $^{31}P\{^{1}H\}$ NMR spectrum (162 MHz, $(CD_3)_2CO$, 25 °C) of the reaction mixture following the reaction of *cis*-$[PtI_2(py)]_2$ and triethylphosphine.

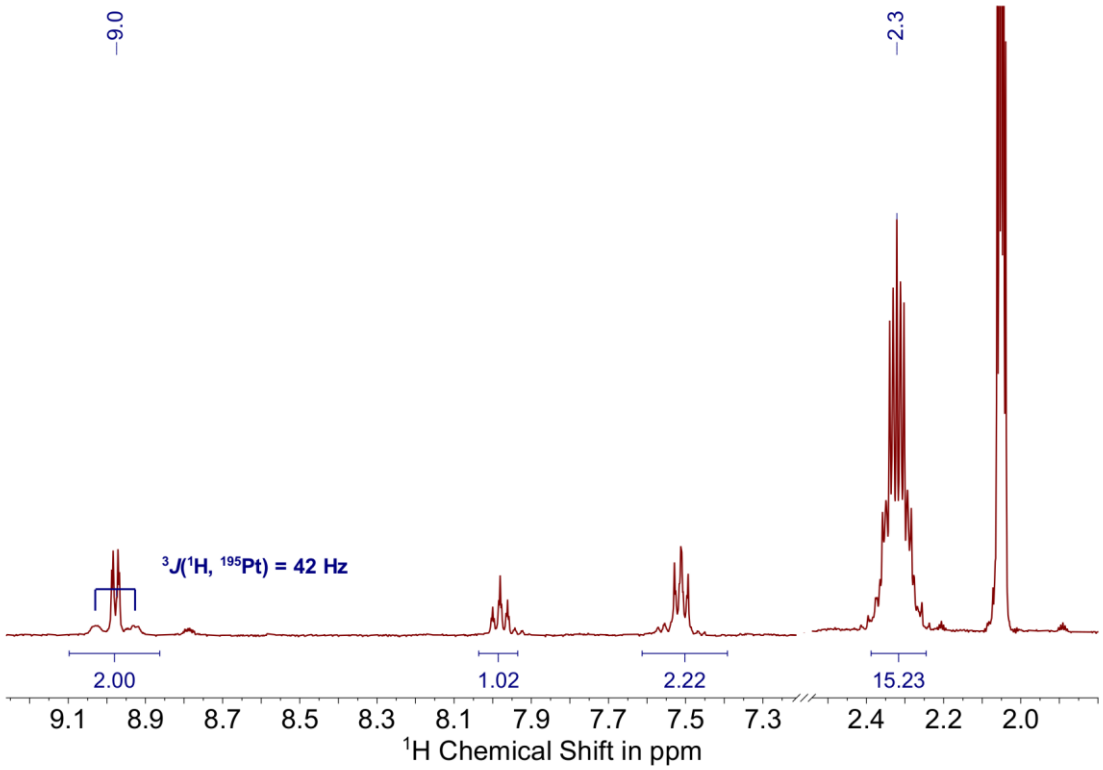

Figure 26: ^{1}H NMR spectrum (400 MHz, $(CD_3)_2CO$, 25 °C) of the reaction mixture following the reaction of *cis*-$[PtI_2(py)]_2$ and triethylphosphine.

Crystals of the platinum dimer suitable for X-ray diffraction analysis were isolated as red blocks for both of the respective phosphine ligands from concentrated solutions in acetone. Due to literature-known cell parameters and unambiguous refinement of the structural motif of *cis*-$[PtI_2(PPh_3)]_2$, no full measurement of this structure was performed. The cell parameters of the unit cells determined after the fast scan with 180 frames are in good agreement with those in literature for *cis*-$[PtI_2(PPh_3)]_2$ (Table 7). The slightly decreased lattice parameters are due to a change in lattice vibrations as the experimental data was collected at a lower temperature compared to the data in literature.

Table 7: Comparison of experimentally determined cell parameters (Exp.) for *cis*-$[PtI_2(PPh_3)]_2$ collected at −173.15 °C compared to values in literature (Lit.) collected at 19.85 °C[120]

	a	***b***	***c***	***α, γ***	***β***
Exp.	15.9539(14) Å	15.7565(9) Å	16.6969(15) Å	90°	118.507(3)°
Lit.	16.036(4) Å	15.874(4) Å	16.882(4) Å	90°	117.980(4)°

Complex *trans*-$[PtI_2(PEt_3)]_2$ crystallises with two formula units in the monoclinic space group $P2_1/n$ (Figure 27) (R_1 = 2.61%, wR_2 = 5.89%, R_{int} = 4.64%, *GooF* = 1.201, $e_{min/max}$ = −1.58/1.43 $Å^{-3}$). Comparison of selected bond lengths and angles for both of the complexes *trans*-$[PtI_2(PR_3)]_2$ (R = Et, Ph) reveals no significant difference with regards to the structure of the Pt–I–Pt bridging unit (Table 8).

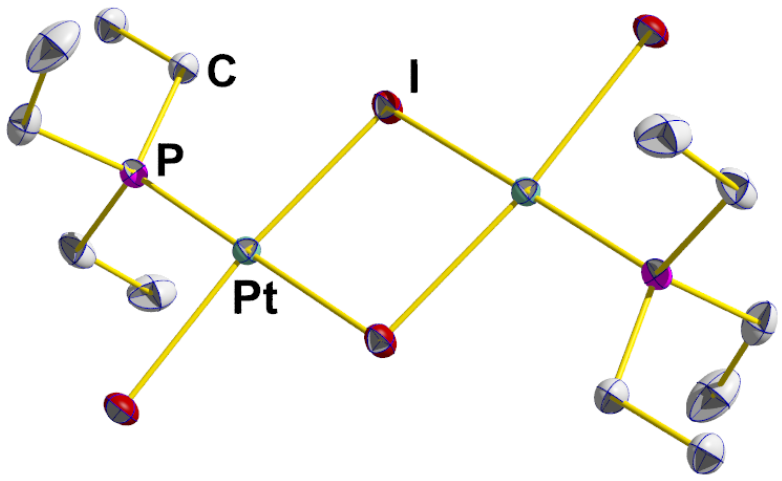

Figure 27: Molecular structure of *trans*-$[PtI_2(PEt_3)]_2$ in the solid state. Hydrogen atoms are omitted for clarity. Displacement ellipsoids are shown at the 50% probability level.

Table 8: Selected bond lengths and angles of the molecular structures of complexes *trans*-$[PtI_2(PR_3)]_2$ (R = Et, Ph) in the solid state. For R = Ph, data were previously reported,[120] whereas for R = Et, the values were obtained experimentally

	***trans*-$[PtI_2(PPh_3)]_2$**	***trans*-$[PtI_2(PEt_3)]_2$**
Pt1–Pt1	3.9198(8) Å	3.9172(4) Å
I1–I1	3.4970(9) Å	3.5403(5) Å
I1–Pt1–I1	83.455(15)°	84.211(13)°
I1–Pt1–I2	172.337(4)°	172.866(15)°
I1–Pt1–P1	176.76(4)°	174.67(4)°

Isolation of compounds *trans*-$[PtI_2(PR_3)]_2$ (R = Et, Ph) is unexpected considering the reaction mechanism proposed in Scheme 18. These observations suggest a higher lability of the pyridyl ligands in the chosen experimental conditions in comparison to the phosphine ligands, resulting in exchange of both of the *N*-donor with the added *P*-donor ligands. However, in addition to identifying the dimers, crystals suitable for X-ray diffraction analysis of the mixed ligand complexes *trans*-$[PtI_2(py)(PR_3)]$ (R = Et, Ph) were further isolated. Crystals of concentrated reaction mixtures of the compounds in chloroform confirmed the successful formation of *trans*-$[PtI_2(py)(PPh_3)]$ (R_1 = 1.42%, wR_2 = 3.17%, R_{int} = 5.10%, *GooF* = 1.034, $e_{min/max}$ = −0.67/0.53 Å^{-3}) and *trans*-$[PtI_2(py)(PEt_3)]$ (R_1 = 1.43%, wR_2 = 3.43%, R_{int} = 3.49%, *GooF* = 1.223, $e_{min/max}$ = −0.73/0.85 Å^{-3}), respectively. The complexes crystallise as yellow blocks in the monoclinic space group $P2_1/n$ with four formula units in the unit cell (Figure 28, Figure 29). Comparison of selected bond lengths and angles confirm the analogous structure motifs of the square-planar platinum(II) complexes, with only minor differences which mostly lie within the scope of the error (Table 9).

With an average Pt–I bond length of 2.60 Å this is significantly larger compared to the Pt–N bond length of 2.0969(19)–2.100(2) Å or the Pt–P bond length of 2.444(6)–2.2484(6) Å. This observation is in agreement with the phosphine and pyridyl ligands receiving *π*-backbonding from the metal centre which strengthens the bond, whereas the iodido ligands solely act as *σ*- and *π*-donors.[121–124]

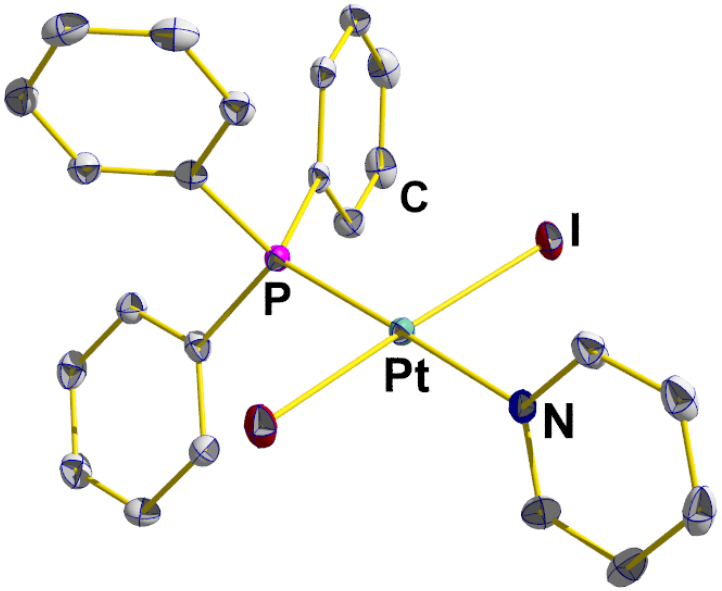

Figure 28: Molecular structure of *trans*-[PtI_2(*py*)(PPh_3)] in the solid state. Calculated hydrogen atoms are omitted for clarity. Displacement ellipsoids are shown at the 50% probability level.

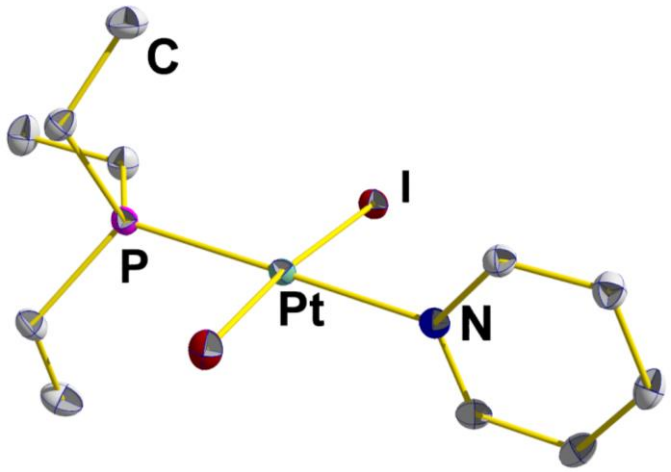

Figure 29: Molecular structure of *trans*-[PtI_2(*py*)(PEt_3)] in the solid state. Calculated hydrogen atoms are omitted for clarity. Displacement ellipsoids are shown at the 50% probability level.

Table 9: Selected bond lengths and angles of the molecular structures of complexes *trans*-[PtI_2(*py*)(PR_3)] (R = Et, Ph) in the solid state[120]

	***trans*-[PtI_2(*py*)(PPh_3)]**	***trans*-[PtI_2(*py*)(PEt_3)]**
Pt1–I1	2.5922(2) Å	2.5960(3) Å
Pt1–I2	2.6131(2) Å	2.6055(3) Å
Pt1–N1	2.100(2) Å	2.0969(19) Å
Pt1–P1	2.2444(6) Å	2.2484(6) Å
I1–Pt1–I2	172.606(14)°	171.738(11)°
N1–Pt1–P1	178.765(62)°	178.497(55)°
I1–Pt1–P1	94.277(21)°	96.114(17)°
N1–Pt1–I2	87.204(61)°	86.899(50)°

According to the reaction mechanism in Scheme 17, targeting compounds with a mixed ligand system *via* the iodido-bridged dimer provides access to the *cis*-isomers. However, with the examples at hand, in both cases, the *trans*-isomers of [PtI_2(*py*)(PR_3)] (R = Et, Ph) were isolated. Due to the exchange of the pyridyl

to the phosphine ligands on the dimeric complex, the forces of the competitive *trans*-effect of the ligands involved have been revoked. Following the trend of the *trans*-effect of ligands $PR_3 > I^- > py$,[125] the iodido ligands dominate which bonds are cleaved in the dimer *trans*-$[PtI_2(py)]_2$, yielding the *cis*-isomers of $[PtI_2(py)(L)]$. Contrary to this, phosphine groups exhibit a stronger *trans*-effect than iodido ligands. Reacting a second ligand with *trans*-$[PtI_2(PR_3)]_2$ as the dimer thus results in cleavage along the bonds in *trans*-position to the phosphine groups, leading to the formation of *trans*-$[PtI_2(PR_3)(L)]$ (Scheme 19). It should further be noted, that previous reports in literature have informed on the isolation of *trans*-$[PtI_2(L)(py)]$ for syntheses in which pyridine was added as the second ligand to dimers with iodido and tetramethylene sulphoxide ligands.[126]

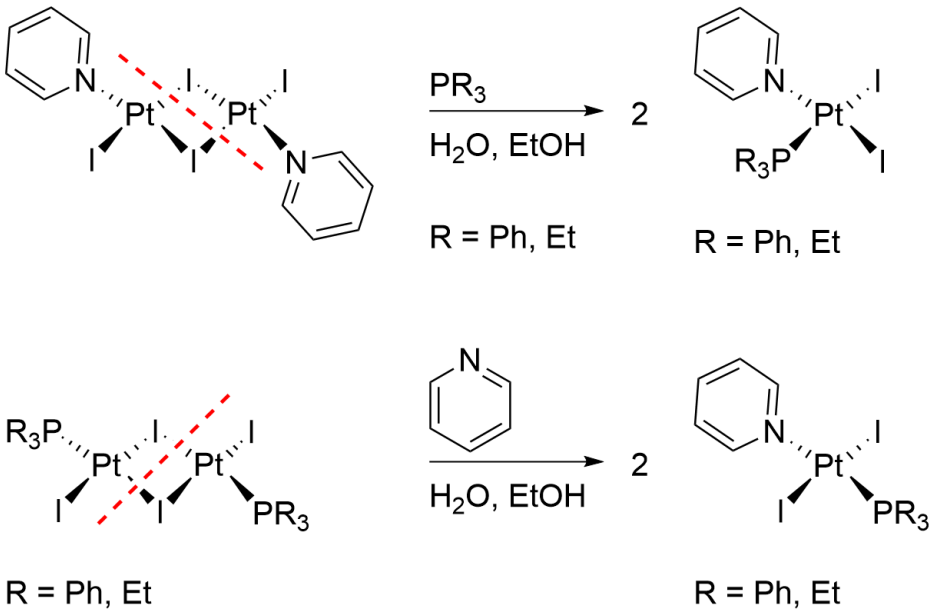

Scheme 19: Synthetic approaches to *cis*- and *trans*-$[PtI_2(py)(PR_3)]$ (R = Et, Ph).

3.6 Synthesis of *trans*-Diazidopyridylphosphineplatinum(II) Complexes

After synthesising the mixed diiodidopyridylphosphine platinum(II) complexes *trans*-[PtI_2(*py*)(PR_3)] (R = Et, Ph), the next step was exchanging the iodido ligands for azido ligands. The direct addition of sodium azide to a solution of the complexes was attempted with various solvent systems (Scheme 20). In order to have both components in solution to promote reactivity, sodium azide was added in an aqueous solution to solvents miscible with water, such as tetrahydrofuran, acetonitrile or chloroform, and stirred at room temperature for 4 hours. An alternative approach was an adaptation from the literature for the reaction of dihalidoplatinum(II) complexes with sodium azide after the addition of silver nitrate.[114]

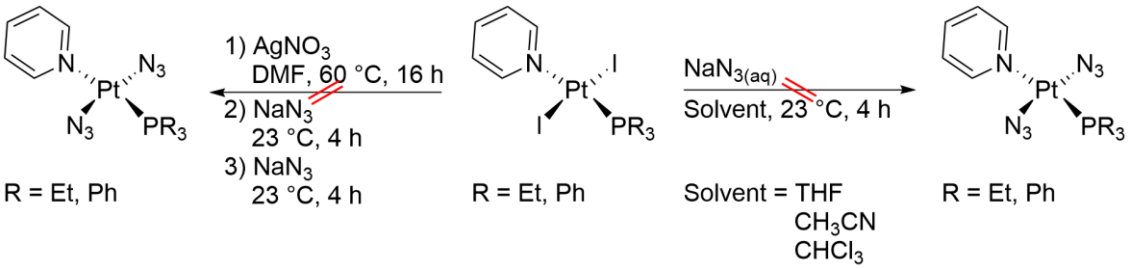

Scheme 20: Synthetic approaches to *trans*-[$Pt(N_3)_2$(*py*)(PR_3)] (R = Et, Ph).

The attempted metathesis reaction of the iodido ligands on *trans*-[PtI_2(*py*)(PPh_3)] with sodium azide in tetrahydrofuran resulted in the decomposition of the complex under the formation of triphenylphosphine oxide as the main reaction

product. Interestingly, the reaction with sodium azide in chloroform as well as the synthetic approach *via* silver nitrate in dimethylformamide resulted in the cleavage and oxidation of the triphenylphosphine groups (singlet at 29.5 ppm), as well as the isolation of *cis*-[$Pt(N_3)_2(PPh_3)_2$] (singlet at 12.0 ppm), as determined by $^{31}P\{^1H\}$ NMR spectroscopy (Figure 30). Although the resonance for the triphenylphosphine ligand in *cis*-[$Pt(N_3)_2(PPh_3)_2$] is very close to the corresponding signal in *trans*-[PtI_2(*py*)(PPh_3)], the structure can be assigned unambiguously due to the change in the $^1J(^{31}P, ^{195}Pt)$ coupling constant of 3507 Hz *vs* 2512 Hz. This observation suggests the platinum-pyridyl bond to be more labile under the chosen experimental conditions compared to the platinum-phosphine bond, which then in turn leads to the formation of the *cis*-diazido platinum complex as the thermodynamically more favoured isomer, as previously demonstrated. Pursuing the metathesis reaction in acetonitrile resulted in multiple new resonances in the $^{31}P\{^1H\}$ NMR spectrum displaying phosphorus-platinum coupling. The most prominent signals are a singlet at 17.1 ppm with a $^1J(^{31}P, ^{195}Pt)$ coupling constant of 2853 Hz and a singlet at −2.3 ppm with a $^1J(^{31}P, ^{195}Pt)$ coupling constant of 3370 Hz. Figure 31 depicts exemplary IR spectra of two of the reaction mixtures from the reaction of compound *trans*-[PtI_2(*py*)(PPh_3)] with sodium azide displaying the asymmetric stretching frequency for azido ligands at 2050 cm^{-1} and 2054 cm^{-1}, respectively. No isolation of a single species in the syntheses aiming at *trans*-[$Pt(N_3)_2$(*py*)(PPh_3)] enabling unambiguous assignment was successful.

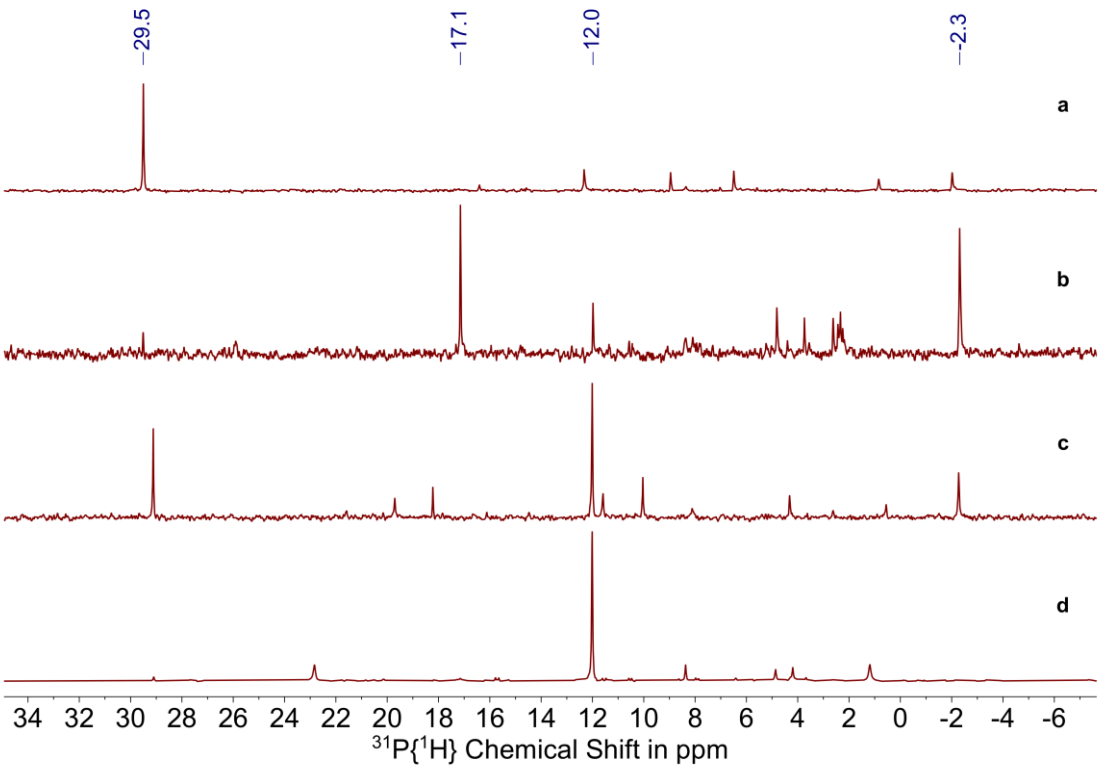

Figure 30: $^{31}P\{^{1}H\}$ NMR spectra (162 MHz, $CDCl_3$, 25 °C) of the reaction mixtures of the synthetic approaches to *trans*-$[Pt(N_3)_2(py)(PPh_3)]$ outlined in Scheme 20. *trans*-$[PtI_2(py)(PPh_3)]$ was reacted with sodium azide in tetrahydrofuran (a), acetonitrile (b), chloroform (c) or the reaction *via* silver nitrate (d).

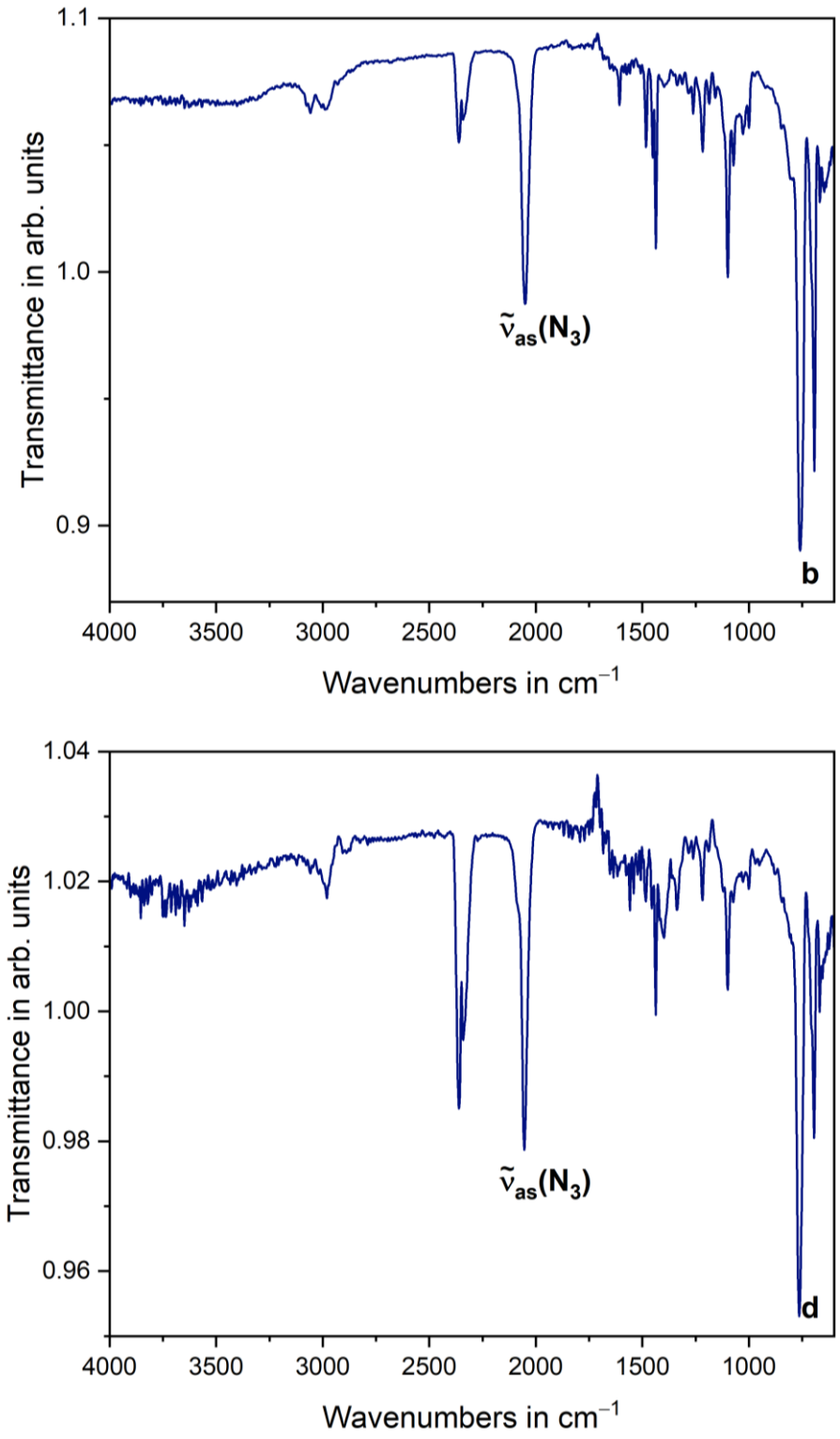

Figure 31: Selected IR spectra (23 °C) of the reaction mixtures of the synthetic approaches to *trans*-[Pt(N_3)$_2$(*py*)(PPh_3)] outlined in Scheme 20. *trans*-[PtI_2(*py*)(PPh_3)] was reacted with sodium azide in acetonitrile (b) or *via* a reaction with silver nitrate (d).

The analogous metathesis reactions of *trans*-[PtI_2(*py*)(PEt_3)] with sodium azide resulted in unreacted starting material in most of the approaches, as determined by the singlet at 0.3 ppm in the $^{31}P\{^1H\}$ NMR spectrum (Figure 32). For the reaction in acetonitrile, a second clear singlet begins to appear at 12.7 ppm with a $^1J(^{31}P, ^{195}Pt)$ coupling constant of 2417 Hz. In comparison to this, the synthetic path *via* silver nitrate resulted in a new resonance at 18.4 ppm with a $^1J(^{31}P, ^{195}Pt)$ coupling constant of 2580 Hz.

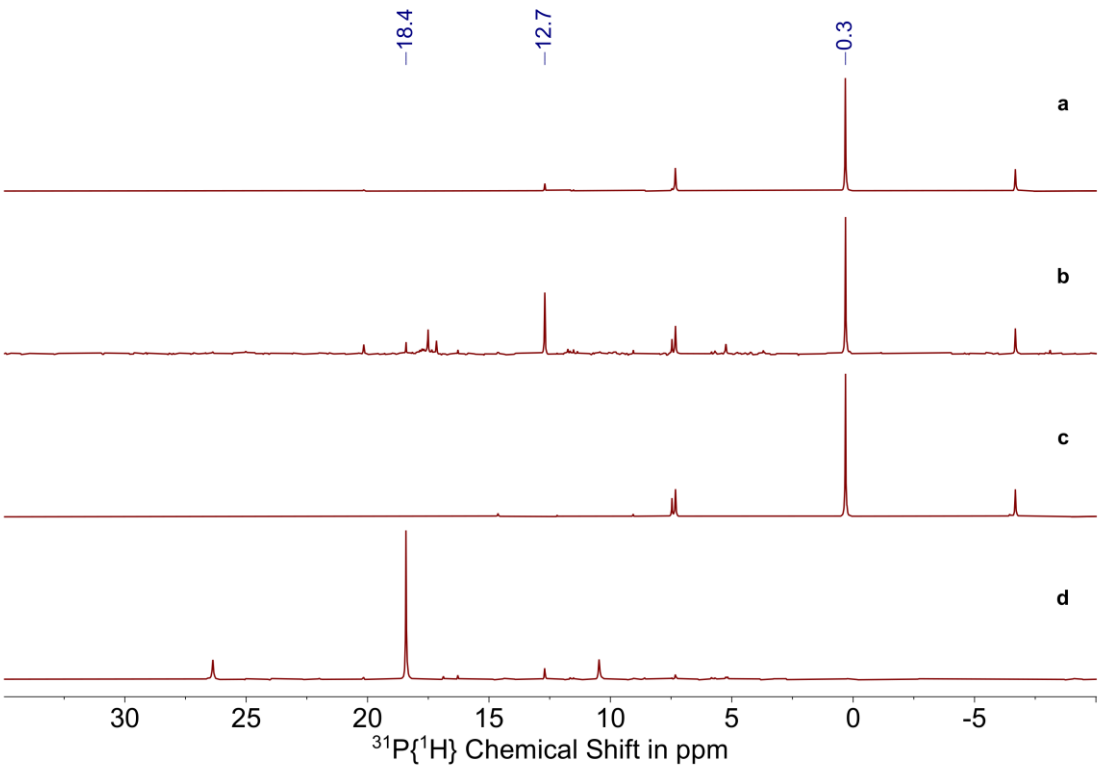

Figure 32: $^{31}P\{^1H\}$ NMR spectra (162 MHz, $CDCl_3$, 25 °C) of the reaction mixtures of the synthetic approaches to *trans*-[$Pt(N_3)_2$(*py*)(PEt_3)] outlined in Scheme 20. *trans*-[PtI_2(*py*)(PEt_3)] was reacted with sodium azide in tetrahydrofuran (a), acetonitrile (b), chloroform (c) or the reaction *via* silver nitrate (d).

The corresponding ^{1}H NMR spectrum of the reaction *via* silver nitrate confirms the presence of pyridyl ligands, however, the resonance at 8.6 ppm likely corresponding to the protons in *ortho*-position on the pyridyl ligand does not display a clear coupling to the platinum centre (Figure 33). The signals in the aromatic region suggest the formation of multiple species.

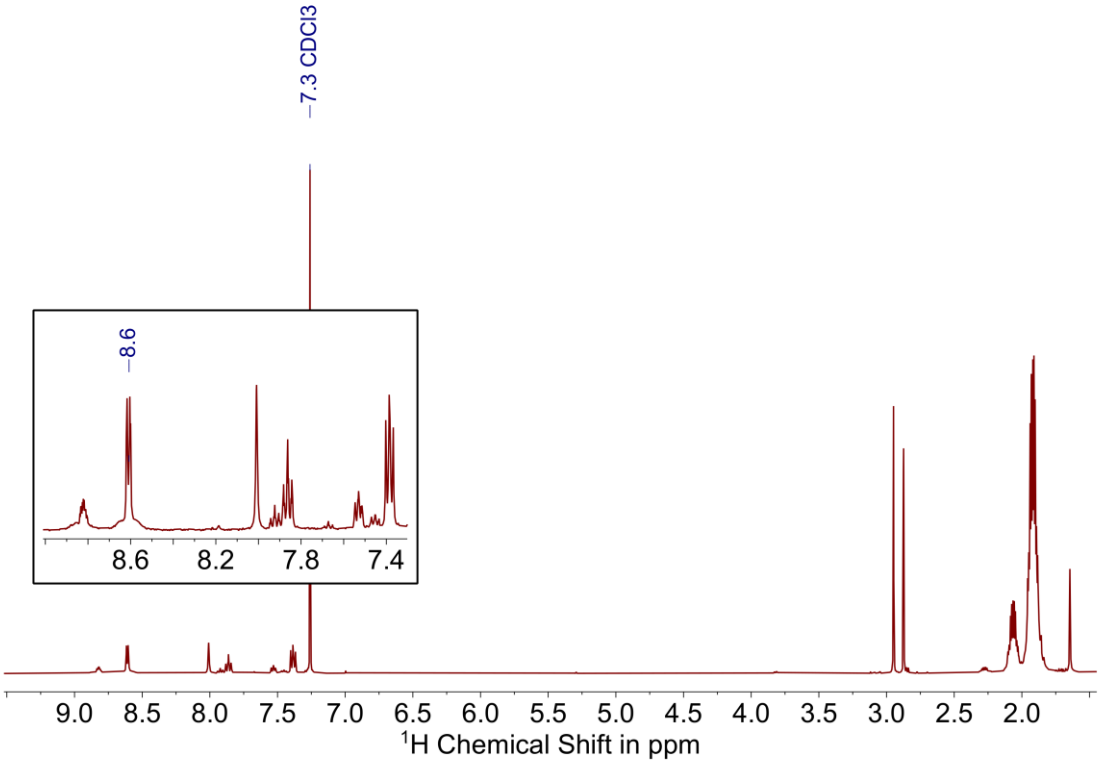

Figure 33: ^{1}H NMR spectrum (400 MHz, $CDCl_3$, 25 °C) of the reaction mixture following the reaction of *trans*-[PtI_2(*py*)(PEt_3)] and sodium azide *via* a reaction with silver nitrate (Scheme 20). Inset displays resonances in the aromatic region.

Figure 34 depicts the ^{195}Pt NMR spectrum of the reaction mixture *via* silver nitrate which was recorded between −3200 ppm and −4000 ppm. One clear triplet was

recorded at −3675 ppm with a coupling constant of 2580 Hz, in accordance with the $^{1}J(^{31}P, ^{195}Pt)$ coupling constant detected for the new singlet at 18.4 ppm in the $^{31}P\{^{1}H\}$ NMR spectrum. The splitting of the resonance for the platinum nuclei into a triplet, rather than a doublet, reveals that the signal does in fact correspond to a symmetrical complex with two phosphine ligands rather than one phosphine and one pyridyl ligand.

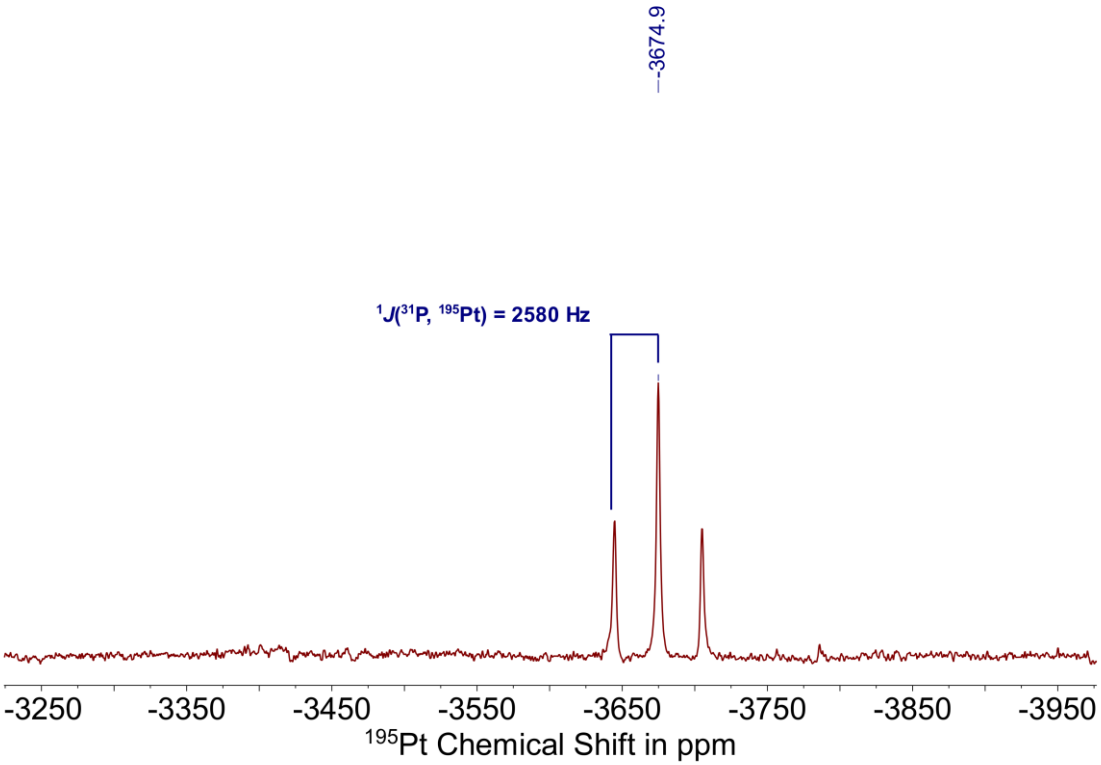

Figure 34: ^{195}Pt NMR spectrum (86 MHz, $CDCl_3$, 25 °C) of the reaction mixture following the reaction of *trans*-[PtI_2(*py*)(PEt_3)] and sodium azide *via* a reaction with silver nitrate (Scheme 20).

The IR spectrum confirms the presence of azido ligands with a strong band for the asymmetric stretching frequency at 2053 cm^{-1} (Figure 35). Compiling all of

these observations together, and considering the magnitude of the $^{1}J(^{31}P, ^{195}Pt)$ coupling constant of 2580 Hz, the data suggest that the resonance at 18.4 ppm in the $^{31}P\{^{1}H\}$ NMR spectrum corresponds to a symmetrical *trans*-isomer of a diphosphineplatinum(II) complex with an azido ligand, most likely *trans*-$[Pt(N_3)_2(PEt_3)_2]$. This conclusion is in line with the experimental data of pursuing the synthesis of *trans*-diazidobis(triethylphosphine)platinum(II) directly (Chapter 3.3).

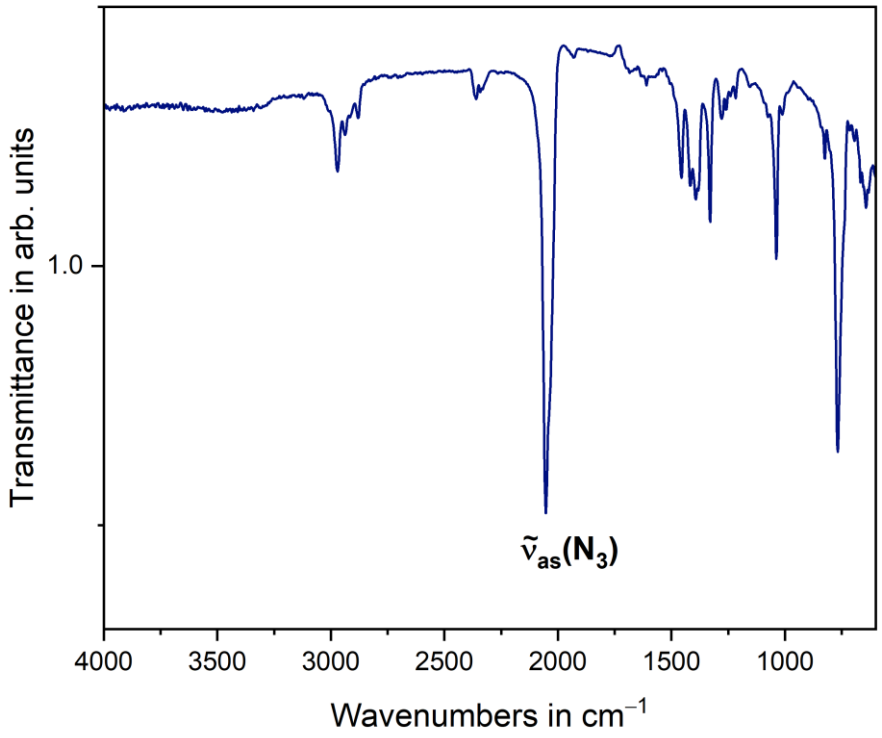

Figure 35: IR spectrum (23 °C) of the reaction mixture following the reaction of *trans*-$[PtI_2(py)(PEt_3)]$ and sodium azide *via* a reaction with silver nitrate (Scheme 20).

To conclude, various attempts of exchanging the iodido ligands for azido ligands on *trans*-[PtI_2(*py*)(PR_3)] (R = Et, Ph) were pursued. Both of the complexes showed varied results, ranging from the decomposition of the compounds to the formation of the *cis*-diazidodiphosphine complexes. Synthetic approaches eliminating the iodido ligands as silver iodide in a first step yielded a clear novel product, as determined *via* $^{31}P\{^1H\}$ spectroscopy. Crystallisation attempts were unsuccessful, requiring further investigations in order to conclude the structures unambiguously.

3.7 Synthesis of Gold(I) Alkynes

Synthesis of the gold(I) alkyne [$Au(PPh_3)(CC(C_6H_4)NO_2)$] (Scheme 11, page 60) has previously been reported and was prepared by modification of literature procedures.[127] Alkynes [$Au(PPh_3)(CC(C_6H_4)X)$] (X = NO_2, Br, CN) were synthesised analogously according to the synthetic pathway in Scheme 21. The formation of a potassium methanolate leads to the deprotonation of the terminal alkyne, which subsequently undergoes ligand exchange with the chlorido ligand on the gold(I) complex [$Au(PPh_3)Cl$] when stirred in methanol at 23 °C for 16 hours. [$Au(PPh_3)(CC(C_6H_4)X)$] (X = NO_2, Br, CN) were characterised by NMR, IR and UV-visible spectroscopy, as well as mass spectrometry. For all gold(I) alkynes, the $^{31}P\{^1H\}$ NMR spectra show a clear shift from the singlet at 33 ppm for [$Au(PPh_3)Cl$] to a new resonance at 42 ppm, which is largely insensitive to substitution on the phenyl group (Figure 36). The product was checked for

residual terminal alkyne *via* thin layer chromatography and ^{1}H NMR spectroscopy.

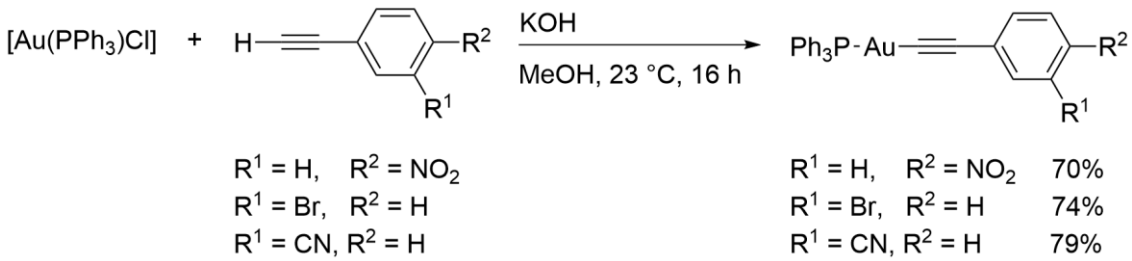

Scheme 21: Synthetic approach to gold(I) alkynes $[Au(PPh_3)(CC(C_6H_4)X)]$ (X = NO_2, Br, CN).[127]

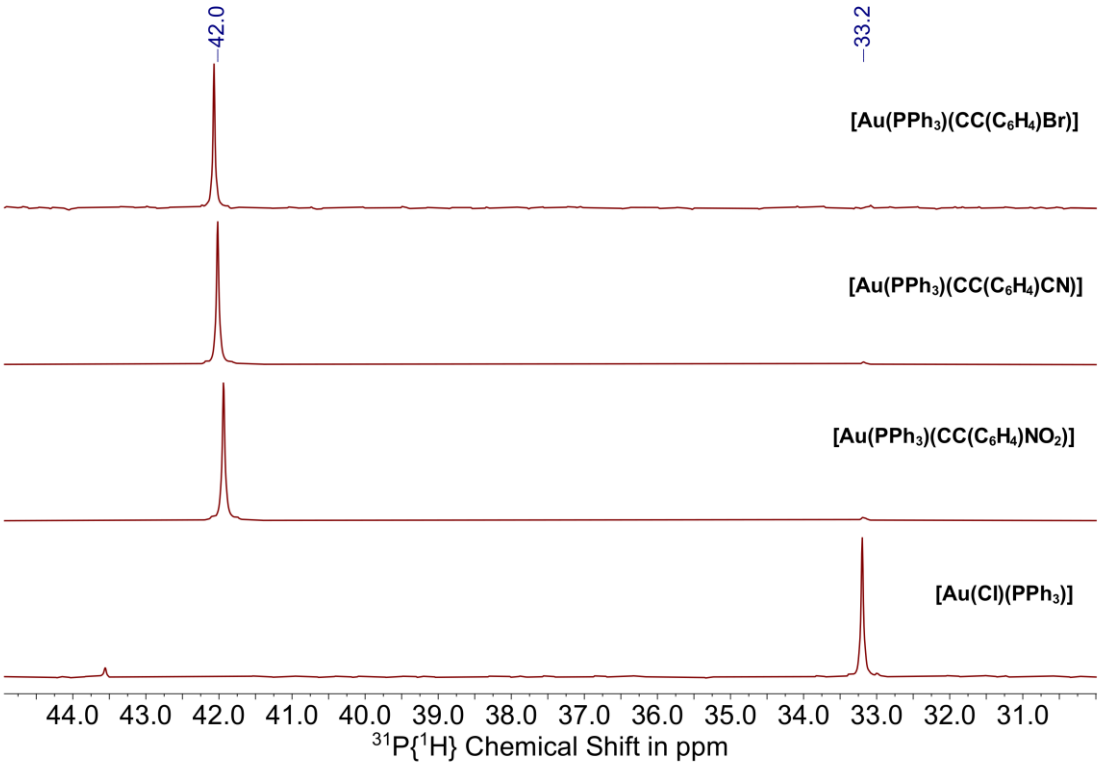

Figure 36: $^{31}P\{^{1}H\}$ NMR spectra (162 MHz, $CDCl_3$, 25 °C) of $[Au(PPh_3)Cl]$ and gold(I) alkynes $[Au(PPh_3)(CC(C_6H_4)X)]$ (X = NO_2, Br, CN).

The IR spectra of the solids of the gold(I) alkynes depict the characteristic stretching vibration for the C–C triple bond at 2117 cm^{-1} ([Au(PPh_3)(CC(C_6H_4)NO_2)]), 2120 cm^{-1} ([Au(PPh_3)(CC(C_6H_4)Br)]) and 2115 cm^{-1} ([Au(PPh_3)(CC(C_6H_4)CN)]), respectively. Complex [Au(PPh_3)(CC(C_6H_4)CN)] confirms the nitrile substituted phenyl group with a stretching vibration for the nitrile group at 2231 cm^{-1} (Figure 37).[128]

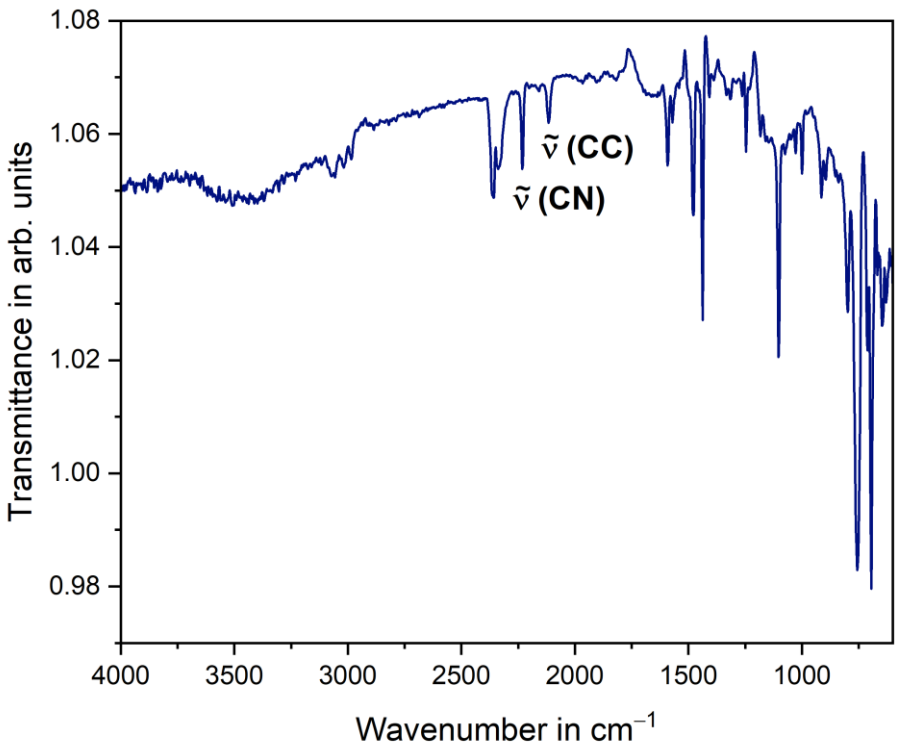

Figure 37: IR spectrum (23 °C) of gold(I) alkyne [Au(PPh_3)(CC(C_6H_4)CN)].

Mass spectra of the compounds were recorded following electron spray ionisation (ESI) of a chloroform solution. Gold(I) alkynes [Au(PPh_3)(CC(C_6H_4)X)]

(X = NO_2, Br, CN) display analogous fragmentation patterns with the main positive fragments being $[M + Au(PPh_3)]^+$ (98-100% relative intensity) at 1099 Da, $[Au(PPh_3)_2]^+$ (98-100% relative intensity) at 721 Da and $[2M + Au(PPh_3)]^+$ (38–93% relative intensity) at 1737 Da for $[Au(PPh_3)(CC(C_6H_4)Br)]$. Fragmentation occurs by loss of the acetylido ligand or triphenylphosphine groups, resulting in positively charged triphenylphosphine gold(I) fragments, which can pair up with the neutral complex.

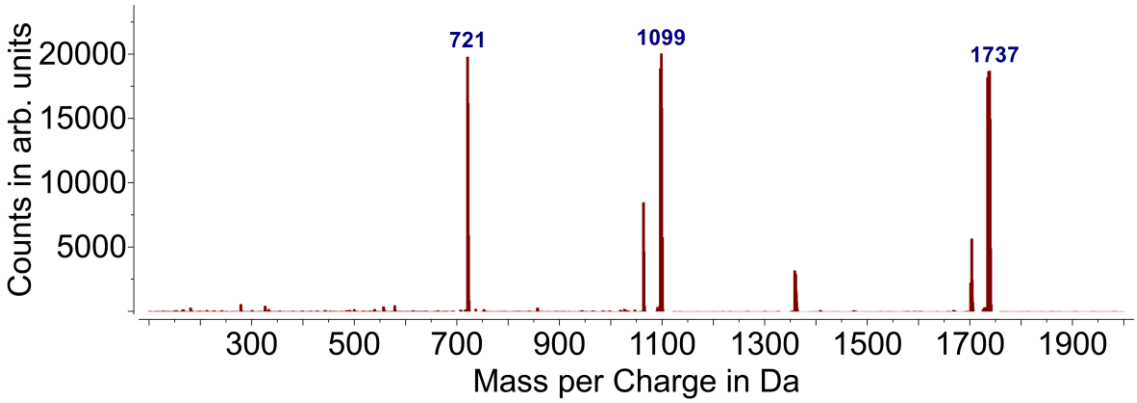

Figure 38: Mass spectrum ($CHCl_3$, 23 °C) of gold(I) alkyne $[Au(PPh_3)(CC(C_6H_4)Br)]$.

The UV-visible spectra of complexes $[Au(PPh_3)(CC(C_6H_4)X)]$ (X = NO_2, Br, CN) were recorded in the range of 200–800 nm in solutions in tetrahydrofuran at a concentration of 23.4 µM. The wavelength of maximal absorption λ_{max} stems from metal-to-ligand charge transfer bands with molar extinction coefficients ranging from 37714 $L \cdot mol^{-1} \cdot cm^{-1}$ for compound $[Au(PPh_3)(CC(C_6H_4)CN)]$, to 30875 $L \cdot mol^{-1} \cdot cm^{-1}$ for compound $[Au(PPh_3)(CC(C_6H_4)NO_2)]$ for absorbance above 250 nm (

Table 10). Changing the substitution pattern on the phenylacetylido ligand from a nitro group in *para*-position to a nitrile group or bromine in *meta*-position causes a hypsochromic shift of 53 nm for the charge transfer bands of the acetylido ligand. Transitions from $\sigma(Au{\leftarrow}P) \rightarrow \pi^*(PPh_3)$ are observed for all three compounds at lower wavelengths, such as 232 nm and 236 nm.

The experimental data are in good agreement with the characterisation for compound $[Au(PPh_3)(CC(C_6H_4)NO_2)]$ in the literature.[127]

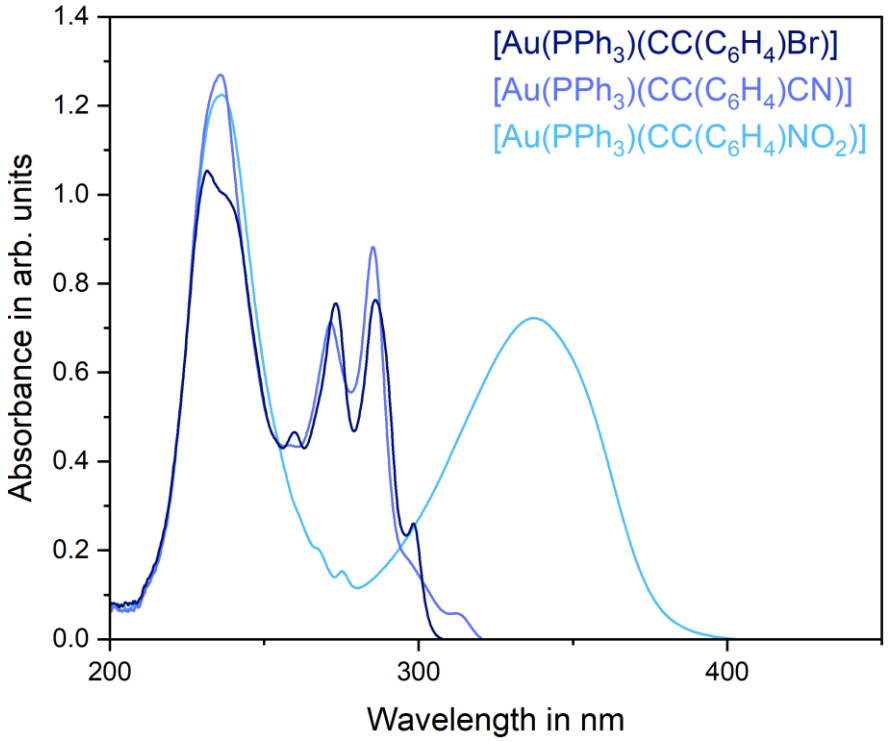

Figure 39: UV-visible spectra (THF, 23 °C) of gold(I) alkynes $[Au(PPh_3)(CC(C_6H_4)X)]$ (X = NO_2, Br, CN).

Table 10: Wavelength λ of local absorbance maxima and molar extinction coefficient ε of UV-visible spectra (THF, 23 °C) of gold(I) alkynes [Au(PPh_3)(CC(C_6H_4)X)] (X = NO_2, Br, CN)

	λ	**Molar Extinction Coefficient ε**
[Au(PPh_3)(CC(C_6H_4)NO_2)]	338 nm	30875 $L \cdot mol^{-1} \cdot cm^{-1}$
[Au(PPh_3)(CC(C_6H_4)NO_2)]	236 nm	54259 $L \cdot mol^{-1} \cdot cm^{-1}$
[Au(PPh_3)(CC(C_6H_4)Br)]	286 nm	32612 $L \cdot mol^{-1} \cdot cm^{-1}$
[Au(PPh_3)(CC(C_6H_4)Br)]	273 nm	32294 $L \cdot mol^{-1} \cdot cm^{-1}$
[Au(PPh_3)(CC(C_6H_4)Br)]	232 nm	45043 $L \cdot mol^{-1} \cdot cm^{-1}$
[Au(PPh_3)(CC(C_6H_4)CN)]	285 nm	37714 $L \cdot mo\ l^{-1} \cdot cm^{-1}$
[Au(PPh_3)(CC(C_6H_4)CN)]	272 nm	30464 $L \cdot mo\ l^{-1} \cdot cm^{-1}$
[Au(PPh_3)(CC(C_6H_4)CN)]	263 nm	54259 $L \cdot mo\ l^{-1} \cdot cm^{-1}$

Single crystals suitable for X-ray diffraction analysis were grown from vapour diffusion of *n*-pentane into a concentrated solution of each of the gold(I) alkynes [Au(PPh_3)(CC(C_6H_4)Br)] and [Au(PPh_3)(CC(C_6H_4)CN)] in dichloromethane. Figure 40 displays the molecular structure of [Au(PPh_3)(CC(C_6H_4)Br)] in the solid state. The alkyne crystallises in the orthorhombic space group *Pbca* with eight formula units in the unit cell (R_1 = 2.09%, wR_2 = 5.29%, R_{int} = 4.75%, *GooF* = 1.054, $e_{min/max}$ = −1.15/0.86 $Å^{-3}$). In contrast, the gold(I) alkyne [Au(PPh_3)(CC(C_6H_4)CN)] crystallises with one molecule of dichloromethane with eight formula units in the unit cell in the monoclinic space group *C*2/*c* (R_1 = 5.97%, wR_2 = 17.73%, R_{int} = 5.97%, *GooF* = 1.134, $e_{min/max}$ = −2.50/2.80 $Å^{-3}$). The molecular structure of [Au(PPh_3)(CC(C_6H_4)CN)] in the solid state is depicted in Figure 41. The solvent molecule is disordered over six positions and has been refined applying a solvent mask modelling 32 electrons in an area of 88 $Å^3$. In addition, one of the phenyl groups of the

triphenylphosphine ligand appears to be disordered, however, it was not possible to fully resolve the disorder in the model.

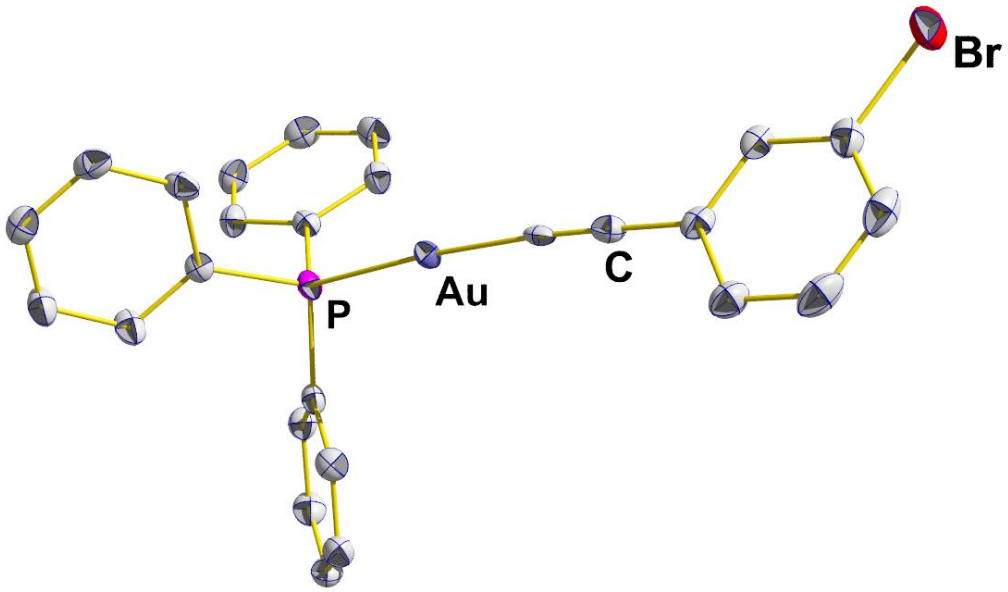

Figure 40: Molecular structure of gold(I) alkyne [Au(PPh_3)(CC(C_6H_4)Br)] in the solid state. Calculated hydrogen atoms are omitted for clarity. Displacement ellipsoids are shown at the 50% probability level.

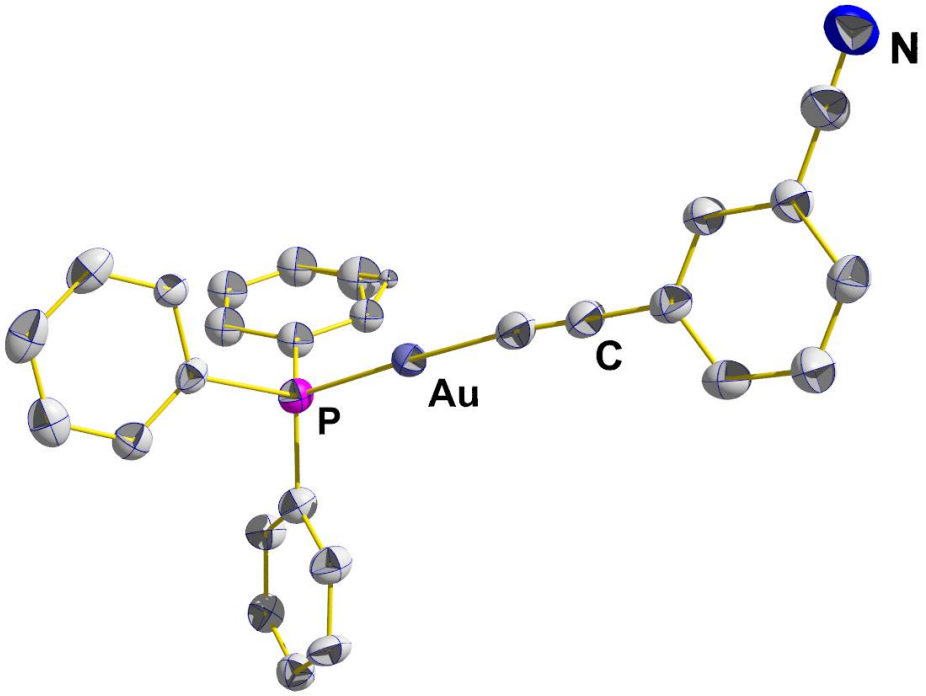

Figure 41: Molecular structure of gold(I) alkyne [Au(PPh$_3$)(CC(C$_6$H$_4$)CN)]·CH$_2$Cl$_2$ in the solid state. Calculated hydrogen atoms and solvent molecules are omitted for clarity. Displacement ellipsoids are shown at the 50% probability level.

The linearly coordinated gold(I) complexes [Au(PPh$_3$)(CC(C$_6$H$_4$)X)] (X = NO$_2$, Br, CN) display similar values for the Au1–P1 and the Au1–C1 bond lengths (Table 11). In comparison, with a Au1–C1 bond length of 1.1759(41) Å in [Au(PPh$_3$)(CC(C$_6$H$_4$)Br)] and 1.1816(162) Å for the respective bond in [Au(PPh$_3$)(CC(C$_6$H$_4$)CN)], the C–C triple bond is slightly shorter than in [Au(PPh$_3$)(CC(C$_6$H$_4$)NO$_2$)] (1.206(6) Å).[127] Interestingly, RI-DFT calculations of the complexes in the gas phase predict the C–C triple bond to be 1.20960 Å ([Au(PPh$_3$)(CC(C$_6$H$_4$)NO$_2$)]), 1.20945 Å ([Au(PPh$_3$)(CC(C$_6$H$_4$)Br)]) and 1.20917 Å ([Au(PPh$_3$)(CC(C$_6$H$_4$)CN)]), which is in good agreement for complex [Au(PPh$_3$)(CC(C$_6$H$_4$)NO$_2$)], and slightly overestimated for compounds

[Au(PPh_3)(CC(C_6H_4)Br)] and [Au(PPh_3)(CC(C_6H_4)CN)]. These deviations can likely be attributed to packing effects in the solid state leading to a difference in electron density along the triple bond, however, no immediate interactions could be identified when modelling the packing of the molecules in the solid state.

Table 11: Selected bond lengths and angles of [Au(PPh_3)(CC(C_6H_4)X)] (X = NO_2, Br, CN) (Scheme 21). Data for [Au(PPh_3)(CC(C_6H_4)NO_2)] (Au:NO_2) was previously reported,[127] whereas the values for [Au(PPh_3)(CC(C_6H_4)Br)] (Au:Br) and [Au(PPh_3)(CC(C_6H_4)CN)] (Au:CN) were obtained experimentally

	Au:NO_2	**Au:Br**	**Au:CN**
Au1–P1	2.277(1) Å	2.2738(9) Å	2.2700(26) Å
Au1–C1	1.973(5) Å	2.0175(29) Å	2.0204(114) Å
C1–C2	1.206(6) Å	1.1759(41) Å	1.1816(162) Å
P1–Au1–C1	178.1(2)°	176.056(85)	178.066(363)°
Au1–C1–C2	175.1(5)°	176.212(262)°	173.20(113)°

3.8 [2+3]-Cycloaddition Reaction of Diazidoplatinum(II) Complexes and Gold(I) Alkynes

After pursuing the synthesis of *cis*- and *trans*-diazidoplatinum(II) complexes containing phosphine or pyridyl ligands, as well as a mixture of both, the following platinum(II) complexes were chosen for examination of the [2+3]-cycloaddition under mild conditions with gold(I) alkynes [Au(PPh_3)(CC(C_6H_4)X)] (X = NO_2, Br, CN) (Scheme 22).

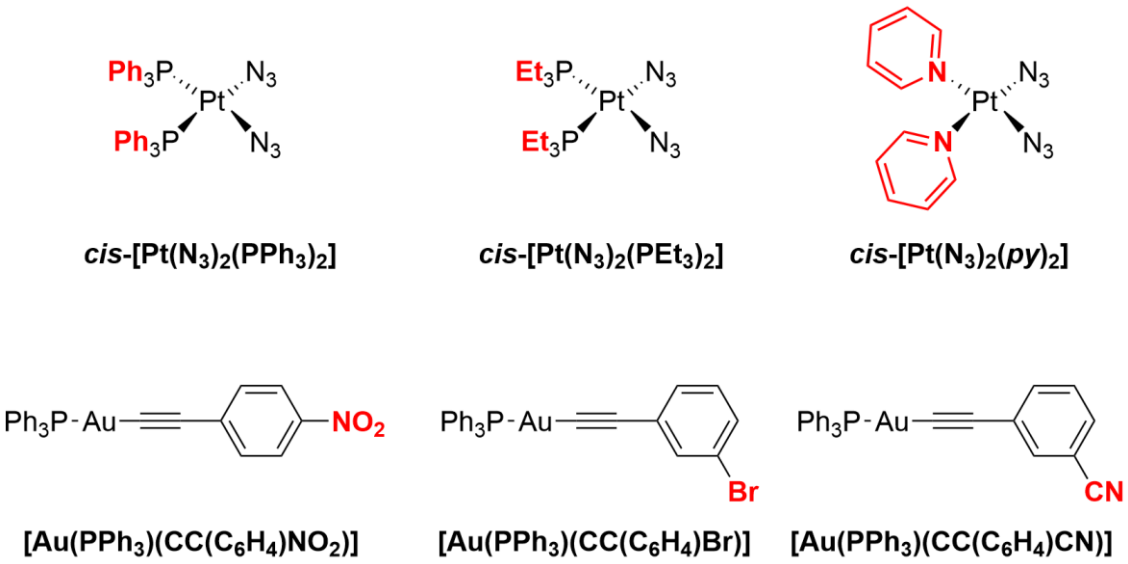

Scheme 22: Overview of the six compounds which were chosen for investigating [2+3]-cycloaddition reactions under mild conditions. Structural differences are highlighted in red.

Following on from well-established procedures using copper(I) salts to activate alkynes enabling [2+3]-cycloaddition reactions,[77,78] the gold(I) centre in complexes [Au(PPh$_3$)(CC(C$_6$H$_4$)X)] (X = NO$_2$, Br, CN) withdraws electron density from the C–C triple bond of the end-on coordinated acetylido ligand yielding a similarly activated alkyne and facilitating the attack of the azido ligand.

The successful [2+3]-cycloaddition reaction between compounds [Au(PPh$_3$)(CC(C$_6$H$_4$)NO$_2$)] and *cis*-[Pt(N$_3$)$_2$(PPh$_3$)] was previously reported by A. S. Veige and co-workers.[85] Building on this, the analogous synthesis with complex *cis*-[Pt(N$_3$)$_2$(PEt$_3$)] was performed (Scheme 23). Varying reaction conditions were explored as alternatives to the literature procedure in benzene,[85] including toluene, or dried and degassed tetrahydrofuran under nitrogen.

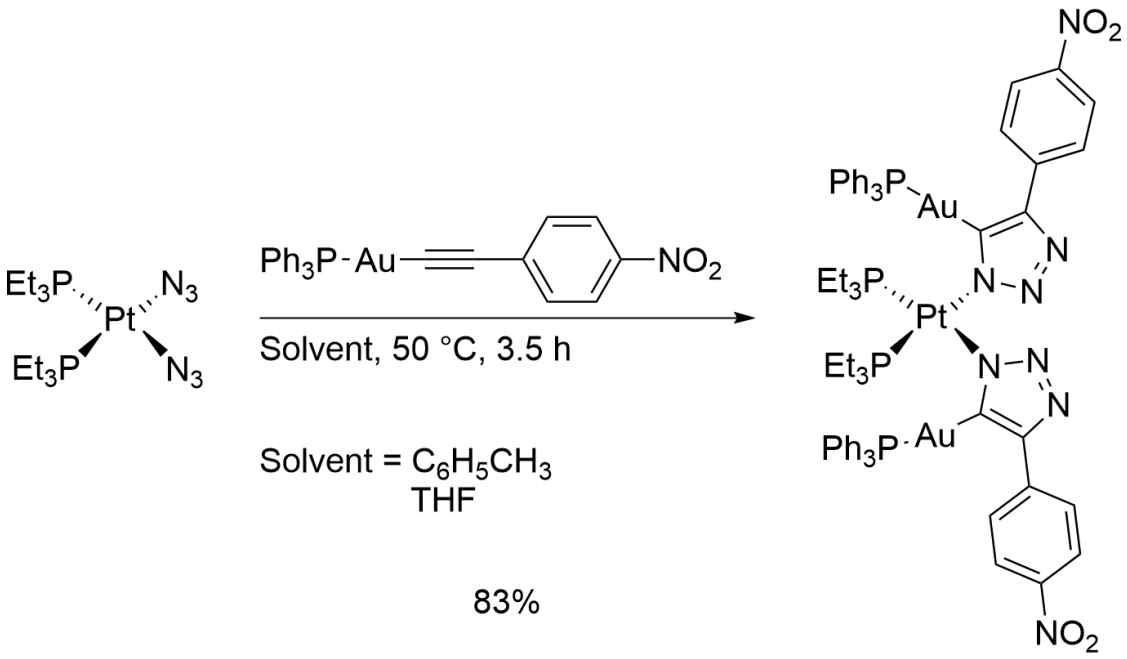

Scheme 23: Synthetic approach to the [2+3]-cycloaddition reaction mixture between platinum(II) complex *cis*-[Pt(N_3)$_2$(PEt_3)$_2$] and gold(I) alkyne [Au(PPh_3)(CC(C_6H_4)NO2)].

The cycloaddition product was fully characterised with the means of NMR and IR spectroscopy, mass spectrometry, as well as single crystal X-ray diffraction analysis. The $^{31}P\{^1H\}$ NMR spectrum displays a clear shift of the resonances from the starting materials (Figure 42). The singlet corresponding to the triphenylphosphine group on the gold(I) alkyne is slightly shifted downfield to higher energies. In comparison, the resonance stemming from the triethylphosphine ligands attached to the platinum centre experiences an upfield shift to 0.4 ppm. The $^1J(^{31}P, ^{195}Pt)$ coupling constant has decreased by 404 Hz upon cycloaddition, indicating a substantial change in the electron density in proximity to the platinum centre. The corresponding triplet in the ^{195}Pt NMR spectrum was detected at −4235 ppm and confirms a symmetrical complex including two phosphine groups (Figure 43).

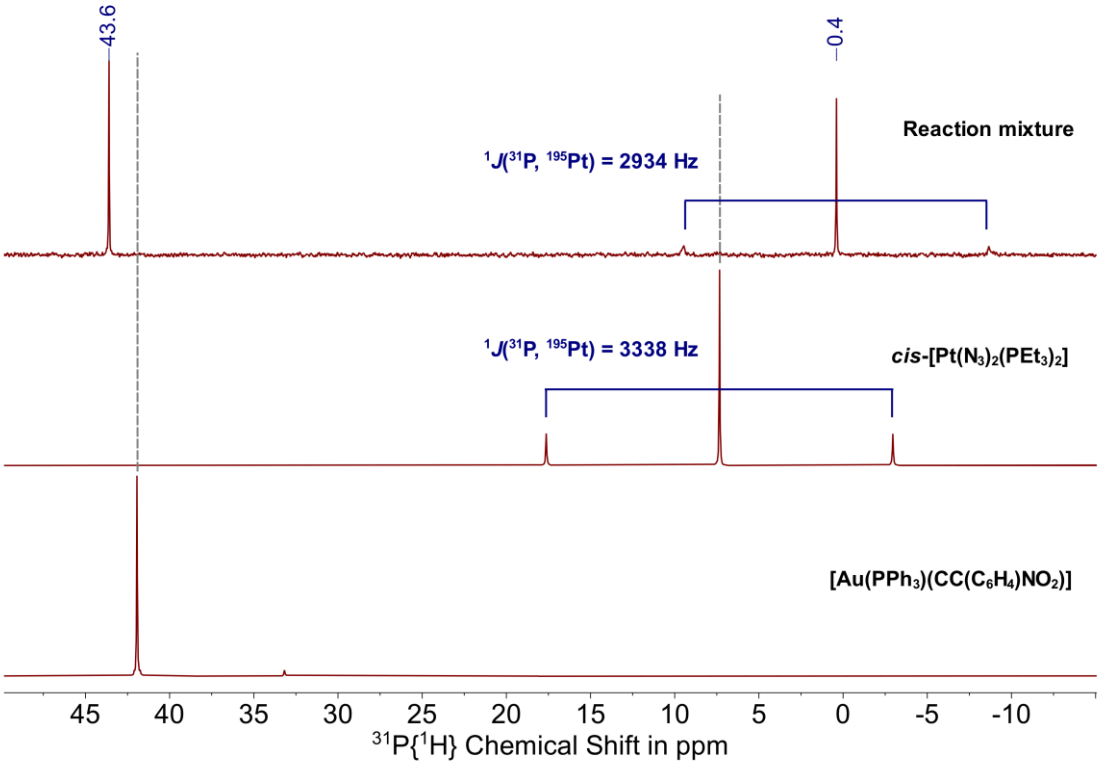

Figure 42: $^{31}P\{^1H\}$ NMR spectra (162 MHz, $CDCl_3$, 25 °C) of the [2+3]-cycloaddition reaction mixture following the reaction of *cis*-[Pt(N$_3$)$_2$(PEt$_3$)$_2$] and gold(I) alkyne [Au(PPh$_3$)(CC(C$_6$H$_4$)NO$_2$)].

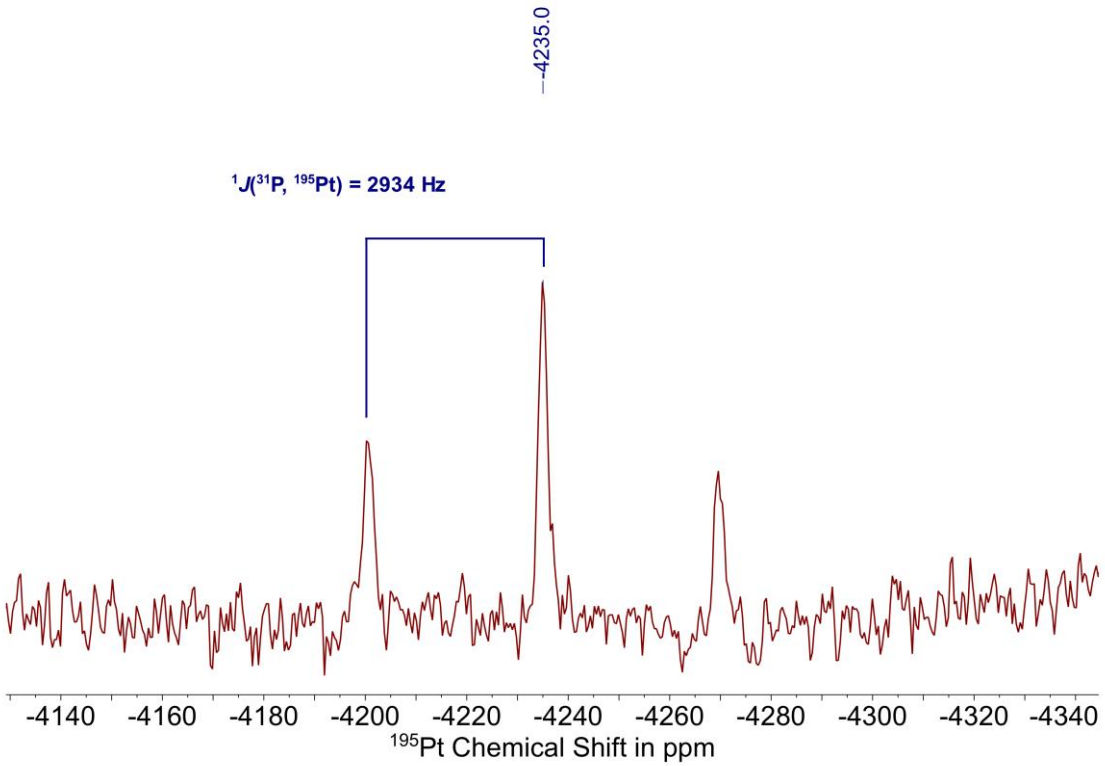

Figure 43: ^{195}Pt NMR spectrum (86 MHz, $CDCl_3$, 25 °C) of the [2+3]-cycloaddition reaction mixture following the reaction of *cis*-$[Pt(N_3)_2(PEt_3)_2]$ and gold(I) alkyne $[Au(PPh_3)(CC(C_6H_4)NO_2)]$.

Comparison of the IR spectra of the platinum(II) complex before and after the reaction with the gold(I) alkyne $[Au(PPh_3)(CC(C_6H_4)NO_2)]$, shows a clear change in transmittance and confirms the loss of the azido ligand on the platinum complex (Figure 44).

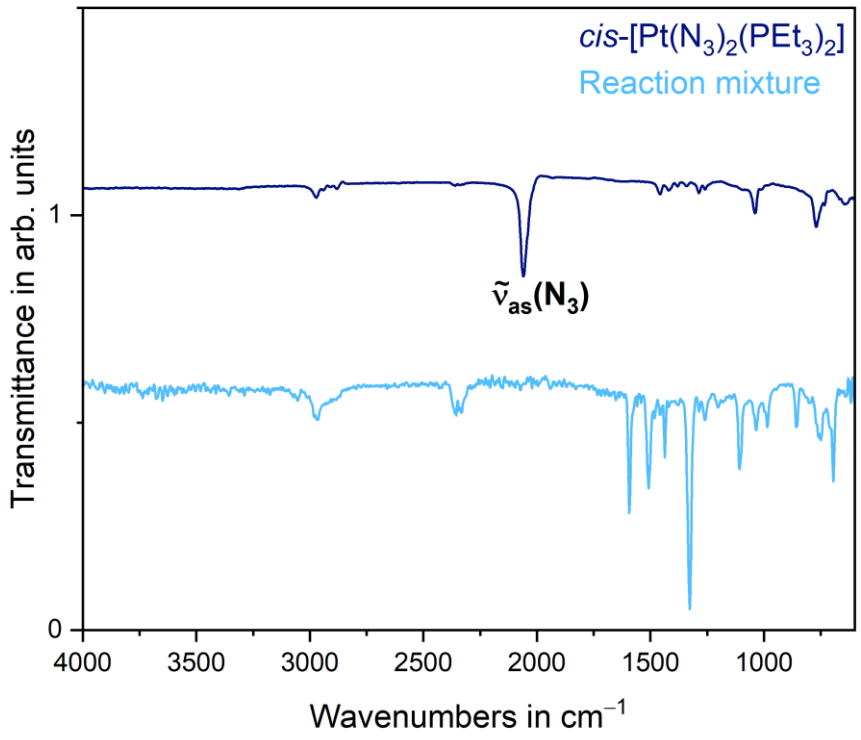

Figure 44: IR spectra (23 °C) of *cis*-[Pt(N$_3$)$_2$(PEt$_3$)$_2$] and of the [2+3]-cycloaddition reaction mixture following the reaction of *cis*-[Pt(N$_3$)$_2$(PEt$_3$)$_2$] and gold(I) alkyne [Au(PPh$_3$)(CC(C$_6$H$_4$)NO$_2$)].

The compound crystallises in the space group *I*2/a next to three molecules of chloroform in the asymmetric unit (Figure 45) (R_1 = 5.95%, wR_2 = 16.13%, R_{int} = 6.24%, *GooF* = 1.070, $e_{min/max}$ = −4.43/4.24 Å^{-3}). One of the solvent molecules is heavily disordered and was modelled applying a solvent mask (62 electrons in an area of 137 Å^3). In addition, one of the phenyl groups of the triphenylphosphine ligand on the gold(I) centre is disordered. After applying a numerical absorption correction to the experimental data, a residual electron density of 4.2 e·Å^{-3} is found close to the platinum atom in the crystallographic model. A comparison of selected bond lengths and angles of the cycloaddition

products of *cis*-[Pt(N_3)$_2$(PR_3)$_2$] (R = Et, Ph) with the nitro substituted gold(I) alkyne [Au(PPh_3)(CC(C_6H_4)NO_2)], reveals no large deviation between the two analogous complexes (Table 12).

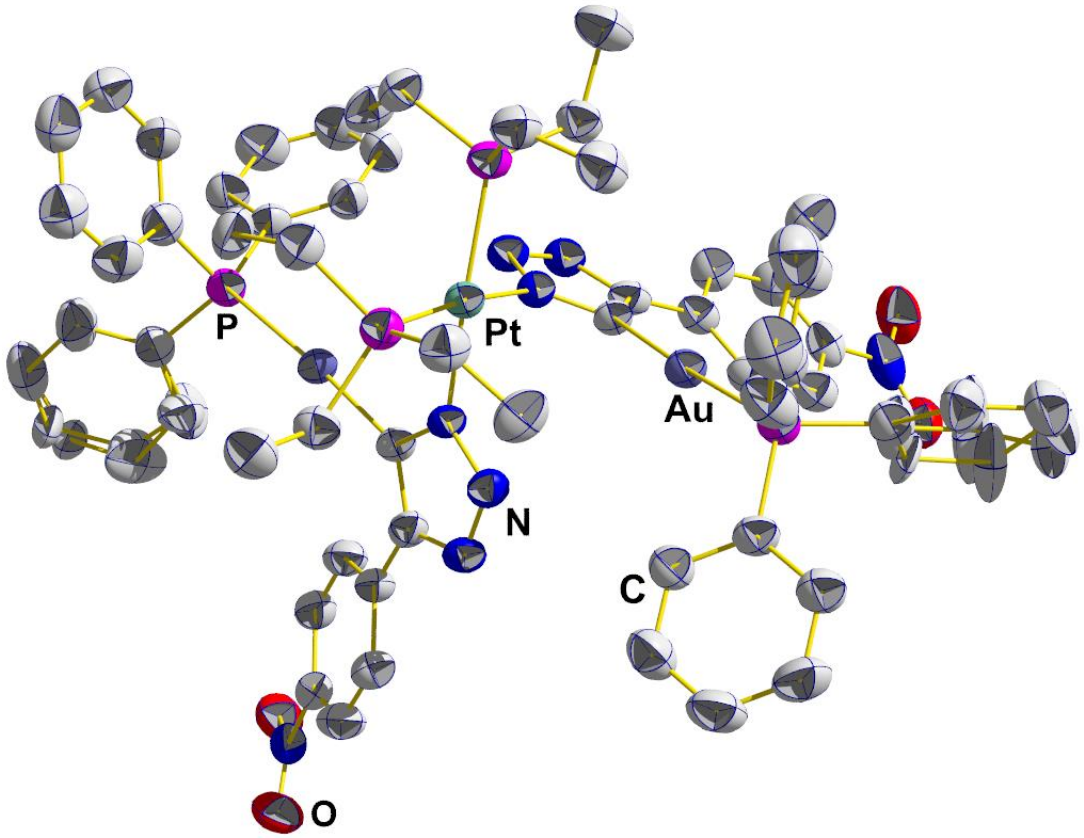

Figure 45: Molecular structure of the [2+3]-cycloaddition product **Pt,Et[2+3]Au,NO_2** of the reaction of *cis*-[Pt(N_3)$_2$(PEt_3)$_2$] and gold(I) alkyne [Au(PPh_3)(CC(C_6H_4)NO_2)] in the solid state. Calculated hydrogen atoms and solvent molecules are omitted for clarity. Displacement ellipsoids are shown at 50% probability level.

Table 12: Selected bond lengths and angles of the molecular structures of **Pt,Ph[2+3]Au,NO$_2$** and **Pt,Et[2+3]Au,NO$_2$** in the solid state. Data for **Pt,Ph[2+3]Au,NO$_2$** was previously reported,[85] whereas the values for **Pt,Et[2+3]Au,NO$_2$** were obtained experimentally

	Pt,Ph[2+3]Au,NO$_2$	**Pt,Et[2+3]Au,NO$_2$**
Pt–N	(2.040–2.073)(7) Å	2.0522(62) Å
Pt–P	(2.278–2.286)(3) Å	2.2668(21) Å
P–Pt–N	175.3(2)°	173.774(177)°
P–Pt–N	89.3(2)°	89.261(175)°

The analogous reactions of the diazidodiphosphineplatinum(II) complexes *cis*-[Pt(N_3)$_2$(PR_3)] (R = Et, Ph) with alkynes [Au(PPh3)(CC(C_6H_4)Br)] and [Au(PPh_3)(CC(C_6H_4)CN)] in toluene each yielded the respective cycloaddition product successfully (Scheme 24).

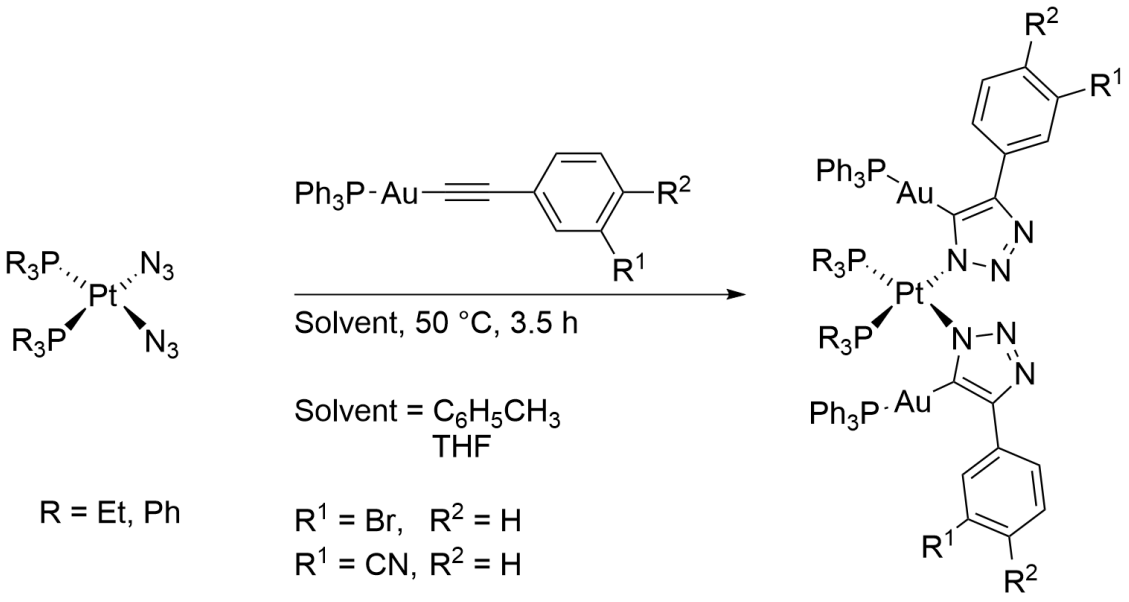

R = Et,	R^1 = Br,	R^2 = H	77%	R = Et,	Ph
R = Et,	R^1 = CN,	R^2 = H	88%	R^1 = Br,	R^2 = H
R = Ph,	R^1 = Br,	R^2 = H	42%	R^1 = CN,	R^2 = H
R = Ph,	R^1 = CN,	R^2 = H	83%		

Scheme 24: Synthetic approach to the [2+3]-cycloaddition reaction between platinum(II) complexes *cis*-[Pt$(N_3)_2(PR_3)_2$] (R = Et, Ph) and gold(I) alkynes [Au$(PPh_3)(CC(C_6H_4)X)$] (X = Br, CN).

Based on the reported NMR data for the reaction of *cis*-[Pt$(N_3)_2(PPh_3)$] with [Au$(PPh_3)(CC(C_6H_4)NO_2)$], an upfield shift of the resonance in the $^{31}P\{^1H\}$ NMR spectrum for the triphenylphosphine ligands is expected upon a successful cycloaddition reaction. While the $^{31}P\{^1H\}$ NMR spectrum of the reaction mixture of *cis*-[Pt$(N_3)_2(PPh_3)$] and [Au(PPh3)$(CC(C_6H_4)Br)$] shows the formation of small quantities of triphenylphosphine oxide as well as another phosphine platinum complex with a resonance at 18.0 ppm, the spectrum further indicates the formation of a cycloaddition product (Figure 46). The $^1J(^{31}P, ^{195}Pt)$ coupling

constant has changed from 3507 Hz for the diazidodiphosphineplatinum(II) complex *cis*-[Pt(N_3)$_2$(PPh_3)] to 3098 Hz for the cycloaddition product.

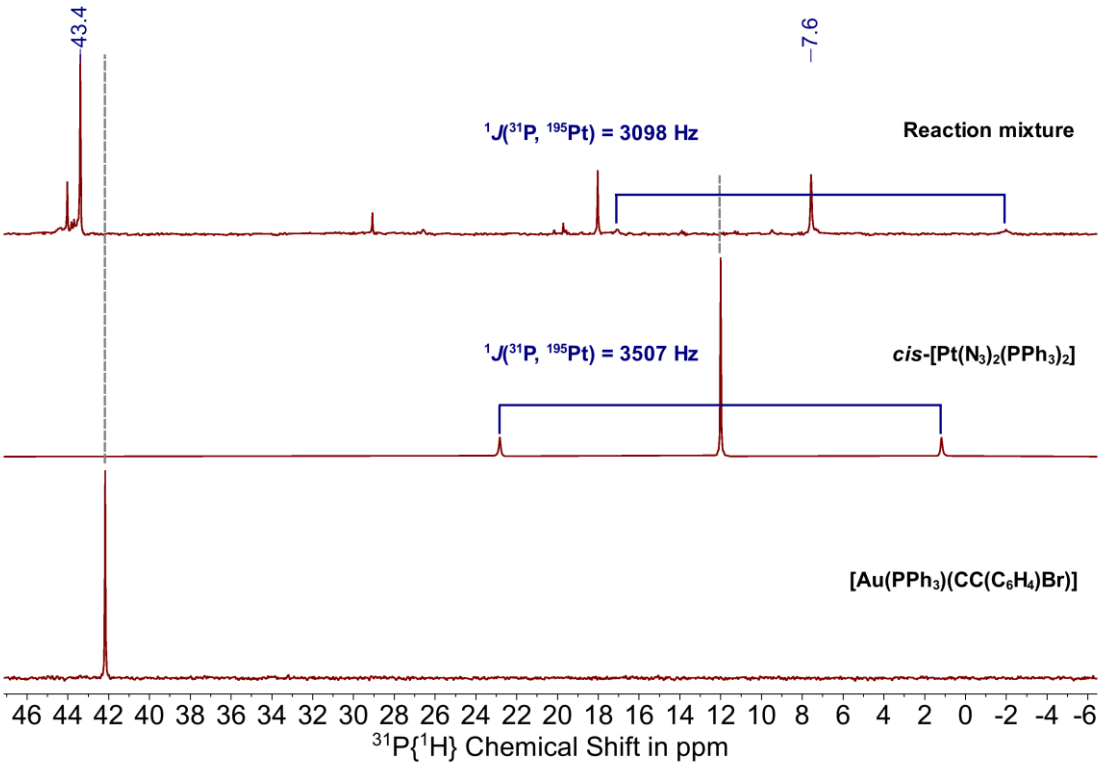

Figure 46: $^{31}P\{^1H\}$ NMR spectra (162 MHz, $CDCl_3$, 25 °C) of the [2+3]-cycloaddition reaction mixture following the reaction of *cis*-[Pt(N_3)$_2$(PPh_3)$_2$] and gold(I) alkyne [Au(PPh_3)(CC(C_6H_4)Br)].

The reaction of diazidobis(triethylphosphine)platinum(II) with gold(I) alkyne [Au(PPh3)(CC(C_6H_4)Br)] yields similar results. The $^{31}P\{^1H\}$ NMR spectrum confirms a successful cycloaddition reaction with the characteristic downfield shift for the singlet corresponding to the triphenylphosphine ligand on the gold(I) centre and an upfield shift for the resonance corresponding to the triethylphosphine ligands coordinated to the platinum(II) centre (Figure 47). The cycloaddition product displays a $^1J(^{31}P, ^{195}Pt)$ coupling constant of 2945 HZ,

which is reduced by 393 Hz compared to the unreacted diazidoplatinum(II) complex. The successful reactions were further supported by absence of the asymmetric stretching frequency in the IR spectra.

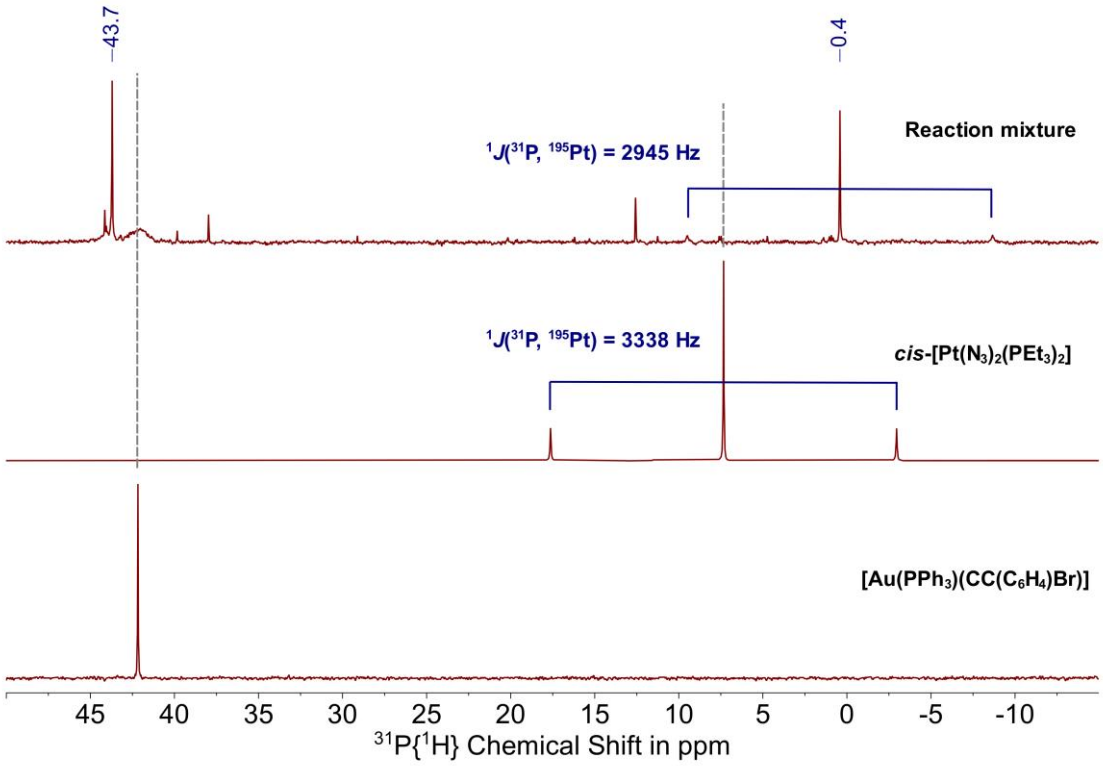

Figure 47: $^{31}P\{^1H\}$ NMR spectra (162 MHz, $CDCl_3$, 25 °C) of the [2+3]-cycloaddition reaction mixture following the reaction of *cis*-[Pt(N3)2(PEt3)2] and gold(I) alkyne [Au(PPh3)(CC(C6H4)Br)].

Both reactions of the diazidodiphosphineplatinum complexes *cis*-[Pt(N3)2(PR3)] (R = Et, Ph) with the bromine substituted gold(I) alkyne [Au(PPh3)(CC(C6H4)Br)] display side products in the reaction mixture. Unfortunately, crystallisation attempts were not successful and it was not possible to fully isolate or synthesise the cycloaddition products in a clean manner thus far.

The formation of the [2+3]-cycloaddition product for the reaction of diazidobis(triphenylphoshine)platinum(II) and the nitrile substituted gold(I) alkyne [Au(PPh$_3$)(CC(C$_6$H$_4$)CN)] was confirmed *via* NMR and IR spectroscopy, mass spectrometry as well as X-ray diffractometry. The ^{31}P{^{1}H} NMR spectrum exhibits the characteristic shift of the resonances corresponding to the phosphine ligands to higher and lower energies, respectively, supported by the decrease in the ^1J(^{31}P, ^{195}Pt) coupling constant (Figure 48). The ^{195}Pt NMR spectrum exhibits a triplet at −4077 ppm with a matching ^1J(^{31}P, ^{195}Pt) coupling constant of 3093 HZ, confirming a symmetrical complex including two phosphine ligands in *cis*-position to each other (Figure 49).

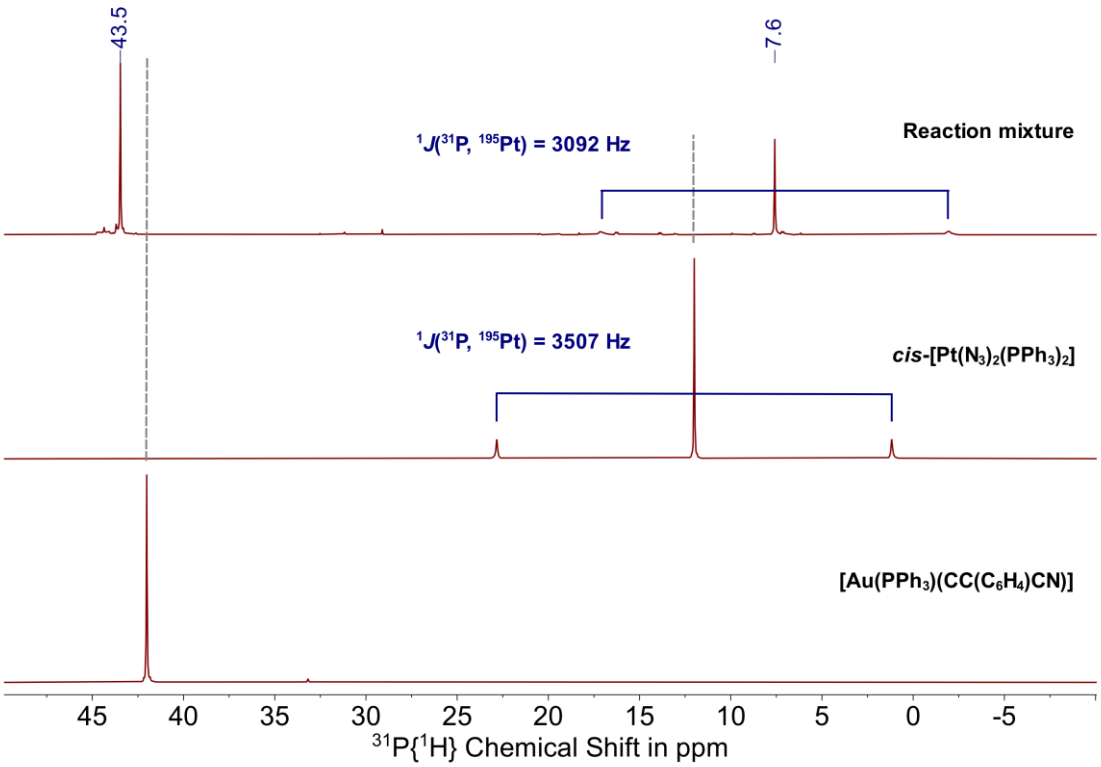

Figure 48: ^{31}P{^{1}H} NMR spectra (162 MHz, CDCl$_3$, 25 °C) of the [2+3]-cycloaddition reaction mixture following the reaction of *cis*-[Pt(N$_3$)$_2$(PPh$_3$)$_2$] and gold(I) alkyne [Au(PPh$_3$)(CC(C$_6$H$_4$)CN)].

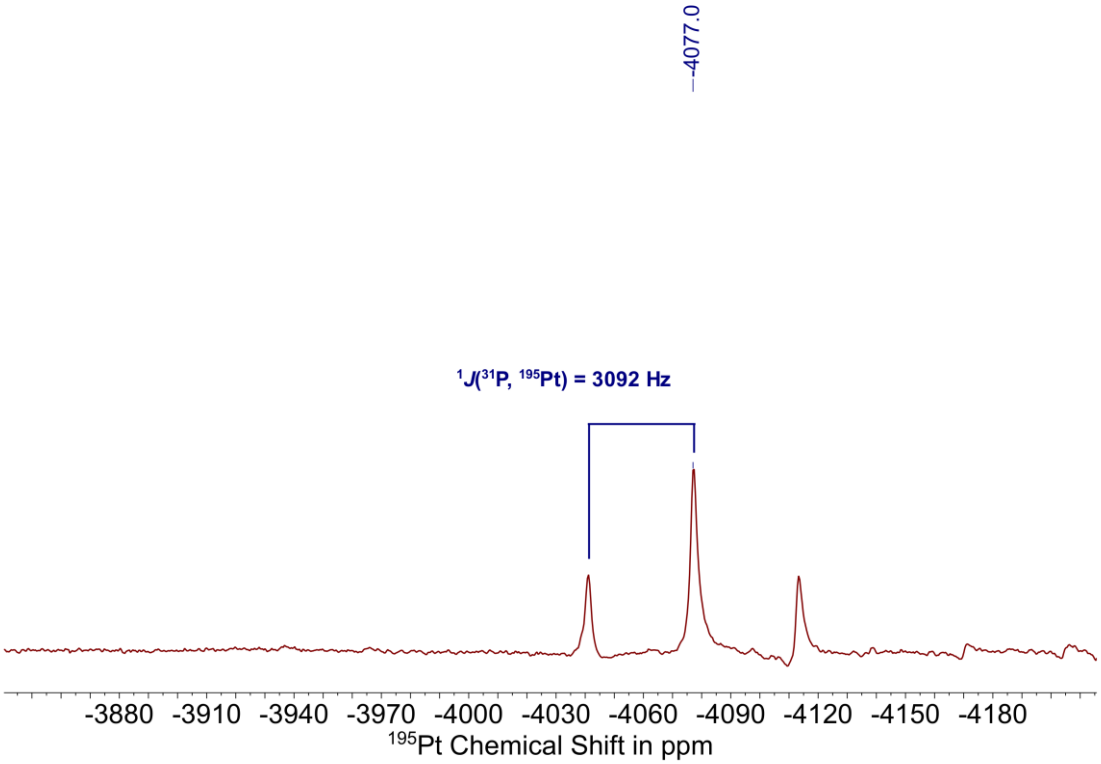

Figure 49: ^{195}Pt NMR spectrum (86 MHz, $CDCl_3$, 25 °C) of the [2+3]-cycloaddition reaction mixture following the reaction of *cis*-$[Pt(N_3)_2(PPh_3)_2]$ and gold(I) alkyne $[Au(PPh_3)(CC(C_6H_4)CN)]$.

Comparison of the IR spectra of both of the starting materials and the isolated product confirm the absence of the intense band for the asymmetric stretching frequency of the azido ligand at 2060 cm^{-1} as well as the vibration attributed to the C–C triple bond at 2115 cm^{-1} (Figure 50). However, the IR spectrum of the product confirms a nitrile group in the structure with a band for the stretching frequency being recorded at 2226 cm^{-1}.

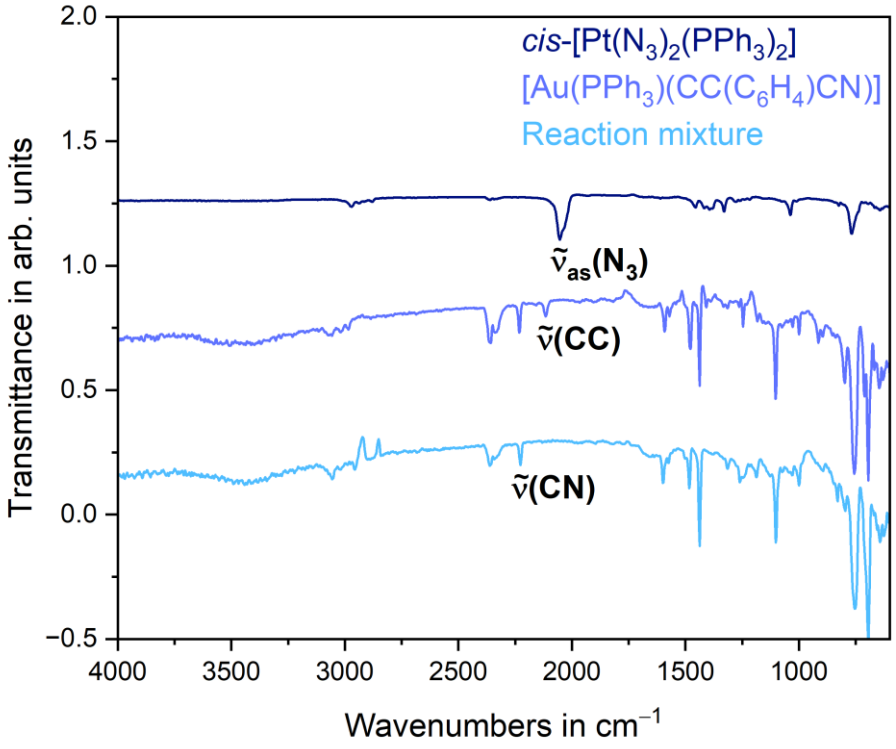

Figure 50: IR spectra (23 °C) of *cis*-[Pt(N$_3$)$_2$(PPh$_3$)$_2$], gold(I) alkyne [Au(PPh$_3$)(CC(C$_6$H$_4$)CN)] and of their [2+3]-cycloaddition reaction mixture.

Single crystals suitable for X-ray diffraction analysis were isolated as yellow blocks after cooling a concentrated reaction mixture at 8 °C overnight. The cycloaddition product crystallises together with two molecules of toluene in the monoclinic space group $P2_1/n$ with four formula units in the unit cell (R_1 = 9.97%, wR_2 = 35.92%, R_{int} = 11.55%, *GooF* = 1.238, $e_{min/max}$ = −4.50/8.40 Å^{-3}). Figure 51 displays the molecular structure of the platinum(II) complex in the solid state. Despite exhibiting a promising diffraction pattern after careful crystal selection, the structure solution and refinement of the model did not yield satisfying results. The residual factors R_{int}, R_1 and wR_2 help to determine the quality of correlation

between the experimental data and the crystallographic model. While the measurement confirms the structural motif unambiguously, with an R_{int} of 11.55 %, there is a clear divergence between the data and model, further supported by unassigned residual electron density of 8.4 $e \cdot Å^{-3}$ close to one of the phenyl groups. As one of the toluene molecules is heavily disordered, a solvent mask was applied. The solvent mask detected 26 electrons within a volume of 298 $Å^3$, suggesting a toluene molecule with an average occupancy of 0.5. Next to examining the data for twinning and disorder, a numerical absorption correction was applied, however, the refinement factors indicate poor crystal quality and suggest that the measurement will need to be repeated with a different crystal. As the current discrepancy between model and data yields uncertainty with regards to bond lengths and angles, these will not be discussed at this point.

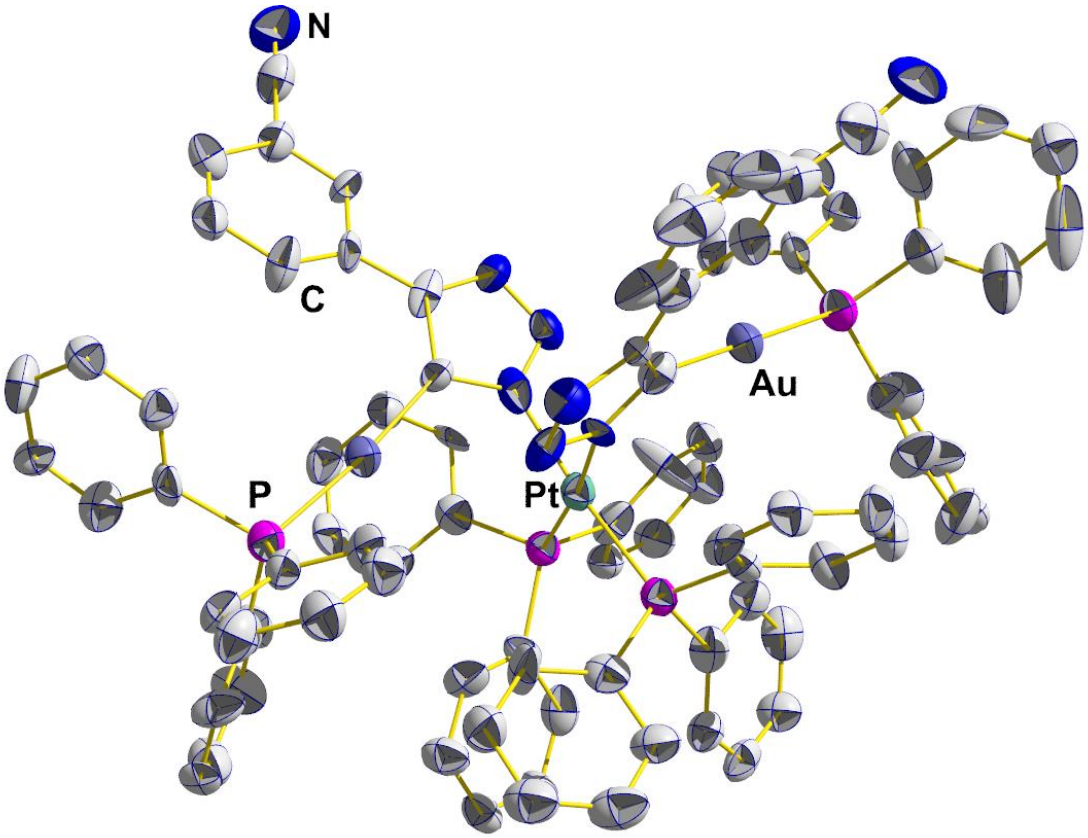

Figure 51: Molecular structure of the [2+3]-cycloaddition product **Pt,Ph[2+3]Au,CN** of *cis*-[Pt(N_3)$_2$(PPh_3)$_2$] and gold(I) alkyne [Au(PPh_3)(CC(C_6H_4)CN)] in the solid state. Calculated hydrogen atoms and solvent molecules are omitted for clarity. Displacement ellipsoids are shown at 50% probability level.

In similar manner to the triphenylphosphine analogue, diazidobis(triethylphosphine)platinum(II) undergoes successful [2+3]-cycloaddition with the nitrile substituted gold(I) alkyne [Au(PPh_3)(CC(C_6H_4)CN)] as determined *via* NMR spectroscopy. The ^{195}Pt NMR spectrum displays the expected resonances for the respective phosphine groups, with the triethylphosphine ligands coordinated to the platinum(II) centre exhibiting a ^{1}J(^{31}P, ^{195}Pt) coupling constant of 2942 HZ, which is in line with the observed values for the previously discussed cycloaddition products (Figure 52). The

corresponding ^{195}Pt NMR spectrum shows a clear triplet at −4231 ppm with a matching $^{1}J(^{31}P, ^{195}Pt)$ coupling constant (Figure 53).

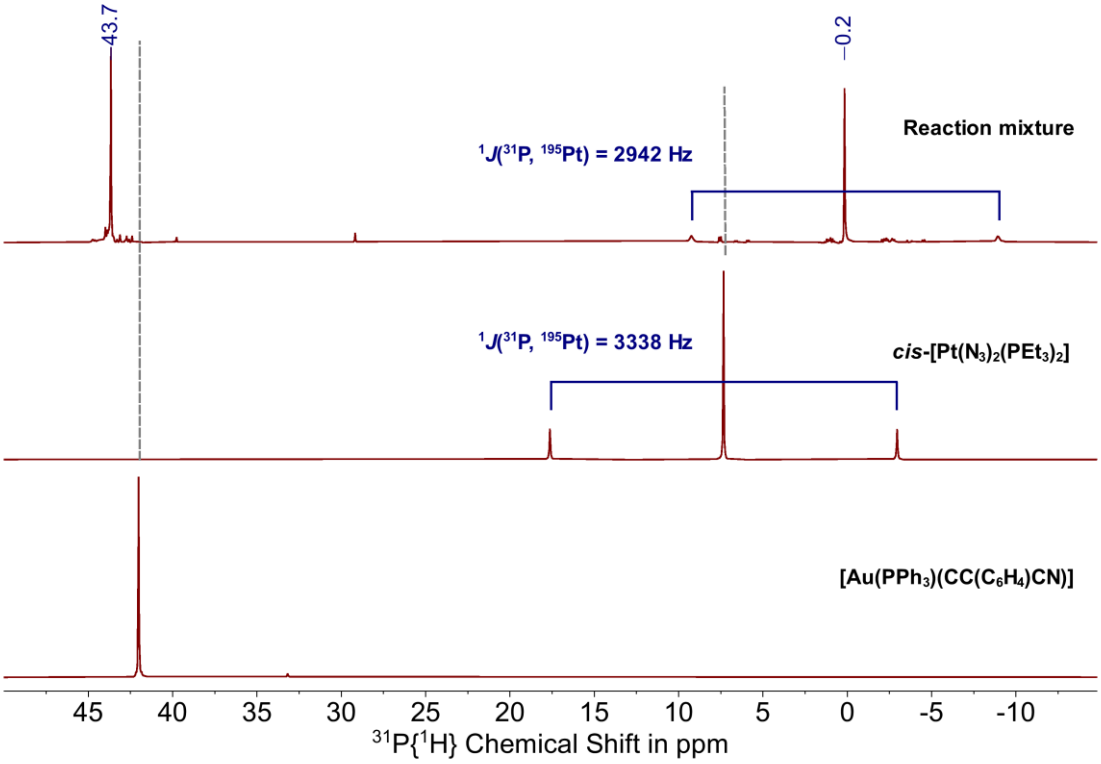

Figure 52: $^{31}P\{^{1}H\}$ NMR spectra (162 MHz, $CDCl_3$, 25 °C) of the [2+3]-cycloaddition reaction mixture following the reaction of *cis*-[Pt(N$_3$)$_2$(PEt$_3$)$_2$] and gold(I) alkyne [Au(PPh$_3$)(CC(C$_6$H$_4$)CN)].

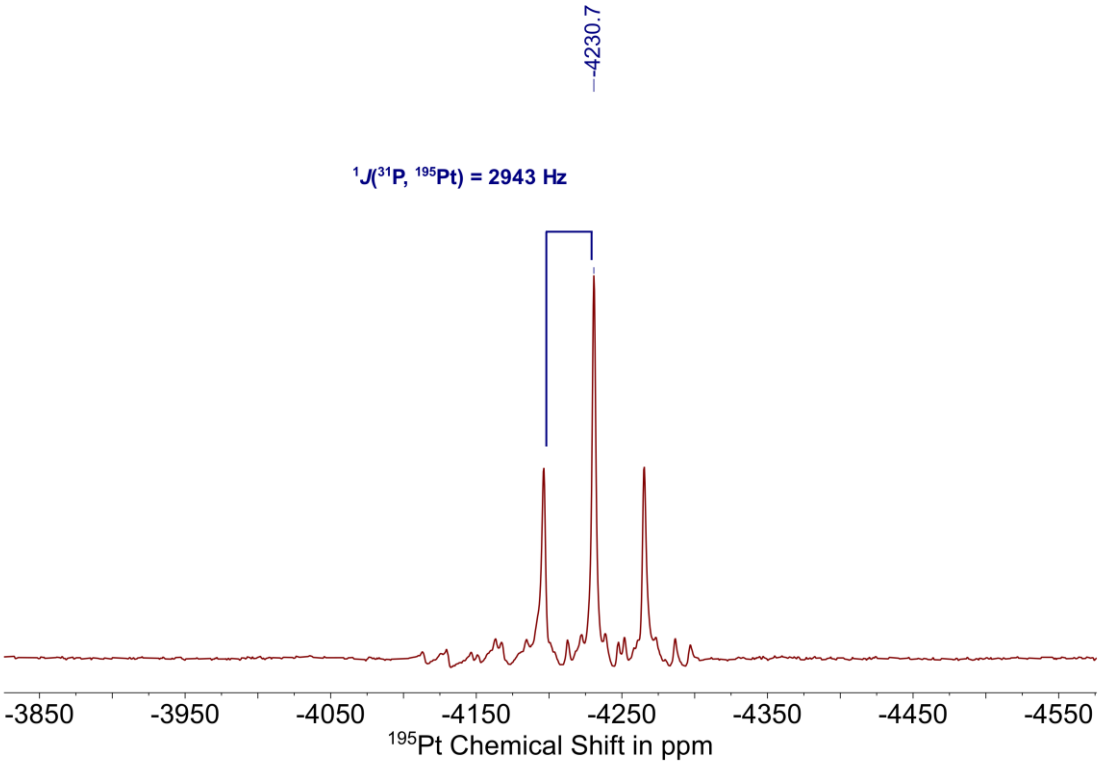

Figure 53: ^{195}Pt NMR spectrum (86 MHz, $CDCl_3$, 25 °C) of the [2+3]-cycloaddition reaction mixture following the reaction of *cis*-$[Pt(N_3)_2(PEt_3)_2]$ and gold(I) alkyne $[Au(PPh_3)(CC(C_6H_4)CN)]$.

As a contrast to diazidoplatinum(II) complexes with *P*-donors, the cycloaddition reactions of *cis*-$[Pt(N_3)_2(py)_2]$ towards the selected gold(I) alkynes was pursued. Under the chosen experimental conditions, the reactions yielded unreacted starting material in all cases, with prolonged heating times leading to decomposition of the compounds. The experimental results will be discussed for the reaction of *cis*-$[Pt(N_3)_2(py)_2]$ and the nitro substituted gold(I) alkyne $[Au(PPh_3)(CC(C_6H_4)NO_2)]$, as an example, however, the observations and conclusions can be extended to the reactions with all three alkynes.

The diazidodipyridylplatinum(II) complex *cis*-[Pt(N_3)$_2$(*py*)$_2$] was reacted with the gold(I) alkyne [Au(PPh_3)(CC(C_6H_4)NO_2)] in dried and degassed tetrahydrofuran (Scheme 25).

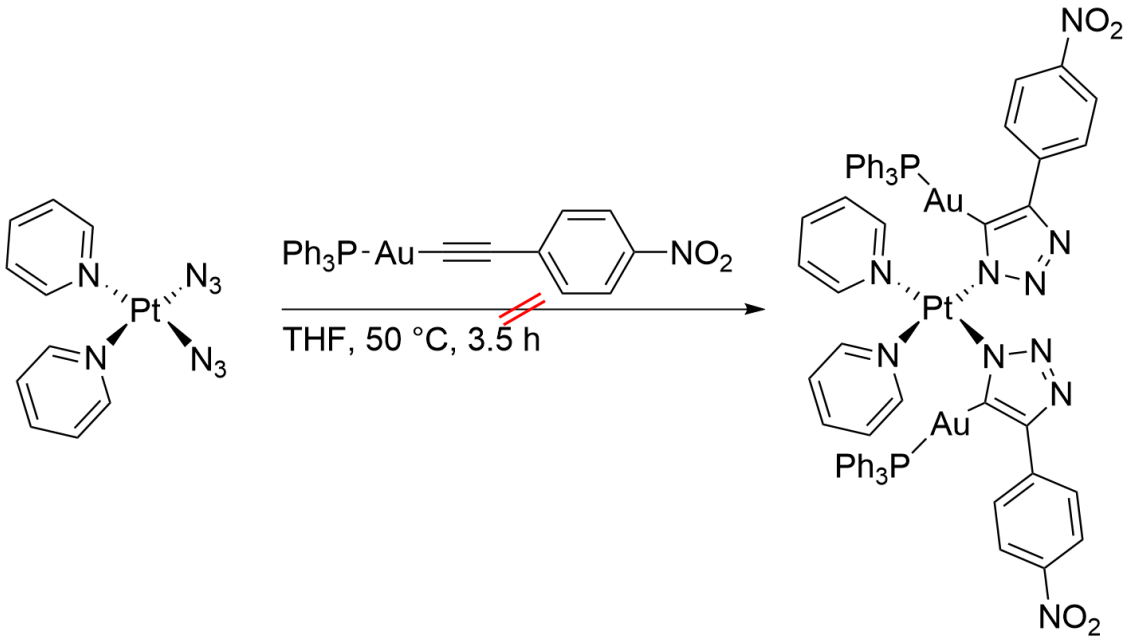

Scheme 25: Synthetic approach to the [2+3]-cycloaddition reaction mixture between platinum(II) complex *cis*-[Pt(N_3)$_2$(*py*)$_2$] and gold(I) alkyne [Au(PPh_3)(CC(C_6H_4)NO_2)].

Comparison of the NMR spectra of the starting materials and the reaction product suggest no cycloaddition reaction has occurred. The ^{195}Pt NMR spectrum displays a broad singlet characteristic for the diazidodipyridyl complex at −2076 ppm, which is in agreement with the unreacted starting material (Figure 54). The successful cycloaddition reactions with *cis*-[Pt(N_3)$_2$(PR_3)$_2$] (R = Et, Ph) showed a slight downfield shift of the resonance for the triphenylphosphine ligand attached to the gold(I) centre upon cycloaddition. However, when comparing the

$^{31}P\{^{1}H\}$ spectra before and after the cycloaddition reaction of the diazidodipyridylplatinum(II) complex with the gold(I) alkyne, the signal appears at 41.9 ppm in both cases (Figure 55).

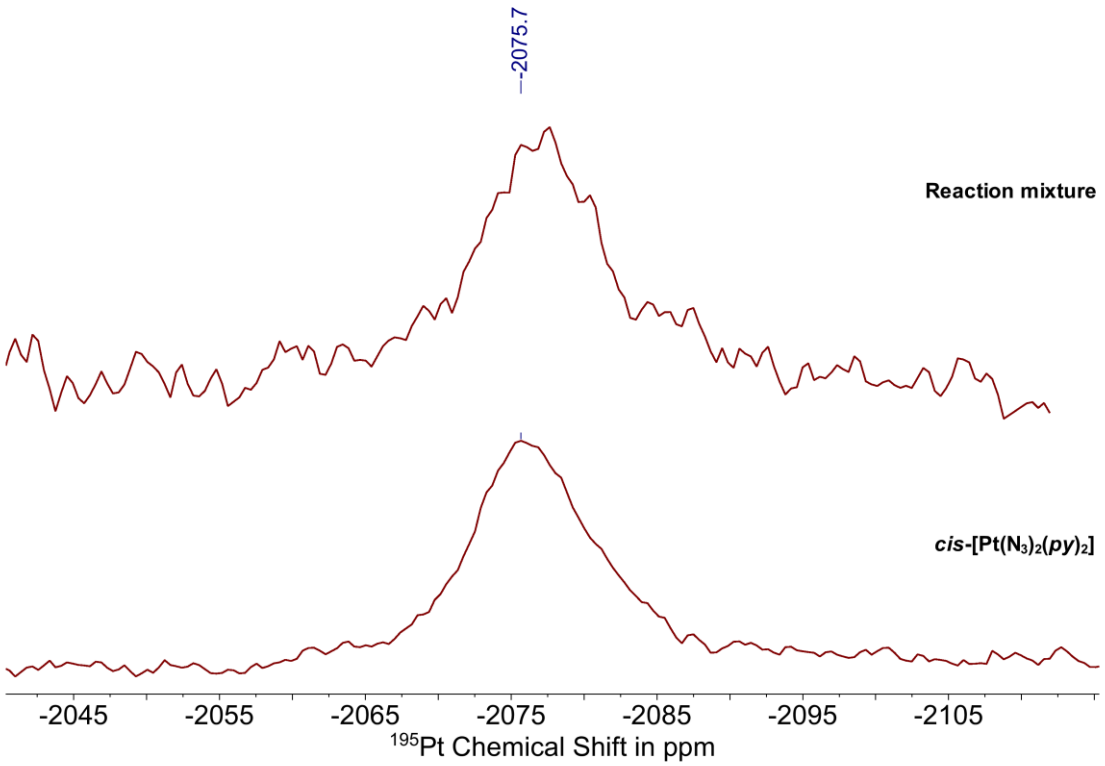

Figure 54: ^{195}Pt NMR spectrum (86 MHz, $CDCl_3$, 25 °C) of the [2+3]-cycloaddition reaction mixture following the reaction of *cis*-$[Pt(N_3)_2(py)_2]$ and gold(I) alkyne $[Au(PPh_3)(CC(C_6H_4)NO_2)]$.

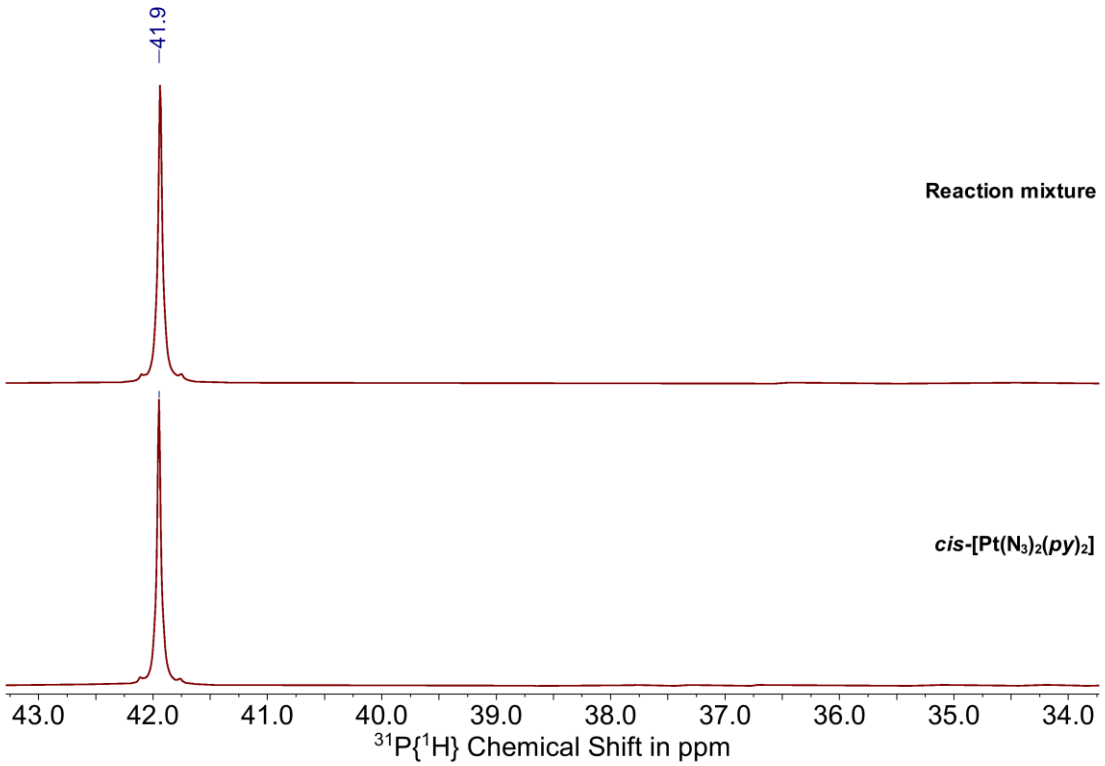

Figure 55: $^{31}P\{^{1}H\}$ NMR spectra (162 MHz, $CDCl_3$, 25 °C) of the [2+3]-cycloaddition reaction mixture following the reaction of *cis*-$[Pt(N_3)_2(py)_2]$ and gold(I) alkyne $[Au(PPh_3)(CC(C_6H_4)NO_2)]$.

The most indicative change in the ^{1}H NMR spectrum is expected to occur for the protons in the *ortho*-position on the pyridyl ligand. Comparison of the chemical shifts of the protons on the *N*-donor ligand show a negligible shift of 0.02 ppm (Figure 56) for the doublet of doublets of the corresponding resonance. Due to strong signals stemming from the aromatic protons from the phenyl groups on the gold(I) alkyne, the resonances for the protons on the pyridyl ligands are comparatively weak and do not display any clear coupling to the platinum centre.

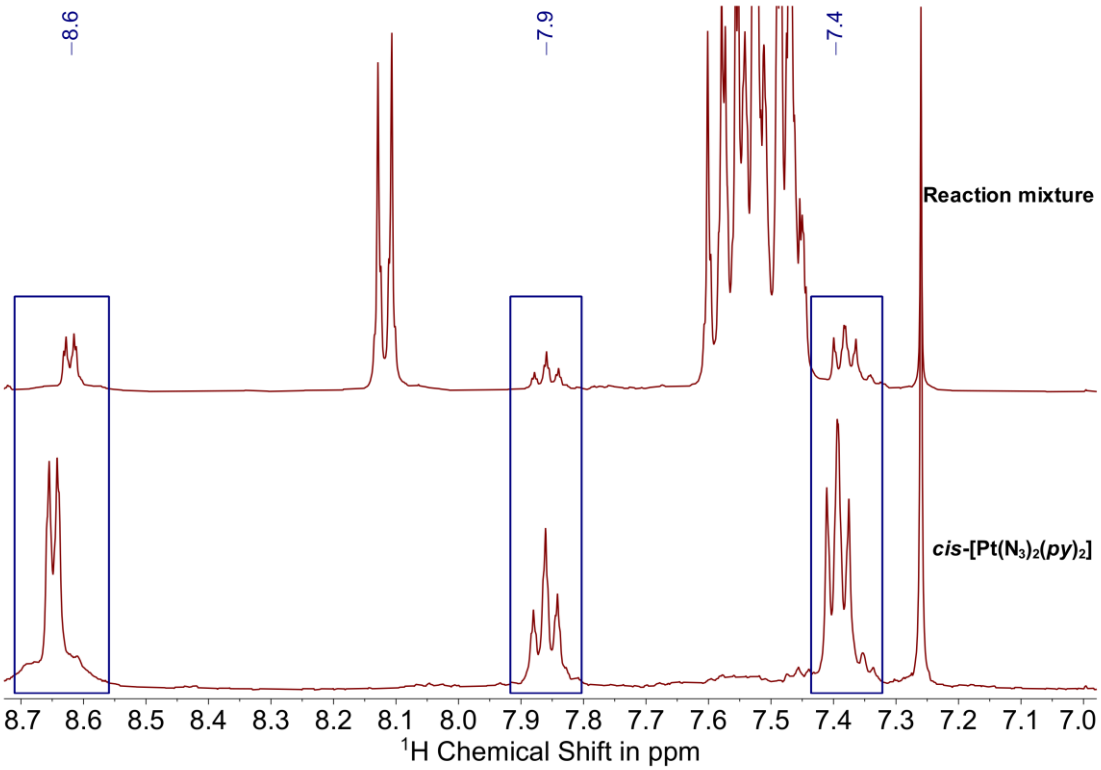

Figure 56: ^{1}H NMR spectra (400 MHz, $CDCl_3$, 25 °C) of the [2+3]-cycloaddition reaction mixture following the reaction of *cis*-[$Pt(N_3)_2(py)_2$] and gold(I) alkyne [$Au(PPh_3)(CC(C_6H_4)NO_2)$].

Considering the collective NMR data, all observations suggest that the diazidodipyridylplatinum(II) complex has not undergone a successful cycloaddition reaction with the nitro substituted gold(I) alkyne. This is further supported by the IR spectrum of the reaction product. The spectrum shows a band at 2048 cm^{-1}, corresponding to the asymmetric stretching frequency of the azido ligand on the platinum(II) complex, as well as a band at 2118 cm^{-1}, which can be assigned to the stretching frequency of the C–C triple bond. This data confirms irrevocably that no cycloaddition between the azido ligands and the alkyne has occurred.

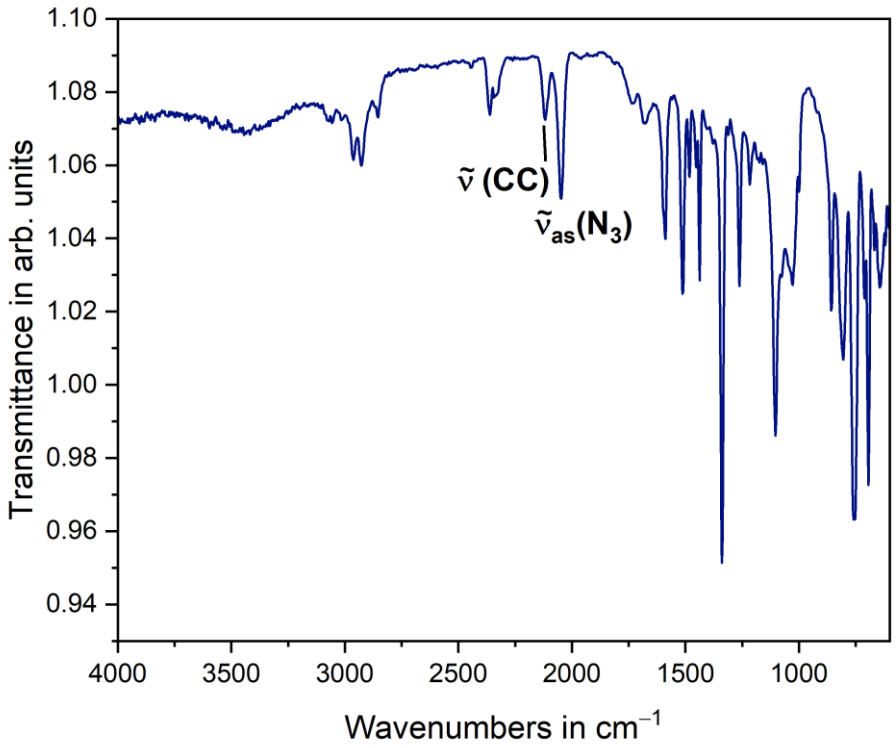

Figure 57: IR spectrum (23 °C) of *cis*-[Pt(N_3)$_2$(*py*)$_2$] and of the [2+3]-cycloaddition reaction mixture following the reaction of *cis*-[Pt(N_3)$_2$(*py*)$_2$] and gold(I) alkyne [Au(PPh_3)(CC(C_6H_4)NO_2)].

UV-visible spectroscopy was performed for the cleanly isolated cycloaddition products of the [2+3]-cycloaddition reaction between *cis*-[Pt(N_3)$_2$(PR_3)$_2$] (R = Et, Ph) and gold(I) alkynes [Au(PPh_3)(CC(C_6H_4)X)] (X = NO_2, CN), respectively. The spectra were recorded in the range of 200–800 nm in solutions in tetrahydrofuran at a concentration of 23.4 µM.

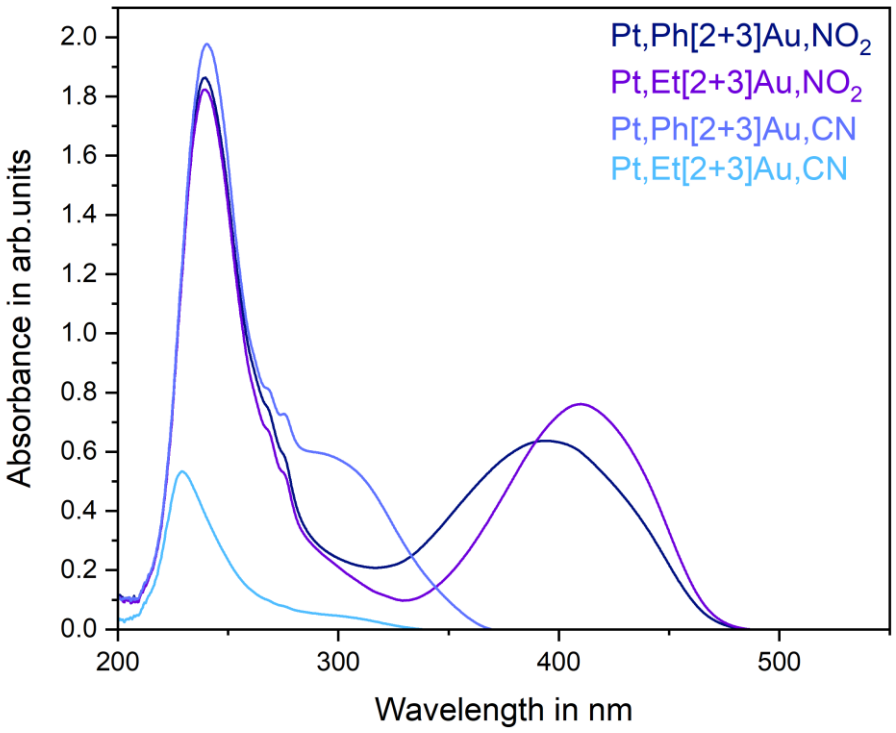

Figure 58: UV-visible spectra (THF, 23 °C) of cycloaddition products **Pt,Ph[2+3]Au,NO$_2$**, **Pt,Et[2+3]Au,NO$_2$**, **Pt,Ph[2+3]Au,CN** and **Pt,Et[2+3]Au,CN**.

With a change in electron density around the metal centres due to the cycloaddition reaction, the absorbance band stemming from the metal-to-ligand-charge-transfer within the nitro substituted gold(I) alkyne [Au(PPh$_3$)(CC(C$_6$H$_4$)NO$_2$)] has shifted from 338 nm to a lower energy of 395 nm for the cycloaddition product with *cis*-[Pt(N$_3$)$_2$(PPh$_3$)$_2$] and to 410 nm for the reaction product with *cis*-[Pt(N$_3$)$_2$(PEt$_3$)$_2$] (Table 13). The cycloaddition product of the nitrile substituted alkyne [Au(PPh$_3$)(CC(C$_6$H$_4$)CN)] and *cis*-[Pt(N$_3$)$_2$(PPh$_3$)$_2$] exhibits multiple peaks in the UV-visible spectra in close proximity to each other. In analogous manner, the absorbance bands have shifted to slightly higher

wavelengths compared to the isolated gold(I) alkyne: 285 nm *vs* 296 nm and 272 nm *vs* 289 nm. The absorbance bands in the UV-region are largely attributed to the aromatic groups in the phenyl groups, and appear to be less affected by the cycloaddition reaction. With molar extinction coefficients of 77921–84507 $L \cdot mol^{-1} \cdot cm^{-1}$, the absorbance in the UV-region is distinctly stronger compared to the metal-to-ligand-charge-transfer bands (molar extinction coefficients of 25154–34588 $L \cdot mol^{-1} \cdot cm^{-1}$). The cycloaddition product of *cis*-$[Pt(N_3)_2(PEt_3)_2]$ with the nitrile substituted gold(I) alkyne exhibits a distinctly weaker absorbance compared to the other three cycloaddition products, with a low molar extinction coefficient of 22831 $L \cdot mol^{-1} \cdot cm^{-1}$ for the absorption in the UV-region.

Table 13: Wavelength λ of local absorbance maxima and molar extinction coefficient ε of UV-visible spectra (THF, 23 °C) of cycloaddition products **Pt,Ph[2+3]Au,NO_2**, **Pt,Et[2+3]Au,NO_2**, **Pt,Ph[2+3]Au,CN** and **Pt,Et[2+3]Au,CN**.

	λ	Molar Extinction Coefficient ε
Pt,Ph[2+3]Au,NO_2	395 nm	27226 $L \cdot mol^{-1} \cdot cm^{-1}$
Pt,Ph[2+3]Au,NO_2	240 nm	79666 $L \cdot mol^{-1} \cdot cm^{-1}$
Pt,Et[2+3]Au,NO_2	410 nm	32527 $L \cdot mol^{-1} \cdot cm^{-1}$
Pt,Et[2+3]Au,NO_2	240 nm	77921 $L \cdot mol^{-1} \cdot cm^{-1}$
Pt,Ph[2+3]Au,CN	296 nm	25154 $L \cdot mol^{-1} \cdot cm^{-1}$
Pt,Ph[2+3]Au,CN	289 nm	30939 $L \cdot mol^{-1} \cdot cm^{-1}$
Pt,Ph[2+3]Au,CN	276 nm	34588 $L \cdot mol^{-1} \cdot cm^{-1}$
Pt,Ph[2+3]Au,CN	240 nm	84507 $L \cdot mol^{-1} \cdot cm^{-1}$
Pt,Et[2+3]Au,CN	229 nm	22831 $L \cdot mol^{-1} \cdot cm^{-1}$

The bimetallic complexes from the [2+3]-cycloaddition products of *cis*-[$Pt(N_3)_2(PR_3)_2$] (R = Et, Ph) and [$Au(PPh_3)(CC(C_6H_4)X)$] (X = NO_2, Br, CN) bear the potential to act as multi-modal anti-cancer agents with distinct and synergistic modes of toxicity. Further steps will include oxidising these compounds to platinum(IV) prodrugs with the goal of spatial and temporal control over their cytotoxic action. Irradiation with both visible light and X-rays will provide insight into activation of the compounds *via* this non-invasive exogenously applied stimulus.

3.9 Correlating ^{195}Pt NMR Data

As discussed in Chapter 1.6, there are multiple contributions to the scalar coupling constant in NMR experiments, however, for heavy nuclei such as platinum, the Fermi contact term appears to be the most dominant.[93,94] This allows for the derivation that the magnitude as well as variations of the coupling constant directly relate to the electronic configuration around the nuclei. Table 14 provides an overview of the chemical shifts in the ^{195}Pt NMR spectra and the $^{1}J(^{31}P, ^{195}Pt)$ coupling constants of the three diazidoplatinum(II) complexes which were investigated for [2+3]-cycloaddition reaction with the chosen gold(I) alkynes *cis*-[$Pt(N_3)_2R_3$] (R = *py*, PPh_3, PEt_3). It further includes the values and differences of the resonances in the ^{195}Pt NMR spectra as well as the respective $^{1}J(^{31}P, ^{195}Pt)$ coupling constants of the cycloaddition products compared to the unreacted diazidoplatinum(II) complexes.

Table 14: ^{195}Pt chemical shifts and $^{1}J(^{31}P, ^{195}Pt)$ coupling constants observed for a selection of compounds (86 MHz, $CDCl_3$, 25 °C). Differences are calculated in reference to *cis*-$[Pt(N_3)_2(PR_3)]$ (R = Et, Ph)

	$\delta(^{195}Pt)$	$\Delta(\delta)$	$^{1}J_{P,Pt}$	$\Delta^{1}J$
***cis*-[Pt(N$_3$)$_2$(*py*)$_2$]**	−2076 ppm	-	-	-
***cis*-[Pt(N$_3$)$_2$(PPh$_3$)$_2$]**	−4261 ppm	-	3507 Hz	-
***cis*-[Pt(N$_3$)$_2$(PEt$_3$)$_2$]**	−4335 ppm	-	3338 Hz	-
Pt,Ph[2+3]Au,NO$_2$	−4079 ppm	180 ppm	3110 Hz	397 Hz
Pt,Ph[2+3]Au,CN	−4077 ppm	184 ppm	3092 Hz	415 Hz
Pt,Ph[2+3]Au,Br	-	-	3098 Hz	409 Hz
Pt,Et[2+3]Au,NO$_2$	−4235 ppm	100 ppm	2934 Hz	404 Hz
Pt,Et[2+3]Au,CN	−4231 ppm	104 ppm	2942 Hz	396 Hz
Pt,Et[2+3]Au,Br	-	-	2945 Hz	393 Hz

The resonance for *cis*-$[Pt(N_3)_2(PPh_3)_2]$ is shifted downfield by 74 ppm compared to the triethylphosphine analogue. In addition, the $^{1}J(^{31}P, ^{195}Pt)$ coupling constant in *cis*-diazidobis(triphenylphosphine)platinum(II) is 169 Hz larger than the corresponding coupling constant in *cis*-$[Pt(N_3)_2(PEt_3)_2]$. Interestingly, this trend is further observed for the respective cycloaddition products when comparing the analogous complexes with the differently substituted phosphines. Comparison of the data for the cycloaddition reactions reveals no large influence of a change in substitution of the acetylido ligand in the gold(I) alkyne on the chemical shifts in the ^{195}Pt NMR spectra or the $^{1}J(^{31}P, ^{195}Pt)$ coupling constants, rendering the influence of the phosphine ligands bound to the platinum(II) centre the decisive factor. Upon successful cycloaddition, in all cases the resonance for the platinum nuclei experiences a shift to higher frequencies compared to the unreacted diazido complexes. The change in coupling constants lies in the same range

independent of the phosphine ligands and is observed to be 393–409 Hz. Figure 59 depicts a schematic overview of the chemical shifts in the ^{195}Pt NMR spectra and the $^{1}J(^{31}P, ^{195}Pt)$ coupling constants observed for *cis*-[Pt(N$_3$)$_2$R$_3$] (R = *py*, PPh$_3$, PEt$_3$) as well as the cycloaddition products from the reactions with the three gold(I) alkynes [Au(PPh$_3$)(CC(C$_6$H$_4$)X)] (X = NO$_2$, Br, CN).

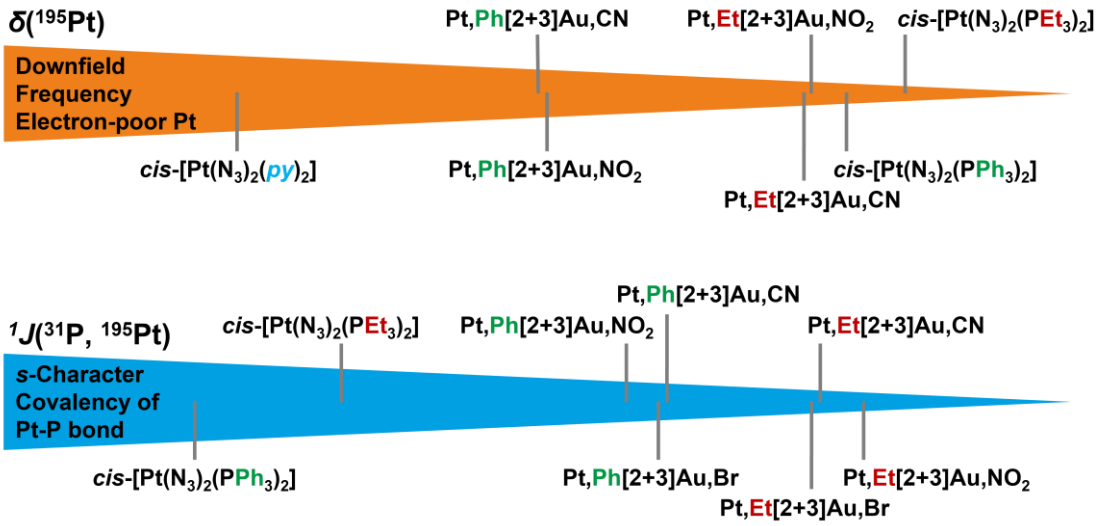

Figure 59: Schematic overview of the ^{195}Pt chemical shifts and $^{1}J(^{31}P, ^{195}Pt)$ coupling constants observed for a selection of compounds (86 MHz, CDCl$_3$, 25 °C).

The magnitude of the chemical shift provides insight into electron density close to the nuclei in question. Due to an opposing magnetic field created by the electrons, nuclei exhibiting higher electron density are subject to stronger shielding from the externally applied magnetic field in a NMR experiment. Resonances of nuclei experiencing a higher amount of shielding appear at lower frequencies, upfield, compared to less shielded nuclei which signals are detected

at higher frequencies, downfield.[86,89] Evaluating the observed data for the chemical shifts of the platinum(II) compounds in this context, suggests that with an upfield shift of 2185 ppm, the platinum centre in the diazidodiphosphine complexes are significantly more electron-rich compared to the pyridyl analogue. The readiness for the platinum(II) complexes to undergo [2+3]-cycloaddition reactions with the gold(I) alkynes under the chosen experimental conditions is directly related to the electron density within the complex. The experimental observations propose that the cycloaddition reaction is more likely to proceed with a more electron-rich platinum(II) centre than is the case for *cis*-[Pt(N_3)$_2$(*py*)$_2$]. The difference in the inductive effect of the substituted phosphine ligands explains the divergence in chemical shift for the parent compounds: whereas the negative inductive effect of the phenyl group renders the phosphine ligand a weaker *σ*-donor, the positive inductive effect of the ethyl groups increases the *σ*-donor properties of the phosphine ligand and with that in turn the electron density surrounding the platinum(II) centre, resulting in an upfield shift of the resonance. Upon cycloaddition, electron density has been shifted away from the platinum ion, leading to a downfield shift of all of the cycloaddition products.

In addition to the chemical shift, coupling constants are highly sensitive to the electronic surroundings of the respective nuclei.[93] The magnitude of the $^1J(^{31}P, ^{195}Pt)$ coupling constant reflects on the *s*-character and covalency of the platinum-phosphorus bond, with larger coupling constants indicating a higher *s*-character.[92–94] *cis*-[Pt(N_3)$_2$(PPh_3)$_2$] displays the largest coupling constant which suggests a mildly stronger *s*-character and covalency of the metal-phosphorus bond compared to the triethylphosphine analogue. Whilst the *s*-character of the

platinum-phosphorus bond appears to be reduced after successful cycloaddition, the trend between the nature of the phosphine substituents remains the same.

Correlating the chemical shift of the resonances in the ^{195}Pt NMR spectra as well as the $^{1}J(^{31}P, ^{195}Pt)$ coupling constants to the electron density on the platinum centre in conjunction with the ligands, could help determine viable diazidoplatinum complexes that undergo cycloaddition reaction under mild conditions. Ligands contributing to an electron-rich platinum centre appear to be more promising compared to complexes including electron-withdrawing ligands. Including further complexes in this correlation could help specify a narrow range of frequencies in the ^{195}Pt NMR spectrum indicating complexes with platinum centres of suitable electronic configuration, which could be used as a practical handle for synthesis rationale of [2+3]-cycloaddition reactions.

4. Oxidation of Platinum(II) Complexes

In order to explore the platinum(II)-gold(I) conjugates as potential candidates for prodrugs, next steps included the investigation towards the oxidation of the metal centre to platinum(IV), either prior to or post cycloaddition reaction. Oxidation attempts post [2+3]-cycloaddition reaction are more likely to result in a variation of side products. For this reason, efforts were focused on oxidising the platinum(II) complexes prior to formation of the triazole.

Hydrogen peroxide is a well-established oxidation agent with a wide application in the oxidation of platinum(II) centres.[29,98,108,114] Oxidation with hydrogen peroxide results in axial hydroxido ligands which have proven to increase the solubility of platinum(IV) complexes in protic and polar solvents.[98] Diazidodiphosphineplatinum(II) complexes were either directly added to 30% hydrogen peroxide or dissolved in tetrahydrofuran prior to adding the reagent (Scheme 26). In both cases the reaction mixtures were stirred for multiple hours at 45 °C and monitored *via* $^{31}P\{^{1}H\}$ spectroscopy. All reactions either led to the oxidation of the phosphine ligands or resulted in unreacted starting material. In an attempt to reduce the ratio of water in the reaction mixture, dibenzoyl peroxide was chosen as an alternative peroxide, which yielded unreacted starting material.

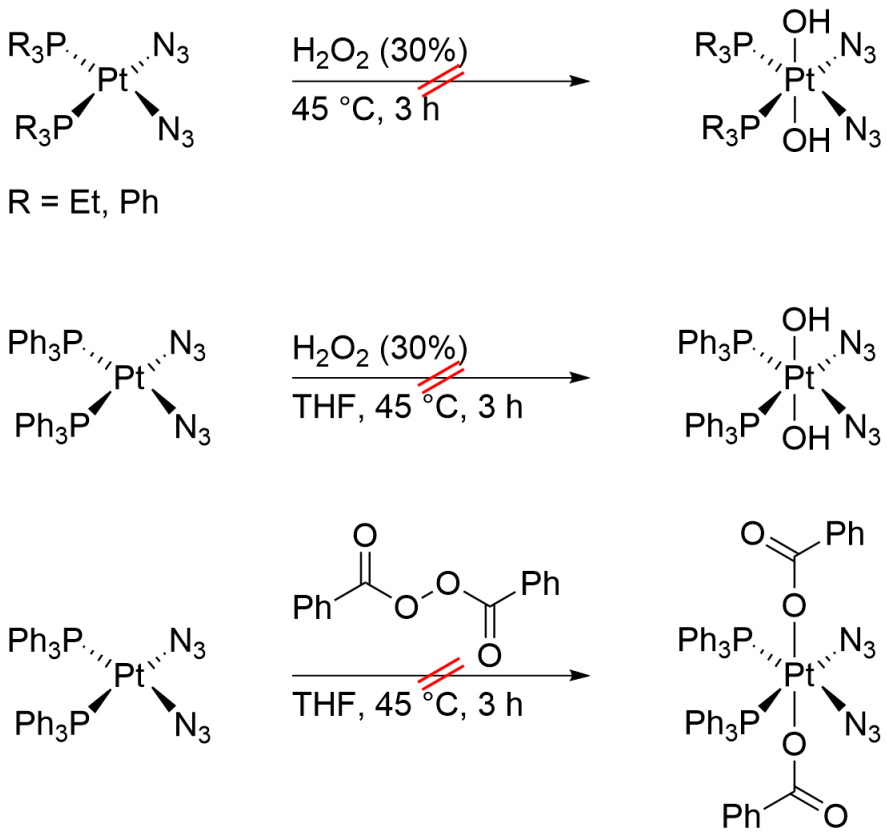

Scheme 26: Synthetic approaches to *cis*,*cis*,*trans*-[Pt(N$_3$)$_2$(PR$_3$)$_2$(OH)$_2$] (R = Et, Ph).

An alternative less polar peroxide for oxidation of platinum(II) complexes is *tert*-butyl hydrogen peroxide.[129,130] The peroxide was reacted with diazidodiphosphineplatinum(II) with variation of the experimental conditions (Scheme 27). Unreacted starting material was recovered from the reaction of *cis*-[Pt(N$_3$)$_2$(PPh$_3$)$_2$] with *tert*-butyl hydrogen peroxide (70%) with water as solvent. Heating the reaction mixture in tetrahydrofuran to 45–90 °C for 48 hours whilst monitoring with NMR spectroscopy, initiated cleavage and oxidation of the phosphine ligands. Reacting the diazidobis(triphenylphosphine)platinum(II) complex with *tert*-butyl hydrogen peroxide (70%) in acetic acid (98%) or in a solvent system including equal equivalents of acetic acid (98%), dichloromethane

and dimethylformamide, resulted in a clear change in the $^{31}P\{^{1}H\}$ NMR spectra (Figure 60). This particular solvent system has shown promising results for the oxidation of Oxaliplatin with *tert*-butyl hydrogen peroxide.[130]

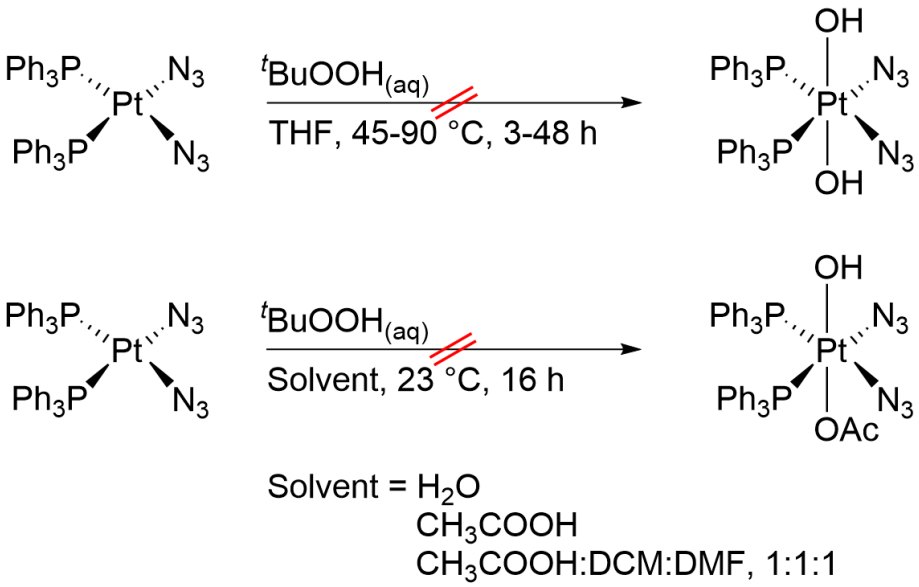

Scheme 27: Synthetic approaches to *cis*,*cis*,*trans*,*trans*-$[Pt(N_3)_2(PPh_3)_2(OH)(OR)]$ (R = H, Ac).

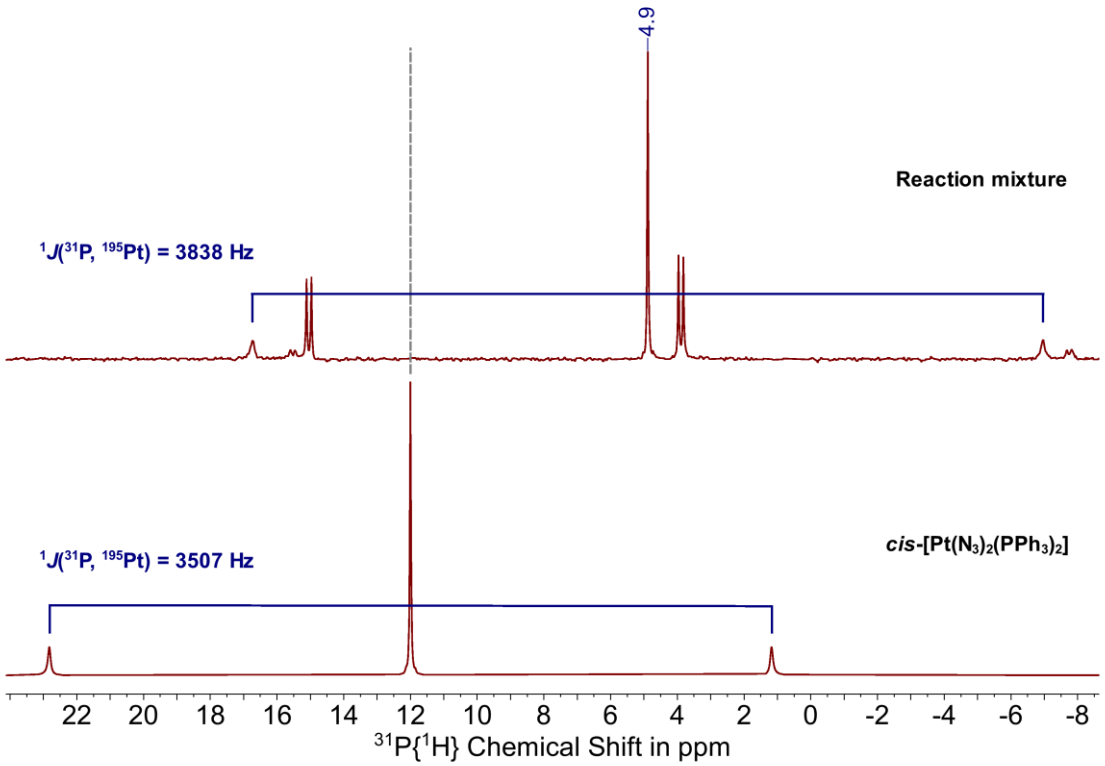

Figure 60: $^{31}P\{^1H\}$ NMR spectra (162 MHz, $CDCl_3$, 25 °C) of the reaction mixture following the reaction of *cis*-[Pt(N$_3$)$_2$(PPh$_3$)$_2$] and *tert*-butyl hydrogen peroxide in acetic acid.

The $^{31}P\{^1H\}$ NMR spectra show that all of the starting material has reacted. A new singlet is recorded at 4.9 ppm with a $^1J(^{31}P, ^{195}Pt)$ coupling constant of 3838 Hz. The upfield shift of the resonance in comparison to the platinum(II) parent compound indicates a more electron-rich platinum centre, which does not support the formation of a platinum(IV) centre. The new signal could intimate an exchange of one of the phosphine or azido ligands for either a hydroxido or acetato ligand. Two sets of doublets appear at 15.0 ppm and 4.0 ppm which may occur due to intermediates in the substitution reaction yielding an unsymmetric phosphine-platinum complex. The IR spectra of the mixtures of the reactions including acetic acid (Scheme 27) display a clear change in vibrations, however,

a prominent band at 2052 cm^{-1} which can be attributed to the asymmetric stretching frequency of an azide group confirms at least one azido ligand in the complex (Figure 61).

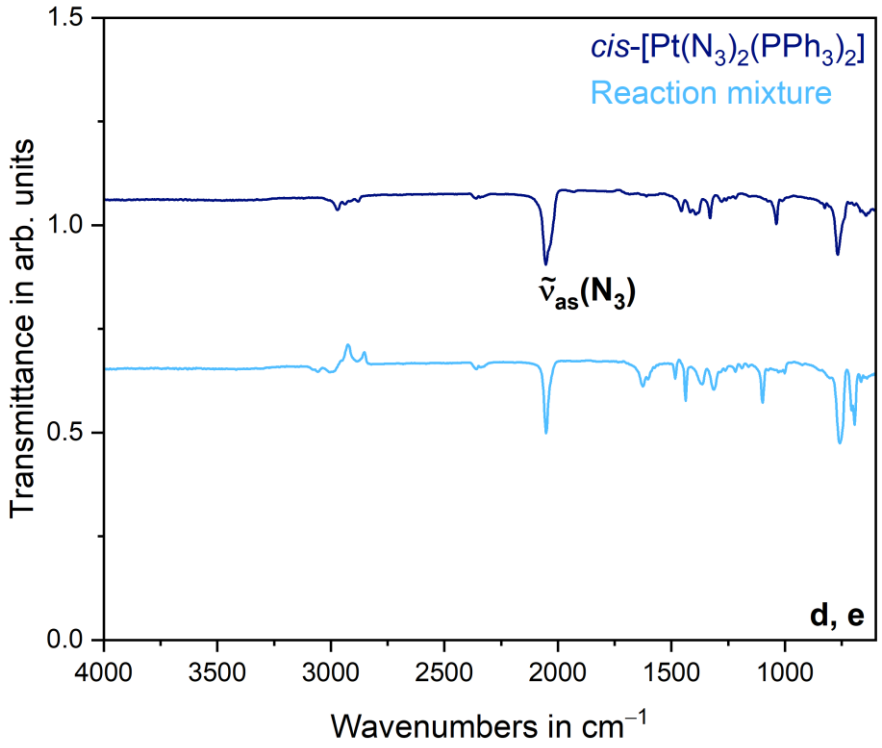

Figure 61: IR spectra (23 °C) of *cis*-$[Pt(N_3)_2(PPh_3)_2]$ and of the reaction mixtures of the synthetic approaches to *cis*,*cis*,*trans*-$[Pt(N_3)_2(PPh_3)(OAc)(OH)]$ outlined in Scheme 27. *cis*-$[Pt(N_3)_2(PPh_3)_2]$ was reacted with aqueous *tert*-butyl hydrogen peroxide in acetic acid (98%) (d) or in equal equivalents of acetic acid (98%), dichloromethane and dimethylformamide (e).

Crystals suitable for X-ray diffraction analysis were isolated from a concentrated reaction mixture in chloroform. The experimental data confirms the exchange of one of the azido ligands for an acetato ligand, yielding the formation of *cis*-

[Pt(N$_3$)(OAc)(PPh$_3$)$_2$]. Figure 62 depicts the molecular structure of the complex in the solid state (R_1 = 1.96%, wR_2 = 4.59%, R_{int} = 3.54%, *GooF* = 1.107, $e_{min/max}$ = −1.64/1.18 Å^{-3}). The platinum(II) compound crystallises in the orthorhombic spacegroup $P2_12_12_1$ with four formula units in the unit cell. Comparison of selected bond lengths and angles of *cis*-[Pt(N$_3$)(OAc)(PPh$_3$)$_2$] and the unreacted parent compound *cis*-[Pt(N$_3$)$_2$(PPh$_3$)$_2$] show no major deviations upon ligand exchange (Table 15).

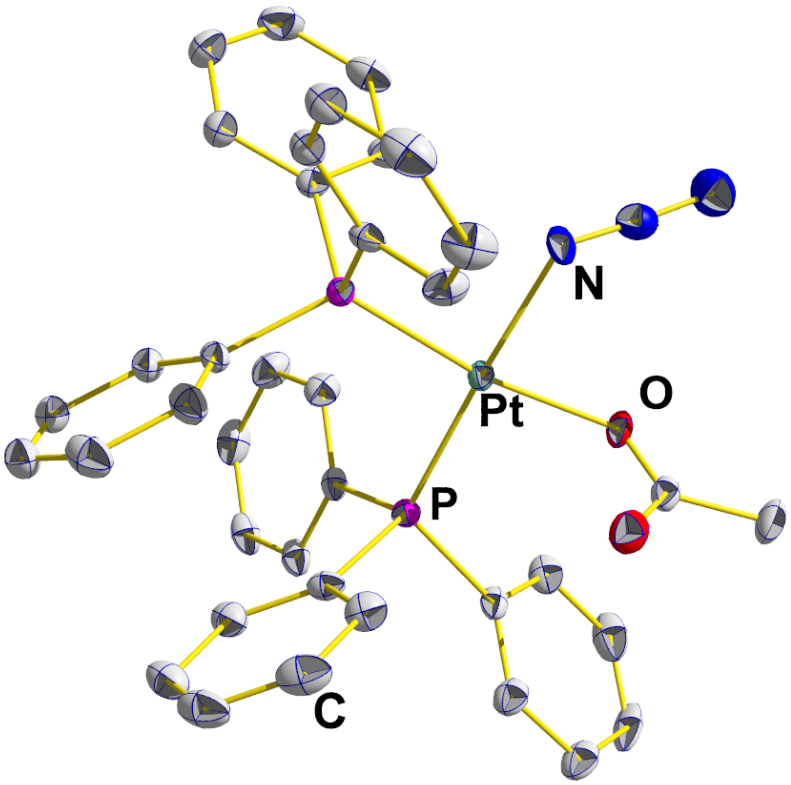

Figure 62: Molecular structure of *cis*-[Pt(N$_3$)(OAc)(PPh$_3$)$_2$] in the solid state. Calculated hydrogen atoms are omitted for clarity. Displacement ellipsoids are shown at the 50% probability level.

Table 15: Selected bond lengths and angles of the molecular structures of complexes *cis*-$[Pt(N_3)_2(PPh_3)_2]\cdot CHCl_3$ and *cis*-$[Pt(N_3)(OAc)(PPh_3)_2]$ in the solid state

	***cis*-$[Pt(N_3)_2(PPh_3)_2]\cdot CHCl_3$**	***cis*-$[Pt(N_3)(OAc)(PPh_3)_2]$**
Pt1–N1	2.091(2) Å	2.0813(34) Å
Pt1–P1	2.2755(7) Å	2.2477(9) Å
Pt1–P2	2.2593(7) Å	2.2466(10) Å
N1–N2	1.180(4) Å	1.1750(51) Å
N2–N3	1.169(4) Å	1.1709(64) Å
N1–Pt1–P1	84.43(7)°	84.139(106)°
P1–Pt1–P2	97.92(3)°	99.347(35)°
N1–Pt1–P2	174.03(7)°	176.100(96)°

Building on *N*-chlorosuccinimide (NCS) previously been shown to act as an effective oxidative chlorination agent for platinum(II) complexes,[131–133] the imide was employed in effort to oxidise the diazidodiphosphine platinum(II) complexes. The oxidation agent was added in combination with various solvents including acetic acid (50–98%), dimethylformamide, dimethyl sulfoxide and acetonitrile (Scheme 28).

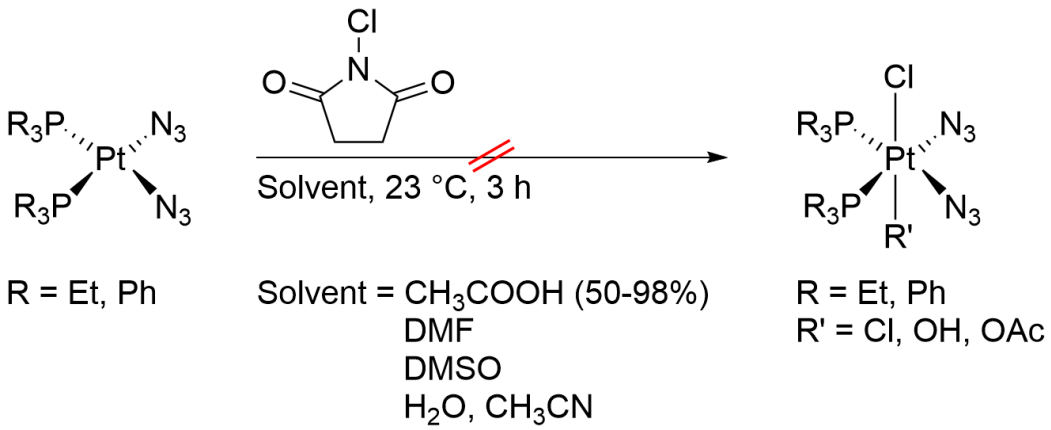

Scheme 28: Synthetic approaches to *cis*,*cis*,*trans,trans*-[Pt(N$_3$)$_2$(PR$_3$)$_2$(Cl)(R')] (R = Et, Ph; R' = Cl, OH, OAc).

Reaction progression was monitored by means of $^{31}P\{^1H\}$ NMR spectroscopy. The reactions in dimethylformamide, dimethyl sulfoxide and acetic acid (50–70%) resulted in an exchange of the azido for chlorido ligands and the formation of dichloridodiphosphineplatinum(II) and/or oxidation of the phosphine ligands. The reaction of *cis*-[Pt(N$_3$)$_2$(PPh$_3$)$_2$] with NCS in acetic acid of concentrations ≥80% resulted in a clear new singlet in the $^{31}P\{^1H\}$ NMR spectra at 4.9 ppm with a $^1J(^{31}P, ^{195}Pt)$ coupling constant of 3838 Hz, next to some doublets of minor intensity (Figure 63). From the attempted oxidation reactions with *tert*-butyl hydrogen peroxide in acetic acid, it was previously shown that the resonance at 4.9 ppm can be assigned to *cis*-[Pt(N$_3$)(OAc)(PPh$_3$)$_2$].

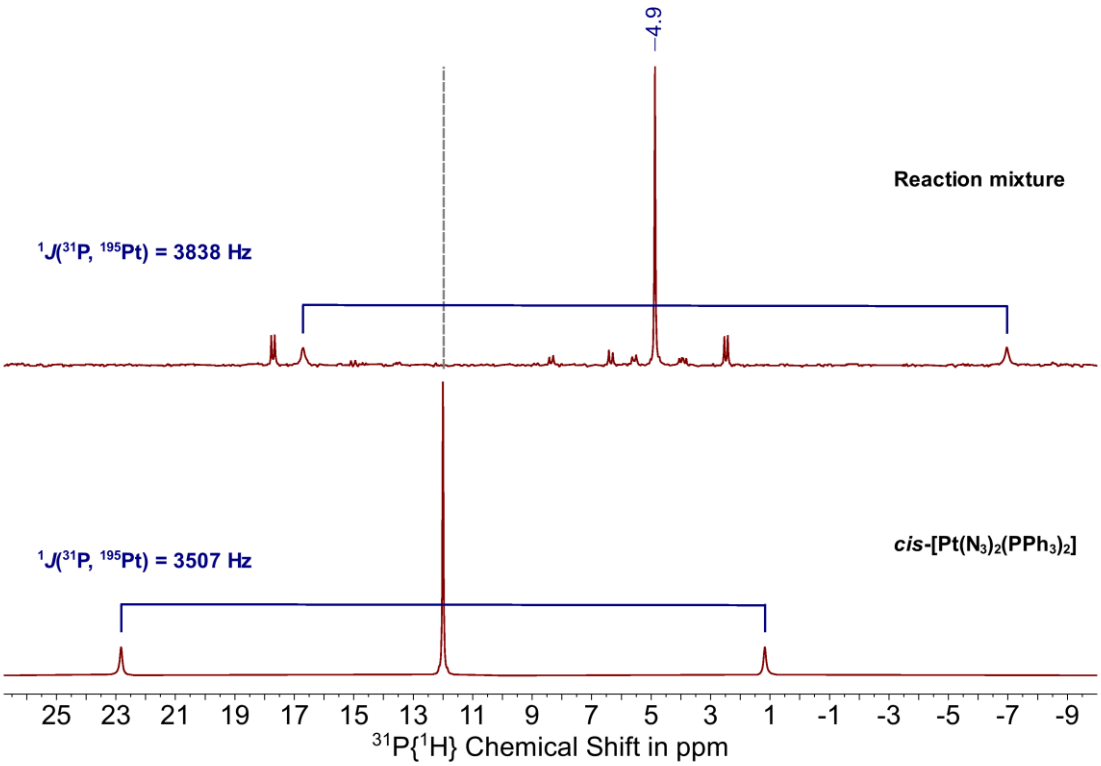

Figure 63: $^{31}P\{^1H\}$ NMR spectra (162 MHz, $CDCl_3$, 25 °C) of the reaction mixture following the reaction of *cis*-[Pt(N$_3$)$_2$(PPh$_3$)$_2$] and *N*-chlorosuccinimide in acetic acid (98%).

Single crystals suitable for X-ray diffraction analysis were isolated from a concentrated reaction mixture in an NMR sample in deuterated chloroform. Structure solution and refinement confirm the formation of a chloridosuccinimidatoplatinum(II) compound in which both of the azido ligands have been substituted. Figure 64 depicts the molecular structure of the complex *cis*-[Pt(Cl)(N(CO$_2$)$_2$(CH$_2$)$_2$)(PPh$_3$)$_2$] in the solid state (R_1 = 3.54%, wR_2 = 7.68%, R_{int} = 5.61%, *GooF* = 1.127, $e_{min/max}$ = −0.83/1.17 Å^{-3}). The compound crystallises as yellow blocks in the monoclinic space group $P2_1/n$ with four formula units in the unit cell.

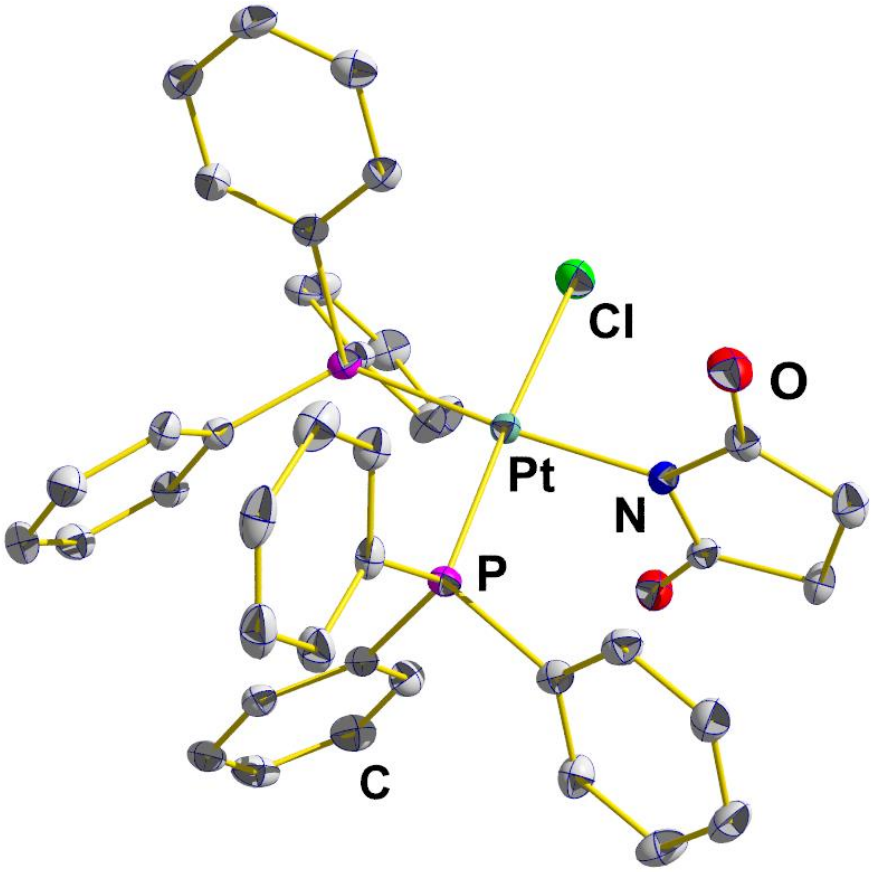

Figure 64: Molecular structure of *cis*-[Pt(Cl)(N(CO)$_2$(CH$_2$)$_2$)(PPh$_3$)$_2$] in the solid state. Calculated hydrogen atoms are omitted for clarity. Displacement ellipsoids are shown at the 50% probability level.

Considering the oxidation state of the platinum centre as well as diazidobis(triphenylphosphine)platinum(II) as the starting material reacting with NCS, the reaction mechanism leading to the formation of the observed product does not appear as straightforward. The analogous bromido complex has previously been reported *via* an oxidative addition reaction of *N*-bromosuccinimide and tetrakis(triphenylphosphine)platinum(0).[134] This account suggests the *in situ* reduction of the diazidoplatinum(II) parent compound to [Pt(PPh$_3$)$_4$] which then subsequently undergoes oxidative addition with NCS

whilst displacing two triphenylphosphine ligands in the process. With the recorded experimental data, it is not possible to determine the reducing agent or the exact reaction mechanism without further investigations. The two halido analogues crystallise in the same crystal system and space group with similar lattice parameters, rendering them isotypic.[134] A comparison of selected bond lengths and angles of both complexes shows slightly shorter values for the Pt–N and Pt–X (X = Br, Cl) bond length in the chlorido analogue (Table 16).

Table 16: Selected bond lengths and angles of the molecular structures of complexes *cis*-[Pt(X)(N(CO)$_2$(CH$_2$)$_2$)(PPh$_3$)$_2$] (X = Br, Cl) in the solid state. For X = Br, data was previously reported,[134] whereas for X = Cl, the values were obtained experimentally

	***cis*-[Pt(Br)(N(CO$_2$)$_2$(CH$_2$)$_2$)(PPh$_3$)$_2$]**	***cis*-[Pt(Cl)(N(CO$_2$)$_2$(CH$_2$)$_2$)(PPh$_3$)$_2$]**
Pt–N	2.125(6) Å	2.0559(39) Å
Pt–X	2.4785(7) Å	2.3533(13) Å
Pt–P	2.2601(16) Å	2.2483(13) Å
Pt–P	2.2764(18) Å	2.2731(13) Å
N–Pt–P	90.03(14)°	90.317(116)°
N–Pt–X	86.57(13)°	86.797(115)°
P–Pt–P	97.74(6)°	97.665(47)°
P–Pt–X	85.86(5)°	85.156(46)°
N–Pt–P	170.45(14)°	169.967(114)°
P–Pt–X	176.47(4)°	177.076(46)°

Repeating the synthesis yielded an improved ratio of the two products in the $^{31}P\{^1H\}$ NMR spectrum, however, no selective synthesis of *cis*-[Pt(Cl)(N(CO$_2$)$_2$(CH$_2$)$_2$)(PPh$_3$)$_2$] was achieved. Due to the lack of symmetry in the

complex resulting in two non-chemically equivalent phosphorus atoms, the resonances in the $^{31}P\{^{1}H\}$ NMR spectrum appear as AX-type doublets at 15.0 ppm and at 3.84 ppm, with $^{2}J(^{31}P, ^{31}P)$ coupling constants of 23.8 HZ and 23.7 Hz, respectively (Figure 65).

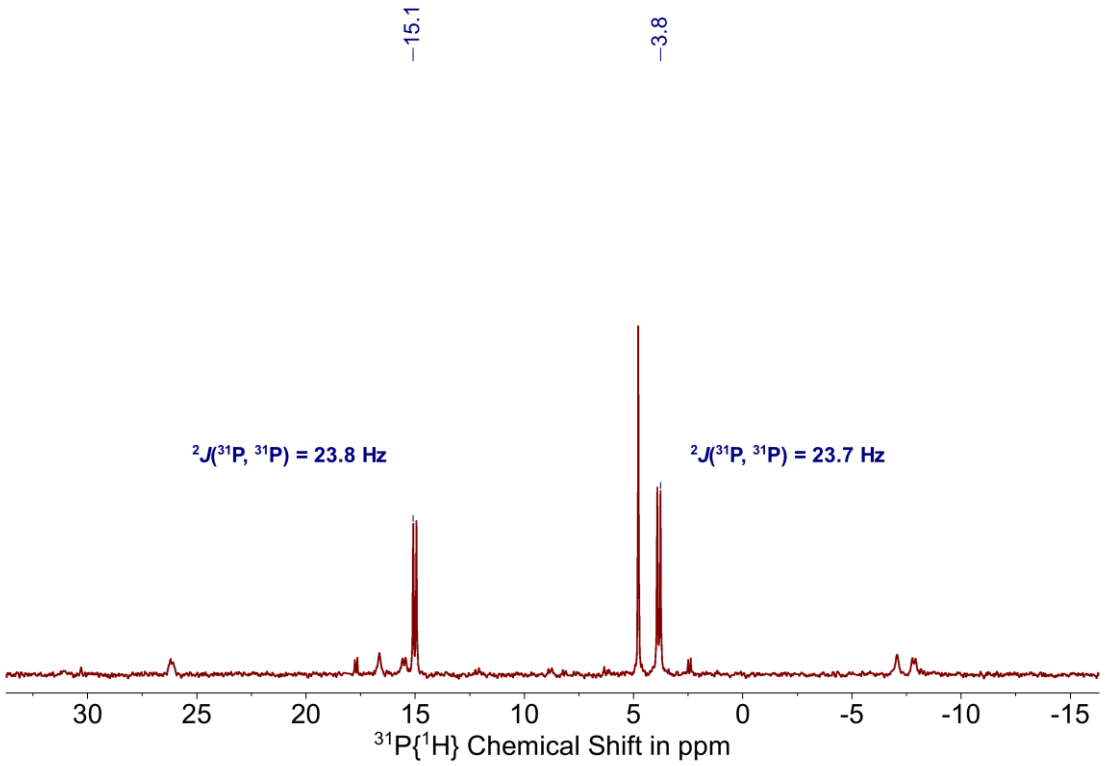

Figure 65: $^{31}P\{^{1}H\}$ NMR spectra (162 MHz, $CDCl_3$, 25 °C) of *cis*-$[Pt(Cl)(N(CO)_2(CH_2)_2)(PPh_3)_2]$ in the reaction mixture following the reaction of *cis*-$[Pt(N_3)_2(PPh_3)_2]$ and *N*-chlorosuccinimide in acetic acid (98%).

When applying acetonitrile as the main solvent, NCS was dissolved in a small volume of water to promote reactivity of both compounds in solution. The $^{31}P\{^{1}H\}$ NMR spectrum of the reaction of diazidobis(triphenylphosphine)platinum(II) and

NCS in acetonitrile reveals the formation of a novel phosphine platinum complex with a singlet at 0.4 ppm next to the formation of multiple minor species (Figure 66). The change in the magnitude of the $^{1}J(^{31}P, ^{195}Pt)$ coupling constant of 3507 Hz for the parent compound to 1584 Hz for the reaction product suggests a significant change in the electron density around the platinum centre. However, the upfield shift of the resonance indicates at the formation of a more electron-rich platinum ion. No isolation of the complex with the resonance at 0.4 ppm to enable further characterisation was possible.

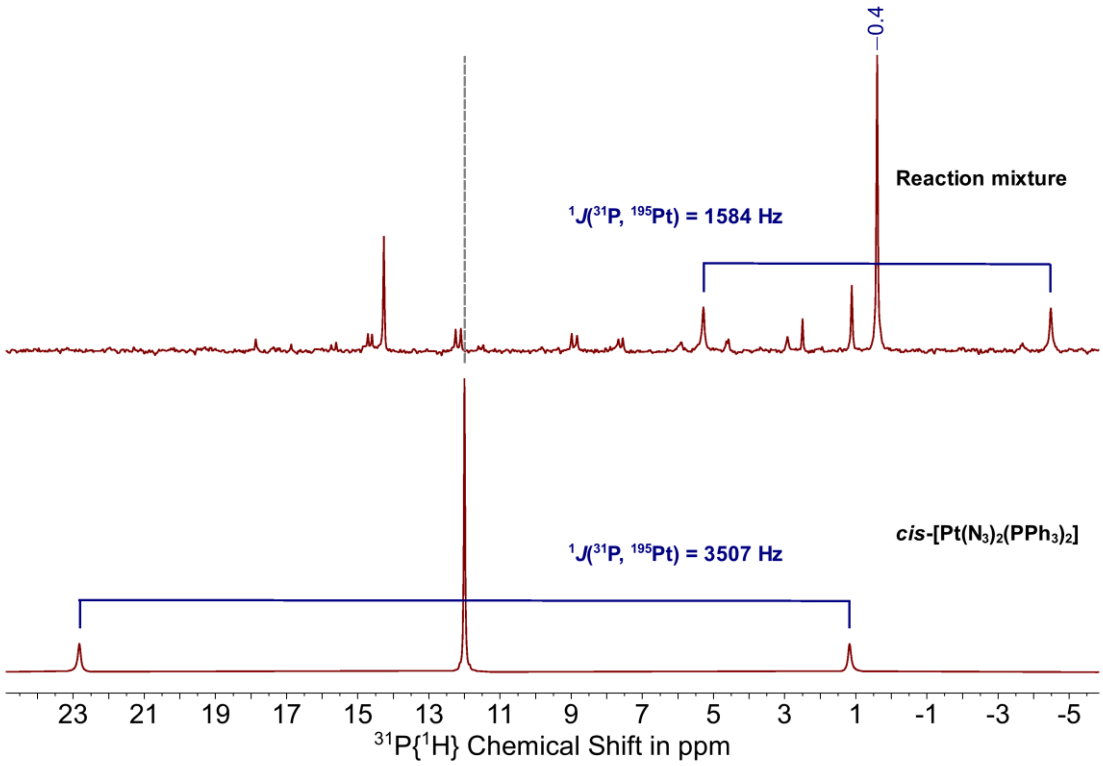

Figure 66: $^{31}P\{^{1}H\}$ NMR spectra (162 MHz, $CDCl_3$, 25 °C) of the reaction mixture following the reaction of *cis*-$[Pt(N_3)_2(PPh_3)_2]$ and *N*-chlorosuccinimide in acetonitrile.

The analogous reaction with diazidobis(triethylphosphine)platinum(II) results in one clear resonance at 5.7 ppm in the $^{31}P\{^{1}H\}$ NMR spectrum which is shifted slightly upfield compared to the starting material (Figure 67). The $^{1}J(^{31}P, ^{195}Pt)$ coupling constant was determined to be 1461 Hz which is 1877 Hz smaller than for the diazidoplatinum(II) complex.

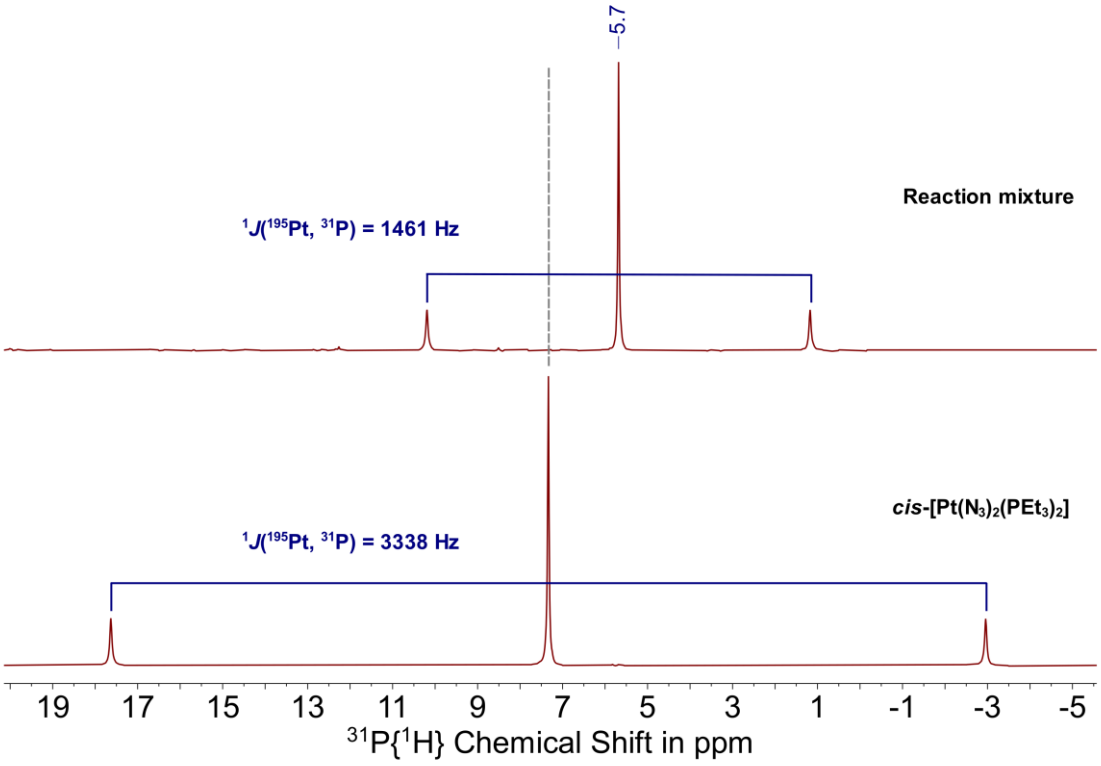

Figure 67: $^{31}P\{^{1}H\}$ NMR spectra (162 MHz, $CDCl_3$, 25 °C) of the reaction mixture following the reaction of *cis*-[Pt(N$_3$)$_2$(PEt$_3$)$_2$] and *N*-chlorosuccinimide in acetonitrile.

One single crystal suitable for X-ray diffractometry was isolated from a concentrated solution in chloroform. The complex was determined as *trans*-[PtCl$_4$(PEt$_3$)$_2$], confirming the oxidation of the platinum(II) to a platinum(IV) centre,

however, under displacement of the azido ligands in exchange for chlorido ligands. The platinum(IV) complex crystallises in the monoclinic space group $P2_1/n$ with two formula units in the unit cell (R_1 = 2.05%, wR_2 = 5.24%, R_{int} = 4.20%, *GooF* = 1.100, $e_{min/max}$ = −1.62/2.13 Å^{-3}). Figure 68 depicts the molecular structure in the solid state confirming the *trans*-configuration of the phosphine groups.

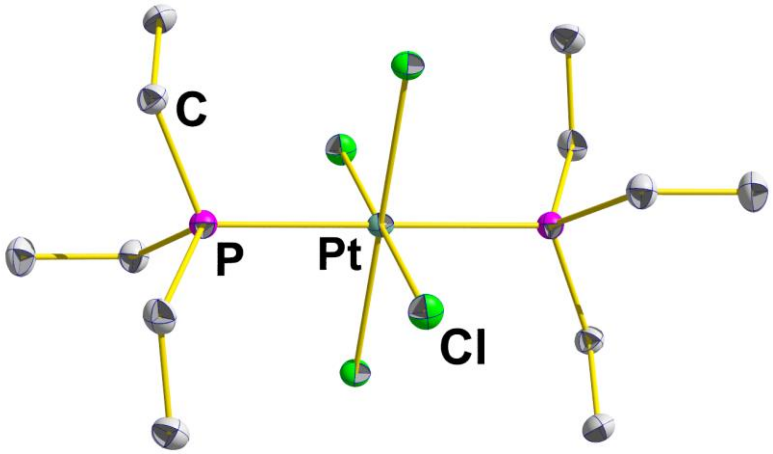

Figure 68: Molecular structure of *trans*-[$PtCl_4(PEt_3)_2$] in the solid state. Calculated hydrogen atoms are omitted for clarity. Displacement ellipsoids are shown at the 50% probability level.

Table 17 lists the values of selected bond lengths and angles of the molecular structure of the tetrachloridodiphosphineplatinum(IV) complex. The bond angles of the six ligands around the platinum centre confirm a near-to octahedral coordination of the metal centre. Whilst the mean bond lengths for the Pt–P and Pt–Cl bonds in *trans*-[$PtCl_4(PEt_3)_2$] have been reported previously, no extensive information and no crystallographic dataset is available for an in-depth

comparison.[135] The determined bond lengths are in good agreement with the literature. Comparing the Pt–L (L = P, Cl) bond length of the tetrachloridoplatinum(IV) complex to its dichloridoplatinum(II) analogue (2.314(5) Å for Pt–P, 2.301(4) Å for Pt–Cl) demonstrates that the electronic configuration of the metal ion has a greater influence on the metal-phosphine bond compared to the metal-halide bond.[136] A reduction in electron density around the platinum centre leads to a weaker Pt–P bond with less covalent *s*-character. This change manifests itself in the elongation of the Pt–P bond as well as the decrease in the $^{1}J(^{31}P, ^{195}Pt)$ coupling constant.

Table 17: Selected bond lengths and angles of the molecular structure in the solid state of *trans*-$[PtCl_4(PEt_3)_2]$

	***trans*-$[PtCl_4(PEt_3)_2]$**
Pt1–P1	2.3961(6) Å
Pt1–Cl1	2.3286(6) Å
Pt1–Cl2	2.3309(7) Å
P1–Pt–Cl1	88.224(21)°
P1–Pt–Cl2	88.646(22)°
Cl1–Pt-Cl2	89.109(22)°
P1–Pt–P1'	179.984(21)°
Cl2–Pt–Cl2'	179.988(22)°

To conclude the oxidation attempts of *cis*-$[Pt(N_3)_2(PR_3)_2]$ (R = Et, Ph) with well-established oxidation agents for the oxidation of platinum(II) complexes, it became obvious that in all examined cases the Pt–N bond appears to be more labile under the chosen experimental conditions compared to the Pt–P bond. Due

to the electronic configuration of an azide, an azido ligand is likely to display a similar *trans*-effect to a halide, in which case the *trans*-effect of substituted phosphine ligands will outweigh this force, facilitating ligand substitution reactions of the azido ligands above the oxidation of the platinum(II) centre.

An alternative approach to isolating the corresponding diazidodiphosphineplatinum(IV) compounds is starting with a platinum(IV) complex, such as potassium hexachloridoplatinate(IV), followed by ligand substitution (Scheme 29).

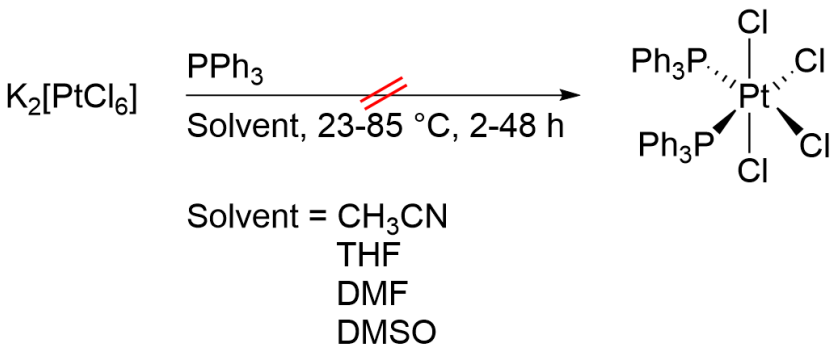

Scheme 29: Synthetic approaches to *cis*-$[PtCl_4(PEt_3)_2]$.

Thorough investigations aiming at exchanging the chlorido ligands for triphenylphosphine ligands were performed both at room temperature and elevated temperatures under the exclusion of air and with dry solvents. Reaction progress was monitored by means of $^{31}P\{^1H\}$ NMR spectroscopy. In all cases the syntheses yielded dichloridobis(triphenylphosphine)platinum(II) alongside triphenylphosphine oxide. These observations indicate residual oxygen within the

reaction mixtures as well as the reduction of the platinum species, however, without further investigation it is unclear as to what species is acting as the reducing agent.

Since oxidation of the complexes *cis*-[$Pt(N_3)_2(PR_3)_2$] (R = Et, Ph) in a controlled manner with the goal of next reacting them with the gold(I) alkynes [$Au(PPh_3)(CC(C_6H_4)X)$] (X = NO_2, Br, CN) was not successful within the scope of this work, a selection of the platinum(II) complexes was chosen for the subsequent cytotoxicity and irradiation studies. Comparing the behaviour of the platinum(II) with the platinum(II)-gold(I) complexes will reveal whether a combination of the two metallic compounds enhances their cytotoxicity and helps reduce cell numbers at a lower drug concentration. Examining the complexes' response to irradiation with visible light and X-rays will provide insight into potential structural changes following absorption processes which could promote the breakdown of the compounds into their toxic entities.

5. Cytotoxicity of Platinum(II)-Gold(I) Complexes

In order to explore the viability of the novel platinum(II)-gold(I) complexes as anti-cancer agents, both the diazidodiphosphineplatinum(II) complexes *cis*-$[Pt(N_3)_2(PR_3)]$ (R = Et, Ph) as well as the products of the [2+3]-cycloaddition reactions with the gold(I) alkynes $[Au(PPh_3)(CC(C_6H_4)NO_2)]$ and $[Au(PPh_3)(CC(C_6H_4)CN)]$ were examined in different cancer cell lines. Platinum(II)-gold(I) complexes **Pt,Ph[2+3]Au,Br** and **Pt,Et[2+3]Au,Br** were not included in the cell studies as it was not possible to isolate these in the necessary purity.

Cell testing was carried out in collaboration with the research group of Prof G. Higgins in the Department of Oncology at the University of Oxford.

Activity of the complexes as potential radiosensitisers was pursued through irradiation with X-rays. The objective of these investigations was the effect of irradiation of the compounds on their respective anti-cancer activity. Considering the structural features of the complexes at hand, the generation of reactive azidyl radicals as well as cleavage between the active platinum(II) and gold(I)-containing fragments were feasible. Upon breakdown of the compounds in this manner, each of the entities would be likely to exhibit their own specific anti-cancer activity, targeting the tumour cells with multiple modes of action, yielding multi-modal anti-cancer agents which are activated selectively upon irradiation. The absence of cytotoxicity in the dark combined with anti-cancer activity after irradiation with X-rays, would pose a starting point for radiosensitive

diphosphineplatinum(II) prodrugs compared to the conventional approach of platinum-based prodrugs in the higher oxidation state +IV.

Scheme 30 shows an overview of the six compounds that were chosen for cell testing, highlighting their structural differences.

Cell viability assays were performed with the human colorectal carcinoma cell line HCT116 with 500 cells per well and six technical replicates per condition. The compounds were investigated towards their radiosensitivity using X-rays of 4 Gy generated by a caesium-source with a photon energy of 662 keV and a dose rate of 1.2 $Gy \cdot min^{-1}$. The compounds were dissolved in 12 mM solutions in dimethyl sulfoxide and added to the cells in varying concentration (0–15 µM) 2 hours prior to irradiation. The stability of the compounds in dimethyl sulfoxide was confirmed prior to commencing the cell studies. The cell-medium was changed 18 hours after irradiation and the resazurin-based dye Alamar Blue was added on day eight. Metabolism of the dye by viable cells reduces the resazurin to resorufin, yielding a fluorescent response which is detected by a fluorescence intensity microplate reader. The detected fluorescence is directly proportional to the number of living cells, which in turn is used to infer the cytotoxicity. All cell counts were normed to the first point on the scale at which the concentration of the added compound was 0 µM, effectively considering any toxic effect the solvent alone displays. Cell testing was performed in triplicate.

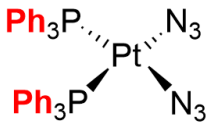

***cis*-[Pt(N$_3$)$_2$(PPh$_3$)$_2$]**

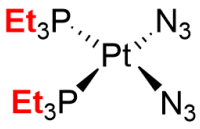

***cis*-[Pt(N$_3$)$_2$(PEt$_3$)$_2$]**

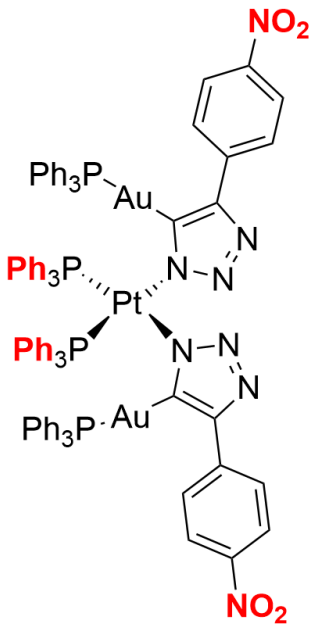

Pt,Ph[2+3]Au,NO$_2$

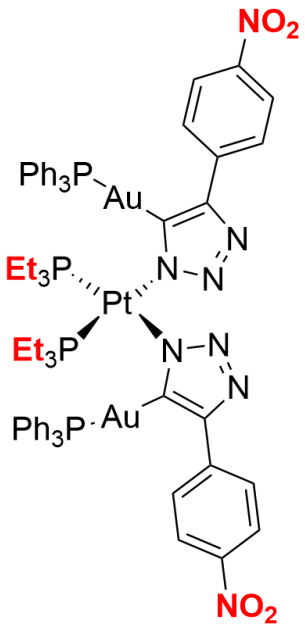

Pt,Et[2+3]Au,NO$_2$

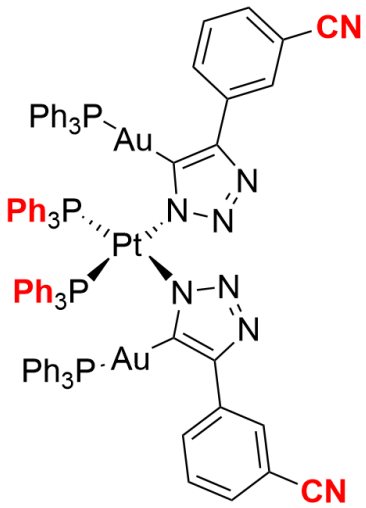

Pt,Ph[2+3]Au,CN

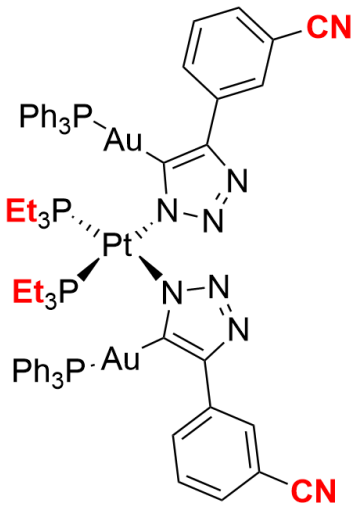

Pt,Et[2+3]Au,CN

Scheme 30: Overview of the six compounds which were chosen for cell studies. Structural differences are highlighted in red.

Figure 69 depicts the graphical output of the cell viability assays for compound *cis*-[Pt(N_3)$_2$(PPh_3)] for no irradiation and with a radiation dose of 4 Gy. Since the data vary somewhat significantly for some of the complexes, the graphs of all three sets are displayed. One of the representations allows for straightforward comparison of cell viability at explicit concentrations, while the other enables an easy conclusion of a trend.

In all three cases the results indicate clear radiosensitisation at concentrations of around 7.5 µM. Addition of the compound alone without radiation does not appear to be toxic until concentrations above 10 µM are reached. The average IC_{50}-value of compound *cis*-[Pt(N_3)$_2$(PPh_3)] after radiation of 4 Gy was calculated to be 5.39 µM. In comparison to these observations, the results from the cell viability studies of the analogous triethylphosphineplatinum(II) complex *cis*-[Pt(N_3)$_2$(PEt_3)] does not display a clear trend (Figure 70). While the compound seems to exhibit little or no cytotoxicity in the dark below concentrations of 10 µM, the cell count after the radiation dose of 4 Gy is significantly reduced from concentrations as low as 1.25 µM onwards, though it displays a minor reduction in cell numbers with concentrations >10 µM relative to the unirradiated sample. This variation leads to the calculated IC_{50}-value to scale from 0.0003 µM and 25.2 µM, clearly indicating the necessity for further investigation.

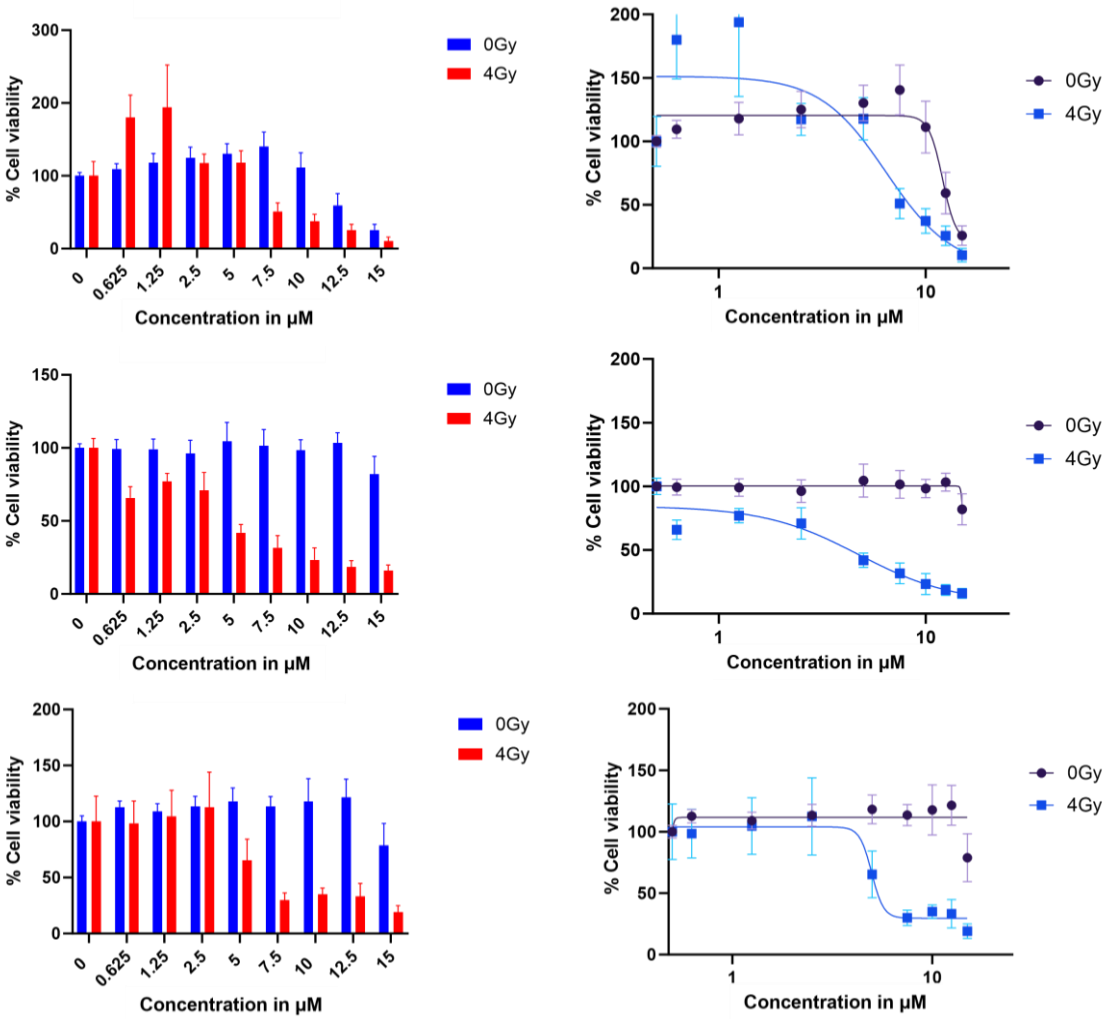

Figure 69: Graphical representation of the cell counts of the cell viability assays of compound *cis*-$[Pt(N_3)_2(PPh_3)]$ (HCT116, 500 cells for 0/4 Gy).

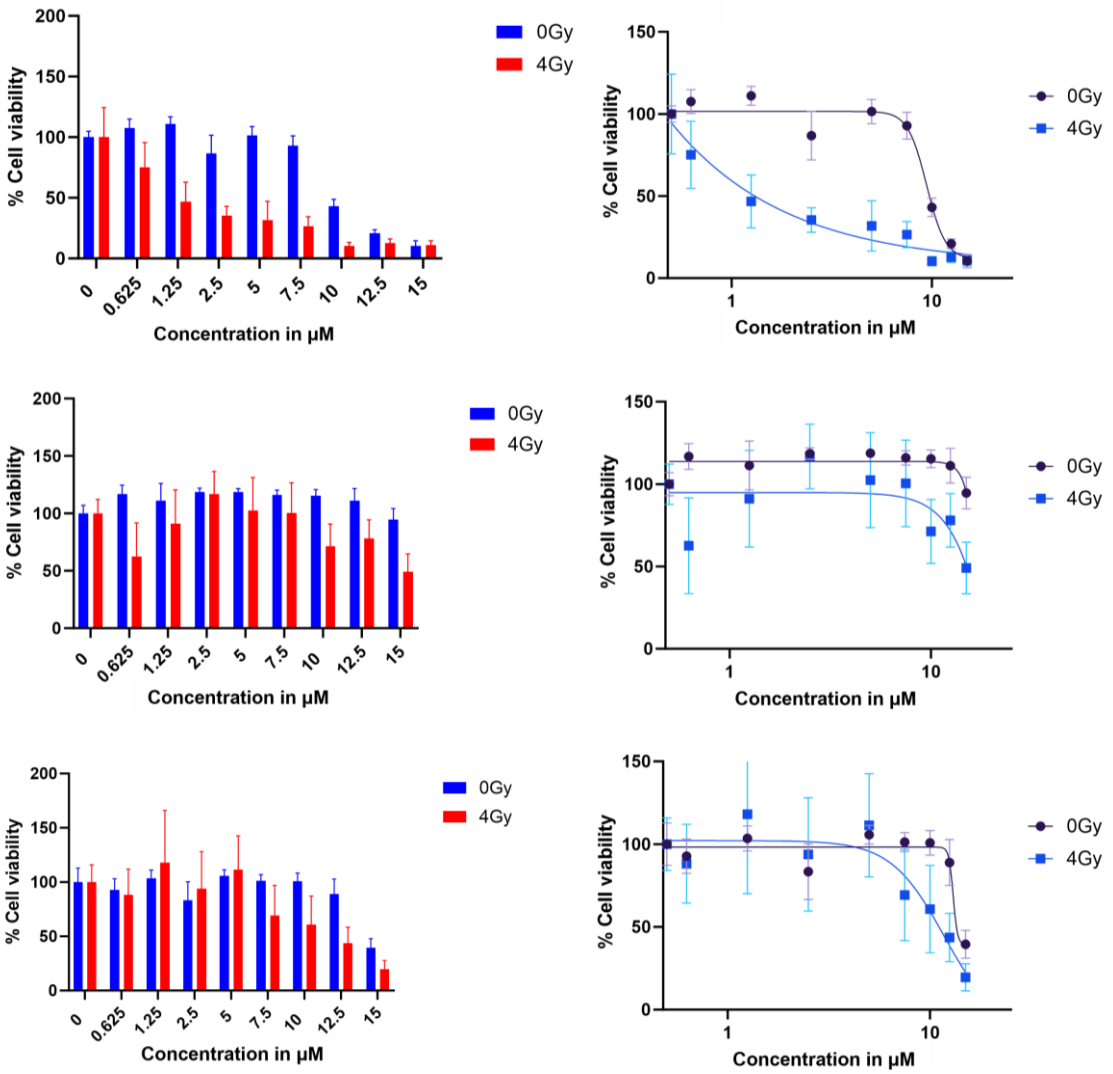

Figure 70: Graphical representation of the cell counts of the cell viability assays of compound *cis*-[Pt(N_3)$_2$(PEt_3)] (HCT116, 500 cells for 0/4 Gy).

Evaluating the cytotoxic behaviour of cycloaddition products **Pt,Ph[2+3]Au,CN**, **Pt,Et[2+3]Au,CN** and **Pt,Ph[2+3]Au,NO$_2$** resulted in inconsistent observations which suggested more cell-testing was required. Whilst cell viability assays on compound **Pt,Et[2+3]Au,CN** indicate that the platinum-gold conjugate exhibits enhanced toxicity upon radiation, the complex alone already appears to display strong cytotoxicity at concentrations >5 µM. However, the variation between the

replicates is significant, resulting in IC_{50}-values spanning from 0.128–3.12 µM, rendering these results unreliable. The triphenylphosphine analogue **Pt,Ph[2+3]Au,CN** reveals a clear window for activation *via* X-rays at concentrations as low as 2.5 µM (Figure 71). The compound alone seems to be non-toxic in the dark until concentrations of 7.5–10 µM.

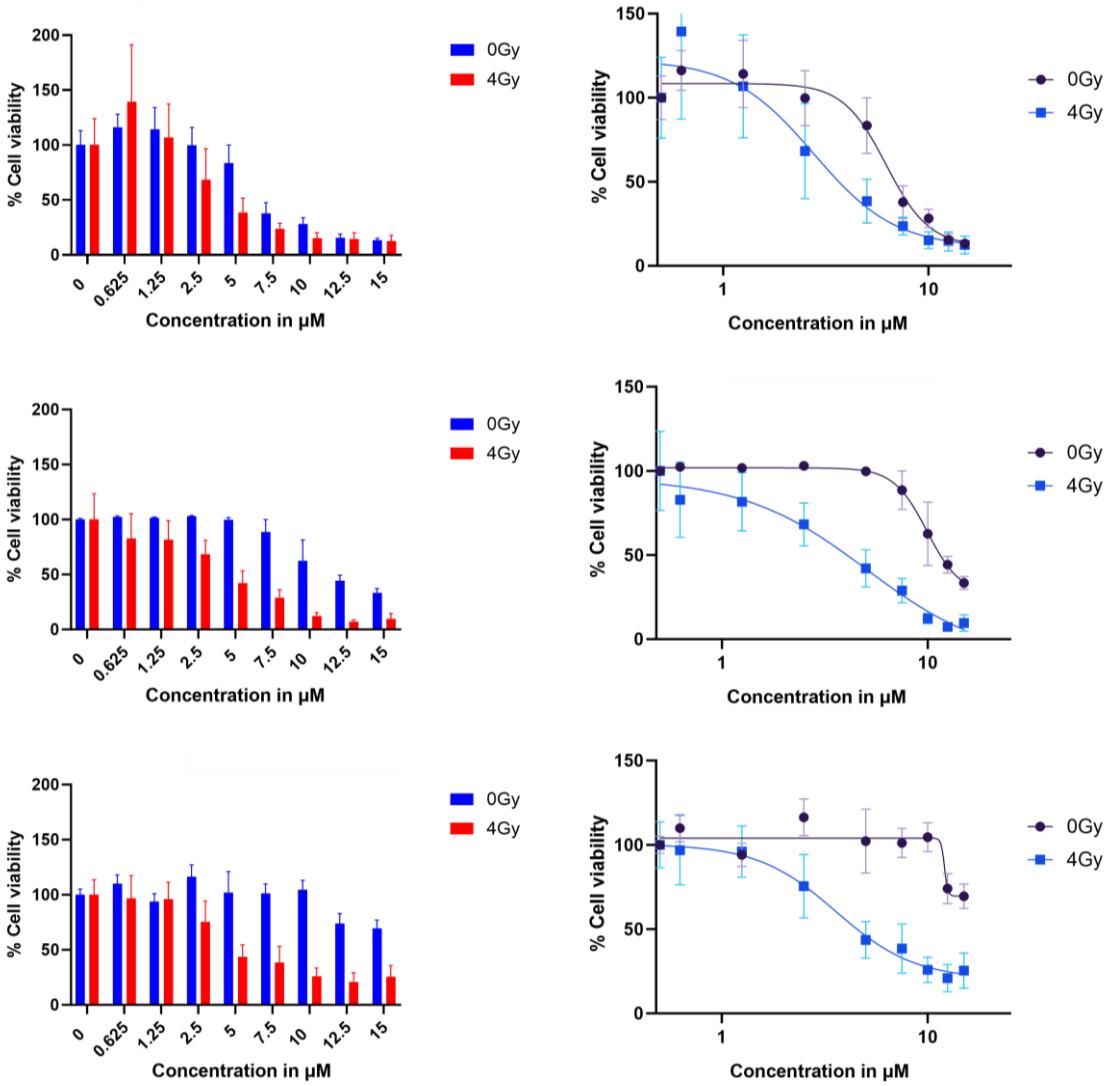

Figure 71: Graphical representation of the cell counts of the cell viability assays of compound **Pt,Ph[2+3]Au,CN** (HCT116, 500 cells for 0/4 Gy).

The significantly enhanced cytotoxicity of the platinum-gold compound at lower concentrations is a promising result towards the prospect of administering lower doses to patients without the loss of the therapeutic effect on the cancer cells. Taking the variation of the replicates into consideration, the average IC_{50}-value of **Pt,Ph[2+3]Au,CN** with a radiation dose of 4 Gy was determined to be 3.80 µM compared to a value of 9.40 µM with no radiation.

The triphenylphosphineplatinum(II)-gold(I) conjugate **Pt,Ph[2+3]Au,NO_2**, which includes a nitro group instead of a nitrile group, exhibits low cytotoxicity without radiation (Figure 72). After radiation the same drug concentration leads to approximately half of the cell numbers, resulting in an average IC_{50}-value of 4.39 µM.

Due to technical difficulties no cell studies were performed on compound **Pt,Et[2+3]Au,NO_2** in this round of testing.

Table 18 includes the IC_{50}-values of this initial cell testing of compounds *cis*-[$Pt(N_3)_2(PPh_3)$], *cis*-[$Pt(N_3)_2(PEt_3)$], **Pt,Ph[2+3]Au,CN**, **Pt,Et[2+3]Au,CN** and **Pt,Ph[2+3]Au,NO_2** on the cancer cell line HCT116 for no radiation and a treatment of the cells with 4 Gy of X-rays. All five compounds display enhanced cytotoxicity upon radiation albeit the level of radiosensitisation appears to vary in between the complexes. Compound **Pt,Et[2+3]Au,CN** exhibits the highest level of toxicity of the complex alone in the absence of irradiation. Both the diazidodiphosphineplatinum(II) complexes as well as the [2+3]-cycloaddition products demonstrate activation *via* X-rays, however, the platinum-gold-conjugates indicate a slightly increased response to radiosensitisation. The congeners with the triethylphosphine groups exhibit mildly improved activation

via X-rays compared to the compounds with triphenylphosphine groups. In order to evaluate the observations in the context of established anti-cancer agents, Cisplatin was dissolved in water and tested alongside the novel compounds. With a radiation dose of 4 Gy, the drug exhibits a cytotoxic effect from concentrations of 2.5–5 µM and above, leading to a calculated IC_{50}-value of 2.73 µM, with the cell counts remaining unchanged until concentrations of 7.5 µM in the dark (Figure 73).

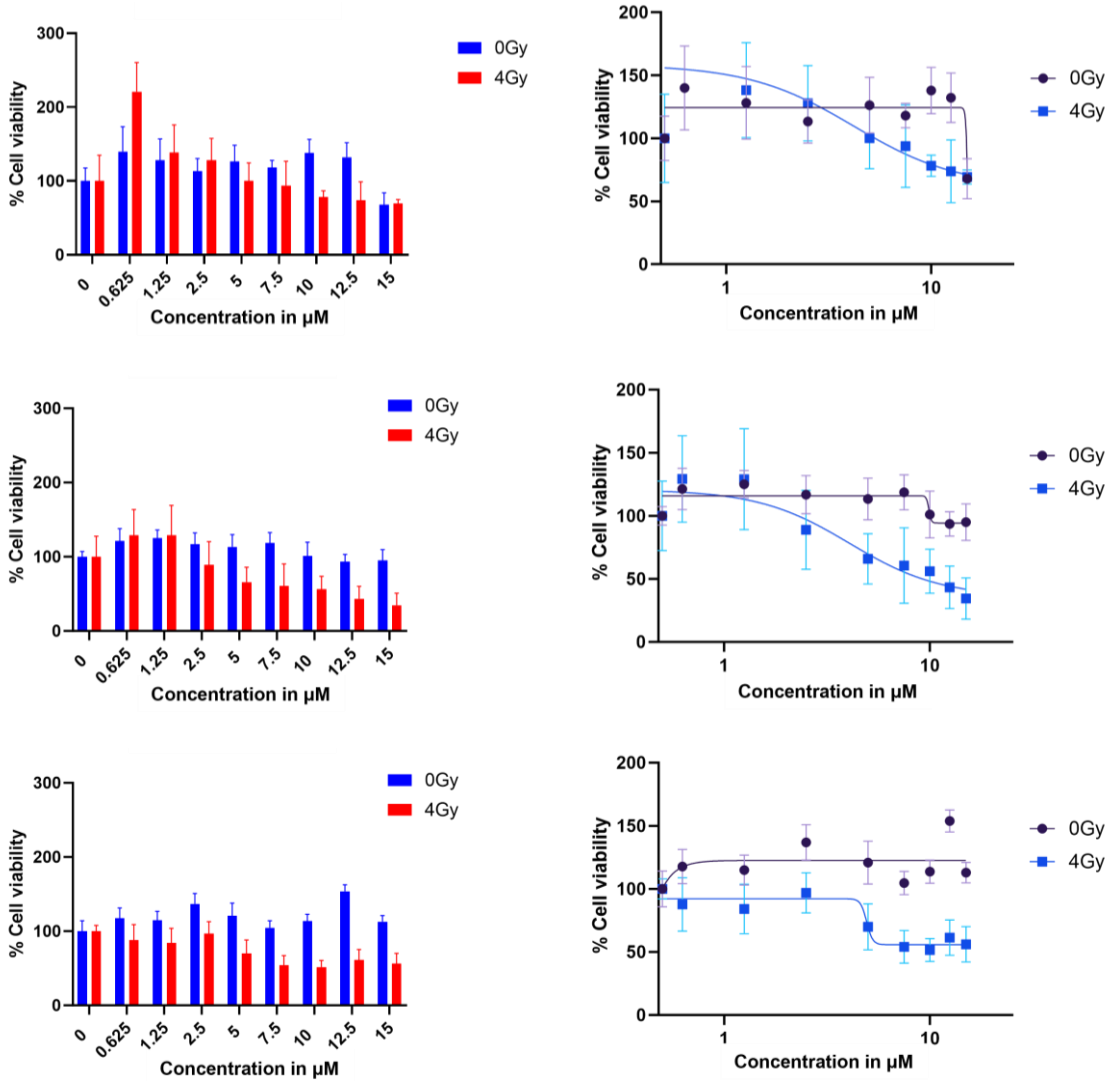

Figure 72: Graphical representation of the cell counts of the cell viability assays of compound **Pt,Ph[2+3]Au,NO_2** (HCT116, 500 cells for 0/4 Gy).

Table 18: Average IC_{50}-value of initial cell studies of compounds *cis*-$[Pt(N_3)_2(PPh_3)]$, *cis*-$[Pt(N_3)_2(PEt_3)]$, **Pt,Ph[2+3]Au,CN**, **Pt,Et[2+3]Au**, **CN**, **Pt,Ph[2+3]Au,NO_2** and Cisplatin (HCT116, 500 wells for 0/4 Gy)

	Avg. IC_{50}-value (0 Gy)	**Avg. IC_{50}-value (4 Gy)**
***cis*-$[Pt(N_3)_2(PPh_3)]$**	13.9 µM	5.39 µM
***cis*-$[Pt(N_3)_2(PEt_3)]$**	19.9 µM	12.3 µM
Pt,Ph[2+3]Au,CN	9.40 µM	3.80 µM
Pt,Et[2+3]Au,CN	5.15 µM	1.62 µM
Pt,Ph[2+3]Au,NO_2	13.5 µM	4.39 µM
Cisplatin	5.74 µM	2.74 µM

In conclusion, while preliminary cell testing on the human colon cancer cell line HCT116 reveals cytotoxicity for the selected compounds, further studies are necessary in order to improve reproducibility and to draw any consistent trends. In particular for Cisplatin no radiosensitivity would be expected, suggesting that a methodical error might be contributing to the obtained results.

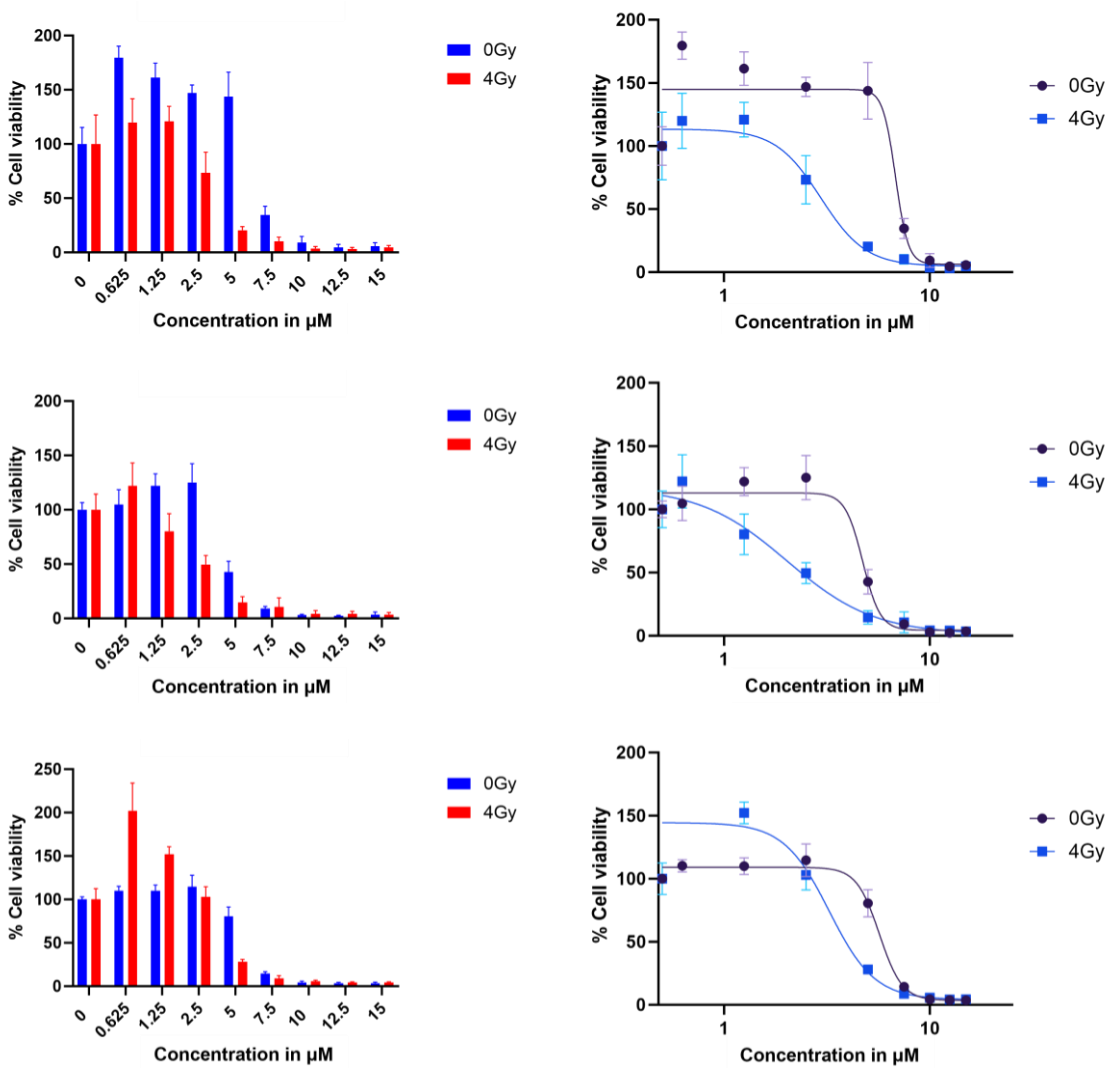

Figure 73: Graphical representation of the cell counts of the cell viability assays of Cisplatin (HCT116, 500 cells for 0/4 Gy).

The second stage of cell testing was extended to three cell lines: the two human cell lung carcinoma cell lines H1299 and A549, next to the human colorectal cell line HCT116 again. A substantial difference between this second stage was the approach to mitigate the toxic effect the irradiation in itself might be causing on the cell count. To this end, the number of tested cells was modified depending on whether they were being irradiated or not. Per well, 400 cells of each cancer

cell line were treated with the compounds and received a dose of 4 Gy, compared to the reduced number of 175 cells per well for cell testing of the compound alone without radiation. With this alteration, the dose of potential anti-cancer agent on the cells without radiation effectively is ~2.3 times as high as that on the cells receiving irradiation. This factor was determined from previous research within the workgroup of Prof Higgins. All testing proceeded in triplicate with six technical replicates per condition. Complexes *cis*-[$Pt(N_3)_2(PPh_3)$], *cis*-[$Pt(N_3)_2(PEt_3)$], **Pt,Ph[2+3]Au,NO_2** and **Pt,Ph[2+3]Au,CN** were dissolved in dimethyl sulfoxide to form 12 mM stock solutions, whereas due to solubility issues, complexes **Pt,Et[2+3]Au,NO_2** and **Pt,Et[2+3]Au,CN** were dissolved in dimethylformamide to form 12 mM solutions. Analogously to the first round of cell studies, the compounds were added 2 hours prior to and the medium was changed after 18 hours post radiation. The cell cultures were stained with the Alamar Blue dye when displaying 75–80% confluency, which was after seven days for the cell lines H1299 and A549 and after eight days for the cell line HCT116.

Figure 74 depicts a representative overview of the cell viability assays selected from the replicates for the diazidodiphosphine platinum(II) complex *cis*-[$Pt(N_3)_2(PPh_3)$]. The graphs display the cell counts for the three different cell lines with and without irradiation. Contrary to the initial cell studies, cell numbers follow the same trend independent of irradiation for all three cell lines. In all cases the cell count is reduced significantly when the compound is added in concentrations of 5 µM and above.

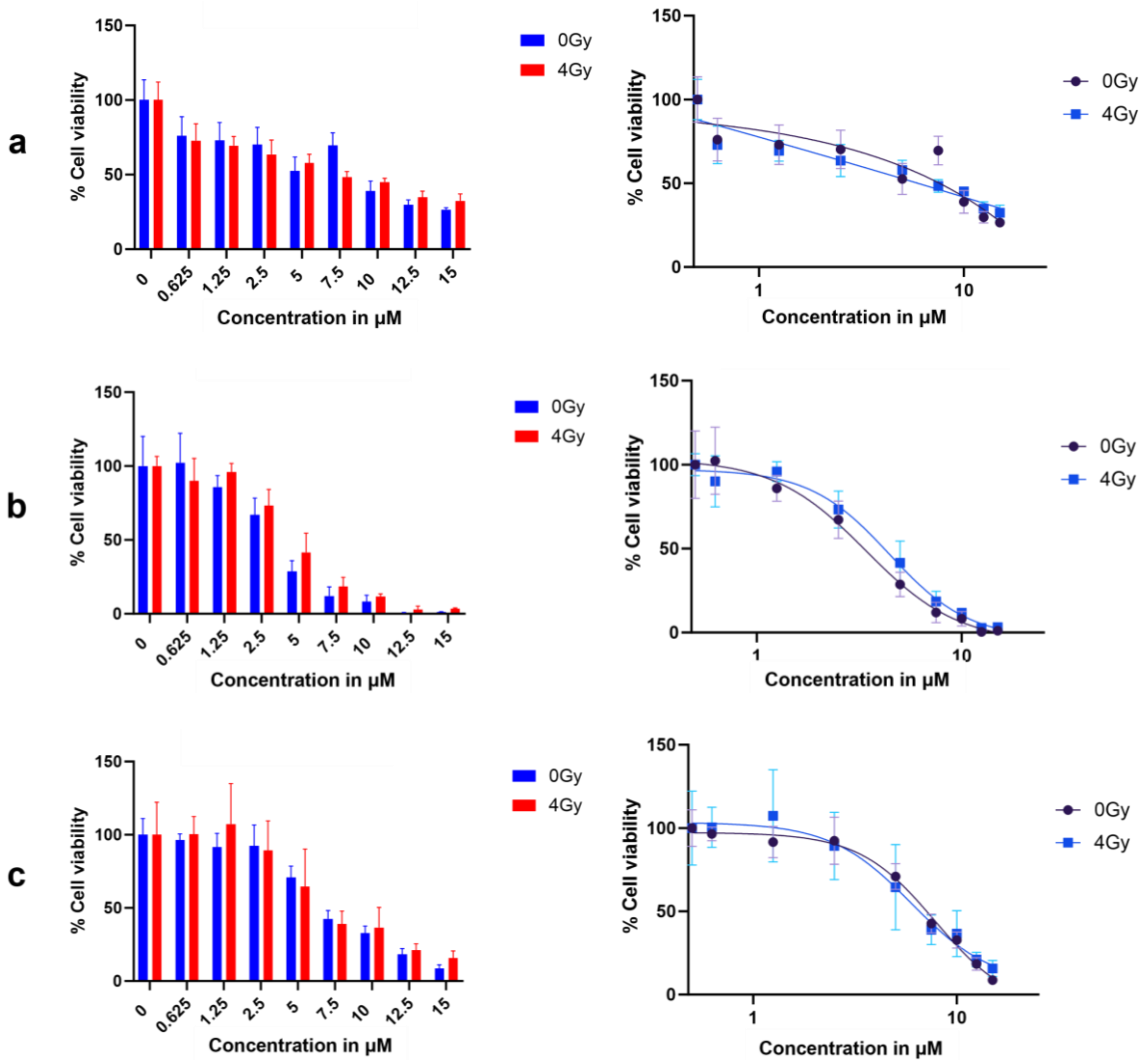

Figure 74: Graphical representation of representative cell counts of the cell viability assays of compound *cis*-[Pt(N$_3$)$_2$(PPh$_3$)] for cell lines A549 (a), H1299 (b) and HCT116 (c) (175 cells for 0 Gy, 400 cells for 4 Gy).

Cell viability studies for the analogous triethylphosphine compound *cis*-[Pt(N$_3$)$_2$(PEt$_3$)] display a similar lack of radiosensitisation in the lung cancer cell lines A549 and H1299. The compound demonstrates little to no toxicity, particularly at concentrations below 10 µM (Figure 75). When added to cells from the colon cancer cell line HCT116, two out of the three replicates suggest a window for activation *via* X-rays. However, even with concentrations as high as

10 µM the cell count is only reduced to 50% (Figure 76).

While both of the diazidodiphosphineplatinum(II) complexes appear to be somewhat toxic, based on the second stage of extensive cell studies, there is no strong indication for successful application as radiosensitisers.

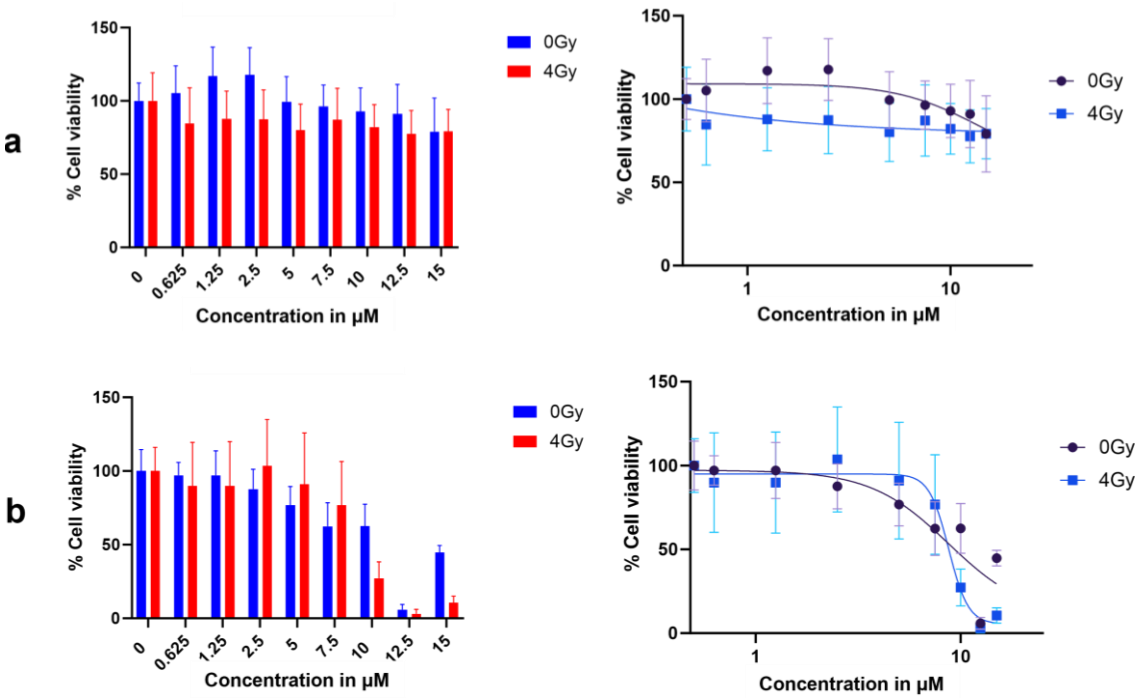

Figure 75: Graphical representation of representative cell counts of the cell viability assays of compound *cis*-[Pt(N$_3$)$_2$(PEt$_3$)] for cell lines A549 (a), H1299 (b) (175 cells for 0 Gy, 400 cells for 4 Gy).

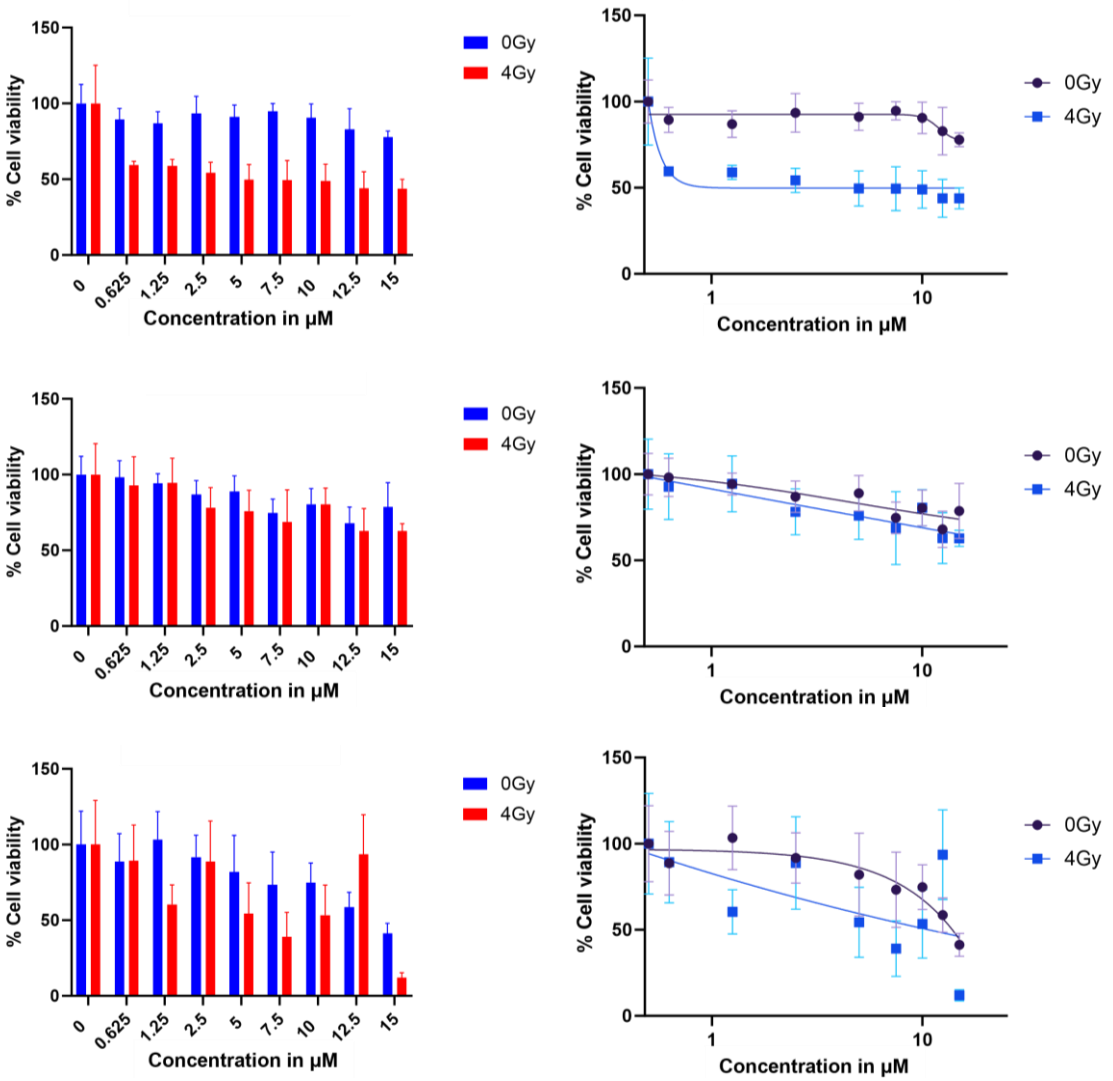

Figure 76: Graphical representation of representative cell counts of the cell viability assays of compound *cis*-[Pt(N$_3$)$_2$(PEt$_3$)] for cell line HCT116 (175 cells for 0 Gy, 400 cells for 4 Gy).

Both platinum(II)-gold(I) cycloaddition products **Pt,Ph[2+3]Au,CN** and **Pt,Et[2+3]Au,CN** with nitrile substituted phenyl rings exhibit no enhanced cytotoxicity upon radiation with 4 Gy for the cell lines A549 and H1299 (Figure 77). The strongest cytotoxic effect is observed in the cancer cell line H1299 with substantially reduced cell numbers with drug concentrations as low as 0.625 µM and near to no viability at concentrations of 2.5 µM. For the cell line A549, the

decrease of living cells is more gradual, resulting in approximately 25% cell viability with concentrations above 10 µM. Addition of the drug to the colon cancer cell line HCT116 suggests a small window of activation *via* X-rays for both compounds **Pt,Ph[2+3]Au,CN** and **Pt,Et[2+3]Au,CN**. Whilst without irradiation the cell viability was detected at ~80%, after a radiation dose of 4 Gy, the cell count drops to <60% at drug concentrations as low as 0.625 µM. However, at higher concentrations, cell-viability is identical independent of radiation.

The cell viability for the three different cancer cell lines behave rather similarly for the other two platinum(II)-gold(I) congeners **Pt,Ph[2+3]Au,NO$_2$** and **Pt,Et[2+3]Au,NO$_2$** (Figure 78). Cell counts are independent of irradiation for the lung cancer cell lines A549 and H1299, with both drugs demonstrating the highest toxicity towards H1299 cells (~10% cell viability at a drug concentration of 5 µM). For the colorectal cancer cell line HCT116, a narrow window of radiosensitivity is displayed for both compounds for concentrations of 0.625–10 µM. Within this range, cell death is increased by approximately 30%.

As a point of reference, analogous cell studies were performed on Cisplatin. Cell death appears to progress near to identically in all three cell lines, with slightly enhanced cytotoxicity within the colon cancer cell line HCT116 (Figure 79).

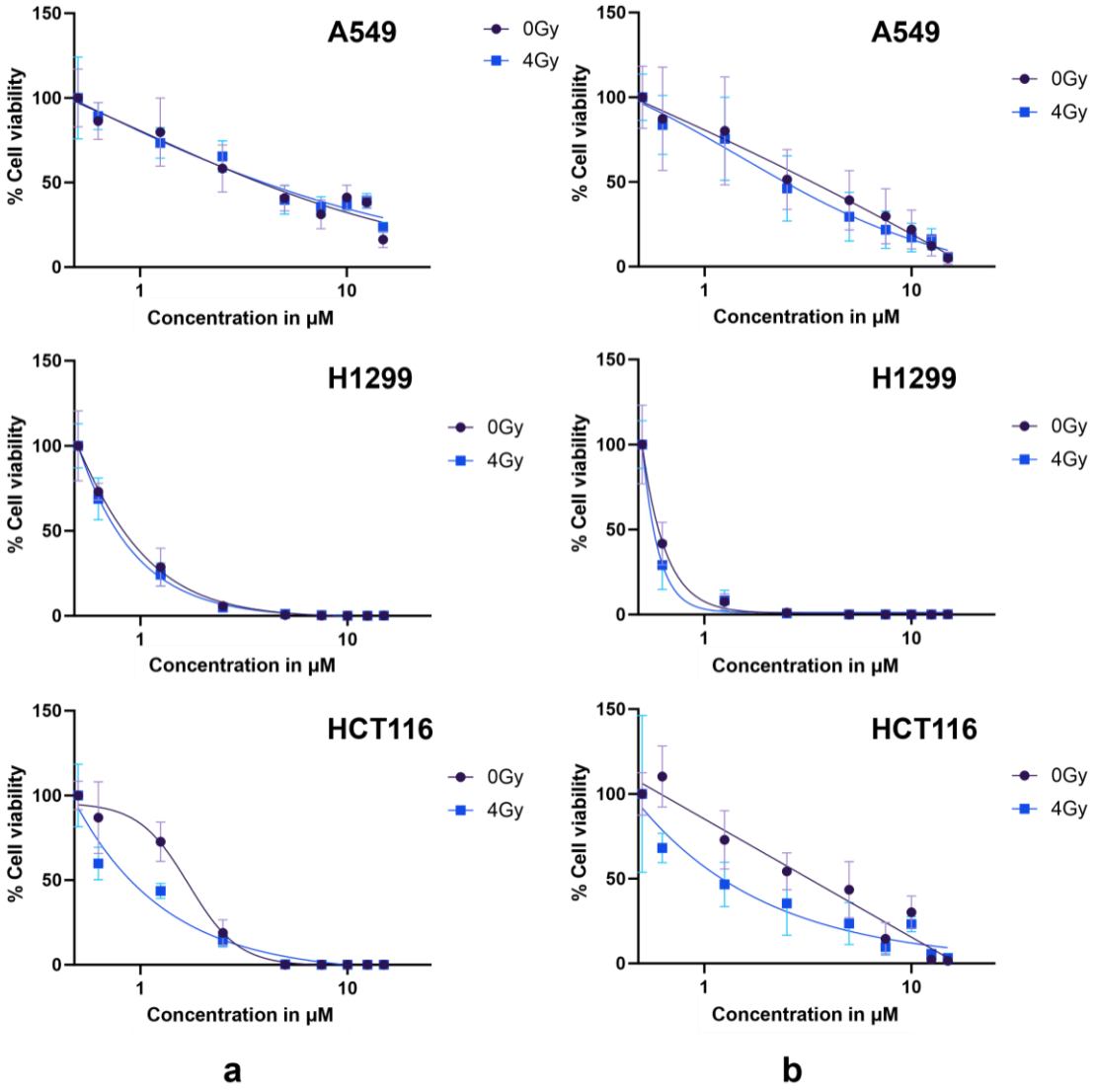

Figure 77: Graphical representation of representative cell counts of the cell viability assays of compounds **Pt,Ph[2+3]Au,CN** (a) and **Pt,Et[2+3]Au,CN** (b) for cell lines A549, H1299 and HCT116 (175 cells for 0 Gy, 400 cells for 4 Gy).

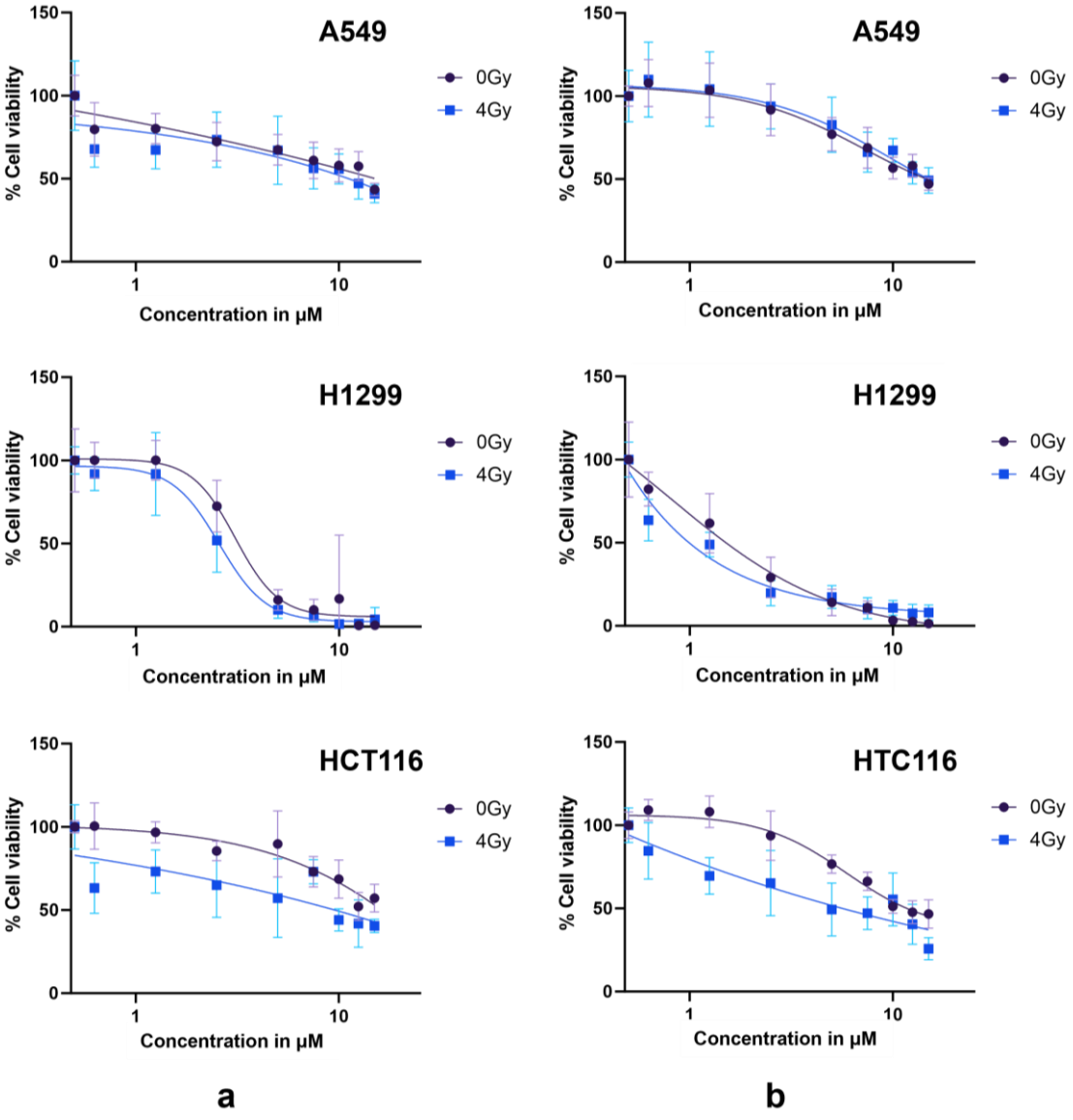

Figure 78: Graphical representation of representative cell counts of the cell viability assays of compounds **Pt,Ph[2+3]Au,NO₂** (a) and **Pt,Et[2+3]Au,NO₂** (b) for cell lines A549, H1299 and HCT116 (175 cells for 0 Gy, 400 cells for 4 Gy).

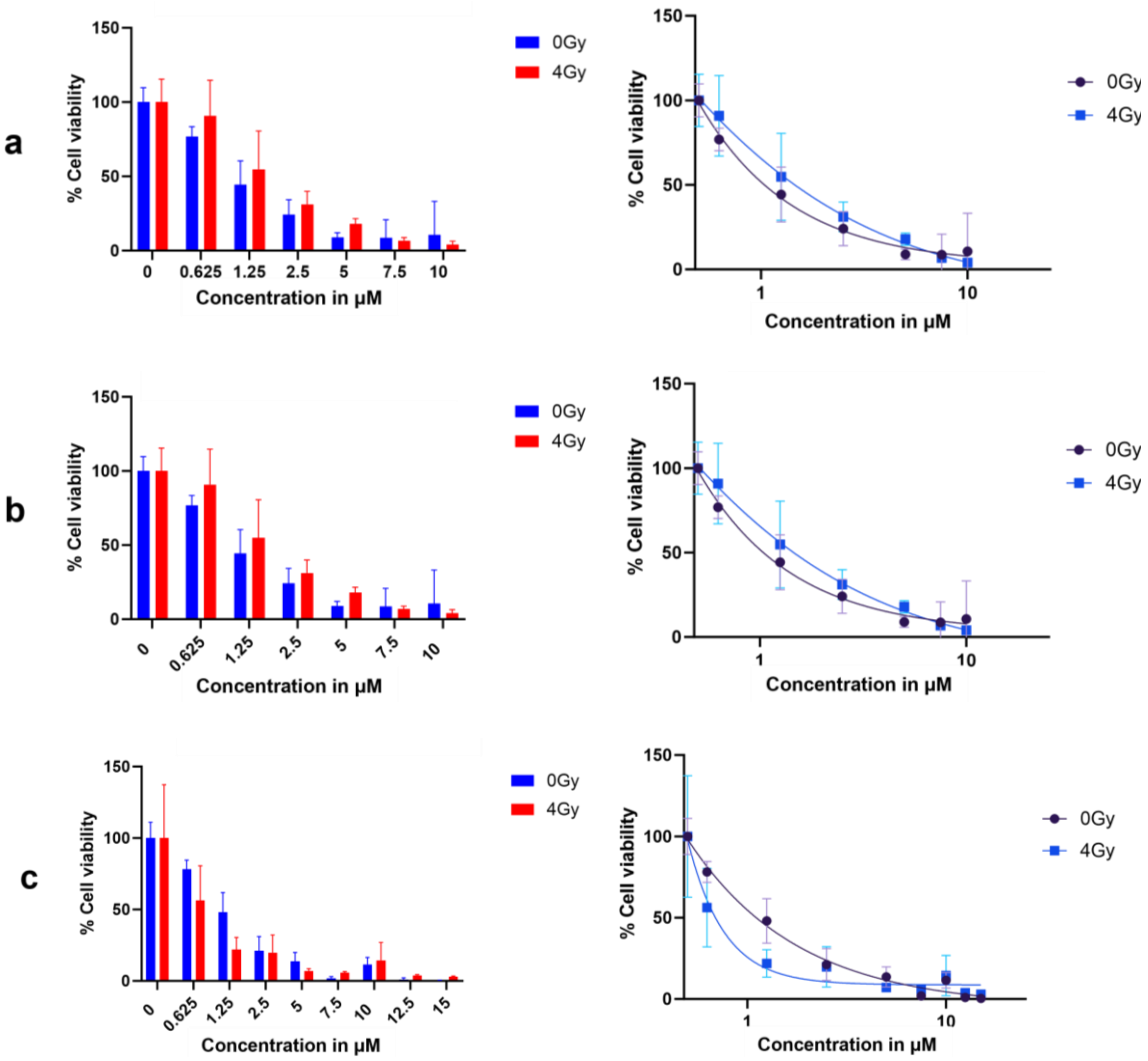

Figure 79: Graphical representation of representative cell counts of the cell viability assays of Cisplatin for cell lines A549 (a), H1299 (b) and HCT116 (c) (175 cells for 0 Gy, 400 cells for 4 Gy).

Comparison of the behaviour of the six platinum-based compounds which were examined during the scope of the second stage of cell testing suggests that combining both the platinum(II) and the gold(I) complexes does indeed yield compounds with enhanced cytotoxicity. The cycloaddition products with nitrile substituted phenyl groups **Pt,Ph[2+3]Au,CN** and **Pt,Et[2+3]Au,CN** display the highest cytotoxicity in general, in particular towards the lung cancer cell line

H1299. *cis*-[Pt(N_3)$_2$(PEt_3)] as well as the four platinum-gold complexes **Pt,Ph[2+3]Au,CN**, **Pt,Et[2+3]Au,CN**, **Pt,Ph[2+3]Au,NO_2** and **Pt,Et[2+3]Au,NO_2** indicate radiosensitising properties when administered to the cell line HCT116 with a radiation dose of 4 G. However, at this point it is not possible to conclude whether this might be due to inherent properties of the cell line and its interactions with the radiation itself, or because the compounds at hand might exhibit higher toxicity specifically towards colorectal cancer cells. Alongside the results with HCR116 cells being the most promising thus far, no activation *via* X-rays was observed for the lung cancer cell lines A549 and H1299. Larger scale screening on alternative colon cancer cell lines will provide more insight into and help determine the scope of this observation.

When comparing the cell viability data from all compounds in the dark from both rounds of cell testing, the change in cell numbers and with that the effective dose of the drugs on the cells needs to be taken into consideration. Within the first stage of cell studies, the compounds overwhelmingly displayed no cytotoxicity in the absence of radiation which suggested low to nil toxicity of the compounds alone towards the cancer cells. This observation might, however, be within the realm of technical error, as reducing the cell numbers per well from 500 to 175 led to a reduction of cell viability, even without radiation. More extensive testing is necessary to be able to determine exactly which is the dominating factor for these distinct results.

Overall the cytotoxicity studies of the six chosen platinum(II) complexes with or without irradiation with X-rays demonstrate small effects on cell numbers with no overwhelming trend. System-to-system variability appears to be significant which

questions reproducibility of the observed results at this stage of testing and demands further studies in order to draw conclusive tendencies in the structure-activity relationship of the platinum(II)-gold(I) complexes with respect to their properties as (radiosensitising) anti-cancer agents.

Probing the behaviour of the complexes under the irradiation with X-rays with a focus on potential structural changes might reveal some of the processes causing a change in cytotoxicity upon irradiation. In addition, the response of the selected compounds to less-invasive blue and green light will be investigated, as these light sources have previously shown potential in the activation of anti-cancer agents (Chapter 1.4).

6. Irradiation of Platinum(II)-Gold(I) Complexes

After investigating the compounds' cytotoxic properties in the presence and absence of X-rays, the behaviour of compounds *cis*-[Pt(N_3)$_2$(PR_3)] (R = Et, Ph), **Pt,Ph[2+3]Au,NO_2**, **Pt,Et[2+3]Au,NO_2**, **Pt,Ph[2+3]Au,CN** and **Pt,Et[2+3]Au,CN** as potential photosensitisers following irradiation with visible light was examined. To this end, the six compounds were irradiated with blue (430–480 nm) and green (480–560 nm) light emitting diodes.[137] Potential structural changes of the complexes were examined *via* UV-visible spectroscopy and mass spectrometry. The samples were each analysed after 10 minutes, 30 minutes, 60 minutes, 120 minutes and 300 minutes irradiation, respectively. All UV-visible spectra were recorded in triplicate at room temperature in 23.4 μM solutions in dimethyl sulfoxide. Considering a possible influence of the solvent on the compounds, dimethyl sulfoxide was chosen due to its application for the majority of the cell studies. The UV-visible spectra of compounds *cis*-[Pt(N_3)$_2$(PR_3)] (R = Et, Ph), **Pt,Ph[2+3]Au,NO_2**, **Pt,Et[2+3]Au,NO_2**, **Pt,Ph[2+3]Au,CN** and **Pt,Et[2+3]Au,CN** recorded in tetrahydrofuran in Chapter 3, revealed strong absorbances in the UV-region around 200–250 nm. As dimethyl sulfoxide itself starts absorbing light at wavelengths below 268 nm, irradiation studies were limited to blue and green light emitting diodes and no UV-light.[138] It is important to note that from the six compounds that were examined, merely compounds **Pt,Ph[2+3]Au,NO_2** and **Pt,Et[2+3]Au,NO_2** display absorbance in regions which suggest they might respond to blue or green light. However, as photoactivation has been reported in

absence of clear absorbance in UV-visible spectra due to energetically low-lying LMCT states,[62] measurements on all six complexes were performed.

A change in the absorbance properties or path of fragmentation could indicate a breakdown of the complexes upon irradiation. The splitting of multi-modal compounds into more active moieties after irradiation would be the first step towards selectively activating the toxic complexes.

Figure 80 depicts the UV-visible spectra of compounds *cis*-[Pt(N_3)$_2$(PR_3)] (R = Et, Ph), **Pt,Ph[2+3]Au,NO$_2$**, **Pt,Et[2+3]Au,NO$_2$**, **Pt,Ph[2+3]Au,CN** and **Pt,Et[2+3]Au,CN** after irradiation with blue light for varying amounts of time. For the diazidodiphosphineplatinum(II) complexes *cis*-[Pt(N_3)$_2$(PR_3)] (R = Et, Ph), the absorbance decreases continuously with increasing irradiation time, this effect being more significant for *cis*-[Pt(N_3)$_2$(PEt_3)]. Comparing the UV-visible spectra of the cycloaddition products **Pt,Ph[2+3]Au,NO$_2$**, **Pt,Et[2+3]Au,NO$_2$**, **Pt,Ph[2+3]Au,CN** and **Pt,Et[2+3]Au,CN**, compounds **Pt,Ph[2+3]Au,CN** and **Pt,Et[2+3]Au,CN** display no clear change of absorbance in dependence of the irradiation time. The spectra of compounds **Pt,Ph[2+3]Au,NO$_2$** and **Pt,Et[2+3]Au,NO$_2$** display absorbance within the region of 362–413 nm. The respective absorbance maxima shift to lower absorbances as well as to shorter wavelengths, intimating a possible structural change to these complexes (Table 19). In particular for **Pt,Ph[2+3]Au,NO$_2$**, the difference of irradiating the compound for 300 minutes compared to 120 minutes displays no further loss of absorbance, however, it causes a shift of the maximum by 51 nm to shorter wavelengths. For both **Pt,Ph[2+3]Au,NO$_2$** and **Pt,Et[2+3]Au,NO$_2$** the hypsochromic shift of the absorbance maxima does not appear until irradiation

times of >120 minutes with no indication of the simultaneous formation of a new species with absorbance at lower wavelengths for shorter irradiation times. This might be due to two subsequent processes occurring within the metal complexes resulting in a change of the structural features demonstrating absorbance.

Table 19: Difference in absorbance and wavelength of the absorbance maxima within 362–413 nm for 23.4 µM solutions of compounds **Pt,Ph[2+3]Au,NO$_2$** and **Pt,Et[2+3]Au,NO$_2$** under irradiation with blue light

	***Δ* Absorbance**	***Δ* Wavelength**
Pt,Ph[2+3]Au,NO$_2$	0.29	51 nm
Pt,Et[2+3]Au,NO$_2$	0.43	41 nm

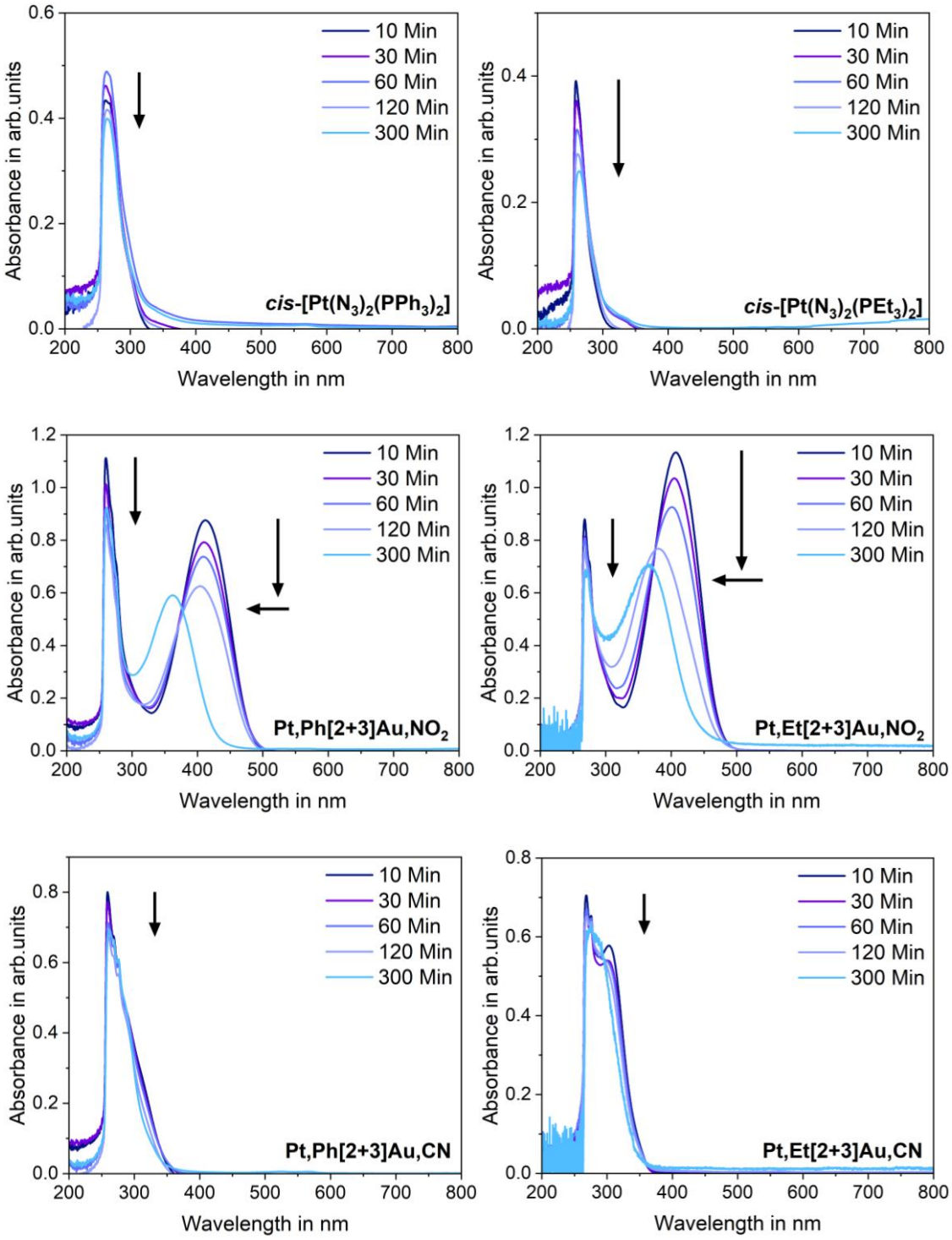

Figure 80: UV-visible spectra (DMSO, 23 °C) of compounds *cis*-[Pt(N$_3$)$_2$(PPh$_3$)], *cis*-[Pt(N$_3$)$_2$(PEt$_3$)], **Pt,Ph[2+3]Au,NO$_2$**, **Pt,Et[2+3]Au,NO$_2$**, **Pt,Ph[2+3]Au,CN** and **Pt,Et[2+3]Au,CN** after irradiation with blue light for varying amounts of time.

Tracking the mass spectra of the complexes after each irradiation step and comparing the detected masses, could provide insight into potential structural changes following irradiation which are leading to the change in the UV-visible spectra.

Both diazidodiphosphine platinum(II) complexes *cis*-[Pt(N_3)$_2$(PR_3)] (R = Et, Ph) display fragments containing platinum in the mass spectra after irradiation with blue light for 300 minutes. The main fragment for *cis*-[Pt(N_3)$_2$(PPh_3)] is found at 761 Da, which corresponds to $[M - N_3]^+$ (Figure 81, top). This fragment is consistently high throughout all of the spectra independent of the time points. Further, it was detected in the mass spectrum of the parent compounds, albeit in lower concentrations. Fragment $[M - N_3]^+$ as the main platinum-congener after irradiation could indicate an enhanced cleavage of the azido ligand induced by the blue light, leading to a decrease in absorbance in the UV-visible spectra.

Compound *cis*-[Pt(N_3)$_2$(PEt_3)] behaves similarly to its triphenylphosphine analogue. The two main fragments containing platinum after irradiating the complex with blue light for 300 minutes were detected at 473 Da and 931 Da. The mass at 473 Da corresponds to $[M - N_3]^+$, which was observed as well for the parent compound in the absence of irradiation. The fragment at 931 Da did not appear until irradiation times of 300 minutes, which suggests it could be a result of interactions with the light, however, it was not possible to assign the mass unambiguously.

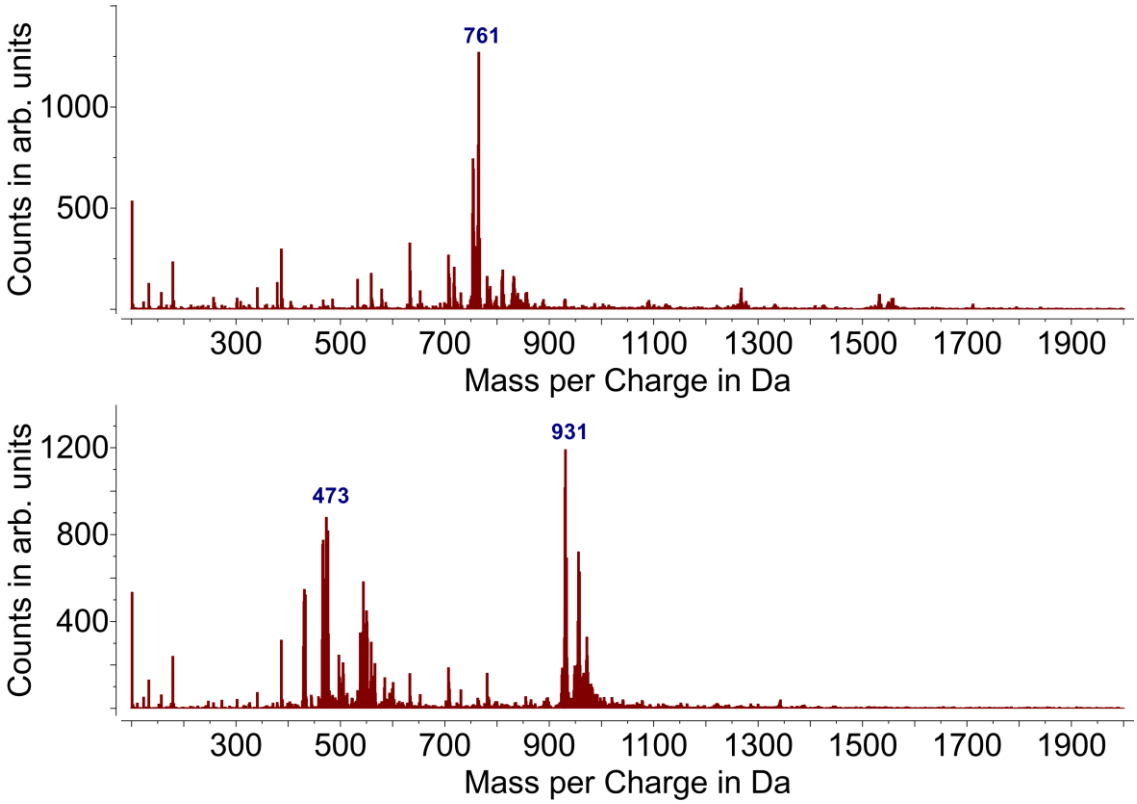

Figure 81: Mass spectra (DMSO, 23 °C) of *cis*-[Pt(N$_3$)$_2$(PPh$_3$)] (top) and *cis*-[Pt(N$_3$)$_2$(PEt$_3$)] (bottom) after irradiation with blue light for 300 minutes.

The mass spectra of **Pt,Ph[2+3]Au,NO$_2$** confirm the breakdown of the parent compound. After 10 minutes irradiation, the main peak is found at 1007 Da which corresponds to fragment $[M + 2H]^{2+}$ (Figure 82). With increasing irradiation times, a new peak appears at 1409 Da. The isotypic pattern suggests this fragment does not contain platinum, however, with a mass this large, and based on the peak patterns identified in the characterisation of the neat compounds, it is likely that the mass at 1409 Da includes gold. Without further investigations, it is not feasible to assign this fragment unambiguously. The mass spectra confirm that irradiating **Pt,Ph[2+3]Au,NO$_2$** with blue light breaks down the bi-metallic complex with the largest structural change occurring between irradiation times of

120 minutes and 300 minutes. Cleavage of the gold-containing fragments from the platinum(II) centre will cause a significant change in the distribution of electron density, which in turn results in a shift of the absorbance observed in the UV-visible spectra.

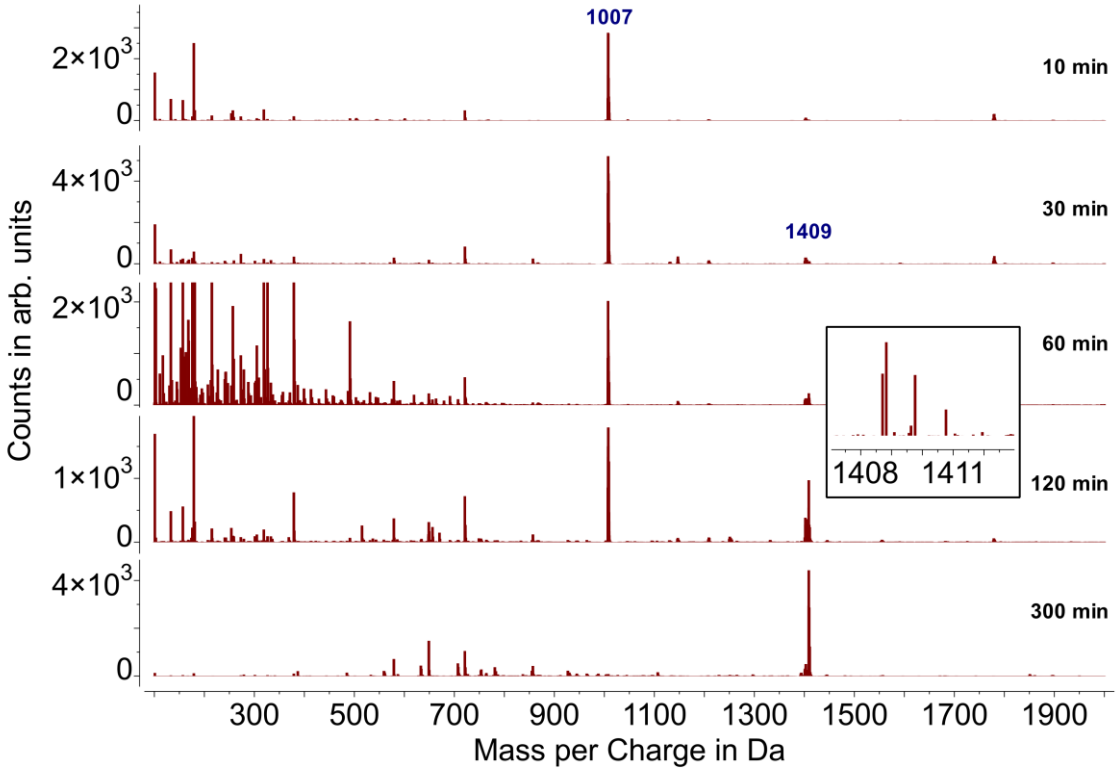

Figure 82: Mass spectra (DMSO, 23 °C) of **Pt,Ph[2+3]Au,NO$_2$** after irradiation with blue light for varying amounts of time. Inset displays the peak pattern of the fragment at 1409 Da.

Compound **Pt,Et[2+3]Au,NO$_2$** demonstrates a similar behaviour to **Pt,Ph[2+3]Au,NO$_2$**. The two main fragments that appear at 864 Da ($[M + 2H]^{2+}$) and 1726 Da ($[M + H]^{+}$) respectively, both correspond to the parent compound prior to cleavage of any moieties (Figure 83). With prolonged irradiation times,

these fragments disappear while various fragments at lower masses and without platinum appear. The fragment at 656 Da matches a cleaved gold moiety on which the nitro group has been reduced to an amine group together with a potassium cation. This mass is the only indication in both of the cycloaddition products containing nitro groups, which suggests a reduction of these has occurred.

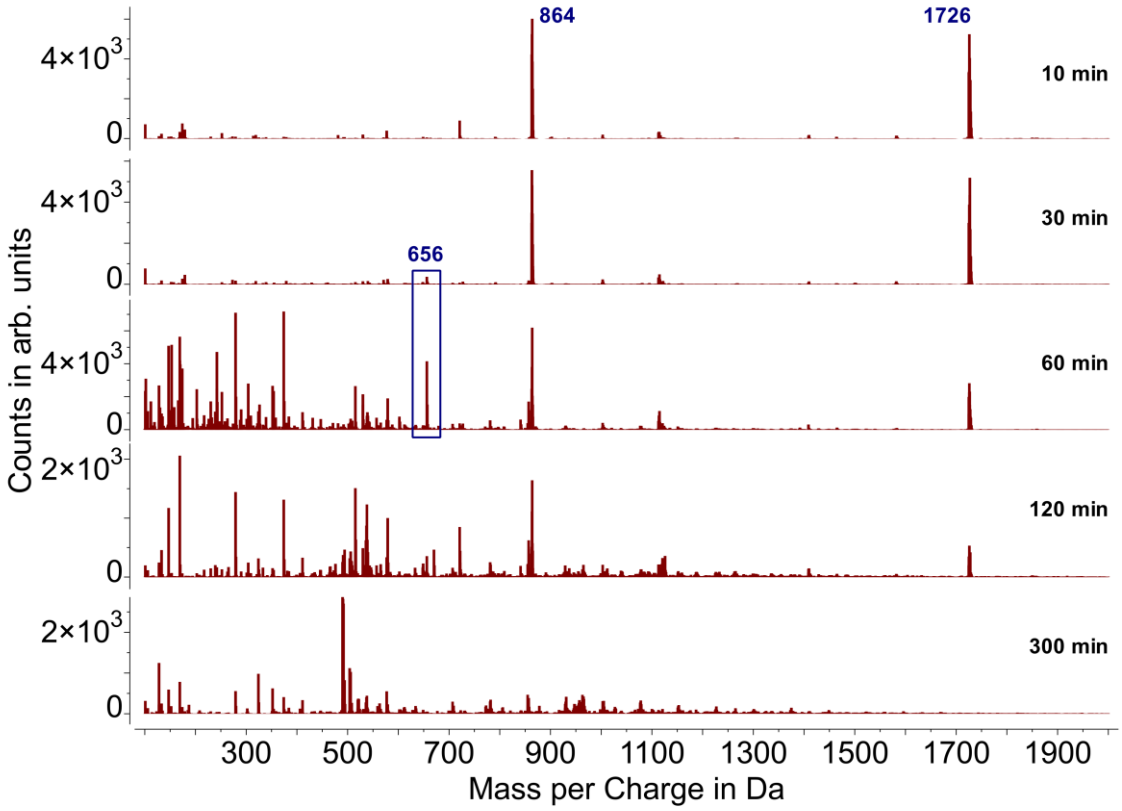

Figure 83: Mass spectra (DMSO, 23 °C) of **Pt,Et[2+3]Au,NO$_2$** after irradiation with blue light for varying amounts of time.

Figure 84 depicts the mass spectra which were recorded for **Pt,Ph[2+3]Au,CN** without irradiation and after irradiating the sample with blue light. Despite the UV-

visible spectra suggesting little to no strong interactions between the compound and the light source, a comparison of the masses in the spectra indicate structural change. The two main fragments of the parent compound in the mass spectrum of neat **Pt,Ph[2+3]Au,CN** appear at 988 Da and 1975 Da, and can be assigned to $[M + 2H]^{2+}$ and $[M + H]^{+}$, respectively. Both of these fragments are detected significantly less until complete disappearance upon irradiation of the compound. In contrast, the fragment indicating the cleavage of gold-containing fragments of **Pt,Ph[2+3]Au,CN** at 721 Da ($[Au(PPh_3)_2]^{+}$) increase under irradiation of the complex and suggest that breakdown of the compound is promoted through the interaction with blue light.

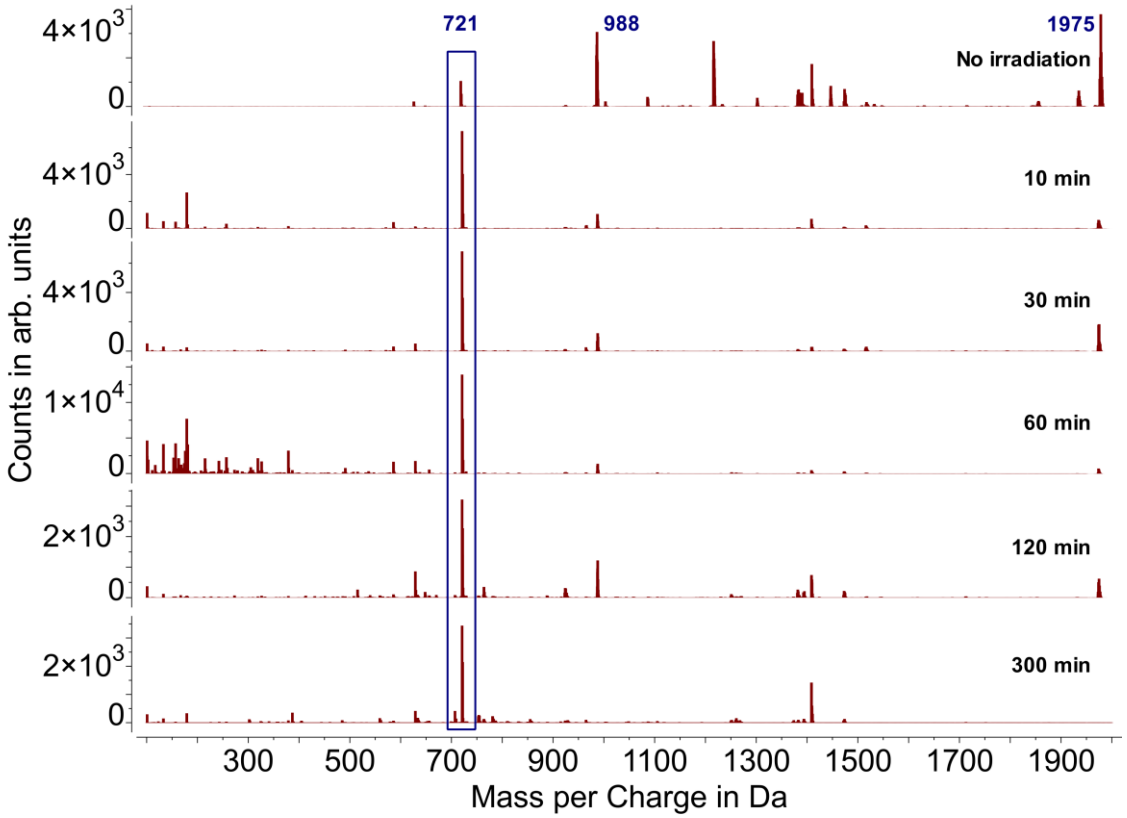

Figure 84: Mass spectra (DMSO, 23 °C) of **Pt,Ph[2+3]Au,CN** after irradiation with blue light for varying amounts of time.

In analogous manner to **Pt,Ph[2+3]Au,CN**, the cycloaddition product **Pt,Et[2+3]Au,CN** demonstrates fewer fragments corresponding to the parent compound as a consequence of irradiation (Figure 85). Counts for the fragments at 844 Da ($[M + 2H]^{2+}$) and at 1686 Da ($[M + H]^{+}$) both reduce with longer irradiation times, however the structural changes appear to be more gradual compared to the triphenylphosphine analogue. With longer exposure times to the blue light source, the mass spectra become increasingly complex, indicating the breakdown of the complex and consequently the detection of new fragments. No significant fragments displaying the typical isotopic peak pattern for platinum

were identified and the assignment of the fragments was not possible without further investigation.

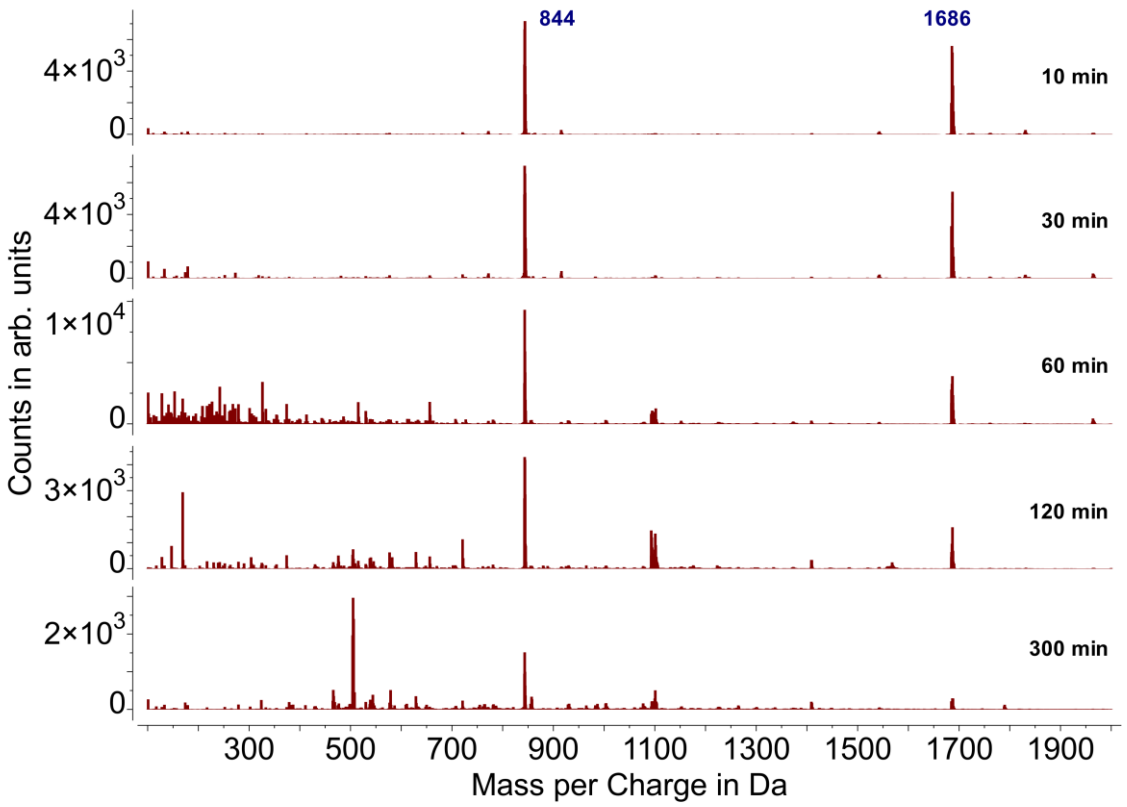

Figure 85: Mass spectra (DMSO, 23 °C) of **Pt,Et[2+3]Au,CN** after irradiation with blue light for varying amounts of time.

The absorbance behaviour of compounds *cis*-[Pt(N$_3$)$_2$(PR$_3$)] (R = Et, Ph), **Pt,Ph[2+3]Au,NO$_2$**, **Pt,Et[2+3]Au,NO$_2$**, **Pt,Ph[2+3]Au,CN** and **Pt,Et[2+3]Au,CN** appears to be similar under irradiation with green light (Figure 86). Whilst the diazido complexes as well as the nitrile substituted platinum(II)-gold(I) products display a minor reduction in the absorbance maxima around 268–305 nm, compounds **Pt,Ph[2+3]Au,NO$_2$** and **Pt,Et[2+3]Au,NO$_2$** exhibit more prominent

changes in their absorbance. With increased exposure to the green light, the absorbance maxima decrease as well as being shifted to lower wavelengths, albeit the effect appears to be less strong compared to irradiation with blue light (Table 19 and Table 20). For **Pt,Ph[2+3]Au,NO_2**, the largest difference is recorded after an irradiation time of 30 minutes. In contrast, moving from an irradiation time of 120 minutes to 300 minutes leads to the most significant shift both in absorbance and wavelength for **Pt,Et[2+3]Au,NO_2**. This suggests that a structural change from triphosphine to triethyl groups bound to the platinum(II) centre, modifies the compound's response under green light, effectively requiring larger dosages.

Table 20: Difference in absorbance and wavelength of the absorbance maxima within 396–413 nm for 23.4 µM solutions of compounds **Pt,Ph[2+3]Au,NO_2** and **Pt,Et[2+3]Au,NO_2** under irradiation with green light

	Δ Absorbance	**Δ Wavelength**
Pt,Ph[2+3]Au,NO_2	0.33	16 nm
Pt,Et[2+3]Au,NO_2	0.25	13 nm

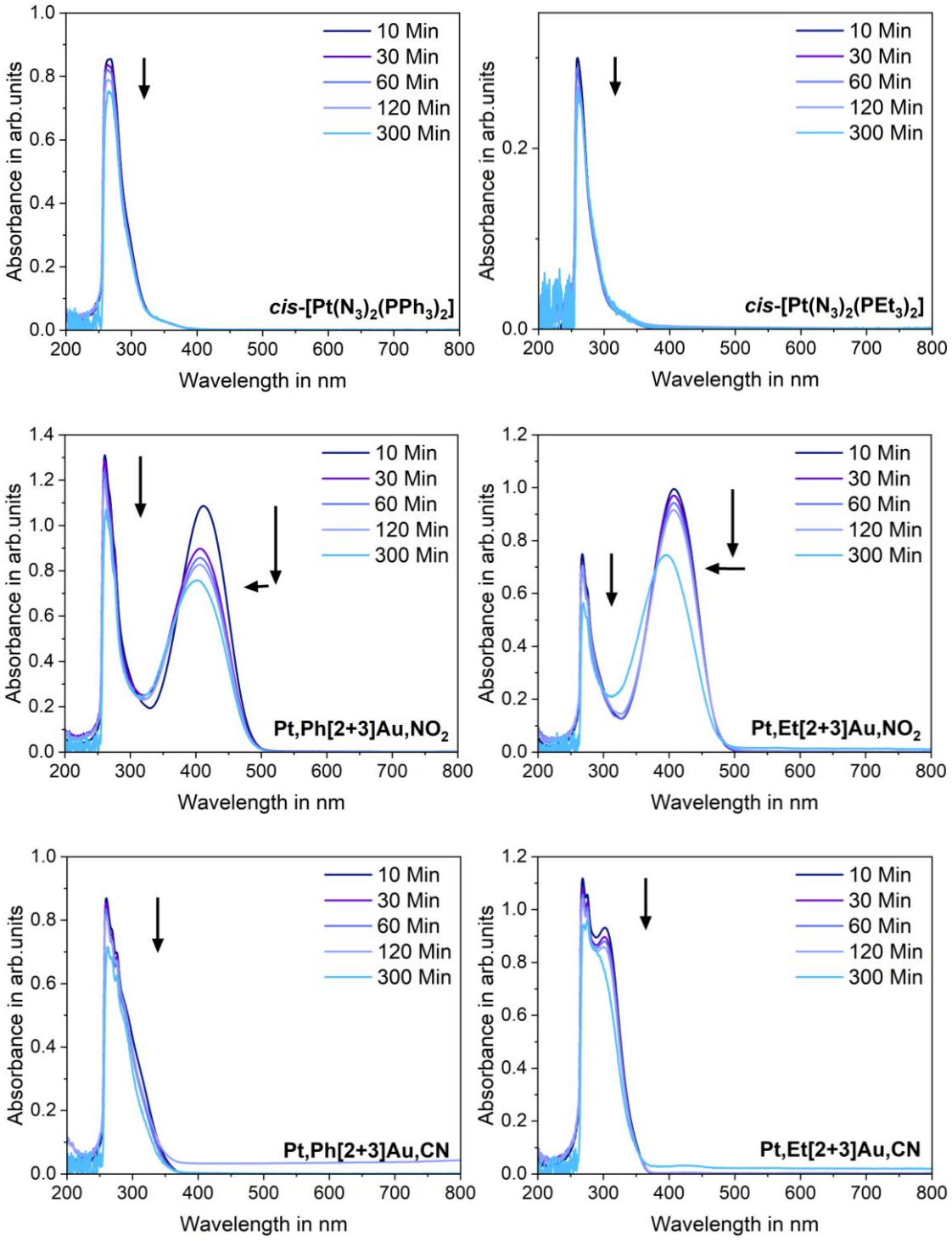

Figure 86: UV-visible spectra (DMSO, 23 °C) of compounds *cis*-[Pt(N$_3$)$_2$(PPh$_3$)], *cis*-[Pt(N$_3$)$_2$(PEt$_3$)], **Pt,Ph[2+3]Au,NO$_2$**, **Pt,Et[2+3]Au,NO$_2$**, **Pt,Ph[2+3]Au,CN** and **Pt,Et[2+3]Au,CN** after irradiation with green light for varying amounts of time.

The mass spectra recorded for *cis*-[Pt(N_3)$_2$(PPh_3)] after irradiation with green light yield inconclusive results. The spectra after 30 minutes and 300 minutes do not display any platinum compounds, suggesting the breakdown of *cis*-[Pt(N_3)$_2$(PPh_3)] (Figure 87). However, the spectra after 60 minutes and 120 minutes include the platinum fragment at 761 Da corresponding to $[M - N_3]^+$, which is in line with the absorbance observed in the UV-visible spectra, which suggested no major structural differences to *cis*-[Pt(N_3)$_2$(PPh_3)] over the course of time. Considering the inconsistencies, no final conclusions on structural changes of the complex can be drawn from these measurements.

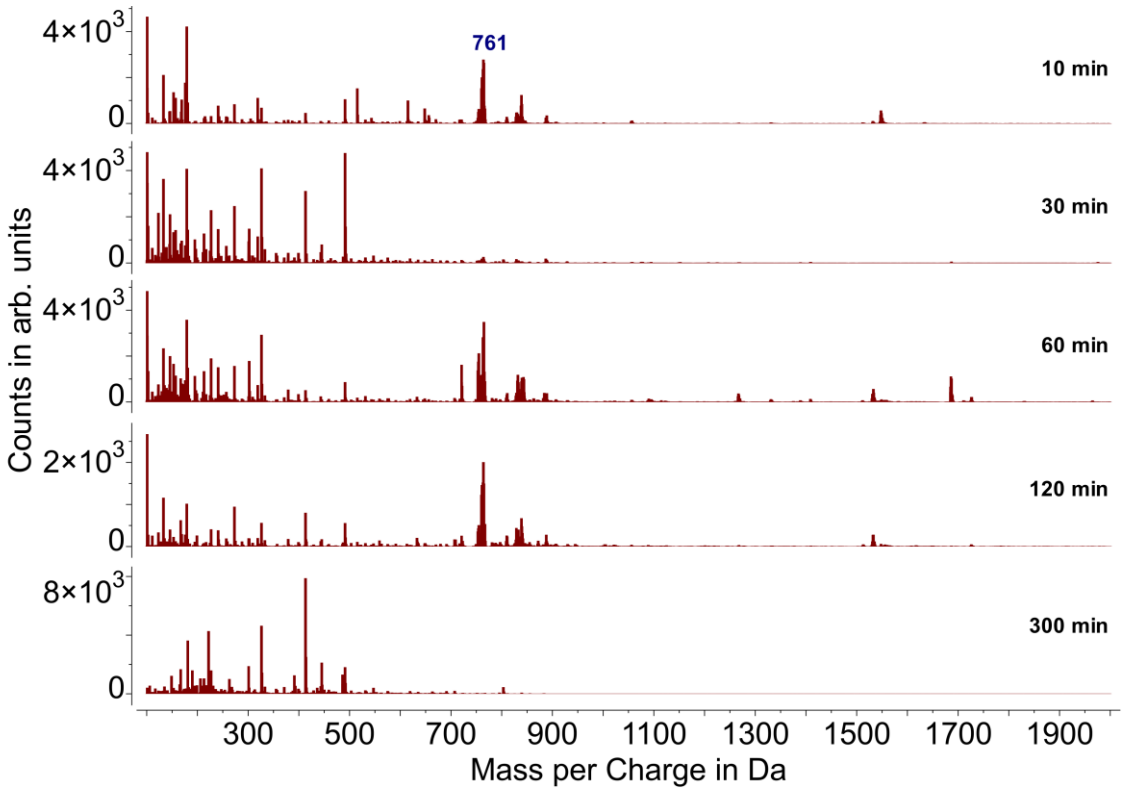

Figure 87: Mass spectra (DMSO, 23 °C) of *cis*-[Pt(N_3)$_2$(PPh_3)] after irradiation with green light for varying amounts of time.

Comparison of the mass spectra of *cis*-[Pt(N_3)$_2$(PEt_3)] with and without irradiation with a green light source, show a clear change in the fragments upon irradiation. The two main fragments relating to the neat parent compound appear at 473 Da ([M −N_3]$^+$) and 988 Da ([2M −N_3]$^+$) (Figure 88). Both of these are reduced significantly in counts after only 10 minutes of irradiation, with various new fragments without platinum appearing at lower masses. These recordings indicate that the irradiation leads to the fragmentation of *cis*-[Pt(N_3)$_2$(PEt_3)], however, this contradicts the observations in the UV-visible spectra, which did not suggest any major structural changes.

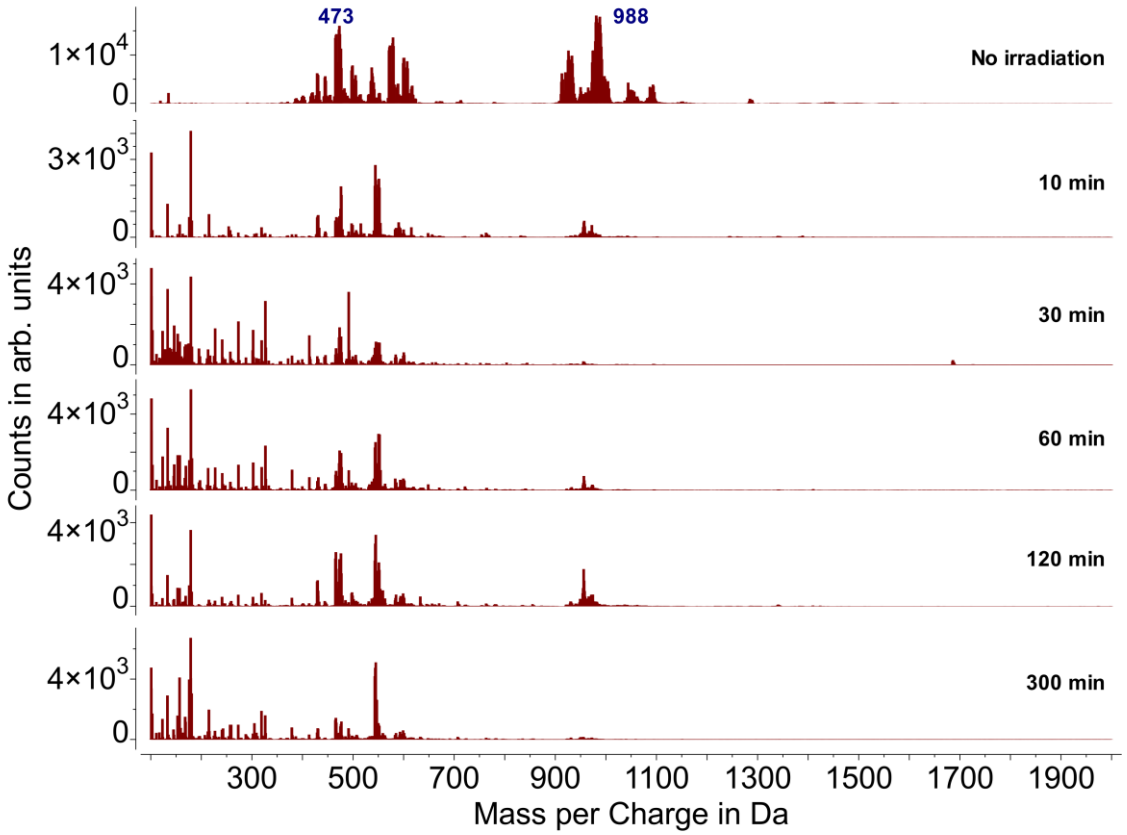

Figure 88: Mass spectra (DMSO, 23 °C) of *cis*-[Pt(N_3)$_2$(PEt_3)] after irradiation with green light for varying amounts of time.

Compared to the gradual changes of **Pt,Ph[2+3]Au,NO$_2$** incurred by blue light, the mass spectra after irradiation with green light reveals the rapid breakdown of the bimetallic complex. Fragment $[M + 2H]^{2+}$ (1007 Da) is observed significantly less upon irradiation of 10 minutes (Figure 89). Concurrent with this, the counts for the gold moiety $[Au(PPh_3)_2]^+$ (721 Da) increase with exposure of the complex to the green light. An increase of fragments at lower masses with no traces of platinum, support the breakdown of the compound which is in agreement with the change of absorbance and wavelength reported from the UV-visible spectra.

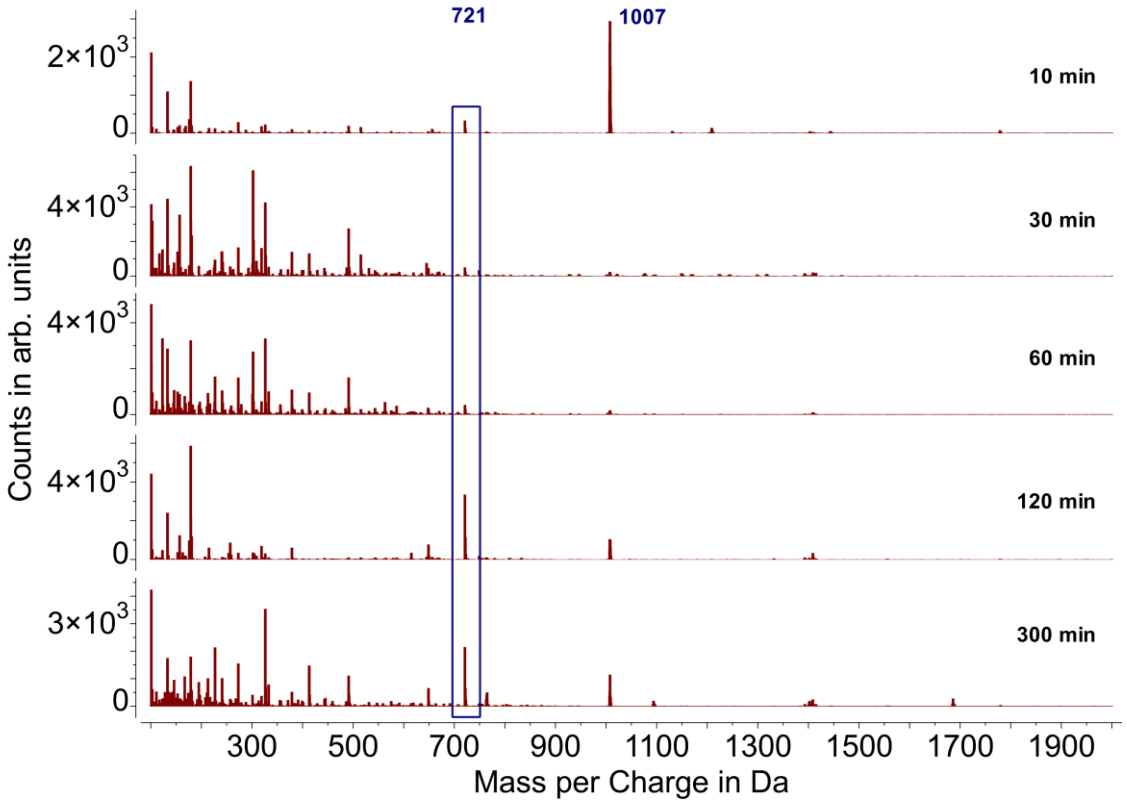

Figure 89: Mass spectra (DMSO, 23 °C) of **Pt,Ph[2+3]Au,NO$_2$** after irradiation with green light for varying amounts of time.

The behaviour of **Pt,Et[2+3]Au,NO$_2$** under green light appears to be somewhat similar to that under blue light. The structural changes resulting in the breakdown of the parent compound and the disappearance of the fragments at 864 Da ($[M + 2H]^{2+}$) and 1726 Da ($[M + H]^{+}$) are gradual, and do not occur until a prolonged irradiation time of 300 minutes, albeit the counts for these fragments appear to fluctuate in the spectra at earlier time points. A substantial structural change occurring in the last irradiation step confirms the observations within the UV-visible spectra for **Pt,Et[2+3]Au,NO$_2$** under green light.

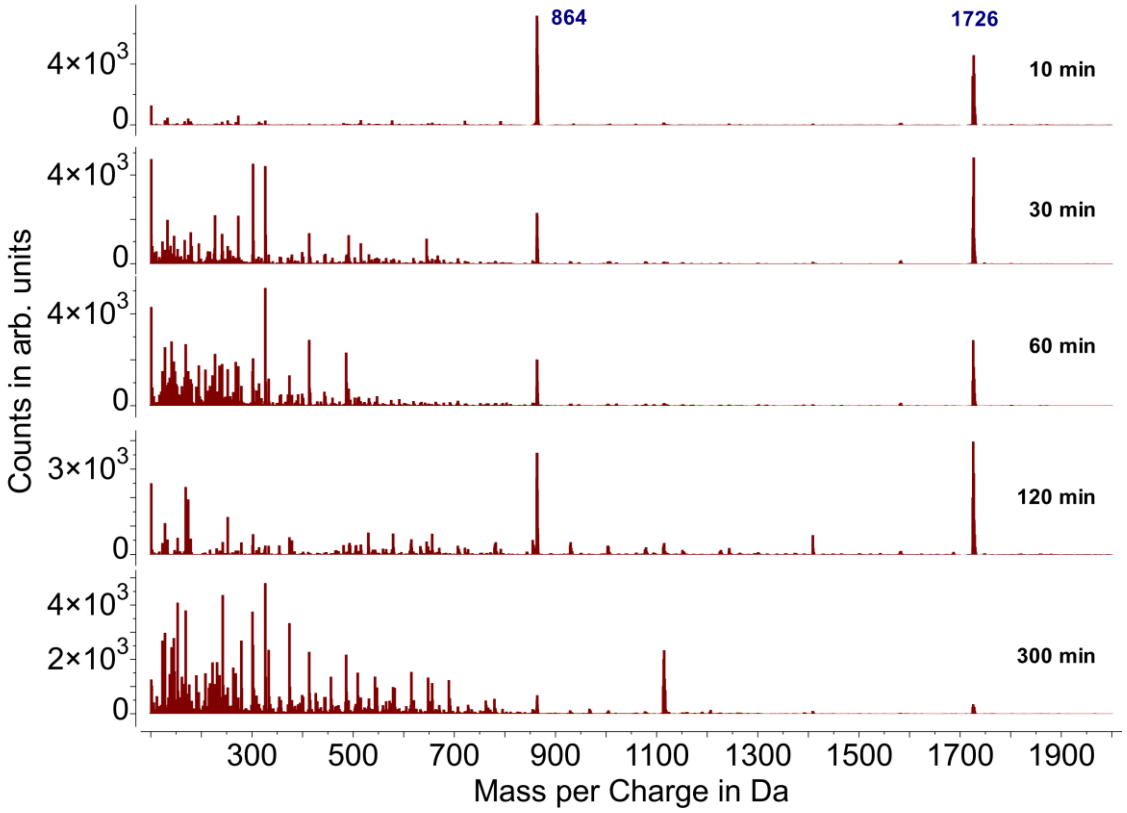

Figure 90: Mass spectra (DMSO, 23 °C) of **Pt,Et[2+3]Au,NO$_2$** after irradiation with green light for varying amounts of time.

For both nitrile substituted cycloaddition products **Pt,Ph[2+3]Au,CN** and **Pt,Et[2+3]Au,CN**, the UV-visible spectra indicated little to no structural changes incurred by irradiating the compounds with green light. For **Pt,Et[2+3]Au,CN** the mass spectra after 10 minutes and after 300 minutes, respectively, display high counts of the fragments at 844 Da ($[M + 2H]^{2+}$) and 1686 Da ($[M + H]^{+}$), both corresponding to adducts of the net compound with protons (Figure 91). After 300 minutes, many more fragments were detected, however, none of which suggest directed breakdown of the complex.

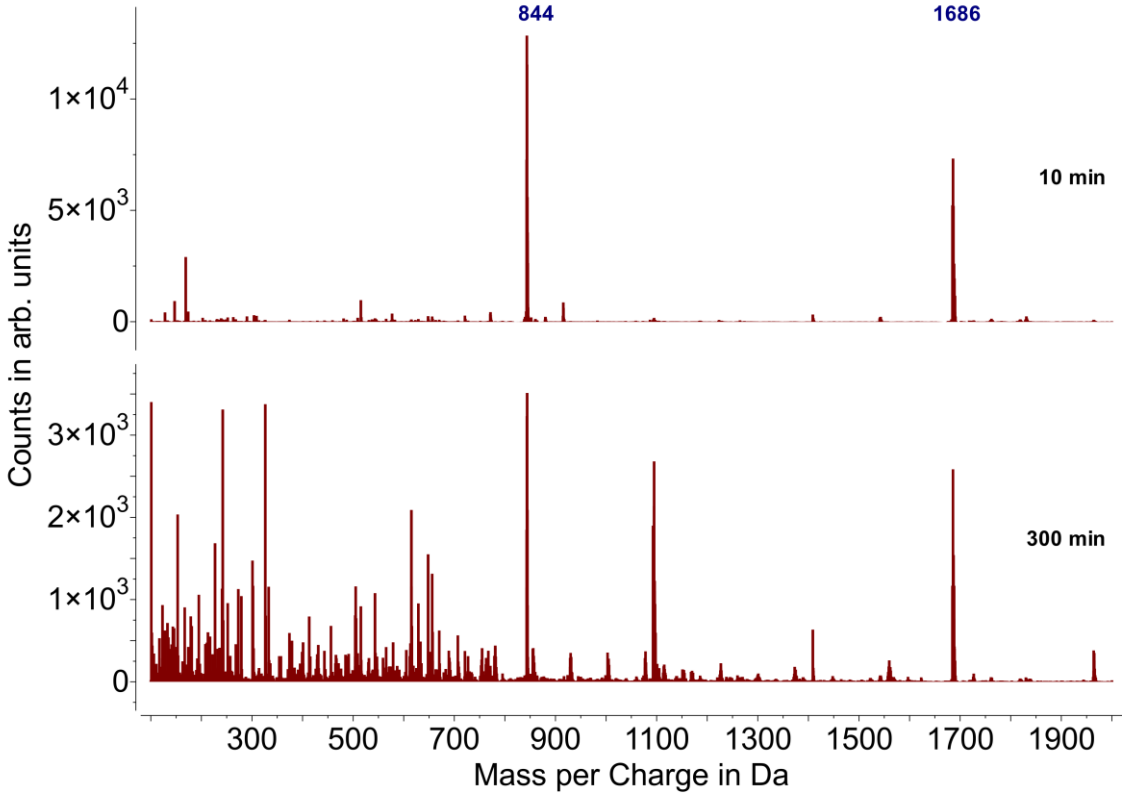

Figure 91: Mass spectra (DMSO, 23 °C) of **Pt,Et[2+3]Au,CN** after irradiation with green light for varying amounts of time.

Contrary to this and similar to the behaviour of **Pt,Et[2+3]Au,CN** under the irradiation of blue light, the mass spectra of the triphenylphosphine analogue display a high count of the fragment $[Au(PPh_3)_2]^+$ upon irradiation with green light (Figure 92). This dominance of this fragment in the spectra together with the loss of fragments relating to the parent compound such as $[M + 2H]^{2+}$ at 988 Da and $[M + H]^+$ at 1976 Da, support the cleavage of the gold moiety of the cycloaddition product as a result of irradiation with green light, explaining the change in absorbance behaviour observed in the UV-visible spectra.

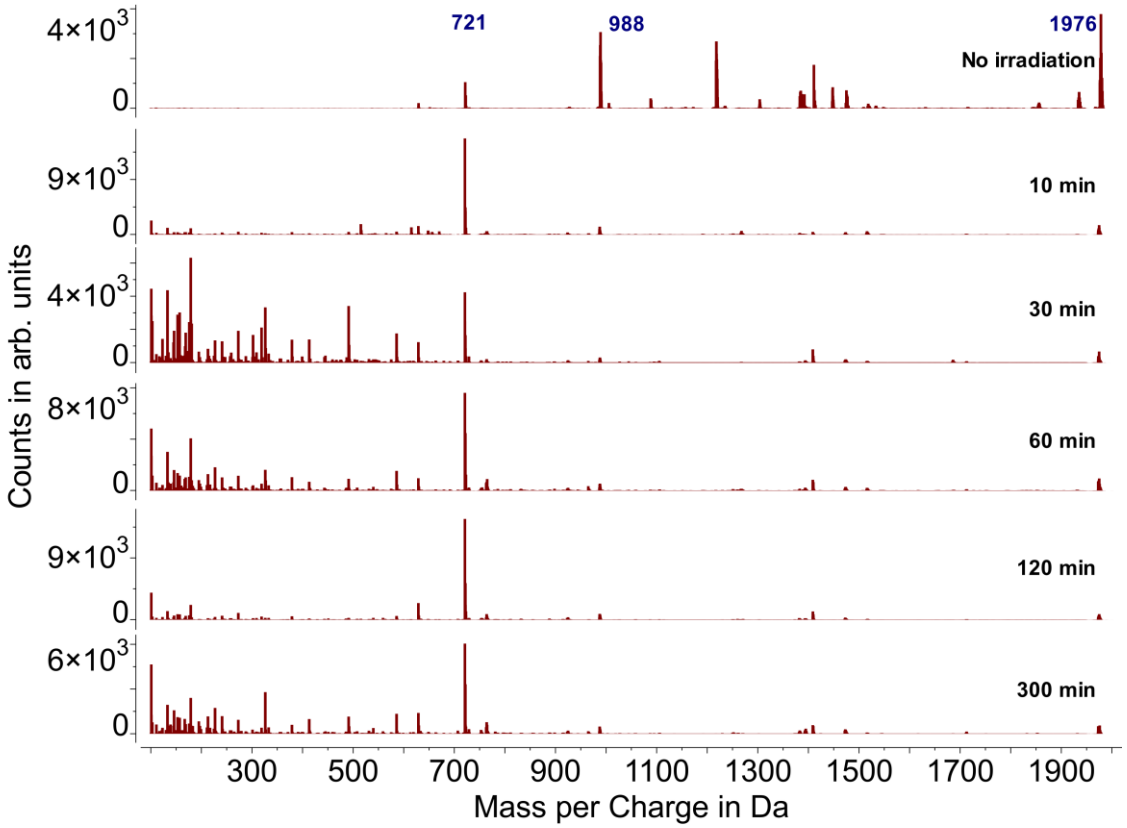

Figure 92: Mass spectra (DMSO, 23 °C) of **Pt,Ph[2+3]Au,CN** after irradiation with green light for varying amounts of time.

Following on from exploring the behaviour of the six metal complexes under the irradiation of blue and green light, further investigations were carried out aimed at elucidating structural changes stemming from X-rays. As a first approach, the complexes were each exposed to a radiation dose of 40 Gy in 12 mM solutions. In order to emulate the conditions chosen for the cell studies, in addition, solutions of a drug concentration of 23.4 µM were subjected to 4 Gy. Taking the different magnitudes of the irradiation dosages and compound concentrations into consideration, it is worth noting, that whilst 40 Gy is a very high dosage, the ratio between the energy and the molecular complexes is more concentrated for the samples which received a dose of 4 Gy. Solvents were identical to the respective solvents during the cytotoxicity studies: Solutions of *cis*-[Pt(N_3)$_2$(PR_3)] (R = Et, Ph), **Pt,Ph[2+3]Au,NO_2** and **Pt,Ph[2+3]Au,CN** were prepared in dimethyl sulfoxide, whereas **Pt,Et[2+3]Au,NO_2** and **Pt,Et[2+3]Au,CN** were dissolved in dimethyl formamide. The compounds were monitored *via* UV-visible spectroscopy and mass spectrometry.

Figure 93 displays the UV-visible spectra of the six compounds after irradiation with varying dosages of X-rays. Comparison of the two diazidoplatinum(II) complexes reveals a significant loss of absorbance for *cis*-[Pt(N_3)$_2$(PPh_3)] with merely a minor reduction of absorbance for *cis*-[Pt(N_3)$_2$(PEt_3)] after being subjected to the X-rays. The responses to the irradiation for the platinum-gold congeners are similar to each other, with no clear trend between the platinum centres substituted with triphenylphosphine or triethylphosphine ligands. All four cycloaddition products demonstrate less absorbance upon irradiation, albeit the effect is significantly stronger when **Pt,Ph[2+3]Au,CN** and **Pt,Et[2+3]Au,CN** receive dosages of 40 Gy.

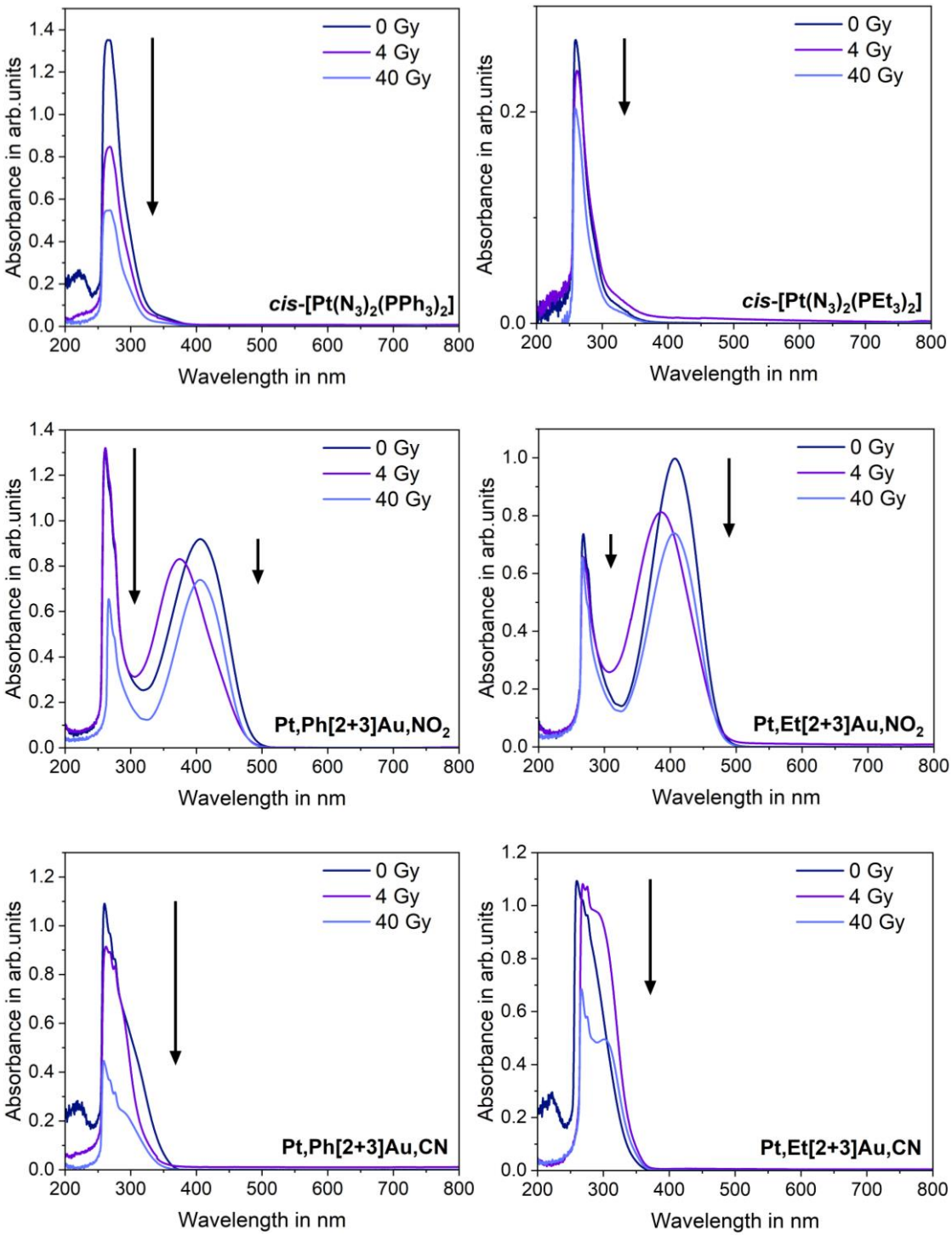

Figure 93: UV-visible spectra (DMSO, 23 °C) of compounds *cis*-[$Pt(N_3)_2(PPh_3)$], *cis*-[$Pt(N_3)_2(PEt_3)$], **Pt,Ph[2+3]Au,NO$_2$**, **Pt,Et[2+3]Au,NO$_2$**, **Pt,Ph[2+3]Au,CN** and **Pt,Et[2+3]Au,CN** after irradiation with varying dosages of X-rays.

Performing mass spectrometry of the respective compounds after the irradiation helped to identify any structural changes contributing to the differences in the absorbance behaviour. The mass spectra for *cis*-[Pt(N_3)$_2$(PPh_3)] display the loss of two of the main fragments: $[M + K]^+$ at 842 Da and $[2M – N_3]^+$ at 1564 Da (Figure 94). However, substantial concentrations of the fragment $[M – N_3]^+$ with a mass of 761 Da were detected even after irradiation. This observation appears to be independent of the radiation dosage. The differences in the spectra suggest an interaction between the compounds and the X-rays resulting in promoted cleavage of the azido ligand from the parent compound. In comparison, counts for the analogous fragments in *cis*-[Pt(N_3)$_2$(PEt_3)] such as $[M – N_3]^+$ at 473 Da and $[2M – N_3]^+$ at 988 Da reduce significantly for both 4 Gy and 40 Gy at the respective concentrations (Figure 95).

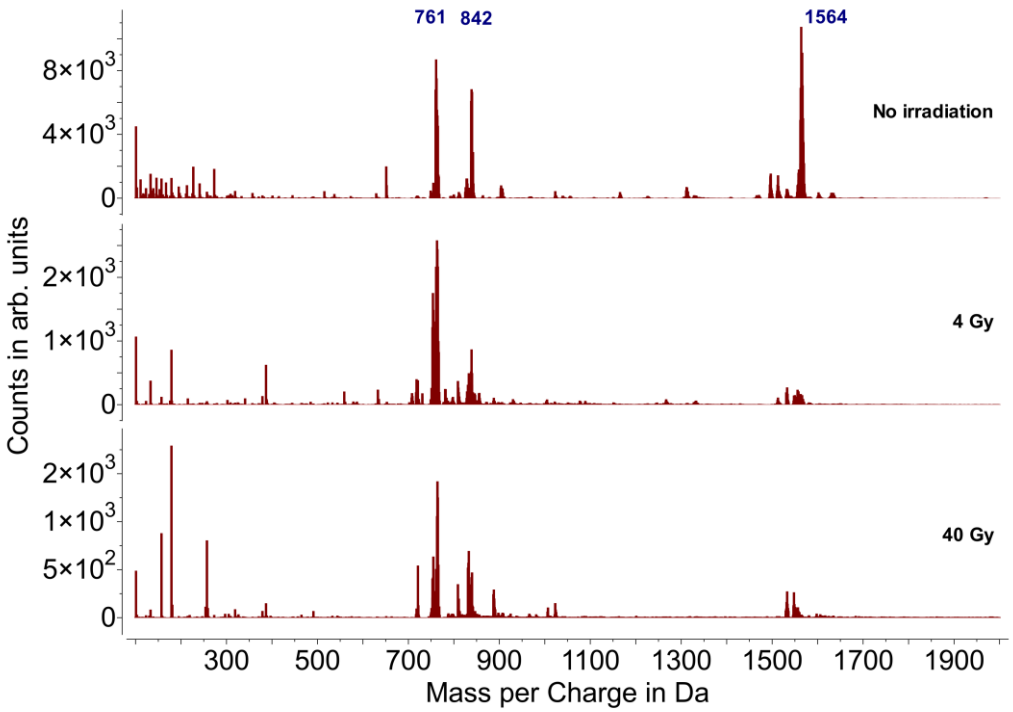

Figure 94: Mass spectra (DMSO, 23 °C) of *cis*-[Pt(N_3)$_2$(PPh_3)] after irradiation with varying dosages of X-rays.

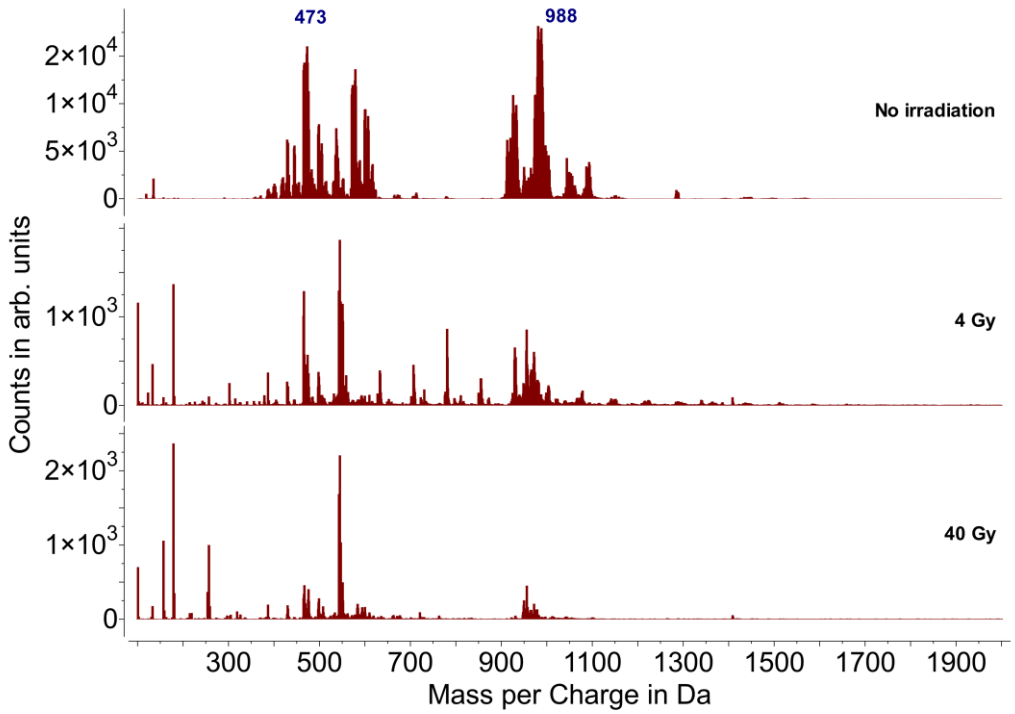

Figure 95: Mass spectra (DMSO, 23 °C) of *cis*-[Pt(N3)2(PEt3)] after irradiation with varying dosages of X-rays.

Considering the minor change in absorbance behaviour observed in the UV-visible spectra for *cis*-[Pt(N3)2(PEt3)] after exposure to X-rays, the fragmentation pattern would be expected to be similar for all three mass spectra, independent of the radiation dose. After irradiation, the spectra include various fragments including some peak patterns confirming platinum moieties, however, without further investigations it was not possible to identify these unambiguously.

Both of the nitro substituted cycloaddition products **Pt,Ph[2+3]Au,NO2** and **Pt,Et[2+3]Au,NO2** exhibit structural changes within their mass spectra recorded after irradiation with X-rays. Whilst the sample of **Pt,Ph[2+3]Au,NO2** which was subjected to 4 Gy irradiation continues to reveal considerable amounts of the

fragment $[M + 2H]^{2+}$ at 1007 Da corresponding to the parent compound, significant concentrations of the fragment $[Au(PPh_3)_2]^+$ were detected alongside it (Figure 96). This effect is further visible for the sample which received an X-ray dosage of 4 Gy, however, it appears to be less prominent. An enhanced formation of $[Au(PPh_3)_2]^+$ suggests promoted cleavage of the gold-moiety, which could lead to subsequent follow-up reactions and multi-modal activity within the cells.

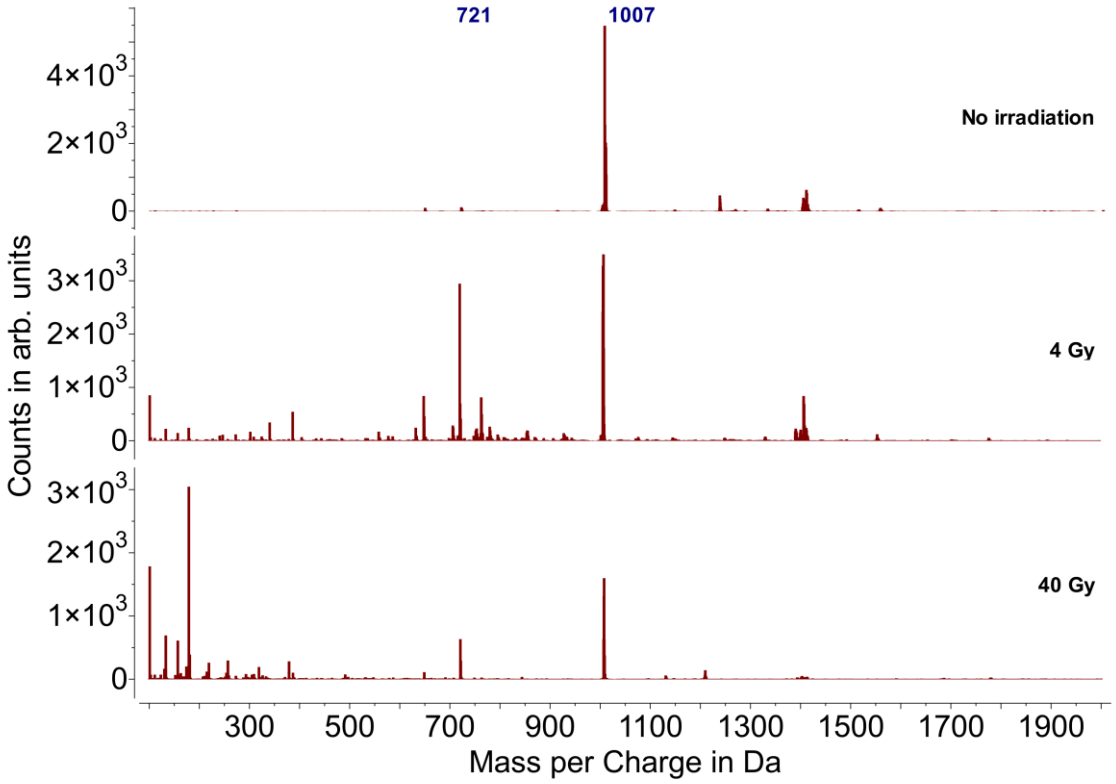

Figure 96: Mass spectra (DMSO, 23 °C) of **Pt,Ph[2+3]Au,NO₂** after irradiation with varying dosages of X-rays.

Pt,Et[2+3]Au,NO$_2$ responds slightly differently than its triphenylphosphine analogue. After irradiation with 4 Gy, the fragment $[M + 2H]^{2+}$ at 864 Da remains unchanged, while the concentration of the fragment corresponding to $[M + H]^+$ at 1726 Da is strongly reduced (Figure 97). Both of these fragments disappear entirely with radiation doses of 40 Gy. Whilst new fragments are detected, $[Au(PPh_3)_2]^+$ (721 Da) is not recorded amongst these. The mass spectra confirm the breakdown of the platinum(II) complex in line with the results from the UV-visible spectra, but do not provide insight to the mechanism without further investigations.

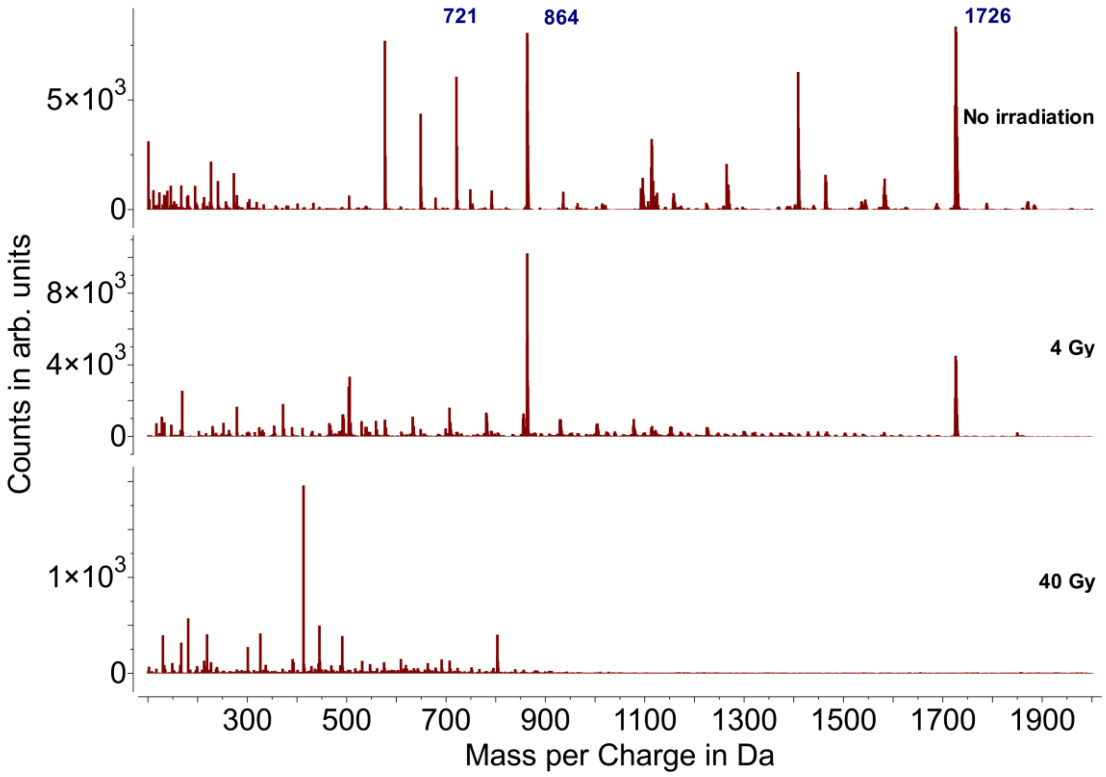

Figure 97: Mass spectra (DMF, 23 °C) of **Pt,Et[2+3]Au,NO$_2$** after irradiation with varying dosages of X-rays.

Irradiation of the nitrile substituted platinum(II)-gold(I) complexes with X-rays yielded results in agreement with the observations after irradiation with blue and green light. The gold moiety in **Pt,Ph[2+3]Au,CN** is cleaved readily, which can be determined by the two fragments $[M + 2H]^{2+}$ (988 Da) and $[M + H]^{+}$ (1975 Da) corresponding to the parent compound fully disappearing, with the fragment $[Au(PPh_3)_2]^{+}$ at 721 Da appearing in high counts (Figure 98). The behaviour of **Pt,Ph[2+3]Au,CN** is independent of the radiation dose and supports the loss of absorbance in the UV-visible spectra.

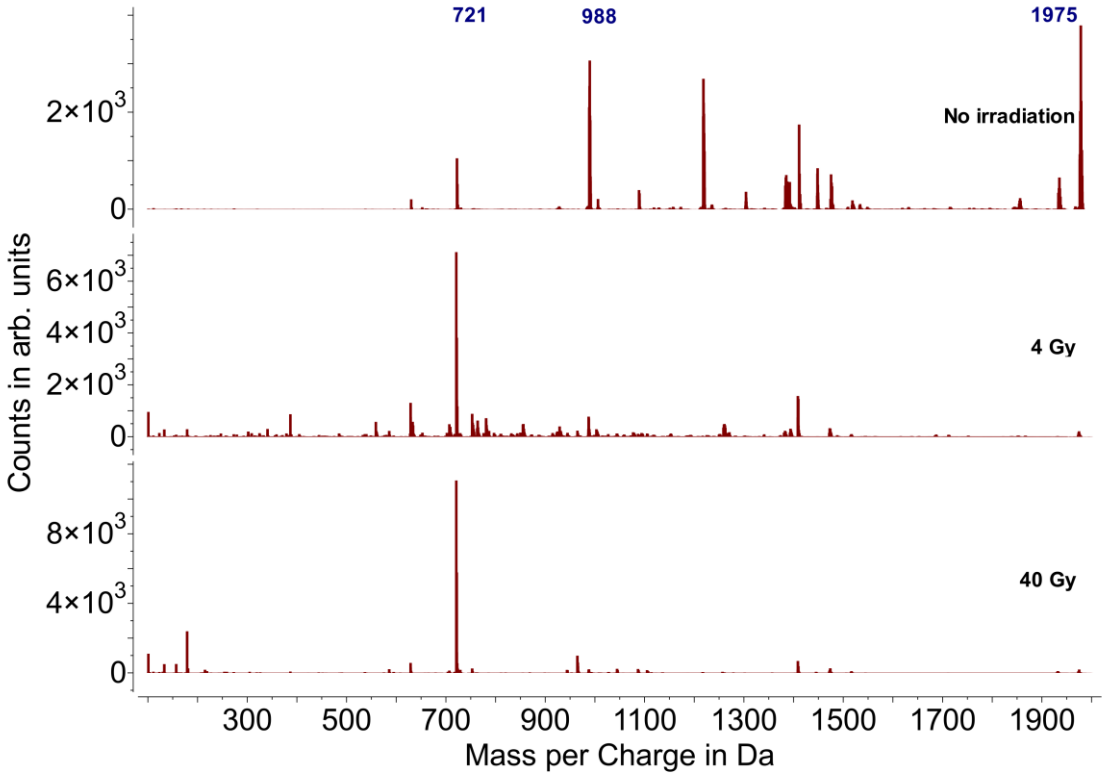

Figure 98: Mass spectra (DMSO, 23 °C) of **Pt,Ph[2+3]Au,CN** after irradiation with varying dosages of X-rays.

In comparison, **Pt,Et[2+3]Au,CN** does not display the mass for the fragment $[Au(PPh_3)_2]^+$. To the contrary, the fragment $[M + 2H]^{2+}$ at 844 Da remains the most prominent mass, whilst the counts for the fragment for $[M + H]^+$ at 1686 Da are reduced slightly (Figure 99). Although the UV-visible spectra suggested a structural change, in particular for the sample subjected to X-rays of 40 Gy, there is no clear indication of this breakdown from the mass spectra.

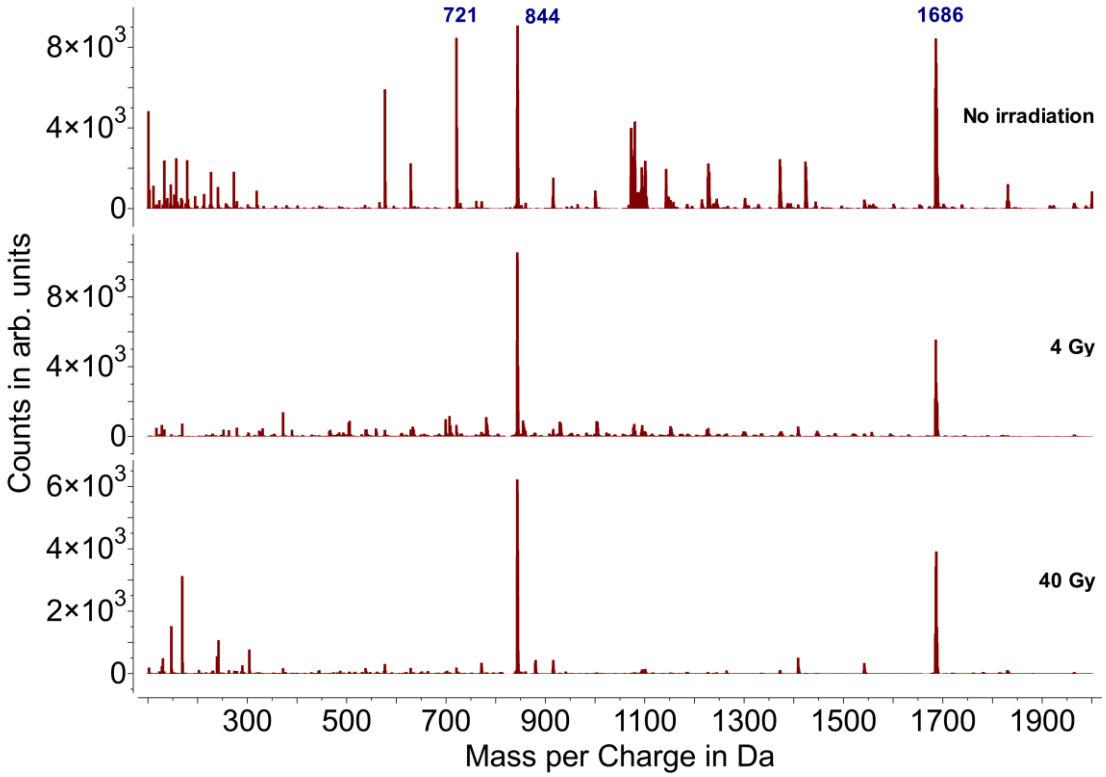

Figure 99: Mass spectra (DMF, 23 °C) of **Pt,Et[2+3]Au,CN** after irradiation with varying dosages of X-rays.

To conclude this chapter, the six compounds *cis*-$[Pt(N_3)_2(PR_3)]$ (R = Et, Ph), **Pt,Ph[2+3]Au,NO_2**, **Pt,Et[2+3]Au,NO_2**, **Pt,Ph[2+3]Au,CN** and **Pt,Et[2+3]Au,CN**

were investigated with regards to their photosensitising properties under the irradiation with blue and green light as well as X-rays. Exposure was varied (10–30 minutes) and the complexes were monitored *via* UV-visible spectroscopy and mass spectrometry. The aim was to explore whether changes in the absorbance behaviour of the compounds were supported with a change in fragments detected in the mass spectra to confirm the breakdown of the complexes. For irradiation under blue and green light, the general trend derives a stronger photosensitisation response from the cycloaddition products compared to the diazidoplatinum(II) complexes. According to the UV-visible spectra, the nitro substituted platinum(II)-gold(I) complexes display a significantly greater change in absorbance. However, when taking the mass spectra into consideration, the fragments for **Pt,Ph[2+3]Au,CN** confirm the unambiguous breakdown of the complex for all three irradiation sources. Compared to that **Pt,Et[2+3]Au,CN** does not decompose as readily, suggesting that for these analogous compounds, changing from the triphenylphosphine to the triethylphosphine ligands has a critical influence on its stability and properties as a photosensitiser.

Table 21 shows a condensed overview of the observations noted for the six compounds each under the irradiation of blue and green light, as well as X-rays and their respective responses detected *via* UV-visible spectroscopy and mass spectrometry. To enable a simplified comparison, the respective observations were rated using the following terms: negligible, minor, medium, strong, significant or inconclusive along with a colour code. It should be noted, that in multiple cases the results are contradictory, which might be due to different analytical methods highlighting diverse aspects. These results provide

indications towards the interactions between the compounds and light sources; however, further investigations at scale will be necessary in order to yield more conclusive results and facilitate concrete identifications of the complexes formed following irradiation.

Table 21: Detected differences in behaviour in the UV-visible spectra (UV) and mass spectra (MS) for compounds *cis*-[Pt(N$_3$)$_2$(PPh$_3$)] (A), *cis*-[Pt(N$_3$)$_2$(PEt$_3$)] (B), **Pt,Ph[2+3]Au,NO$_2$** (C), **Pt,Et[2+3]Au,NO$_2$** (D), **Pt,Ph[2+3]Au,CN** (E) and **Pt,Et[2+3]Au,CN** (F) after irradiation with blue light (B), green light (G) or X-rays (X). Colour-coding was used to highlight the responses

	A	**B**	**C**	**D**	**E**	**F**
Δ UV – B	minor	medium	significant	strong	negligible	negligible
Δ MS – B	inconclusive	inconclusive	significant	medium	significant	minor
Δ UV – G	negligible	negligible	medium	medium	negligible	negligible
Δ MS – G	inconclusive	significant	significant	medium	significant	negligible
Δ UV – X	significant	minor	medium	medium	significant	significant
Δ MS – X	significant	significant	medium	medium	significant	medium

Direct comparison of the complexes confirms an overall stronger response of the [2+3]-cycloaddition products with the nitro substituted gold(I) alkyne **Pt,Ph[2+3]Au,NO$_2$** and **Pt,Et[2+3]Au,NO$_2$** for all light sources. In particular, activation with blue light appears to be a promising approach for further investigations. The bimetallic complex **Pt,Et[2+3]Au,CN** demonstrates the weakest structural changes upon irradiation with blue or green light. All six complexes appear to respond to the irradiation with X-rays. The results for *cis*-[Pt(N$_3$)$_2$(PR$_3$)$_2$] (R = Et, Ph) include inconclusive data which requires further studies in order to draw conclusive trends.

7. Conclusion and Future work

The objective of this research was the synthesis and evaluation of multi-modal platinum-gold complexes as respective anti-cancer agents and their properties as photosensitisers or radiosensitisers.

In order to focus on a selection of diazidoplatinum(II) complexes and gold(I) alkynes suitable for [2+3]-cycloaddition reactions under mild experimental conditions, RI-DFT calculations were employed with the goal of determining trends in reactivities based on the oxidation state of the platinum centre as well as ligand design.

Diazidodiphosphineplatinum(II) complexes comprising triethylphosphine or triphenylphosphine ligands, as well as diazidodipyridylplatinum(II) for comparison, were targeted. In addition, *cis*-isomers with one *N*- and one *P*-donor ligand were pursued in order to identify ligand-dependent electronic trends in reactivities towards the [2+3]-cycloaddition reaction.

The synthesis of *cis*- and *trans*-$[Pt(N_3)_2(PR_3)_2]$ (R = Et, Ph) was pursued *via* the corresponding dichlorido complexes and adapted from literature. Whilst selective synthesis of *cis*-$[Pt(N_3)_2(PR_3)_2]$ (R = Et, Ph) was achieved, it was not possible to isolate the corresponding *trans*-isomers of the diazidoplatinum(II) complexes. Both *cis*-$[Pt(N_3)_2(PR_3)_2]$ (R = Et, Ph) were fully characterised including determination of their molecular structures in the solid state by means of X-ray diffractometry. *trans*-$[PtI_2(py)(PR_3)_2]$ (R = Et, Ph) were isolated in the pursuit of platinum(II) congeners with mixed ligand systems, and characterised *via* X-ray diffraction analysis alongside reaction intermediates. However, further reactions

with the goal of yielding the diazidopyridylphosphineplatinum(II) complexes were inconclusive.

The gold(I) alkynes [Au(PPh_3)(CC(C_6H_4)X] (X = NO_2, Br, CN) were accessed according to reported procedures for X = NO_2. Following optimisation of the [2+3]-cycloaddition reaction of *cis*-[Pt(N_3)$_2$(PPh_3)$_2$] and [Au(PPh_3)(CC(C_6H_4)NO_2] from reports in literature, the corresponding reactions of *cis*-[Pt(N_3)$_2$(PR_3)$_2$] (R = Et, Ph) with [Au(PPh_3)(CC(C_6H_4)X] (X = NO_2, Br, CN) were completed successfully. The novel gold(I) alkynes for X = Br, CN as well as two of the novel bimetallic platinum-gold complexes were fully characterised in the solid state. *cis*-[Pt(N_3)$_2$(*py*)$_2$] did not exhibit any reactivity towards a cycloaddition reaction with any of the employed gold(I) alkynes.

Correlation of the demonstrated reactivities of the diazidoplatinum(II) complexes with the chemical shift in the ^{195}Pt NMR spectra revealed that more electron-rich platinum centres display higher reactivity towards the cycloaddition reaction with the selected gold(I) alkynes. This observation will be helpful in determining viable diazidoplatinum complexes reactive towards analogous cycloaddition reactions in the future.

Oxidation of *cis*-[Pt(N_3)$_2$(PR_3)$_2$] (R = Et, Ph) prior to the cycloaddition reaction was aimed towards the synthesis of platinum(II)-gold(I) prodrugs. All attempts with well-established oxidising agents indicate the lability of the Pt–N bond resulting in ligand substitution reactions rather than the oxidation of the platinum centre. Synthetic explorations yielded the novel complexes *cis*-[Pt(N_3)(OAc)(PPh_3)$_2$], *cis*-[Pt(Cl)(N(CO_2)$_2$(CH_2)$_2$)(PPh_3)$_2$] and *trans*-[$PtCl_4$(PEt_3)$_2$] which were characterised *via* X-ray diffractometry.

To evaluate the platinum(II)-gold(I) complexes as potential anti-cancer agents activated by X-rays, cytotoxicity studies of a selection of cycloaddition products were performed. Tests were executed on three cancer cell lines and radiation of the compounds with doses of 4 Gy. Whilst combining the platinum(II) and gold(I) complexes to yield multi-modal drugs appears to enhance cytotoxicity, little evidence was observed to support radiosensitivity of the compounds. Discrepancies between different stages of cell testing as well as the chosen cell lines suggest that more extensive studies are required in order to draw conclusive trends with respect to the cytotoxicity and the radiosensitivity of the complexes.

The photosensitising properties of the selected six platinum(II) complexes were examined following irradiation with blue and green light, as well as X-rays. Structural changes in the compounds were monitored by means of UV-visible spectroscopy as well as mass spectrometry. The cycloaddition products of *cis*-$[Pt(N_3)_2(PR_3)_2]$ (R = Et, Ph) and $[Au(PPh_3)(CC(C_6H_4)NO_2]$ yielded the most consistent responses across the three light sources indicating structural change and the breakdown of the bimetallic complexes.

Figure 100 provides a schematic overview of the results obtained within the scope of this research.

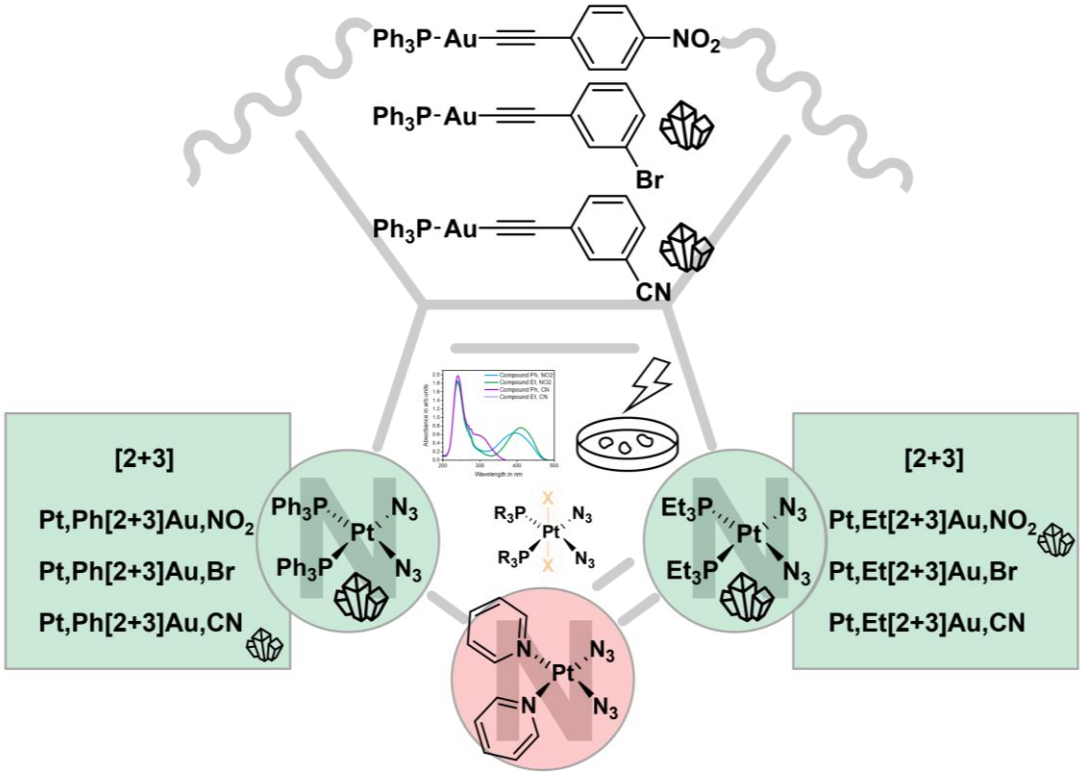

Figure 100: Schematic overview of the results observed within this research.

The findings confirm a reliable synthetic pathway to the synthesis of diphosphineplatinum(II)-gold(I) complexes with potential as multi-modal anti-cancer agents. Since the application of established procedures was not successful in oxidising the platinum(II) centres, investigating the redox-potential of *cis*-$[Pt(N_3)_2(PR_3)_2]$ (R = Et, Ph) *via* cyclic voltammetry could provide useful insight into viable oxidation agents for these complexes. These observations could offer a path to further exploring these compounds as candidates for platinum(IV) prodrugs.

Additional complexes with permutations of *N*- and *P*-donor ligands are required in order to specify the trend between the electronic configuration on the platinum

centre and the reactivity towards [2+3]-cycloaddition reactions. More data could help determine a narrow range of frequencies in the ^{195}Pt NMR spectrum as a practical handle indicating facile cycloaddition of platinum(II) complexes. Focusing on the synthesis of compounds with mixed ligand systems of *N*- and *P*-donors could present valuable information with respect to the electronic trends. In particular, comparing the observations of the *cis*-complexes with their corresponding *trans*-isomers would contribute to determining correlations and assist in identifying a chemical shift range in the ^{195}Pt NMR of reactive compounds.

In order to draw more conclusive results pertaining the photo- and radiosensitivity of the respective platinum(II)-gold(I) cycloaddition products, in-depth studies at scale reducing system-to-system variability with focus on human colorectal carcinoma cell lines are necessary. Building on the observations of the irradiation studies, the cytotoxic behaviour of **Pt,Ph[2+3]Au,NO$_2$** and **Pt,Et[2+3]Au,NO$_2$** under the irradiation of blue light could lead to activation of the complexes resulting in potential enhancement of their toxicity. Examining the gold(I) alkynes [Au(PPh$_3$)(CC(C$_6$H$_4$)X] (X = NO$_2$, Br, CN) prior to the [2+3]-cycloaddition reaction will aid in verifying the observed increase in cytotoxicity for the bimetallic-complexes. Subject to successful synthesis of the corresponding *trans*-isomers of the platinum(II) as well as the platinum(II)-gold(I) complexes, exploring their cytotoxic behaviour would be of significant interest in light of the historic development and focus on complexes with *trans*-configuration as anti-cancer agents.

8. Experimental Section

8.1 General Procedures

All reactions, unless stated otherwise, were performed under air and with wet solvents. Reactions performed under inert conditions were carried out under nitrogen applying standard Schlenk-techniques with a vacuum of up to 10^{-3} mbar. Dry solvents were dispatched from a solvent drying system (*MBRAUN, MB SPS-800*), degassed prior to use and stored over molecular sieves (3-4 Å). Chemicals were used as purchased without further purification. Analytical thin layer chromatography (TLC) was carried out using silica gel 60 F254 from *Merck* and visualised by UV absorption (λ = 254 nm) with a 6 W *UVP UVGL-55* handheld UV lamp. Irradiation experiments were performed in a dark set-up with a 4 W GU10 LTSMD4 SMD LED (blue) or a 7 W GU10 high power LED (green) at a distance of 10 cm.

8.2 Analytical Techniques

Nuclear magnetic resonance (NMR) spectra were recorded on a *Bruker Avance III HD nanobay* equipped with a 9.4 T magnet 400 MHz spectrometer. Tetramethylsilane was used as a reference standard for the chemical shifts of ^{1}H and ^{13}C nuclei, ^{31}P nuclei are referenced to 85% phosphoric acid, and potassium hexachloridoplatinate(IV) in deuterium oxide was used as a reference for ^{195}Pt nuclei. The resonances in the ^{1}H and ^{13}C NMR spectra are referenced internally to the deuterated solvent and set to the following values: CD_2Cl_2: 5.320 ppm (^{1}H),

54.000 ppm (^{13}C), $CDCl_3$: 7.260 ppm (^{1}H), 77.160 ppm (^{13}C), CD_3CN: 1.940 ppm (^{1}H) 118.260 ppm (^{13}C); C_6D_6: 7.160 ppm (^{1}H), 128.060 ppm (^{13}C); THF-d_8: 3.580 ppm (^{1}H), 67.570 ppm (^{13}C); toluene-d_8: 7.090 ppm (^{1}H), 137.860 ppm (^{13}C). Resonances are reported as s (singlet), d (doublet), t (triplet), q (quartet), m (multiplet) and b (broad).

Infrared (IR) spectra were recorded on a *Bruker Tensor 27* Fourier-transform infrared spectrometer with a diamond attenuated total reflection unit. Solids were dissolved in appropriate solvents and measured as thin films after placing a drop on the diamond and evaporation of the solvent.

UV-visible spectra were recorded on a *Jasco V-770* double-beam UV-visible/NIR spectrophotometer with a single monochromator and photomultiplier tube detector for the UV to visible region and a Peltier-cooled PbS detector for the NIR region.

Mass spectra were recorded on a *Waters LCT Premier XE* bench-top orthogonal acceleration time-of-flight liquid chromatography mass spectrometry (LC-MS) system with electronspray ionisation. The system is connected to a *Waters 1525u Binary HPLC Pump* and a *Waters/CTC Analytics 2777C Sample Manager*.

All crystallographic data besides from compound **Pt,Et[2+3]Au,NO_2** was obtained during research visits to the Freie Universität Berlin.
X-ray diffraction (XRD) data were collected on a *Bruker D8 Venture CMOS area detector* (Photon 100) diffractometer with Mo-K_α radiation (λ = 0.71073 Å) at temperatures ≤ –141.15 °C under nitrogen flow. Data were processed using the *APEX5* software suite and equivalent reflections were merged.

Data for **Pt,Et[2+3]Au,NO$_2$** were recorded on an *Oxford Diffraction / Agilent Technologies dual source SuperNova* with a CCD detector (*ATLAS*) with Cu-K_α radiation (λ = 1.54184 Å) at –123.15 °C under nitrogen flow. Collected data were processed using the *CrysAlis^{Pro}* package including merging equivalent reflections.

Single crystals were selected under crystallographic oil and mounted on a 0.1-0.2 mmm micromount. The structures were solved with the *ShelXT* structure solution program using intrinsic phasing and refined with the *ShelXL* refinement package using least square refinement on weighted F^2 values for all reflections using *OLEX2*.[139–141]

8.3 Cell Studies

Cell testing was carried out in collaboration with the research group of Prof G. Higgins in the Department of Oncology at the University of Oxford.

Unless stated otherwise, all chemicals were purchased from *Sigma Aldrich* and used without further purification. Cell lines HCT116, H1299 and A549 were purchased from *ATCC*, and are authenticated by short tandem repeat profiling before usage.

Cell lines HCT116 and A549 were grown in a mixture of Dulbecco's Modified Eagles Medium, cell line H1299 was grown in Roswell Park Memorial Institute medium, respectively, with 10% fetal bovine serum and 1% phosphate-buffered saline solution. They were seeded in 96-well plates and left to attach for 4-5 hours. Compounds were stored as solids in the dark and dissolved in 12 mM

solutions prior to addition to the cells. The compounds were prepared in diluted solutions of the following concentrations: 0.625 µM, 1.25 µM, 2.50 µM, 5.00 µM, 7.50 µM, 10.0 µM, 12.5 µM and 15.0 µM. Irradiation dosages on the cells of 4 Gy were delivered 2 hours after addition of the compounds by a *Gamma Service GSR D1* caesium-137 irradiator with a dose rate of 1.2 $Gy \cdot min^{-1}$. The compounds were removed from the cells by changing the cell media 18 hours after irradiation. The resazurin-based dye (R7017) was added on day seven for cell lines H1299 and A549, and after day eight for cell lines HCT116, with a final concentration 0.1 $mg \cdot mL^{-1}$ in the medium. Fluorescence was measured after 3 hours of incubation at 37 °C using a *BMG Labtech PolarStar Omega* plate reader. IC_{50}-values were determined by non-linear curve fitting after normalising readings relative to the vehicle control.

8.4 Density Functional Theory Calculations

Computing time was made available by the North-German Supercomputing Alliance (HLRN) in providing High-Performance Computing (HPC) at the Freie Universität Berlin. Density Functional Theory (DFT) calculations within the scope of this work were performed with *Turbomole 7.3*[142] using resolution of identity (RI) methods,[143] the def2-TZVP basis set,[144] the BP-86 functional,[145,146] the PBE functional,[147] the B2-PLYP functional,[102,148] or the B3-LYP functional.[146,149] Solvent simulation was applied according to the conductor like screening model (COSMO, $\varepsilon = \infty$)[150] level of theory. Minima on the potential energy surface were verified by harmonic vibrational frequency analysis.

8.5 Syntheses

8.5.1 Synthesis of *cis*-Dichloridobis(triphenylphosphine)-platinum(II)[111]

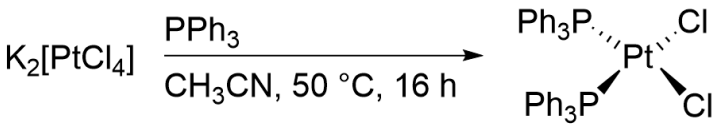

$K_2[PtCl_4]$ (500 mg, 1.20 mmol, 1.0 eq) was suspended in acetonitrile (70 mL). PPh_3 (629.5 mg, 2.41 mmol, 2.0 eq) was added and the reaction mixture was heated to 50 °C for 16 hours yielding a colourless suspension. The reaction mixture was filtered and the solid was washed with cold acetonitrile. The product was isolated as a colourless solid.

***cis*-$[PtCl_2(PPh_3)_2]$** (873 mg, 1.10 mmol, 92%):

$^{31}P\{^1H\}$ NMR (162 MHz, $CDCl_3$, 25 °C): δ = 14.3 (s, $^1J(^{31}P, ^{195}Pt)$ = 3675 Hz) ppm.

The NMR signals agree with those in literature.[110]

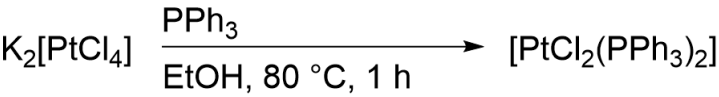

$K_2[PtCl_4]$ (100 mg, 0.24 mmol, 1.0 eq) was dissolved in water (3 mL). A solution of PPh_3 (126.4 mg, 0.48 mmol, 2.0 eq) in ethanol (3 mL) was added dropwise

and the reaction mixture was heated to 80 °C for 1 hour. After removing all solvent under vacuum, the solid was washed with water and diethylether, and dried under vacuum.

The product was identified as a mixture of *cis*- and *trans*-[$PtCl_2(PPh_3)_2$] in a ratio of 1:0.10 as determined by $^{31}P\{^1H\}$ NMR spectroscopy.

8.5.2 Synthesis of *trans*-Dichloridobis(triphenylphosphine)-platinum(II)[110,112]

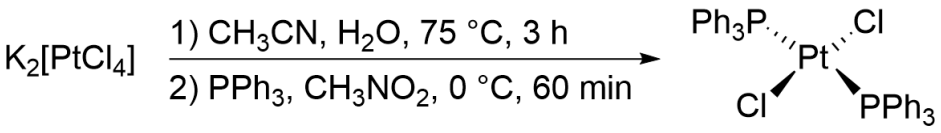

$K_2[PtCl_4]$ (500 mg, 1.20 mmol, 1.0 eq) was dissolved in water (10 mL). Acetonitrile (0.94 mL, 18.1 mmol, 15.6 eq) was added and the reaction mixture was heated to 75 °C for 3 hours. The suspension was filtered and the solid was washed in water and acetonitrile, dried under vacuum and used in the next step without further purification.

trans-[$PtCl_2(CH_3CN)_2$] (300 mg, 0.84 mmol, 1.0 eq) was suspended in nitromethane (5 mL) at 0 °C. PPh_3 (336 mg, 1.32 mmol, 1.5 eq) was dissolved in nitromethane (5 mL), added dropwise and the reaction mixture was stirred at 0 °C for 60 minutes. After filtering the suspension over celite, the solid was redissolved and washed off the celite with chloroform. The solvent was removed under vacuum yielding the product as a colourless solid.

***trans*-[$PtCl_2(PPh_3)_2$]** (806 mg, 1.02 mmol, 85%):

$^{31}P\{^1H\}$ NMR (162 MHz, $CDCl_3$, 25 °C): δ = 20.2 (s, $^1J(^{31}P, ^{195}Pt)$ = 2633 Hz) ppm.

The NMR signals agree with those in literature.[110]

When the reaction mixture was stirred at 50 °C for 30 minutes, the product was identified as a mixture of *cis*- and *trans*-$[PtCl_2(PPh_3)_2]$ in a ratio of 1:0.94 as determined by $^{31}P\{^1H\}$ NMR spectroscopy.

8.5.3 Synthesis of *cis*-Dichloridobis(triethylphosphine)platinum(II)

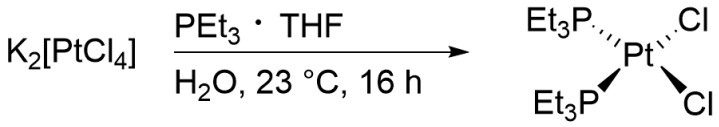

The reaction was performed under a nitrogen atmosphere, the work-up was performed under air. PEt_3 in tetrahydrofuran (1 M) (3.84 mL, 3.84 mmol, 4.0 eq) was added to a solution of $K_2[PtCl_4]$ (300 mg, 0.72 mmol, 1.0 eq) in water (6 mL). The reaction mixture was stirred at 23 °C for 16 hours yielding a colourless suspension. After removing the solvents under vacuum, the solid was extracted three times with toluene (5 mL). The organic phases were filtered over celite and

combined. The solvent was removed under vacuum yielding the product as a colourless solid.

***cis*-[PtCl$_2$(PEt$_3$)$_2$]** (336 mg, 0.67 mmol, 93%):

^{31}P{^{1}H} NMR (162 MHz, $CDCl_3$, 25 °C): δ = 9.1 (s, ^1J(^{31}P, ^{195}Pt) = 3515 Hz) ppm.

The NMR signals agree with those in literature.[93]

8.5.4 Synthesis of *trans*-Dichloridobis(triethylphosphine)platinum(II)

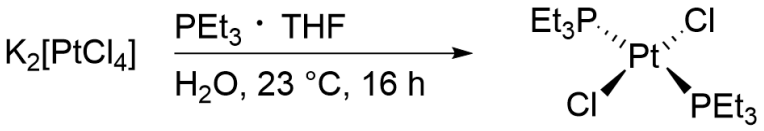

The reaction was performed under a nitrogen atmosphere, the work-up was performed under air. PEt_3 in tetrahydrofuran (1 M) (0.24 mL, 0.24 mmol, 1.0 eq) was added to a solution of $K_2[PtCl_4]$ (100 mg, 0.24 mmol, 1.0 eq) in water (2 mL). The reaction mixture was stirred at 23 °C for 16 hours yielding a colourless suspension. After removing the solvents under vacuum, the solid was extracted three times with toluene (3 mL). The organic phases were filtered over celite and combined. The solvent was removed under vacuum yielding the product as a colourless solid.

***trans*-[PtCl$_2$(PPh$_3$)$_2$]** (98.9 mg, 0.20 mmol, 82%):

^{31}P{^{1}H} NMR (162 MHz, $CDCl_3$, 25 °C): δ = 12.2 (s, ^1J(^{31}P, ^{195}Pt) = 2399 Hz) ppm.

The NMR signals agree with those in literature.[93]

8.5.5 Synthesis of *cis*-Diazidodiphosphineplatinum(II)

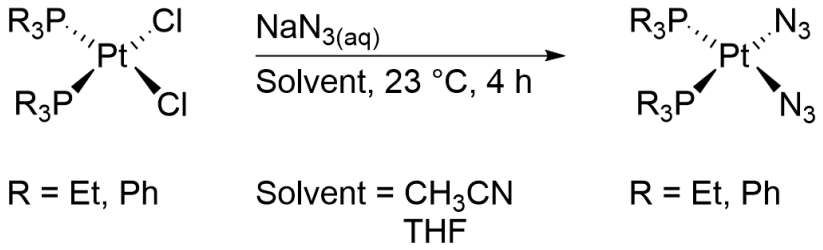

cis-$[PtCl_2(PR_3)_2]$ (R = Et, Ph) (1.0 eq) was suspended in either acetonitrile or tetrahydrofuran (20 mL). A solution of NaN_3 (109 mg, 1.67 mmol, 6.0 eq) in water (<2 mL) was added and the reaction mixture was stirred at 23 °C for 4 hours. After removing the solvents under vacuum, the solid was extracted three times with chloroform (5 mL). The organic phases were filtered over celite and combined. The solvent was removed under vacuum yielding the product as a pale yellow solid.

Crystals of *cis*-$[Pt(N_3)_2(PR_3)_2]$ (R = Et, Ph) suitable for X-ray diffraction analysis were grown from concentrated solutions in chloroform.

***cis*-$[Pt(N_3)_2(PEt_3)_2]$** (766 mg, 1.49 mmol, 89%):

^{1}H NMR (400 MHz, $CDCl_3$, 25 °C): δ = 1.08 (qt, $^3J(^1H, ^1H)$ = 7.6 Hz, *Et*) ppm.

$^{31}P\{^1H\}$ NMR (162 MHz, $CDCl_3$, 25 °C): δ = 7.3 (s, $^1J(^{31}P, ^{195}Pt)$ = 3338 Hz) ppm.

$^{13}C\{^1H\}$ NMR (101 MHz, $CDCl_3$, 25 °C): δ = 15.5 (d, 6C, $^1J(^{31}P, ^{13}C)$ = 38 Hz CH_2), 8.0 (s, 6C, CH_3) ppm.

^{195}Pt NMR (86 MHz, $CDCl_3$, 25 °C): δ = −4335 (t, $^1J(^{31}P, ^{195}Pt)$ = 3340 Hz) ppm.

IR (23 °C): $\tilde{\nu}_{as}(N_3)$ = 2060 cm^{-1}.

UV-Vis (THF, 23 °C): λ = 248 nm.

ESI-MS [*m/z* (fragment, relative intensity)]: 988 ($[2M - N_3)]^+$, 99), 913 ($[2M - PEt_3 + H]^+$, 34), 473 ($[M - N_3)]^+$, 88) Da.

***cis*-[Pt(N$_3$)$_2$(PPh$_3$)$_2$]** (1262 mg, 1.57 mmol, 94%):

^{1}H NMR (400 MHz, $CDCl_3$, 25 °C): δ = 7.48–7.18 (m, *Ph*) ppm.

^{31}P{^{1}H} NMR (162 MHz, $CDCl_3$, 25 °C): δ = 12.0 (s, $^1J(^{31}P, ^{195}Pt)$ = 3507 Hz) ppm.

^{13}C{^{1}H} NMR (101 MHz, $CDCl_3$, 25 °C): δ = 134.5 (t, 6C, J = 6 Hz, *ipso-C*), 131.1,128.9, 128.4 (t, 6C, J = 6 Hz, *ipso-C*) ppm.

^{195}Pt NMR (86 MHz, $CDCl_3$, 25 °C): δ = −4261 (t, $^1J(^{31}P, ^{195}Pt)$ = 3506 Hz) ppm.

IR (23 °C): $\tilde{\nu}_{as}(N_3)$ = 2060 cm^{-1}.

UV-Vis (THF, 23 °C): λ = 269, 233 nm.

ESI-MS [*m/z* (fragment, relative intensity)]: 1564 ($[2M - N_3)]^+$, 100), 840 ($[M + K]^+$, 62), 761 ($[M - N_3)]^+$, 81) Da.

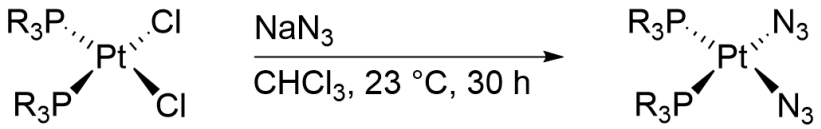

R = Et, Ph R = Et, Ph

NaN_3 (80.0 mg, 1.23 mmol, 100 eq) was added to a solution of *cis*-$[PtCl_2(PR_3)_2]$ (R = Et, Ph) (1.0 eq) in chloroform (5 mL) and the reaction mixture was stirred at 23 °C for 30 hours, yielding a colourless suspension. The reaction mixture was filtered and the solid was extracted with chloroform. The filtrate was reduced under vacuum yielding the product as a pale yellow solid.

***cis*-$[Pt(N_3)_2(PEt_3)_2]$** (5.20 mg, 0.01 mmol, 82%):

$^{31}P\{^1H\}$ NMR (162 MHz, $CDCl_3$, 25 °C): δ = 7.3 (s, $^1J(^{31}P, ^{195}Pt)$ = 3338 Hz) ppm.

***cis*-$[Pt(N_3)_2(PPh_3)_2]$** (8.60 mg, 0.10 mmol, 87%):

$^{31}P\{^1H\}$ NMR (162 MHz, $CDCl_3$, 25 °C): δ = 12.0 (s, $^1J(^{31}P, ^{195}Pt)$ = 3507 Hz) ppm.

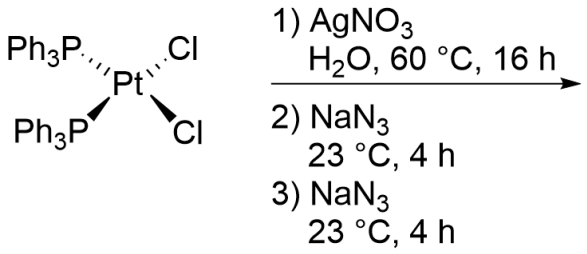

$AgNO_3$ (21.5 mg, 0.13 mmol, 2.0 eq) was added to a suspension of *cis*-$[PtCl_2(PPh_3)_2]$ (50 mg, 0.06 mmol, 1.0 eq) in water (8 mL) and the reaction mixture was stirred at 60 °C for 16 hours. The suspension was filtered over celite and an ionic membrane. NaN_3 (20.6 mg, 0.32 mmol, 5.0 eq) was added to the solution and the mixture was stirred at room temperature. After 4 hours, a second batch of NaN_3 (20.6 mg, 0.32 mmol, 5.0 eq) was added to the solution and the mixture was stirred at room temperature for another 4 hours. After cooling the reaction mixture in the fridge and/or on ice, the suspension was filtered and the solid was washed with cold water, diethylether and acetone.

The $^{31}P\{^1H\}$ NMR spectra showed the formation of triphenylphosphine oxide and unreacted starting material.

$^{31}P\{^1H\}$ NMR (162 MHz, $CDCl_3$, 25 °C): δ = 29.5 (s), 14.3 (s $^1J(^{31}P, ^{195}Pt)$ = 3675 Hz) ppm.

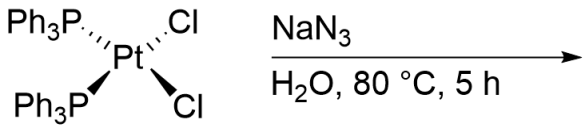

NaN_3 (24.7 mg, 0.38 mmol, 6.0 eq) was added to a suspension of *cis*-$[PtCl_2(PPh_3)_2]$ (50 mg, 0.06 mmol, 1.0 eq) in water (5 mL) and the mixture was stirred at 80 °C for 5 hours. The solvent was removed under vacuum and the solid was extracted three times with chloroform (3 mL). The organic phases were combined and the solvent was removed under vacuum yielding a colourless solid.

The $^{31}P\{^1H\}$ NMR spectra showed the formation of triphenylphosphine oxide and unreacted starting material.

$^{31}P\{^1H\}$ NMR (162 MHz, $CDCl_3$, 25 °C): δ = 29.5 (s), 14.3 (s, $^1J(^{31}P, ^{195}Pt)$ = 3675 Hz) ppm.

8.5.6 Attempted Synthesis of *trans*-Diazidodiphosphineplatinum(II)

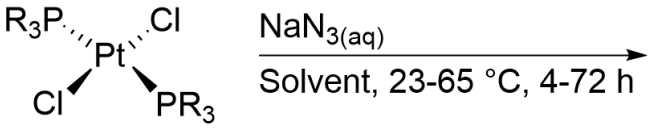

R = Et, Ph

Solvent = THF
CH_3CN
$CHCl_3$

trans-$[PtCl_2(PR_3)_2]$ (R = Et, Ph) (1.0 eq) was suspended in either acetonitrile, tetrahydrofuran or chloroform (20 mL). A solution of NaN_3 (24.7 mg, 0.38 mmol, 6.0 eq) in water (<2 mL) was added and the reaction mixture was stirred at 23–

65 °C for 4–72 hours and monitored *via* $^{31}P\{^{1}H\}$ NMR spectroscopy. After removing the solvents under vacuum, the solid was extracted three times with chloroform (5 mL). The organic phases were filtered over celite and combined. The solvent was removed under vacuum yielding the product as a pale yellow solid.

The $^{31}P\{^{1}H\}$ NMR spectra showed multiple resonances, which could not all be assigned unambiguously.

Starting from ***trans*-[$PtCl_2(PEt_3)_2$]**:

The $^{31}P\{^{1}H\}$ NMR spectra showed the formation of triethylphosphine oxide.

$^{31}P\{^{1}H\}$ NMR (162 MHz, $CDCl_3$, 25 °C): δ = 53.4 (s) ppm.

Starting from ***trans*-[$PtCl_2(PPh_3)_2$]**:

The $^{31}P\{^{1}H\}$ NMR spectra showed the formation of triphenylphosphine oxide and the *cis*- and *trans*-isomers of unreacted starting material.

$^{31}P\{^{1}H\}$ NMR (162 MHz, $CDCl_3$, 25 °C): δ = 29.2 (s), 14.3 (s, $^{1}J(^{31}P, ^{195}Pt)$ = 3675 Hz), 20.2 (s, $^{1}J(^{31}P, ^{195}Pt)$ = 2633 Hz) ppm.

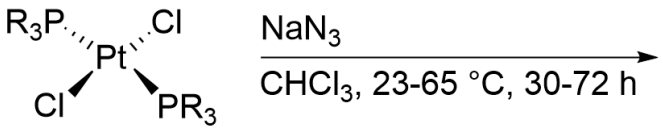

R = Et, Ph

NaN_3 (80.0 mg, 1.23 mmol, 100 eq) was added to a solution of *trans*-$[PtCl_2(PR_3)_2]$ (R = Et, Ph) (1.0 eq) in chloroform (5 mL) and the reaction mixture was stirred at 23–65 °C for 30–72 hours, yielding a colourless suspension. The reaction mixture was filtered and the solid was washed with chloroform. The solvent of the filtrate was reduced under vacuum yielding the product as a pale yellow solid.

The $^{31}P\{^1H\}$ NMR spectra showed multiple resonances, which could not all be assigned unambiguously.

Starting from ***trans*-[$PtCl_2(PEt_3)_2$]**:

$^{31}P\{^1H\}$ NMR (162 MHz, $CDCl_3$, 25 °C): δ = 18.4 (s, $^1J(^{31}P, ^{195}Pt)$ = 2580 Hz), 7.3 (s, $^1J(^{31}P, ^{195}Pt)$ = 3338 Hz) ppm.

Starting from ***trans*-[$PtCl_2(PPh_3)_2$]**:

$^{31}P\{^1H\}$ NMR (162 MHz, $CDCl_3$, 25 °C): δ = 17.1 (s, $^1J(^{31}P, ^{195}Pt)$ = 2851 Hz), 12.0 (s, $^1J(^{31}P, ^{195}Pt)$ = 3507 Hz) ppm.

^{195}Pt NMR (86 MHz, $CDCl_3$, 25 °C): δ = −4261 (t, $^1J(^{31}P, ^{195}Pt)$ = 3506 Hz), −3706 (t, $^1J(^{31}P, ^{195}Pt)$ = 2858 Hz) ppm.

8.5.7 Synthesis of *cis*-Diiodidodipyridylplatinum(II)[151]

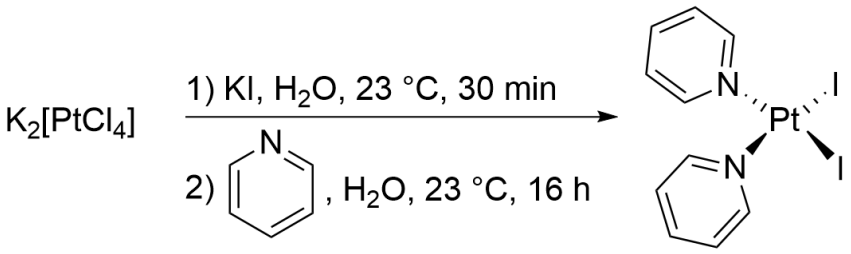

$K_2[PtCl_4]$ (500 mg, 1.20 mmol, 1.0 eq) was dissolved in water (30 mL). A solution of KI (1600 mg, 9.64 mmol, 8.0 eq) in water (1.2 mL) was added and the reaction mixture was stirred at 23 °C for 30 minutes yielding a brown solution. Pyridine (243.6 µL, 3.01 mmol, 2.5 eq) was dissolved in water (6 mL) and added dropwise. The reaction mixture was stirred at room temperature until it had fully reacted to a yellow suspension. The reaction mixture was filtered and the solid was washed with cold water and ethanol. The product was isolated as a yellow solid.

***cis*-[PtI$_2$(*py*)$_2$]** (692 mg, 1.41 mmol, 95%):

^{1}H NMR (400 MHz, $(CD_3)_2CO$, 25 °C): δ = 8.98 (dd, 4H, $^3J(^1H, ^{195}Pt)$ = 42 Hz, $^3J(^1H, ^1H)$ = 5.1 Hz, $^4J(^1H, ^1H)$ = 1.5 Hz, *ortho*-C*H*), 7.98 (tt, 2H, $^3J(^1H, ^1H)$ = 7.7 Hz, $^4J(^1H, ^1H)$ = 1.5 Hz, *para*-C*H*), 7.51 (dd, 4H, $^3J(^1H, ^1H)$ = 7.7, 5.0 Hz, *meta*-C*H*) ppm.

The data is in good agreement with that reported in literature.[117]

8.5.8 Synthesis of *cis*-Diazidodipyridylplatinum(II)

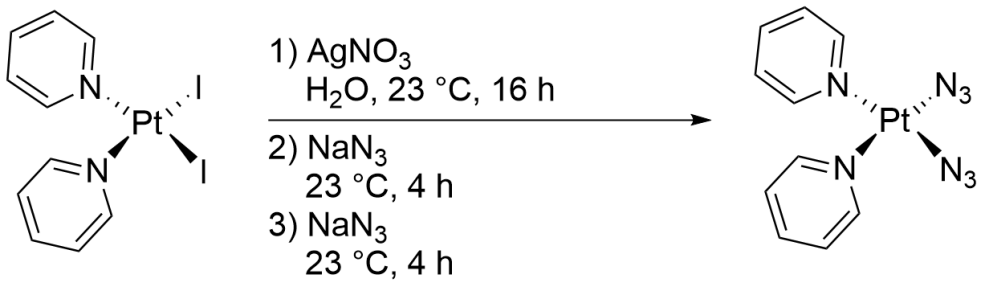

cis-[PtI_2(*py*)$_2$] (150 mg, 0.25 mmol, 1.0 eq) was suspended in water (18 mL). $AgNO_3$ (83.9 mg, 0.49 mmol, 2.0 eq) was added and the reaction mixture was stirred at 23 °C for 16 hours. The colourless suspension was filtered over celite and an ionic membrane. NaN_3 (80.3 mg, 1.24 mmol, 5.0 eq) was added to the solution and the mixture was left to stir at 23 °C. After 4 hours, a second batch of NaN_3 (80.3 mg, 1.24 mmol, 5.0 eq) was added to the solution and the mixture was stirred at 23 °C for another 4 hours. After cooling the reaction mixture in the fridge and/or on ice, the suspension was filtered and the solid was washed with cold water and ethanol. The product was isolated as a yellow solid.

***cis*-[Pt(N_3)$_2$(*py*)$_2$]** (75.4 mg, 0.17 mmol, 69%):

^{1}H NMR (400 MHz, $CDCl_3$, 25 °C): δ = 8.65 (dd, 4H, ^3J(^{1}H, ^{195}Pt) = 34 Hz, ^3J(^{1}H, ^{1}H) = 5.3 Hz, ^4J(^{1}H, ^{1}H) = 1.5 Hz, *ortho*-C*H*), 7.86 (tt, 2H, ^3J(^{1}H, ^{1}H) = 7.7 Hz, ^4J(^{1}H, ^{1}H) = 1.5 Hz, *para*-C*H*), 7.39 (dd, 4H, ^3J(^{1}H, ^{1}H) = 7.7, 5.2 Hz, *meta*-C*H*) ppm.

^{195}Pt NMR (86 MHz, $CDCl_3$, 25 °C): δ = −2076 (b) ppm.

IR (23 °C): $\tilde{\nu}_{as}(N_3)$ = 2042 cm^{-1}.

8.5.9 Synthesis of *trans*-Diiodidopyridylphosphineplatinum(II)

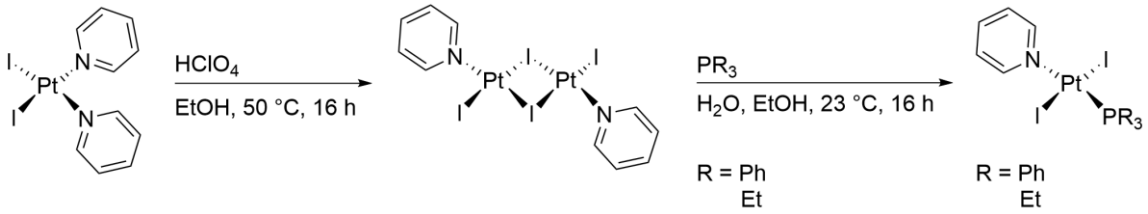

cis-[PtI_2(*py*)$_2$] (285 mg, 0.47 mmol, 1.0 eq) was suspended in water (7.5 mL). $HClO_4$ (60% in water) (153 µL, 1.41 mmol, 3.0 eq) was added and the reaction mixture was stirred at 50 °C for 16 hours or until all of the yellow solid has turned into a reddish brown solid. The suspension was filtered and the solid was washed with cold water and ethanol. The product was isolated as a brown solid and used in the next step without further purification (407 mg, 0.39 mmol, 82%).

trans-[PtI_2(*py*)]$_2$ (50 mg, 0.05 mmol, 1.0 eq) was suspended in water (1.5 mL). PPh_3 or PEt_3 in tetrahydrofuran (1 M) (2.0 eq) was dissolved in ethanol (0.5 mL), added dropwise and the reaction mixture was stirred at 23 °C for 16 hours. The suspension was filtered and the solid was washed with cold water and ethanol.

Crystals of the dimers *trans*-[$PtI_2(PR_3)]_2$ (R = Et, Ph) suitable for X-ray diffraction analysis were isolated from concentrated solutions in acetone.

Crystals of *trans*-[PtI_2(*py*)(PR_3)] (R = Et, Ph) suitable for X-ray diffraction analysis were isolated from concentrated solutions in chloroform.

***trans*-[PtI_2(*py*)(PEt_3)]** (30.4 mg, 0.05 mmol, 94%):

$^{31}P\{^1H\}$ NMR (162 MHz, $(CD_3)_2CO$, 25 °C): δ = 0.6 (s, $^1J(^{31}P, ^{195}Pt)$ = 2263 Hz) ppm.

^{1}H NMR (400 MHz, $(CD_3)_2CO$, 25 °C): δ = 8.98 (dd, 2H, $^{3}J(^{1}H, ^{195}Pt)$ = 42 Hz, $^{3}J(^{1}H, ^{1}H)$ = 5.1 Hz, $^{4}J(^{1}H, ^{1}H)$ = 1.5 Hz, *Py*: *ortho*-C*H*), 7.98 (tt, 1H, $^{3}J(^{1}H, ^{1}H)$ = 7.7 Hz, $^{4}J(^{1}H, ^{1}H)$ = 1.6 Hz, *Py*: *para*-C*H*), 7.51 (dd, 2H, $^{3}J(^{1}H, ^{1}H)$ = 7.7, 5.1 Hz, *Py*: *meta*-C*H*), 2.32 (m, 15H, *Et*) ppm.

***trans*-[PtI$_2$(*py*)(PPh$_3$)]** (34.4 mg, 0.04 mmol, 87%):

^{31}P{^{1}H} NMR (162 MHz, C_4D_8O, 25 °C): δ = 12.4 (s, $^{1}J(^{31}P, ^{195}Pt)$ = 2512 Hz) ppm.

^{1}H NMR (400 MHz, C_4D_8O, 25 °C): δ = 8.94 (dd, 2H, $^{3}J(^{1}H, ^{195}Pt)$ = 42 Hz, $^{3}J(^{1}H, ^{1}H)$ = 6.4 Hz, $^{4}J(^{1}H, ^{1}H)$ = 1.5 Hz, *Py*: *ortho*-C*H*), 7.86–7.70 (m, *Ar*), 7.43–7.34 (m, *Ar*) ppm.

8.5.10 Attempted Synthesis of *trans*-Diazidopyridylphosphine-platinum(II)

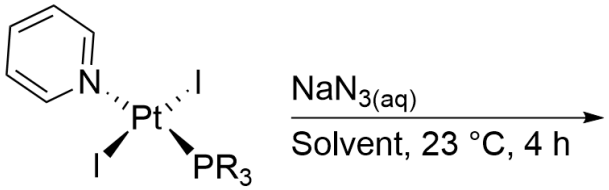

R = Et, Ph

Solvent = THF
CH_3CN
$CHCl_3$

trans-[PtI$_2$(*py*)(PR$_3$)$_2$] (R = Et, Ph) (1.0 eq) was suspended in either acetonitrile, tetrahydrofuran or chloroform (20 mL). A solution of NaN_3 (6.0 eq) in water

(<2 mL) was added and the reaction mixture was stirred at 23 °C for 4 hours. After removing the solvents under vacuum, the solid was extracted three times with chloroform (5 mL). The organic phases were filtered over celite and combined. The solvent was removed under vacuum yielding a solid.

The ^{1}H and $^{31}P\{^{1}H\}$ NMR spectra showed multiple resonances, which could not all be assigned unambiguously.

Reaction in tetrahydrofuran:

Starting from ***trans*-[PtI$_2$(*py*)(PEt$_3$)]**:

$^{31}P\{^{1}H\}$ NMR (162 MHz, $CDCl_3$, 25 °C): δ = 0.3 (s, $^{1}J(^{31}P, ^{195}Pt)$ = 2263 Hz) ppm.

Starting from ***trans*-[PtI$_2$(*py*)(PPh$_3$)]**:

The $^{31}P\{^{1}H\}$ NMR spectra showed the formation of triphenylphosphine oxide.

$^{31}P\{^{1}H\}$ NMR (162 MHz, $CDCl_3$, 25 °C): δ = 29.5 (s) ppm.

Reaction in acetonitrile:

Starting from ***trans*-[PtI$_2$(*py*)(PEt$_3$)]**:

$^{31}P\{^{1}H\}$ NMR (162 MHz, $CDCl_3$, 25 °C): δ = 12.7 (s, $^{1}J(^{31}P, ^{195}Pt)$ = 2417 Hz), 0.3 (s, $^{1}J(^{31}P, ^{195}Pt)$ = 2263 Hz) ppm.

Starting from ***trans*-[PtI$_2$(*py*)(PPh$_3$)]**:

^{31}P{^{1}H} NMR (162 MHz, $CDCl_3$, 25 °C): δ = 17.1 (s, $^1J(^{31}P, ^{195}Pt)$ = 2853 Hz), −2.3 (s, $^1J(^{31}P, ^{195}Pt)$ = 3370 Hz) ppm.

IR (23 °C): $\tilde{\nu}_{as}(N_3)$ = 2050 cm^{-1}.

Reaction in chloroform:

Starting from ***trans*-[PtI$_2$(*py*)(PEt$_3$)]**:

^{31}P{^{1}H} NMR (162 MHz, $CDCl_3$, 25 °C): δ = 0.3 (s, $^1J(^{31}P, ^{195}Pt)$ = 2263 Hz) ppm.

Starting from ***trans*-[PtI$_2$(*py*)(PEt$_3$)]**:

^{31}P{^{1}H} NMR (162 MHz, $CDCl_3$, 25 °C): δ = 29.5 (s), 12.0 (s, $^1J(^{31}P, ^{195}Pt)$ = 3507 Hz), −2.3 (s, $^1J(^{31}P, ^{195}Pt)$ = 3370 Hz) ppm.

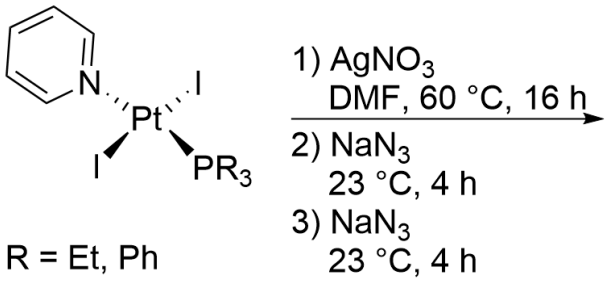

trans-[PtI_2(*py*)(PR_3)] (R = Et, Ph) (1.0 eq) was suspended in dimethylformamide (18 mL). $AgNO_3$ (21.5 mg, 0.13 mmol, 2.0 eq) was added and the reaction mixture was stirred at 60 °C for 16 hours until a colourless solution is formed. The suspension was filtered over celite and an ionic membrane. NaN_3 (20.6 mg, 0.32 mmol, 5.0 eq) was added to the solution and the mixture was left to stir at 23 °C. After 4 hours, a second batch of NaN_3 (20.6 mg, 0.32 mmol, 5.0 eq) was added to the solution and the mixture was stirred at 23 °C for another 4 hours. After cooling the reaction mixture in the fridge and/or on ice, the suspension was filtered and the solid was washed with cold water and ethanol.

Starting from ***trans*-[PtI_2(*py*)(PEt_3)]**:

$^{31}P\{^1H\}$ NMR (162 MHz, $CDCl_3$, 25 °C): δ = 18.4 (s, $^1J(^{31}P, ^{195}Pt)$ = 2580 Hz) ppm.

^{195}Pt NMR (86 MHz, $CDCl_3$, 25 °C): δ = −3675 (t, $^1J(^{31}P, ^{195}Pt)$ = 2580 Hz) ppm.

IR (23 °C): $\tilde{\nu}_{as}(N_3)$ = 2053 cm^{-1}.

Starting from ***trans*-[PtI_2(*py*)(PPh_3)]**:

The $^{31}P\{^1H\}$ NMR spectra showed the formation of *cis*-[$Pt(N_3)_2(PPh_3)_2$].

$^{31}P\{^{1}H\}$ NMR (162 MHz, $CDCl_3$, 25 °C): δ = 12.0 (s, $^{1}J(^{31}P, ^{195}Pt)$ = 3507 Hz) ppm.

IR (23 °C): $\tilde{\nu}_{as}(N_3)$ = 2054 cm^{-1}.

8.5.11 Synthesis of Acetylidotriphenylphosphinegold(I)[127]

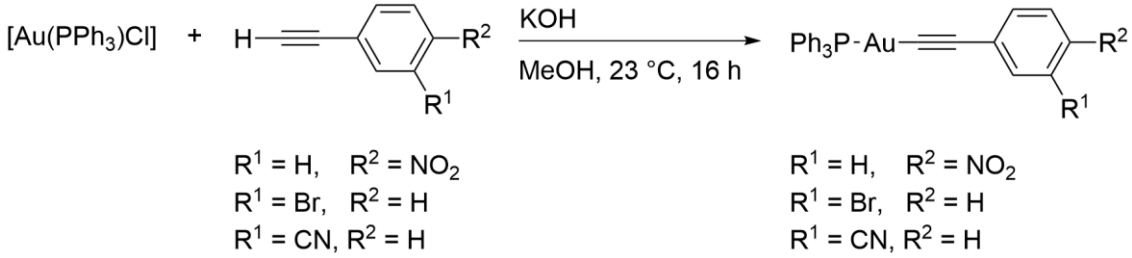

The reaction was performed under a nitrogen atmosphere, the work-up was performed under air. Terminal alkyne (2.0 eq) and $[Au(PPh_3)Cl]$ (500 mg, 1.01 mmol, 1.0 eq) were added to a mixture of KOH (113.4 mg, 2.02 mmol, 2.0 eq) in methanol (25 mL). After the reaction mixture was stirred at 23 °C for 16 hours, the suspension was filtered and the product isolated as a colourless solid.

The product was checked for residual starting materials with thin layer chromatography in ethyl acetate and diethylether in a ratio of 4:1 as the eluent.

Single crystals of $[Au(PPh_3)CC(C_6H_4)Br]$ and $[Au(PPh_3)CC(C_6H_4)CN]$ suitable for X-ray diffraction analysis were grown from vapour diffusion of *n*-pentane into a concentrated solution in dichloromethane.

[Au(PPh$_3$)CC(C$_6$H$_4$)NO$_2$] (428 mg, 0.71 mmol, 70%):

^{1}H NMR (400 MHz, $CDCl_3$, 25 °C): δ = 8.11 (d, 2H, ^3J(^{1}H, ^{1}H) = 9.0 Hz, C*H*-C-NO_2), 7.60–7.43 (m, 17 H, *Ph*) ppm.

^{31}P{^{1}H} NMR (162 MHz, $CDCl_3$, 25 °C): δ = 42.7 (s) ppm.

^{13}C{^{1}H} NMR (101 MHz, $CDCl_3$, 25 °C): δ = 146.1 (s, 1C, *C*-C-NO_2), 134.4 (d, 6C, ^3J(^{31}P, ^{13}C) = 14 Hz, Ph: *ortho*-*C*H), 132.9 (s, 2C, *C*H-CH-C-C-NO_2), 132.4 (s, 1C, C-*C*-NO_2), 131.9 (s, 3C, Ph: *para*-*C*H), 129.4 (d, 6C, ^4J(^{31}P, ^{13}C) = 11 Hz, Ph: *meta*-*C*H), 129.5 (d, 3C, ^2J(^{31}P, ^{13}C) = 56 Hz, Ph: *ipso*-*C*), 123.6 (s, 2C, *C*H-C-C-NO_2) ppm.

IR (23 °C): $\tilde{\nu}_{C\equiv C}$ = 2117 cm^{-1}.

UV-Vis (THF, 23 °C): λ = 338, 236 nm.

ESI-MS [*m/z* (fragment, relative intensity)]: 1669 ([2M + Au(PPh$_3$)]$^+$, 68), 1064 ([M + Au(PPh$_3$)]$^+$, 100), 721 ([Au(PPh$_3$)$_2$]$^+$, 98) Da.

The data is in good agreement with that reported in literature.[127]

[Au(PPh$_3$)CC(C$_6$H$_4$)Br] (479 mg, 0.75 mmol, 74%):

^{1}H NMR (400 MHz, $CDCl_3$, 25 °C): δ = 7.65 (dd, 1H, *para*-C*H*-C-Br), 7.58–7.31 (m, 17 H, Ph), 7.10 (t, 1H, ^1J(^{1}H, ^{1}H) = 7.9 Hz, C*H*-CH-C-Br) ppm.

^{31}P{^{1}H} NMR (162 MHz, $CDCl_3$, 25 °C): δ = 42.0 (s) ppm.

$^{13}C\{^{1}H\}$ NMR (101 MHz, $CDCl_3$, 25 °C): δ = 135.2 (s, 1C, *para*-C*H*-C-Br), 134.5 (d, 6C, $^{3}J(^{31}P, ^{13}C)$ = 13.5 Hz, Ph: *ortho*-CH), 131.8 (s), 131.7 (s), 130.3 (d, 3C, $^{2}J(^{31}P, ^{13}C)$ = 51 Hz, Ph: *ipso*-C), 130.1 (s), 129.5 (s), 129.3 (d, 6C, $^{4}J(^{31}P, ^{13}C)$ = 11 Hz, Ph: *meta*-CH), 127.1 (s), 121.9 (s) ppm.

IR (23 °C): $\tilde{\nu}_{C\equiv C}$ = 2120 cm^{-1}.

UV-Vis (THF, 23 °C): λ = 286, 273, 232 nm.

ESI-MS [*m/z* (fragment, relative intensity)]: 1737 ($[2M + Au(PPh_3)]^+$, 93), 1099 ($[M + Au(PPh_3)]^+$, 100), 721 ($[Au(PPh_3)_2]^+$, 99) Da.

[Au(PPh$_3$)CC(C$_6$H$_4$)CN] (467 mg, 0.80 mmol, 79%):

^{1}H NMR (400 MHz, $CDCl_3$, 25 °C): δ = 7.74 (dd, 1H, *para*-C*H*-C-CN), 7.69–7.44 (m, 17 H, Ph), 7.34 (t, 1H, $^{1}J(^{1}H, ^{1}H)$ = 7.9 Hz, C*H*-CH-C-CN) ppm.

$^{31}P\{^{1}H\}$ NMR (162 MHz, $CDCl_3$, 25 °C): δ = 42.0 (s) ppm.

$^{13}C\{^{1}H\}$ NMR (101 MHz, $CDCl_3$, 25 °C): δ = 136.5 (s), 135.7 (s), 134.4 (d, 6C, $^{3}J(^{31}P, ^{13}C)$ = 14 Hz, Ph: *ortho*-CH), 131.8 (s), 131.8 (s), 129.9 (s), 129.7 (d, 3C, $^{2}J(^{31}P, ^{13}C)$ = 71 Hz, Ph: *ipso*-C), 129.4 (d, 6C, $^{4}J(^{31}P, ^{13}C)$ = 12 Hz, Ph: *meta*-CH), 129.0 (s) ppm.

IR (23 °C): $\tilde{\nu}_{C\equiv N}$ = 2231 cm^{-1}, $\tilde{\nu}_{C\equiv C}$ = 2115 cm^{-1}.

UV-Vis (THF, 23 °C): λ = 285, 272, 263 nm.

ESI-MS [*m/z* (fragment, relative intensity)]: 1629 ([2M + $Au(PPh_3)]^+$, 38), 1044 ([M + $Au(PPh_3)]^+$, 98), 721 ($[Au(PPh_3)_2]^+$, 100) Da.

8.5.12 Reaction of *cis*-Diazidoplatinum(II) with gold(I) alkynes

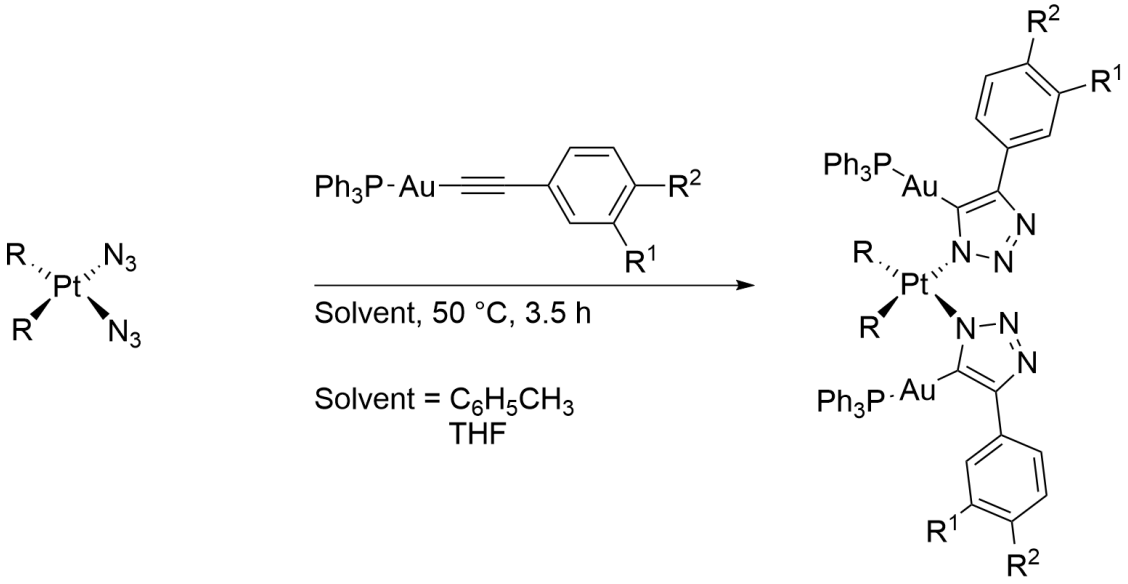

R = PEt_3, PPh_3, *py*

R^1 = H, R^2 = NO_2
R^1 = Br, R^2 = H
R^1 = CN, R^2 = H

R = PEt_3, PPh_3, *py*
R^1 = H, R^2 = NO_2
R^1 = Br, R^2 = H
R^1 = CN, R^2 = H

cis-$[Pt(N_3)_2R_2]$ (R = PEt_3, PPh_3, *py*) (1.0 eq) was dissolved in toluene (5 mL). $[Au(PPh_3)(CC(C_6H_4)NO_2)]$, $[Au(PPh_3)(CC(C_6H_4)Br)]$ or $[Au(PPh_3)(CC(C_6H_4)CN)]$ (2.0 eq) was dissolved in toluene (5 mL), added dropwise and the mixture was stirred at 50 °C for 3.5 hours yielding a suspension. The reaction mixture was filtered and the product was isolated as a colourless solid.

The reaction proceeded analogously in dried and degassed tetrahydrofuran under a nitrogen atmosphere.

Single crystals of **Pt,Et[2+3]Au,NO$_2$** suitable for X-ray diffraction analysis were grown from vapour diffusion of *n*-pentane into a concentrated solution in dichloromethane.

Single crystals of **Pt,Ph[2+3]Au,CN** suitable for X-ray diffraction analysis were isolated as yellow blocks after cooling a concentrated reaction mixture at 8 °C overnight.

Pt,Ph[2+3]Au,NO$_2$ (80%):

^{1}H NMR (400 MHz, $(CD_3)_2SO$, 25 °C): δ = 8.15–7.59 (m, *Ph*), 7.46–7.04 (m, *Ph*), 6.79-6.63 (m, *Ph*) ppm.

^{31}P{^{1}H} NMR (162 MHz, $CDCl_3$, 25 °C): δ = 43.5 (s, 2P, Au-*P*Ph_3), 7.8 (s, 2P, $^1J(^{31}P, ^{195}Pt)$ = 3110 Hz, Pt-*P*Ph_3) ppm.

^{13}C{^{1}H} NMR (101 MHz, $(CD_3)_2SO$, 25 °C): δ = 143.8, 134.5 (d, 3C, *J* = 14 Hz, *ipso-C*), 134.0, 131.8, 130.8, 130.3, 130.2, 129.6 (d, 3C, *J* = 11 Hz, *ipso-C*), 128.9, 128.2, 127.5, 124.6, 123.2 (*Ph*) ppm.

^{195}Pt NMR (86 MHz, $CDCl_3$, 25 °C): δ = −4079 (t, $^1J(^{31}P, ^{195}Pt)$ = 3110 Hz) ppm.

UV-Vis (THF, 23 °C): λ = 395, 240 nm.

ESI-MS [*m/z* (fragment, relative intensity)]: 2015 ($[M + H]^+$, 94), 1007 ($[M + 2H]^{2+}$, 100) Da.

The data is in good agreement with that reported in literature.[85]

Pt,Et[2+3]Au,NO$_2$ (83%):

^{1}H NMR (400 MHz, CDCl3, 25 °C): δ = 8.52 (d, 4H, ^3J(^{1}H, ^{1}H) = 9.0 Hz, *Ph*-NO$_2$), 8.00 (d, 4H, ^3J(^{1}H, ^{1}H) = 9.0 Hz, *Ph*-NO$_2$), 7.83–7.77 (m, 10H, Ph), 7.54–7.52 (m, 20H, Ph), 0.97 (qt, 15H, ^3J(^{1}H, ^{1}H) = 7.4 Hz, *Et*) ppm.

^{31}P{^{1}H} NMR (162 MHz, CDCl$_3$, 25 °C): δ = 43.6 (s, 2P, Au-*P*Ph$_3$), 0.4 (s, 2P, ^1J(^{31}P, ^{195}Pt) = 2934 Hz, Pt-*P*Et$_3$) ppm.

^{13}C{^{1}H} NMR (101 MHz, CDCl$_3$, 25 °C): δ = 135.0, 134.8, 131.2, 129.2, 129.1, 125.7, 123.6 (*Ph*), 14.3 (*C*H$_2$), 8.5 (*C*H$_3$) ppm.

^{195}Pt NMR (86 MHz, CDCl$_3$, 25 °C): δ = −4235 (t, ^1J(^{31}P, ^{195}Pt) = 2934 Hz) ppm.

UV-Vis (THF, 23 °C): λ = 410, 240 nm.

ESI-MS [*m/z* (fragment, relative intensity)]: 1726 ([M + H]$^+$, 100), 864 ([M + 2H]$^{2+}$, 98), 721 ([Au(PPh$_3$)$_2$]$^+$, 64) Da.

Pt,Et[2+3]Au,Br (77% (NMR yield)):

^{31}P{^{1}H} NMR (162 MHz, CDCl$_3$, 25 °C): δ = 43.7 (s, 2P, Au-*P*Ph$_3$), 0.4 (s, 2P, ^1J(^{31}P, ^{195}Pt) = 2945 Hz, Pt-*P*Et$_3$) ppm.

Pt,Ph[2+3]Au,Br (42% (NMR yield)):

$^{31}P\{^{1}H\}$ NMR (162 MHz, $CDCl_3$, 25 °C): δ = 43.4 (s, 2P, Au-*P*Ph_3), 7.6 (s, 2P, $^{1}J(^{31}P, ^{195}Pt)$ = 3098 Hz, Pt-*P*Ph_3) ppm.

Pt,Et[2+3]Au,CN (88%):

^{1}H NMR (400 MHz, CDCl3, 25 °C): δ = 8.63 (dt, 2H, $^{3}J(^{1}H, ^{1}H)$ = 8.0 Hz, $^{4}J(^{1}H, ^{1}H)$ = 1.5 Hz, *para*-C*H*-CCN), 8.58 (t, 2H $^{4}J(^{1}H, ^{1}H)$ = 1.7 Hz, *ortho*-C*H*-CCN), 7.91–7.65 (m, *Ph*), 7.59–7.36 (m, *Ph*), 7.15 (t, 2H, $^{3}J(^{1}H, ^{1}H)$ = 7.7 Hz, *meta*-C*H*-CCN), 1.01–0.81 (m, 15H, *Et*) ppm.

$^{31}P\{^{1}H\}$ NMR (162 MHz, $CDCl_3$, 25 °C): δ = 43.7 (s, 2P, Au-*P*Ph_3), 0.2 (s, 2P, $^{1}J(^{31}P, ^{195}Pt)$ = 2942 Hz, Pt-*P*Et_3) ppm.

$^{13}C\{^{1}H\}$ NMR (101 MHz, $CDCl_3$, 25 °C): δ = 138.6, 134.8, 134.6, 131.4, 131.0, 130.9, 130.2, 129.2, 129.1, 129.0, 128.1, 127.9, 120.0, 111.3 (Ph), 14.3 (d, 3C, $^{1}J(^{31}P, ^{13}C)$ = 36 Hz *C*H_2), 8.3 (s, 3C, *C*H_3) ppm.

^{195}Pt NMR (86 MHz, $CDCl_3$, 25 °C): δ = −4231 (t, $^{1}J(^{31}P, ^{195}Pt)$ = 2943 Hz) ppm.

UV-Vis (THF, 23 °C): λ = 229 nm.

ESI-MS [*m/z* (fragment, relative intensity)]: 1686 ($[M + H]^+$, 93), 1081 ([M – [2+3] + Na]$^{2+}$, 48), 844 ($[M + 2H]^{2+}$, 100), 721 ($[Au(PPh_3)_2]^+$, 93) Da.

Pt,Ph[2+3]Au,CN (83%):

^{1}H NMR (400 MHz, $CDCl_3$, 25 °C): δ = 8.22–6.71 (m, *Ph*) ppm.

^{31}P{^{1}H} NMR (162 MHz, $CDCl_3$, 25 °C): δ = 43.5 (s, 2P, Au-*P*Ph_3), 7.6 (s, 2P, $^{1}J(^{31}P, ^{195}Pt)$ = 3092 Hz, Pt-*P*Ph_3) ppm.

^{13}C{^{1}H} NMR (101 MHz, $CDCl_3$, 25 °C): δ = 139.0, 135.0 (d, 3C, *J* = 14 Hz, *ipso*-*C*), 131.9, 131.4, 131.2, 130.5, 129.9, 129.4 (d, 3C, *J* = 11 Hz, *ipso*-*C*), 129.2, 128.4, 127.9, 127.6, 125.4, 120.2, 111.0 ppm.

^{195}Pt NMR (86 MHz, $CDCl_3$, 25 °C): δ = −4077 (t, $^{1}J(^{31}P, ^{195}Pt)$ = 3093 Hz) ppm.

IR (23 °C): $\tilde{\nu}_{C\equiv N}$ = 2226 cm^{-1}

UV-Vis (THF, 23 °C): λ = 296, 289, 276, 240 nm.

ESI-MS [*m/z* (fragment, relative intensity)]: 1976 ($[M + H]^+$, 100), 988 ($[M + 2H]^{2+}$, 81), 721 ($[Au(PPh_3)_2]^+$, 64) Da.

Starting from ***cis*-[Pt(N$_3$)$_2$(*py*)$_2$]**:

The ^{31}P{^{1}H} NMR spectra showed unreacted starting material.

^{31}P{^{1}H} NMR (162 MHz, $CDCl_3$, 25 °C): δ = 41.9 (s) ppm.

^{1}H NMR (400 MHz, $CDCl_3$, 25 °C): δ = 8.86 (dd, 4H, $^{3}J(^{1}H, ^{1}H)$ = 5.1 Hz, $^{4}J(^{1}H, ^{1}H)$ = 1.5 Hz, *Py*: *ortho*-C*H*), 8.21–8.02 (m, *Ph*), 7.86 (tt, 2H,

$^{3}J(^{1}H, ^{1}H)$ = 7.7 Hz, $^{4}J(^{1}H, ^{1}H)$ = 1.6 Hz, *Py*: *para*-C*H*), 7.68–7.40 (m, *Ph*), 7.39 (dd, 4H, $^{3}J(^{1}H, ^{1}H)$ = 7.7, 5.1 Hz, *Py*: *meta*-C*H*) ppm.

^{195}Pt NMR (86 MHz, $CDCl_3$, 25 °C): δ = −2076 (b) ppm.

IR (23 °C): $\tilde{\nu}_{C\equiv C}$ = 2117 cm^{-1}, $\tilde{\nu}_{as}(N_3)$ = 2048 cm^{-1}.

8.5.13 Reaction of *cis*-Diazidodiphosphineplatinum(II) with Hydrogen Peroxide

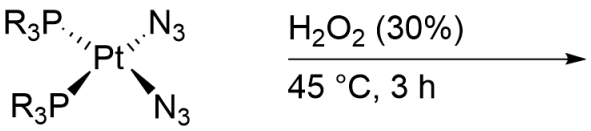

R = Et, Ph

cis-$[Pt(N_3)_2(PR_3)_2]$ (R = Et, Ph) (3.0 eq) was suspended in hydrogen peroxide (30% in water) (2.0 mL, 0.02 mmol, 1.0 eq) and the reaction mixture was stirred at 45 °C for 3 hours yielding a clear solution. The solvent was removed under vacuum and the solid was extracted three times with chloroform (1 mL). The organic phases were combined and the solvent was removed under vacuum.

The $^{31}P\{^{1}H\}$ NMR spectra showed the formation of the phosphine oxides and unreacted starting material.

Starting from ***cis*-$[Pt(N_3)_2(PEt_3)_2]$**:

$^{31}P\{^{1}H\}$ NMR (162 MHz, $CDCl_3$, 25 °C): δ = 53.9 (s), 7.3 (s, $^{1}J(^{31}P, ^{195}Pt)$ = 3338 Hz) ppm.

Starting from ***cis*-[Pt(N$_3$)$_2$(PPh$_3$)$_2$]**:

^{31}P{^{1}H} NMR (162 MHz, $CDCl_3$, 25 °C): δ = 29.2 (s), 12.0 (s, $^1J(^{31}P, ^{195}Pt)$ = 3507 Hz) ppm.

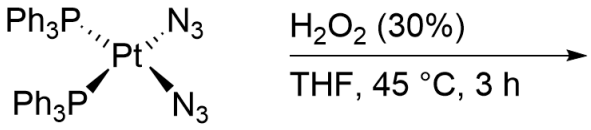

cis-[Pt(N$_3$)$_2$(PPh$_3$)$_2$] (50 mg, 0.06 mmol, 1.0 eq) was dissolved in tetrahydrofuran (0.5 mL). Hydrogen peroxide (30%, 0.1 mL, 0.98 mmol, 16.0 eq) was added and the reaction mixture was stirred at 45 °C for 3 hours yielding a clear solution. The solvent was removed under vacuum and the solid was extracted three times with chloroform (1 mL). The organic phases were combined and the solvent was removed under vacuum.

The ^{31}P{^{1}H} NMR spectra showed the formation of the phosphine oxides and unreacted starting material.

Starting from ***cis*-[Pt(N$_3$)$_2$(PEt$_3$)$_2$]**:

^{31}P{^{1}H} NMR (162 MHz, $CDCl_3$, 25 °C): δ = 53.9 (s), 7.3 (s, $^1J(^{31}P, ^{195}Pt)$ = 3338 Hz) ppm.

Starting from ***cis*-[Pt(N$_3$)$_2$(PPh$_3$)$_2$]**:

^{31}P{^{1}H} NMR (162 MHz, $CDCl_3$, 25 °C): δ = 29.2 (s), 12.0 (s, ^1J(^{31}P, ^{195}Pt) = 3507 Hz) ppm.

8.5.14 Reaction of *cis*-Diazidodiphosphineplatinum(II) with Dibenzoyl Peroxide

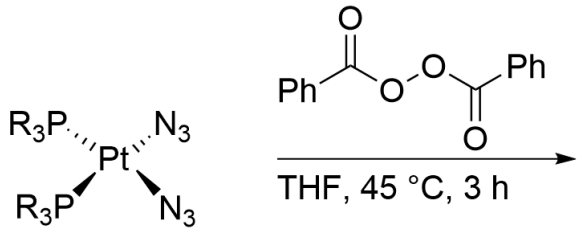

R = Et, Ph

The reaction was performed under a nitrogen atmosphere and with dry and degassed tetrahydrofuran. *cis*-[Pt(N$_3$)$_2$(PR$_3$)$_2$] (R = Et, Ph) (1.0 eq) was dissolved in tetrahydrofuran (0.5 mL). Dibenzoyl peroxide (48.2 mg, 0.20 mmol, 16.0 eq) was added and the reaction mixture was stirred at 45 °C for 3 hours yielding a clear solution. The solvent was removed under vacuum and the solid was extracted three times with chloroform (1 mL). The organic phases were combined and the solvent was removed under vacuum.

The ^{31}P{^{1}H} NMR spectra showed unreacted starting material.

Starting from ***cis*-[Pt(N$_3$)$_2$(PEt$_3$)$_2$]**:

^{31}P{^{1}H} NMR (162 MHz, $CDCl_3$, 25 °C): δ = 7.3 (s, ^1J(^{31}P, ^{195}Pt) = 3338 Hz) ppm.

Starting from ***cis*-[Pt(N$_3$)$_2$(PPh$_3$)$_2$]**:

^{31}P{^{1}H} NMR (162 MHz, $CDCl_3$, 25 °C): δ = 12.0 (s, $^1J(^{31}P, ^{195}Pt)$ = 3507 Hz) ppm.

8.5.15 Reaction of *cis*-Diazidodiphosphineplatinum(II) with *tert*-Butyl Hydrogen Peroxide

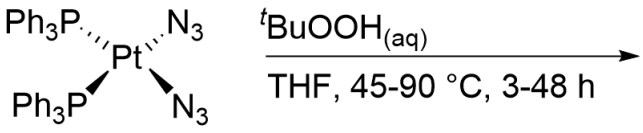

cis-[Pt(N$_3$)$_2$(PPh$_3$)$_2$] (10 mg, 0.01 mmol, 1.0 eq) was dissolved in tetrahydrofuran (0.5 mL). *tert*-Butyl hydrogen peroxide (70% in water) (28.0 µL, 0.20 mmol, 16.0 eq) was added and the reaction mixture was stirred at 45–90 °C for 3–48 hours yielding a clear solution. The solvent was removed under vacuum and the solid was extracted three times with chloroform (1 mL). The organic phases were combined and the solvent was removed under vacuum.

The ^{31}P{^{1}H} NMR spectra showed the formation of triphenylphosphine oxide.

^{31}P{^{1}H} NMR (162 MHz, $CDCl_3$, 25 °C): δ = 29.2 (s) ppm.

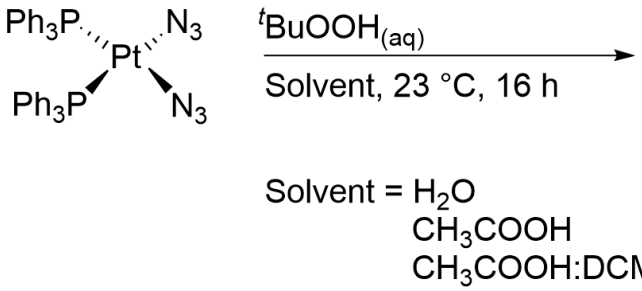

cis-[$Pt(N_3)_2(PPh_3)_2$] (10 mg, 0.012 mmol, 1.0 eq) was suspended in water (0.6 mL), acetic acid (98%) (0.6 mL), or in a mixture of *N*,*N*-dimethylformamide (0.2 mL), dichloromethane (0.2 mL) and acetic acid (98%) (0.2 mL). *tert*-Butyl hydrogen peroxide (70% in water) (14.0 µL, 0.10 mmol, 8.0 eq) was added and the reaction mixture was stirred at 23 °C for 16 hours yielding a clear solution. The solvent was removed under vacuum and the solid was extracted three times with chloroform (1 mL). The organic phases were combined and the solvent was removed under vacuum.

Reaction in water:

The $^{31}P\{^1H\}$ NMR spectra showed unreacted starting material.

$^{31}P\{^1H\}$ NMR (162 MHz, $CDCl_3$, 25 °C): δ = 12.0 (s, 1P, $^1J(^{31}P, ^{195}Pt)$ = 3507 Hz) ppm.

Reaction in acetic acid (98%) or in equal quantities of acetic acid (98%), dichloromethane and dimethylformamide:

Crystals suitable for X-ray diffraction analysis were isolated from a concentrated reaction mixture in chloroform.

***cis*-[Pt(N_3)(OAc)(PPh_3)$_2$]**:

$^{31}P\{^1H\}$ NMR (162 MHz, $CDCl_3$, 25 °C): δ = 4.9 (s, $^1J(^{31}P, ^{195}Pt)$ = 3838 Hz) ppm.

IR (23 °C): $\tilde{\nu}_{as}(N_3)$ = 2052 cm^{-1}.

ESI-MS [*m/z* (relative intensity)]: 1554 (21), 1033 (90), 764 (97), 754 (100) Da.

Further resonances were observed at 15.0 ppm (d, $^2J(^{31}P, ^{31}P)$ = 23.8 Hz) and at 4.0 ppm (d, $^2J(^{31}P, ^{31}P)$ = 23.7 Hz) in the $^{31}P\{^1H\}$ NMR spectrum.

8.5.16 Reaction of *cis*-Diazidodiphosphineplatinum(II) with *N*-Chlorosuccinimide

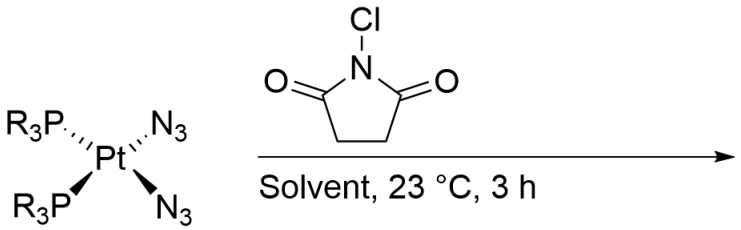

R = Et, Ph

Solvent = CH_3COOH (50-98%)
DMF
DMSO
H_2O, MeCN

cis-[Pt(N_3)$_2$(PR_3)$_2$] (R = Et, Ph) (1.0 eq) and *N*-chlorosuccinimide (1.70 mg, 0.01 mmol, 1.0 eq) were added to acetic acid (50-98%), dimethylformamide, dimethyl sulfoxide, or acetonitrile (0.8 mL). When using acetonitrile as a solvent, *N*-chlorosuccinimide was dissolved in water (<0.5 mL). The reaction mixture was stirred in the dark at 23 °C for 3 hours yielding a clear solution. The solvent was removed under vacuum and the solid was extracted three times with chloroform

(1 mL). The organic phases were combined and the solvent was removed under vacuum.

The $^{31}P\{^{1}H\}$ NMR spectra showed the formation of the phosphine oxides and *cis*-$[PtCl_2(PR_3)_2]$ (R = Et, Ph).

Reaction in dimethylformamide, dimethyl sulfoxide or acetic acid (50-70%):

Starting from ***cis*-[Pt(N$_3$)$_2$(PEt$_3$)$_2$]**:

$^{31}P\{^{1}H\}$ NMR (162 MHz, $CDCl_3$, 25 °C): δ = 53.9 (s), 9.1 (s, $^{1}J(^{31}P, ^{195}Pt)$ = 3515 Hz) ppm.

Starting from ***cis*-[Pt(N$_3$)$_2$(PPh$_3$)$_2$]**:

$^{31}P\{^{1}H\}$ NMR (162 MHz, $CDCl_3$, 25 °C): δ = 29.2 (s), 14.3 (s $^{1}J(^{31}P, ^{195}Pt)$ = 3675 Hz) ppm.

Reaction in acetic acid (≥80%):

The $^{31}P\{^{1}H\}$ NMR spectra showed multiple resonances, which could not all be assigned unambiguously.

Starting from ***cis*-[Pt(N$_3$)$_2$(PPh$_3$)$_2$]**:

$^{31}P\{^{1}H\}$ NMR (162 MHz, $CDCl_3$, 25 °C): δ = 4.9 (s, $^{1}J(^{31}P, ^{195}Pt)$ = 3838 Hz) ppm.

***cis*-[Pt(Cl)(N(CO$_2$)$_2$(CH$_2$)$_2$)(PPh$_3$)$_2$]**:

Single crystals suitable for X-ray diffraction analysis were isolated from a concentrated reaction mixture in an NMR sample in deuterated chloroform.

^{31}P{^{1}H} NMR (162 MHz, $CDCl_3$, 25 °C): δ = 15.0 ppm (d, 1P, ^2J(^{31}P, ^{31}P) = 23.8 Hz), 3.84 ppm (d, 1P, ^2J(^{31}P, ^{31}P) = 23.7 Hz) ppm.

Reaction in acetonitrile:

The ^{31}P{^{1}H} NMR spectra showed multiple resonances, which could not all be assigned unambiguously.

Starting from ***cis*-[Pt(N$_3$)$_2$(PPh$_3$)$_2$]**:

^{31}P{^{1}H} NMR (162 MHz, $CDCl_3$, 25 °C): δ = 0.4 (s, ^1J(^{31}P, ^{195}Pt) = 1584 Hz) ppm.

Starting from ***cis*-[Pt(N$_3$)$_2$(PEt$_3$)$_2$]**:

***trans*-[PtCl$_4$(PEt$_3$)$_2$]**:

One single crystal suitable for X-ray diffractometry was isolated from a concentrated solution in chloroform.

^{31}P{^{1}H} NMR (162 MHz, $CDCl_3$, 25 °C): δ = 5.7 (s, ^1J(^{31}P, ^{195}Pt) = 1461 Hz) ppm.

ESI-MS [*m/z* (relative intensity)]: 817 (76), 764 (100), 754 (63) Da.

8.5.17 Reaction of Potassium Hexachloridoplatinum(IV) and Triphenylphosphine

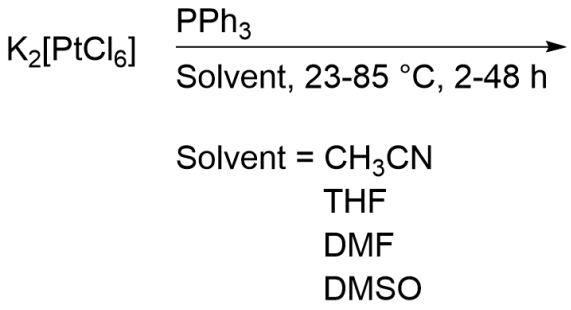

The reaction was performed under a nitrogen atmosphere and with dried and degassed solvents. $K_2[PtCl_6]$ (24.3 mg, 0.05 mmol, 1.0 eq) was suspended in either acetonitrile, tetrahydrofuran, dimethylformamide or dimethyl sulfoxide (4 mL). PPh_3 (26.2 mg, 0.10 mmol, 2.0 eq) was added and the reaction mixture was stirred at temperatures ranging from 23–85 °C for 2–48 hours and monitored *via* NMR spectroscopy.

For all solvents the $^{31}P\{^1H\}$ NMR spectra showed the formation of the triphenylphosphine oxide and cis-$[PtCl_2(PPh_3)_2]$.

$^{31}P\{^1H\}$ NMR (162 MHz, $CDCl_3$, 25 °C): δ = 29.2 (s), 14.3 (s, $^1J(^{31}P, ^{195}Pt)$ = 3675 Hz) ppm.

9. Bibliography

[1] B. Englinger, C. Pirker, P. Heffeter, A. Terenzi, C. R. Kowol, B. K. Keppler, W. Berger, *Chem. Rev.* **2019**, *119*, 1519.

[2] T. C. Johnstone, K. Suntharalingam, S. J. Lippard, *Phil. Trans. R. Soc. A* **2015**, *373*, 20140185.

[3] B. Desoize, *Anticancer Res.* **2004**, *24*, 1529.

[4] J. D. Hoeschele, *Dalton Trans.* **2016**, *45*, 12966.

[5] B. Rosenberg, L. van Camp, T. Krigas, *Nature* **1965**, *205*, 698.

[6] B. Rosenberg, L. van Camp, J. E. Trosko, V. H. Mansour, *Nature* **1969**, *222*, 385.

[7] S. Ghosh, *Bioorg. Chem.* **2019**, *88*, 102925.

[8] L. Kelland, *Nat. Rev. Cancer* **2007**, *7*, 573.

[9] S. Rottenberg, C. Disler, P. Perego, *Nat. Rev. Cancer* **2021**, *21*, 37.

[10] G. B. Kauffman, R. Pentimalli, S. Doldi, M. D. Hall, *Platin. Met. Rev.* **2010**, *54*, 250.

[11] T. C. Johnstone, K. Suntharalingam, S. J. Lippard, *Chem. Rev.* **2016**, *116*, 3436.

[12] M. R. Gill, K. A. Vallis, *Chem. Soc. Rev.* **2019**, *48*, 540.

[13] J. J. V. Branca, M. Maresca, G. Morucci, M. Becatti, F. Paternostro, M. Gulisano, C. Ghelardini, D. Salvemini, L. D. C. Mannelli, A. Pacini, *Oncotarget* **2018**, *9*, 23426.

[14] R. Paprocka, M. Wiese-Szadkowska, S. Janciauskiene, T. Kosmalski, M. Kulik, A. Helmin-Basa, *Coord. Chem. Rev.* **2022**, *452*, 85.

[15] P. M. Bruno, Y. Liu, G. Y. Park, J. Murai, C. E. Koch, T. J. Eisen, J. R. Pritchard, Y. Pommier, S. J. Lippard, M. T. Hemann, *Nat. Med.* **2017**, *23*, 461.

[16] S. Dilruba, G. V. Kalayda, *Cancer Chemother. Pharmacol.* **2016**, *77*, 1103.

[17] A. Kopacz-Bednarska, T. Król, *Nowotw. J. Oncol.* **2022**, *72*, 96.

[18] C. Zhang, C. Xu, X. Gao, Q. Yao, *Theranostics* **2022**, *12*, 2115.

[19] G. Natile, M. Coluccia, *Coord. Chem. Rev.* **2001**, *216–217*, 383.

[20] A. Khoury, K. M. Deo, J. R. Aldrich-Wright, *J. Inorg. Biochem.* **2020**, *207*, 111070.

[21] A. M. Pizarro, R. J. McQuitty, F. S. Mackay, Y. Zhao, J. A. Woods, P. J. Sadler, *ChemMedChem* **2014**, *9*, 1169.

[22] L. Cheng, C. Li, S. Yuan, H. Shi, L. Zhao, L. Zhang, F. Arnesano, G. Natile, Y. Liu, *Inorg. Chem.* **2019**, *58*, 6485.

[23] U. Kalinowska-Lis, J. Ochocki, K. Matlawska-Wasowska, *Coord. Chem. Rev.* **2008**, *252*, 1328.

[24] D. Gibson, *J. Inorg. Biochem.* **2021**, *217*, 111353.

[25] M. J. Cleare, J. D. Hoeschele, *Bioinorg. Chem.* **1973**, *2*, 187.

[26] E. Petruzzella, J. P. Braude, J. R. Aldrich-Wright, V. Gandin, D. Gibson, *Angew. Chemie - Int. Ed.* **2017**, *56*, 11539.

[27] R. G. Kenny, C. J. Marmion, *Chem. Rev.* **2019**, *119*, 1058.

[28] C. M. Giandomenico, M. J. Abrams, B. A. Murrer, J. F. Vollano, M. I. Rheinheimer, S. B. Wyer, G. E. Bossard, J. D. Higgins, *Inorg. Chem.* **1995**, *34*, 1015.

[29] J. J. Wilson, S. J. Lippard, *Chem. Rev.* **2014**, *114*, 4470.

[30] R. G. Kenny, S. W. Chuah, A. Crawford, C. J. Marmion, *Eur. J. Inorg. Chem.* **2017**, *2017*, 1596.

[31] R. G. Kenny, C. J. Marmion, in *Met. Anticancer Agents*, **2019**, pp. 1–30.

[32] A. Kastner, I. Poetsch, J. Mayr, J. V. Burda, A. Roller, P. Heffeter, B. K. Keppler, C. R. Kowol, *Angew. Chemie - Int. Ed.* **2019**, *58*, 7464.

[33] Z. Deng, G. Zhu, *Curr. Opin. Chem. Biol.* **2023**, *74*, DOI 10.1016/j.cbpa.2023.102303.

[34] S. Zheng, G. Li, J. Shi, X. Liu, M. Li, Z. He, C. Tian, K. Kamei, *J. Control. Release* **2023**, *361*, 819.

[35] D. Tsvetkova, S. Ivanova, *Molecules* **2022**, *27*, 2466.

[36] C. Marotta, E. Giorgi, F. Binacchi, D. Cirri, C. Gabbiani, A. Pratesi, *Inorganica Chim. Acta* **2023**, *548*, DOI 10.1016/j.ica.2023.121388.

[37] Z. Xu, Z. Wang, Z. Deng, G. Zhu, *Coord. Chem. Rev.* **2021**, *442*, 213991.

[38] X. Wang, X. Wang, S. Jin, N. Muhammad, Z. Guo, *Chem. Rev.* **2019**, *119*, 1138.

[39] A. Mojaddami, S. Abedanzadeh, M. Bagherzadeh, G. Foroutan, M. J. Khodayar, M. Panahimehr, M. Fereidoonnezhad, *Chem. Biodivers.* **2023**, *20*, e202201177.

[40] B. Saygideł̷er Demir, T. Keleş, O. Serindał̷, *Bioinorg. Chem. Appl.* **2014**, 717421.

[41] F. H. Abdalbari, C. M. Telleria, *Discov. Oncol.* **2021**, *12*, DOI 10.1007/s12672-021-00439-0.

[42] M. Yamashita, *Int. Immunopharmacol.* **2021**, *101*, 108272.

[43] S. Adhikari, P. Nath, A. Das, A. Datta, N. Baildya, A. K. Duttaroy, S. Pathak, *Biomed. Pharmacother.* **2024**, *171*, 116211.

[44] V. Gandin, A. P. Fernandes, M. P. Rigobello, B. Dani, F. Sorrentino, F. Tisato, M. Björnstedt, A. Bindoli, A. Sturaro, R. Rella, C. Marzano, *Biochem. Pharmacol.* **2010**, *79*, 90.

[45] G. Lupidi, L. Avenali, M. Bramucci, L. Quassinti, R. Pettinari, H. K. Khalife, H. Gali-Muhtasib, F. Marchetti, C. Pettinari, *J. Inorg. Biochem.* **2013**, *124*, 78.

[46] C. Icsel, V. T. Yilmaz, M. Aygun, M. Erkisa, E. Ulukaya, R. O. Akar, *Appl. Organomet. Chem.* **2024**, e7433.

[47] A. G. Quiroga, F. J. Ramos-Lima, A. Alvarez-Valdés, M. Font-Bardía, A. Bergamo, G. Sava, C. Navarro-Ranninger, *Polyhedron* **2011**, *30*, 1646.

[48] C. Santini, M. Pellei, G. Papini, B. Morresi, R. Galassi, S. Ricci, F. Tisato, M. Porchia, M. P. Rigobello, V. Gandin, C. Marzano, *J. Inorg. Biochem.* **2011**, *105*, 232.

[49] L. Ma, L. Li, G. Zhu, *Inorg. Chem. Front.* **2022**, *9*, 2424.

[50] W. Villarreal, L. Colina-Vegas, C. Rodrigues De Oliveira, J. C. Tenorio, J. Ellena, F. C. Gozzo, M. R. Cominetti, A. G. Ferreira, M. A. B. Ferreira, M. Navarro, A. A. Batista, *Inorg. Chem.* **2015**, *54*, 11709.

[51] M. Á. Medrano, A. Álvarez-Valdés, X. Huang, J. Lloret-Fillol, S. Muñoz-GalvÁn, A. Carnero, C. Navarro-Ranninger, A. G. Quiroga, *Chem. Commun.* **2013**, *49*, 4806.

[52] E. M. A. Al-Janabi, M. R. Hatshan, S. F. Adil, W. R. Kadhum, S. A. Al-Jibori, A. S. Faihan, A. S. Al-Janabi, *J. Mol. Struct.* **2022**, *1252*, 132227.

[53] M. Hyeraci, M. Colalillo, L. Labella, F. Marchetti, S. Samaritani, V. Scalcon, M. P. Rigobello, L. Dalla Via, *ChemMedChem* **2020**, *15*, 1464.

[54] V. T. Yilmaz, C. Icsel, O. R. Turgut, M. Aygun, M. Erkisa, M. H. Turkdemir, E. Ulukaya, *Eur. J. Med. Chem.* **2018**, *155*, 609.

[55] S. A. Elsayed, H. E. Badr, A. di Biase, A. M. El-Hendawy, *J. Inorg. Biochem.* **2021**, *223*, 111549.

[56] C. B. Smith, L. C. Days, D. R. Alajroush, K. Faye, Y. Khodour, S. J. Beebe, A. A. Holder, *Photochem. Photobiol.* **2022**, *98*, 17.

[57] G. Gunaydin, M. E. Gedik, S. Ayan, *Front. Chem.* **2021**, *9*, 691697.

[58] L. Huang, S. Zhao, J. Wu, L. Yu, N. Singh, K. Yang, M. Lan, P. Wang, J. S. Kim, *Coord. Chem. Rev.* **2021**, *438*, 213888.

[59] Y. Wu, S. Li, Y. Chen, W. He, Z. Guo, *Chem. Sci.* **2022**, *13*, 5085.

[60] H. Shi, P. J. Sadler, *Br. J. Cancer* **2020**, *123*, 871.

[61] L. Larue, A. Ben Mihoub, Z. Youssef, L. Colombeau, S. Acherar, J. C. André, P. Arnoux, F. Baros, M. Vermandel, C. Frochot, *Photochem. Photobiol. Sci.* **2018**, *17*, 1612.

[62] N. J. Farrer, L. Salassa, P. J. Sadler, *Dalton Trans.* **2009**, 10660.

[63] C. Ash, M. Dubec, K. Donne, T. Bashford, *Lasers Med. Sci.* **2017**, *32*, 1909.

[64] T. A. Shell, J. R. Shell, Z. L. Rodgers, D. S. Lawrence, *Angew. Chemie - Int. Ed.* **2014**, *53*, 875.

[65] T. A. Shell, D. S. Lawrence, *Accounts Chem. Res.* **2015**, *48*, 2866.

[66] S. Monro, K. L. Colón, H. Yin, J. Roque, P. Konda, S. Gujar, R. P. Thummel, L. Lilge, C. G. Cameron, S. A. McFarland, *Chem. Rev.* **2019**, *119*, 797.

[67] Z. Wang, N. Wang, S.-C. Cheng, K. Xu, Z. Deng, S. Chen, Z. Xu, K. Xie, M.-K. Tse, P. Shi, H. Hirao, C.-C. Ko, G. Zhu, *Chem Cell Press* **2019**, *5*, 3151.

[68] X. D. Ren, X. Y. Hao, H. C. Li, M. R. Ke, B. Y. Zheng, J. D. Huang, *Drug Discov. Today* **2018**, *23*, 1791.

[69] X. Chen, J. Song, X. Chen, H. Yang, *Chem. Soc. Rev.* **2019**, *48*, 3073.

[70] Z. Dai, Z. Wang, *Molecules* **2020**, *25*, 5167.

[71] S. Bonnet, *Dalton Trans.* **2018**, *47*, 10330.

[72] A. Presa, R. F. Brissos, A. B. Caballero, I. Borilovic, L. Korrodi-Gregório, R. Pérez-Tomás, O. Roubeau, P. Gamez, *Angew. Chemie - Int. Ed.* **2015**, *54*, 4561.

[73] J. Huang, W. Ding, X. Zhu, B. Li, F. Zeng, K. Wu, X. Wu, F. Wang, *Front. Chem.* **2022**, *10*, 876410.

[74] H. Shi, C. Imberti, P. J. Sadler, *Inorg. Chem. Front.* **2019**, *6*, 1623.

[75] R. Huisgen, *Angew. Chemie Int. Ed.* **1963**, *2*, 565.

[76] R. Huisgen, *Angew. Chemie - Int. Ed.* **1963**, *2*, 633.

[77] P. Kalra, R. Kaur, G. Singh, H. Singh, G. Singh, Pawan, G. Kaur, J. Singh, *J. Organomet. Chem.* **2021**, *944*, 121846.

[78] C. Wang, D. Ikhlef, S. Kahlal, J. Y. Saillard, D. Astruc, *Coord. Chem. Rev.* **2016**, *316*, 1.

[79] N. J. Agard, J. A. Prescher, C. R. Bertozzi, *J. Am. Chem. Soc.* **2004**, *126*, 15046.

[80] V. Delplace, *ACS Mater. Lett.* **2024**, *6*, 153.

[81] K. Peng, V. Mawamba, E. Schulz, M. Löhr, C. Hagemann, U. Schatzschneider, *Inorg. Chem.* **2019**, *58*, 11508.

[82] N. J. Farrer, D. M. Griffith, *Curr. Opin. Chem. Biol.* **2020**, *55*, 59.

[83] G. Wittig, A. Krebs, *Chem. Ber.* **1961**, *94*, 3260.

[84] I. V. Alabugin, S. Bresch, G. dos Passos Gomes, *J. Phys. Org. Chem.* **2015**, *28*, 147.

[85] A. R. Powers, X. Yang, T. J. Del Castillo, I. Ghiviriga, K. A. Abboud, A. S. Veige, *Dalton Trans.* **2013**, *42*, 14963.

[86] H. Friebolin, *Ein- Und Zweidimensionale NMR-Spektroskopie*, Wiley-VCH Verlag GmbH & Co. KGaA, **2013**.

[87] B. M. Still, P. G. A. Kumar, J. R. Aldrich-Wright, W. S. Price, *Chem. Soc. Rev.* **2007**, *36*, 665.

[88] J. R. L. Priqueler, I. S. Butler, F. D. Rochon, *Appl. Spectrosc. Rev.* **2006**, *41*, 185.

[89] S. O. Grim, R. L. Keiter, W. McFarlane, *Inorg. Chem.* **1967**, *6*, 1133.

[90] P. H. Kreutzer, J. C. Weis, H. Bock, J. Erbe, W. Beck, *Chem. Ber.* **1983**, *116*, 2691.

[91] P. S. Pregosin, *Coord. Chem. Rev.* **1982**, *44*, 247.

[92] W. McFarlane, *Q. Rev. Chem. Soc.* **1969**, *23*, 187.

[93] G. G. Mather, A. Pidcock, G. H. N. Rapsey, *J. Chem. Soc. Dalt. Trans.* **1973**, 2095.

[94] A. Pidcock, R. E. Richards, L. M. Venanzi, *J. Chem. Soc. A* **1966**, 1707.

[95] M. Van Beusichem, N. Farrell, *Inorg. Chem.* **1992**, *31*, 634.

[96] K. Yao, A. Bertran, J. Morgan, S. M. Hare, N. H. Rees, A. M. Kenwright, K. Edkins, A. M. Bowen, N. J. Farrer, *Dalton Trans.* **2019**, *48*, 6416.

[97] N. J. Farrer, G. Sharma, R. Sayers, E. Shaili, P. J. Sadler, *Dalton Trans.* **2018**, *47*, 10553.

[98] N. J. Farrer, J. A. Woods, L. Salassa, Y. Zhao, K. S. Robinson, G. Clarkson, F. S. Mackay, P. J. Sadler, *Angew. Chemie Int. Ed.* **2010**, *49*, 8905.

[99] E. Shaili, L. Salassa, J. A. Woods, G. Clarkson, P. J. Sadler, N. J. Farrer, *Chem. Sci.* **2019**, *10*, 8610.

[100] K. Yao, A. Bertran, A. Howarth, J. M. Goicoechea, S. M. Hare, N. H. Rees, M. Foroozandeh, A. M. Bowen, N. J. Farrer, *Chem. Commun.* **2019**, *55*, 11287.

[101] L. Goerigk, S. Grimme, *WIREs Comput. Mol. Sci.* **2014**, *4*, 576.

[102] F. Neese, T. Schwabe, S. Grimme, *J. Chem. Phys.* **2007**, *126*, 124115.

[103] M. Ríos-Gutiérrez, L. R. Domingo, *Eur. J. Org. Chem.* **2019**, *2019*, 267.

[104] U. F. Röhrig, S. R. Majjigapu, A. Grosdidier, S. Bron, V. Stroobant, L. Pilotte, D. Colau, P. Vogel, B. J. Van den Eynde, V. Zoete, O. Michielin, *J. Med. Chem.* **2012**, *55*, 5270.

[105] W. Beck, W. P. Fehlhammer, P. Pöllmann, E. Schuierer, K. Feldl, *Chem. Ber.* **1967**, *100*, 2335.

[106] J. E. W. Beck, J. Erbe, *Chem. Ber.* **1983**, *116*, 3867.

[107] Y. Zhao, J. A. Woods, N. J. Farrer, K. S. Robinson, J. Pracharova, J. Kasparkova, O. Novakova, H. Li, L. Salassa, A. M. Pizarro, G. J. Clarkson, L. Song, V. Brabec, P. J. Sadler, *Chem. Eur. J.* **2013**, *19*, 9578.

[108] F. S. Mackay, J. A. Woods, H. Moseley, J. Ferguson, A. Dawson, S. Parsons, P. J. Sadler, *Chem. Eur. J.* **2006**, *12*, 3155.

[109] W. Mcfarlane, *J. Chem. Soc. A* **1967**, 1922.

[110] L. Rigamonti, C. Manassero, M. Rusconi, M. Manassero, A. Pasini, *Dalton Trans.* **2009**, *2*, 1206.

[111] W. Oberhauser, C. Evangelisti, S. Caporali, V. Dal Santo, F. Bossola, F. Vizza, *J. Catal.* **2017**, *350*, 133.

[112] F. P. Fanizzi, F. P. Intini, L. Maresca, G. Natile, *J. Chem. Soc. Dalt. Trans.* **1990**, 199.

[113] E. Matern, J. Pikies, G. Fritz, *Z. Anorg. Allg. Chem.* **2000**, *626*, 2136.

[114] N. J. Farrer, J. A. Woods, V. P. Munk, F. S. MacKay, P. J. Sadler, *Chem. Res. Toxicol.* **2010**, *23*, 413.

[115] T. G. Appleton, H. C. Clark, L. E. Manzer, *Coord. Chem. Rev.* **1973**, *10*, 335.

[116] D. Schweinfurth, M. G. Sommer, M. Atanasov, S. Demeshko, S. Hohloch, F. Meyer, F. Neese, B. Sarkar, *J. Am. Chem. Soc.* **2015**, *137*, 1993.

[117] T. B. T. Ha, J.-P. Souchard, F. L. Wimmer, N. P. Johnson, *Polyhedron* **1990**, *9*, 2647.

[118] F. D. Rochon, P. C. Kong, *Can. J. Chem.* **1986**, *64*, 1894.

[119] E. G. Talman, W. Brüning, J. Reedijk, A. L. Spek, N. Veldman, *Inorg. Chem.* **1997**, *36*, 854.

[120] A. N. Biswas, V. Bagchi, P. Das, P. Bandyopadhyay, *Acta Crystallogr. Sect. E Struct. Reports Online* **2007**, *63*, m2836.

[121] T. Leyssens, D. Peeters, A. G. Orpen, J. N. Harvey, *Organometallics* **2007**, *26*, 2637.

[122] J. K. Burdett, *J. Am. Chem. Soc.* **1979**, *101*, 580.

[123] T. J. Johnson, K. Folting, W. E. Streib, J. D. Martin, J. C. Huffman, S. A. Jackson, O. Eisenstein, K. G. Caulton, *Inorg. Chem.* **1995**, *34*, 488.

[124] M. D. Butts, B. L. Scott, G. J. Kubas, *J. Am. Chem. Soc.* **1996**, *118*, 11831.

[125] L. G. Vanquickenborne, J. Vranckx, C. Görller-Walrand, *J. Am. Chem. Soc.* **1974**, *96*, 4121.

[126] P.-C. Kong, F. . D. Rochon, *Inorganica Chim. Acta* **1979**, *37*, L457.

[127] I. R. Whittall, M. G. Humphrey, S. Houbrechts, D. C. R. Hockless, *Organometallics* **1996**, *15*, 5738.

[128] D. Lin-Vien, N. B. Colthup, W. G. Fateley, J. G. Grasselli, *The Handbook*

of Infrared and Raman Characteristic Frequencies of Organic Molecules, Academic Press Limited, San Diego, **1991**.

[129] J. Z. Zhang, P. Bonnitcha, E. Wexselblatt, A. V. Klein, Y. Najajreh, D. Gibson, T. W. Hambley, *Chem. Eur. J.* **2013**, *19*, 1672.

[130] J. Z. Zhang, E. Wexselblatt, T. W. Hambley, D. Gibson, *Chem. Commun.* **2012**, *48*, 847.

[131] M. Ravera, E. Gabano, G. Pelosi, F. Fregonese, S. Tinello, D. Osella, *Inorg. Chem.* **2014**, *53*, 9326.

[132] Z. Xu, C. Li, Z. Tong, L. Ma, M. K. Tse, G. Zhu, *Eur. J. Inorg. Chem.* **2017**, *2017*, 1706.

[133] S. R. Whitfield, M. S. Sanford, *Organometallics* **2008**, *27*, 1683.

[134] J. L. Serrano, Y. Zheng, J. R. Dilworth, G. Sánchez, *Inorg. Chem. Commun.* **1999**, *2*, 407.

[135] L. Aslanov, R. Mason, A. G. Wheeler, P. O. Whimp, *Chem. Commun.* **1970**, 30.

[136] P. B. Hitchcock, B. Jacobson, A. Pidcock, *J. Organomet. Chem.* **1977**, 397.

[137] J. Zwinkels, *Light, Electromagnetic Spectrum*, Springer US, New York, **2016**.

[138] L. R. Snyder, J. J. Kirkland, J. W. Dolan, *Introduction to Modern Liquid Chromatography*, **2009**.

[139] G. M. Sheldrick, *Acta Crystallogr. Sect. C Struct. Chem.* **2015**, *71*, 3.

[140] G. M. Sheldrick, *Acta Crystallogr. Sect. A Found. Crystallogr.* **2008**, *64*, 112.

[141] O. V. Dolomanov, L. J. Bourhis, R. J. Gildea, J. A. K. Howard, H. Puschmann, *J. Appl. Crystallogr.* **2009**, *42*, 339.

[142] F. Furche, R. Ahlrichs, C. Hättig, W. Klopper, M. Sierka, F. Weigend, *WIREs Comput. Mol. Sci.* **2014**, *4*, 91.

[143] F. Weigend, *Phys. Chem. Chem. Phys.* **2006**, *8*, 1057.

[144] F. Weigend, A. Baldes, *J. Chem. Phys.* **2010**, *133*, 174102.

[145] J. P. Perdew, K. Burke, Y. Wang, *Phys. Rev. B - Condens. Matter Mater. Phys.* **1996**, *54*, 16533.

[146] A. D. Becke, *Phys. Rev. A At. Mol. Opt. Phys.* **1988**, *38*, 3098.

[147] J. P. Perdew, K. Burker, M. Enzerhof, *ACS Appl. Mater. Interfaces* **1996**, *77*, 3865.

[148] S. Grimme, *J. Chem. Phys.* **2006**, *124*, 034108.

[149] C. Lee, W. Yang, R. G. Parr, *Phys. Rev. B Condens. Matter* **1988**, *37*, 785.

[150] A. Klamt, G. Schüürmann, *J. Chem. Soc. Perkin Trans. 2* **1993**, 799.

[151] J. P. Souchard, F. L. Wimmer, T. T. B. Ha, N. P. Johnson, *J. Chem. Soc. Dalt. Trans.* **1990**, 307.

10. Appendix

10.1 Crystallographic Data

Table A1: Crystal data and structure refinement for *cis*-$[Pt(N_3)_2(PPh_3)_2]\cdot CHCl_3$

Compound	*cis*-$[Pt(N_3)_2(PPh_3)_2] \cdot CHCl_3$
Empirical formula	$C_{37}H_{31}Cl_3N_6P_2Pt$
Colour	yellow
Shape	block
Crystal system	orthorhombic
Space group	*Pbca*
a/Å	19.0696(5)
b/Å	16.7523(5)
c/Å	22.2617(6)
α/°	90
β/°	90
γ/°	90
V/Å^3	7111.7(3)
Z	8
ρ_{calc} g/cm^3	1.724
μ/mm^{-1}	4.299
F(000)	3632.0
Crystal size/mm^3	0.45 × 0.237 × 0.128
Radiation	MoK*α* (λ = 0.71073)
2*Θ* range for data collection/°	4.238 to 51.432
Index ranges	$-23 \le h \le 22$, $-20 \le k \le 20$, $-27 \le l \le 26$
Reflections collected	109820
Independent reflections	6757 [R_{int} = 0.0412, R_{sigma} = 0.0153]
Data/restraints/parameters	6757/0/462
Goodness-of-fit on F^2	1.087
Final *R* indexes [*I*>=2*σ* (*I*)]	R_1 = 0.0198, wR_2 = 0.0407
Final *R* indexes [all data]	R_1 = 0.0284, wR_2 = 0.0465
$e_{min/max}$/Å^{-3}	0.68/−0.74

Table A2: Crystal data and structure refinement for *cis*-[$Pt(N_3)_2(PEt_3)_2$]

Compound	*cis*-[$Pt(N_3)_2(PEt_3)_2$]
Empirical formula	$C_{12}H_{30}N_6P_2Pt$
Colour	yellow
Shape	block
Crystal system	monoclinic
Space group	$P2_1/c$
a/Å	10.1765(6)
b/Å	9.1137(5)
c/Å	20.3389(13)
α/°	90
β/°	96.768(2)
γ/°	90
V/Å^3	1873.20(19)
Z	4
ρ_{calc} g/cm^3	1.828
μ/mm^{-1}	7.665
F(000)	1008.0
Crystal size/mm^3	0.314 × 0.214 × 0.172
Radiation	MoKα (λ = 0.71073)
2*Θ* range for data collection/°	4.034 to 53.498
Index ranges	$-12 \leq h \leq 12$, $-11 \leq k \leq 11$, $-25 \leq l \leq 25$
Reflections collected	35569
Independent reflections	3978 [R_{int} = 0.0379, R_{sigma} = 0.0186]
Data/restraints/parameters	3978/0/196
Goodness-of-fit on F^2	1.240
Final *R* indexes [$I>=2\sigma(I)$]	R_1 = 0.0259, wR_2 = 0.0617
Final *R* indexes [all data]	R_1 = 0.0345, wR_2 = 0.0687
$e_{min/max}$/Å^{-3}	2.41/−1.95

Table A3: Crystal data and structure refinement for *trans*-$[PtI_2(PEt_3)]_2$

Compound	*trans*-$[PtI_2(PEt_3)]_2$
Empirical formula	$C_{12}H_{30}I_4P_2Pt_2$
Colour	red
Shape	block
Crystal system	monoclinic
Space group	$P2_1/n$
a/Å	9.0252(4)
b/Å	13.9568(5)
c/Å	9.5741(3)
α/°	90
β/°	92.2370(10)
γ/°	90
V/Å^3	1205.06(8)
Z	2
ρ_{calc} g/cm^3	3.125
μ/mm^{-1}	16.845
F(000)	1000.0
Crystal size/mm^3	0.326 × 0.212 × 0.203
Radiation	MoKα (λ = 0.71073)
2*Θ* range for data collection/°	5.162 to 58.276
Index ranges	$-12 \leq h \leq 12$, $-19 \leq k \leq 19$, $-12 \leq l \leq 13$
Reflections collected	32842
Independent reflections	3253 [R_{int} = 0.0464, R_{sigma} = 0.0229]
Data/restraints/parameters	3253/0/94
Goodness-of-fit on F^2	1.201
Final *R* indexes [$I>=2\sigma(I)$]	R_1 = 0.0261, wR_2 = 0.0539
Final *R* indexes [all data]	R_1 = 0.0334, wR_2 = 0.0589
$e_{min/max}$/Å^{-3}	1.43/−1.58

Table A4: Crystal data and structure refinement for *trans*-[PtI_2(*py*)(PPh_3)]

Compound	*trans*-[PtI_2(*py*)(PPh_3)]
Empirical formula	$C_{23}H_{20}I_2NPPt$
Colour	yellow
Shape	block
Crystal system	monoclinic
Space group	$P2_1/n$
a/Å	12.7312(6)
b/Å	11.1208(4)
c/Å	16.3912(8)
α/°	90
β/°	101.029(2)
γ/°	90
V/Å^3	2277.82(18)
Z	4
ρ_{calc} g/cm^3	2.304
μ/mm^{-1}	8.950
F(000)	1456.0
Crystal size/mm^3	0.233 × 0.187 × 0.178
Radiation	MoKα (λ = 0.71073)
2*Θ* range for data collection/°	4.452 to 51.376
Index ranges	−15 ≤ *h* ≤ 15, −13 ≤ *k* ≤ 13, −19 ≤ *l* ≤ 19
Reflections collected	88045
Independent reflections	4337 [R_{int} = 0.0510, R_{sigma} = 0.0162]
Data/restraints/parameters	4337/0/254
Goodness-of-fit on F^2	1.034
Final *R* indexes [*I*>=2*σ* (*I*)]	R_1 = 0.0142, wR_2 = 0.0303
Final *R* indexes [all data]	R_1 = 0.0180, wR_2 = 0.0317
$e_{min/max}$/Å^{-3}	0.53/−0.67

Table A5: Crystal data and structure refinement for *trans*-[PtI_2(*py*)(PEt_3)]

Compound	*trans*-[PtI_2(*py*)(PEt_3)]
Empirical formula	$C_{11}H_{20}I_2NPPt$
Colour	yellow
Shape	block
Crystal system	monoclinic
Space group	$P2_1/n$
a/Å	10.4873(4)
b/Å	14.4459(5)
c/Å	11.0973(3)
α/°	90
β/°	91.1870(10)
γ/°	90
V/Å^3	1680.86(10)
Z	4
ρ_{calc} g/cm^3	2.553
μ/mm^{-1}	12.096
F(000)	1168.0
Crystal size/mm^3	0.761 × 0.148 × 0.137
Radiation	MoKα (λ = 0.71073)
2*Θ* range for data collection/°	4.63 to 58.324
Index ranges	−14 ≤ *h* ≤ 14, −19 ≤ *k* ≤ 19, −15 ≤ *l* ≤ 15
Reflections collected	60588
Independent reflections	4519 [R_{int} = 0.0349, R_{sigma} = 0.0163]
Data/restraints/parameters	4519/0/149
Goodness-of-fit on F^2	1.223
Final *R* indexes [*I*>=2*σ* (*I*)]	R_1 = 0.0143, wR_2 = 0.0331
Final *R* indexes [all data]	R_1 = 0.0158, wR_2 = 0.0343
$e_{min/max}$/Å^{-3}	0.85/−0.73

Table A6: Crystal data and structure refinement for [Au(PPh$_3$)(CC(C$_6$H$_4$)Br)]

Compound	[Au(PPh$_3$)(CC(C$_6$H$_4$)Br)]
Empirical formula	$C_{26}H_{19}AuBrP$
Colour	yellow
Shape	block
Crystal system	orthorhombic
Space group	*Pbca*
a/Å	13.4726(4)
b/Å	16.3717(5)
c/Å	20.0796(6)
α/°	90
β/°	90
γ/°	90
V/Å^3	4428.9(2)
Z	8
ρ_{calc} g/cm^3	1.917
μ/mm^{-1}	8.530
F(000)	2432.0
Crystal size/mm^3	0.777 × 0.199 × 0.191
Radiation	MoKα (λ = 0.71073)
2Θ range for data collection/°	4.056 to 51.402
Index ranges	$-16 \leq h \leq 16$, $-19 \leq k \leq 19$, $-24 \leq l \leq 24$
Reflections collected	36034
Independent reflections	4218 [R_{int} = 0.0475, R_{sigma} = 0.0256]
Data/restraints/parameters	4218/0/263
Goodness-of-fit on F^2	1.054
Final *R* indexes [$I>=2\sigma(I)$]	R_1 = 0.0209, wR_2 = 0.0516
Final *R* indexes [all data]	R_1 = 0.0237, wR_2 = 0.0529
$e_{min/max}$/Å^{-3}	0.86/−1.15

Table A7: Crystal data and structure refinement for $[Au(PPh_3)(CC(C_6H_4)CN)]\cdot CH_2Cl_2$

Compound	$[Au(PPh_3)(CC(C_6H_4)CN)]$
Empirical formula	$C_{28}H_{19}AuNP\cdot CH_2Cl_2$
Colour	colourless
Shape	block
Crystal system	monoclinic
Space group	*C*2/*c*
a/Å	32.627(2)
b/Å	8.6259(5)
c/Å	18.2352(12)
α/°	90
β/°	107.635(2)
γ/°	90
V/Å^3	4890.9(5)
Z	8
ρ_{calc} g/cm^3	1.614
μ/mm^{-1}	6.095
F(000)	2280.0
Crystal size/mm^3	0.242 × 0.195 × 0.062
Radiation	MoK*α* (*λ* = 0.71073)
2*Θ* range for data collection/°	4.626 to 51.426
Index ranges	−39 ≤ *h* ≤ 39, −10 ≤ *k* ≤ 10, −22 ≤ *l* ≤ 22
Reflections collected	54426
Independent reflections	4675 [R_{int} = 0.0597, R_{sigma} = 0.0275]
Data/restraints/parameters	4675/0/246
Goodness-of-fit on F^2	1.134
Final *R* indexes [*I*>=2*σ* (*I*)]	R_1 = 0.0597, wR_2 = 0.1386
Final *R* indexes [all data]	R_1 = 0.0906, wR_2 = 0.1773
$e_{min/max}$/Å^{-3}	2.80/−2.50

Table A8: Crystal data and structure refinement for **Pt,Et[2+3]Au,NO_2**·2 $CHCl_3$

Compound	**Pt,Et[2+3]Au,NO_2** · 2 $CHCl_3$
Empirical formula	$C_{68}H_{73}Au_2Cl_{12}N_8O_4P_4Pt$
Colour	yellow
Shape	needle
Crystal system	monoclinic
Space group	*I*2/*a*
a/Å	26.4475(7)
b/Å	11.3589(5)
c/Å	29.3985(10)
α/°	90
β/°	94.870(3)
γ/°	90
V/Å^3	8799.9(5)
Z	4
ρ_{calc} g/cm^3	1.664
μ/mm^{-1}	13.471
F(000)	4276.0
Crystal size/mm^3	0.51 × 0.135 × 0.109
Radiation	CuK*α* (*λ* = 1.54184)
2*Θ* range for data collection/°	8.348 to 156.12
Index ranges	−30 ≤ *h* ≤ 33, −14 ≤ *k* ≤ 13, −36 ≤ *l* ≤ 36
Reflections collected	45738
Independent reflections	9159 [R_{int} = 0.0624, R_{sigma} = 0.0359]
Data/restraints/parameters	9159/0/481
Goodness-of-fit on F^2	1.070
Final *R* indexes [*I*>=2*σ* (*I*)]	R_1 = 0.0595, wR_2 = 0.1547
Final *R* indexes [all data]	R_1 = 0.0663, wR_2 = 0.1613
$e_{min/max}$/Å^{-3}	4.24/−4.43

Table A9: Crystal data and structure refinement for **Pt,Ph[2+3]Au,CN**·*n* $C_6H_5CH_3$

Compound	**Pt,Ph[2+3]Au,CN** · *n* $C_6H_5CH_3$
Empirical formula	$C_{97}H_{76}Au_2N_8P_4Pt$
Colour	yellow
Shape	block
Crystal system	monoclinic
Space group	$P2_1/n$
a/Å	21.0307(16)
b/Å	19.2985(13)
c/Å	23.5600(16)
α/°	90
β/°	113.843(2)
γ/°	90
V/Å^3	8746.0(11)
Z	4
ρ_{calc} g/cm^3	1.569
μ/mm^{-1}	5.066
F(000)	4040.0
Crystal size/mm^3	0.234 × 0.123 × 0.053
Radiation	MoK*α* (*λ* = 0.71073)
2*Θ* range for data collection/°	3.78 to 50.73
Index ranges	−25 ≤ *h* ≤ 25, −23 ≤ *k* ≤ 23, −28 ≤ *l* ≤ 28
Reflections collected	277574
Independent reflections	16027 [R_{int} = 0.1155, R_{sigma} = 0.0440]
Data/restraints/parameters	16027/0/1010
Goodness-of-fit on F^2	1.238
Final *R* indexes [*I*>=2*σ* (*I*)]	R_1 = 0.0997, wR_2 = 0.2537
Final *R* indexes [all data]	R_1 = 0.1700, wR_2 = 0.3592
$e_{min/max}$/Å^{-3}	8.40/−4.50

Table A10: Crystal data and structure refinement for *cis*-[Pt(N$_3$)(OAc)(PPh$_3$)$_2$]

Compound	*cis*-[Pt(N$_3$)(OAc)(PPh$_3$)$_2$]
Empirical formula	$C_{38}H_{33}N_3O_2P_2Pt$
Colour	yellow
Shape	block
Crystal system	orthorhombic
Space group	$P2_12_12_1$
a/Å	10.4269(3)
b/Å	17.2351(4)
c/Å	18.4440(6)
α/°	90
β/°	90
γ/°	90
V/Å^3	3314.55(16)
Z	4
ρ_{calc} g/cm^3	1.645
μ/mm^{-1}	4.369
F(000)	1624.0
Crystal size/mm^3	0.488 × 0.234 × 0.167
Radiation	MoK*α* (λ = 0.71073)
2*Θ* range for data collection/°	4.416 to 58.282
Index ranges	$-14 \leq h \leq 14$, $-23 \leq k \leq 23$, $-25 \leq l \leq 24$
Reflections collected	71846
Independent reflections	8852 [R_{int} = 0.0354, R_{sigma} = 0.0269]
Data/restraints/parameters	8852/0/417
Goodness-of-fit on F^2	1.107
Final *R* indexes [$I>=2\sigma(I)$]	R_1 = 0.0196, wR_2 = 0.0443
Final *R* indexes [all data]	R_1 = 0.0214, wR_2 = 0.0459
$e_{min/max}$/Å^{-3}	1.18/−1.64

Table A11: Crystal data and structure refinement for *cis*-[Pt(Cl)(N(CO)$_2$(CH$_2$)$_2$)(PPh$_3$)$_2$]

Compound	*cis*-[Pt(Cl)(N(CO)$_2$(CH$_2$)$_2$)(PPh$_3$)$_2$]
Empirical formula	$C_{40}H_{34}ClNO_2P_2Pt$
Colour	yellow
Shape	block
Crystal system	monoclinic
Space group	$P2_1/n$
a/Å	12.2283(4)
b/Å	19.8908(7)
c/Å	13.6429(4)
α/°	90
β/°	90.351(3)
γ/°	90
V/Å^3	3318.31(19)
Z	4
ρ_{calc} g/cm^3	1.708
μ/mm^{-1}	4.444
F(000)	1688.0
Crystal size/mm^3	0.239 × 0.181 × 0.133
Radiation	MoKα (λ = 0.71073)
2Θ range for data collection/°	3.62 to 52.79
Index ranges	$-13 \leq h \leq 15$, $-24 \leq k \leq 23$, $-17 \leq l \leq 17$
Reflections collected	34701
Independent reflections	6721 [R_{int} = 0.0561, R_{sigma} = 0.0459]
Data/restraints/parameters	6721/0/424
Goodness-of-fit on F^2	1.127
Final *R* indexes [I>=2σ (I)]	R_1 = 0.0354, wR_2 = 0.0719
Final *R* indexes [all data]	R_1 = 0.0470, wR_2 = 0.0768
$e_{min/max}$/Å^{-3}	1.17/−0.83

Table A12: Crystal data and structure refinement for *trans*-$[PtCl_4(PEt_3)_2]$

Compound	*trans*-$[PtCl_4(PPh_3)_2]$
Empirical formula	$C_{12}H_{30}Cl_4P_2Pt$
Colour	yellow
Shape	block
Crystal system	monoclinic
Space group	$P2_1/n$
a/Å	8.0495(7)
b/Å	12.3209(9)
c/Å	10.0187(8)
α/°	90
β/°	99.892(3)
γ/°	90
V/Å^3	978.85(14)
Z	2
ρ_{calc} g/cm^3	1.945
μ/mm^{-1}	7.864
F(000)	556.0
Crystal size/mm^3	0.549 × 0.357 × 0.236
Radiation	MoK*α* (λ = 0.71073)
2*Θ* range for data collection/°	5.288 to 51.42
Index ranges	$-9 \le h \le 9$, $-15 \le k \le 15$, $-12 \le l \le 12$
Reflections collected	15356
Independent reflections	1853 [R_{int} = 0.0420, R_{sigma} = 0.0237]
Data/restraints/parameters	1853/0/91
Goodness-of-fit on F^2	1.100
Final *R* indexes [*I*>=2*σ* (*I*)]	R_1 = 0.0205, wR_2 = 0.0514
Final *R* indexes [all data]	R_1 = 0.0214, wR_2 = 0.0524
$e_{min/max}$/Å^{-3}	2.13/−1.62

10.2 Cartesian Coordinates from DFT Calculations

Table A13: Cartesian coordinates of converged structure of **A** after geometry optimisation with *Turbomole 7.3*, the basis set def2-TZVP and the functional B2-PLYP (COSMO $\varepsilon = \infty$)

Atom	*x*	*y*	*z*
C	0.955542	-0.64851	-2.68797
N	0	0	-2.0183
C	-0.95554	0.648509	-2.68797
C	-0.98516	0.669216	-4.06434
C	0	0	-4.7674
C	0.985164	-0.66922	-4.06434
Pt	0	0	0.039251
N	-0.03142	-2.0612	0.05614
N	-1.05603	-2.58926	-0.27437
N	-1.98381	-3.14455	-0.57304
N	0	0	2.09377
C	-0.96489	-0.63374	2.762406
C	-0.99445	-0.65537	4.138779
C	0	0	4.841711
C	0.994452	0.655371	4.138779
C	0.964893	0.633739	2.762406
O	1.995525	-0.04934	0.032062
O	-1.99553	0.04934	0.032062
N	0.031425	2.061202	0.05614
N	1.05603	2.589257	-0.27437
N	1.983808	3.14455	-0.57304
H	1.723545	1.111248	2.174033
H	1.787929	1.178896	4.640478
H	0	0	5.91798
H	-1.78793	-1.1789	4.640478
H	-1.72354	-1.11125	2.174033
H	-2.26833	0.917127	0.320583
H	2.26833	-0.91713	0.320583
H	-1.70276	1.141536	-2.09901
H	-1.7717	1.20292	-4.56611
H	0	0	-5.84367

H	1.771704	-1.20292	-4.56611
H	1.702764	-1.14154	-2.09901

Table A14: Cartesian coordinates of converged structure of **A** after geometry optimisation with *Turbomole 7.3*, the basis set def2-TZVP and the functional B3-LYP (COSMO $\varepsilon = \infty$)

Atom	*x*	*y*	*z*
C	0.992595	-0.60713	-2.7041
N	0	0	-2.03149
C	-0.99259	0.607129	-2.7041
C	-1.01994	0.624098	-4.08728
C	0	0	-4.79394
C	1.019943	-0.6241	-4.08728
Pt	0	0	0.038137
N	-0.03945	-2.07996	0.054503
N	-1.07479	-2.61221	-0.26549
N	-2.01694	-3.18837	-0.55592
N	0	0	2.102699
C	-0.99528	-0.60238	2.774023
C	-1.0223	-0.62052	4.157214
C	0	0	4.863539
C	1.022304	0.620524	4.157214
C	0.995278	0.60238	2.774023
O	2.023787	-0.06002	0.03089
O	-2.02379	0.060023	0.03089
N	0.039453	2.079955	0.054503
N	1.074785	2.612209	-0.26549
N	2.016939	3.188371	-0.55592
H	1.775324	1.049215	2.177651
H	1.839057	1.116747	4.662454
H	0	0	5.945648
H	-1.83906	-1.11675	4.662454
H	-1.77532	-1.04922	2.177651
H	-2.27376	0.94373	0.330809
H	2.27376	-0.94373	0.330809
H	-1.76772	1.059318	-2.1065
H	-1.83547	1.122229	-4.59253

H	0	0	-5.87606
H	1.835473	-1.12223	-4.59253
H	1.767718	-1.05932	-2.1065

Table A15: Cartesian coordinates of converged structure of **A** after geometry optimisation with *Turbomole 7.3*, the basis set def2-TZVP and the functional BP-86 (COSMO $\varepsilon = \infty$)

Atom	*x*	*y*	*z*
C	0.987188	-0.63048	-2.69757
N	0	0	-2.02297
C	-0.98719	0.630479	-2.69757
C	-1.01282	0.646335	-4.08757
C	0	0	-4.79758
C	1.01282	-0.64633	-4.08757
Pt	0	0	0.037019
N	-0.01797	-2.08027	0.056595
N	-1.0526	-2.63058	-0.26969
N	-1.99142	-3.23987	-0.56533
N	0	0	2.093892
C	-1.00774	-0.59694	2.767139
C	-1.03356	-0.61292	4.157233
C	0	0	4.866913
C	1.03356	0.612922	4.157233
C	1.007738	0.59694	2.767139
O	2.036165	-0.048	0.026324
O	-2.03616	0.047999	0.026324
N	0.017967	2.080273	0.056595
N	1.0526	2.630585	-0.26969
N	1.991419	3.239871	-0.56533
H	1.796278	1.03408	2.158388
H	1.861614	1.104195	4.666247
H	0	0	5.956958
H	-1.86161	-1.10419	4.666247
H	-1.79628	-1.03408	2.158388
H	-2.27452	0.940226	0.342134
H	2.274515	-0.94023	0.342134
H	-1.75801	1.096284	-2.08866

H	-1.82481	1.163657	-4.59654
H	0	0	-5.88766
H	1.82481	-1.16366	-4.59654
H	1.758006	-1.09628	-2.08866

Table A16: Cartesian coordinates of converged structure of **A** after geometry optimisation with *Turbomole 7.3*, the basis set def2-TZVP and the functional PBE (COSMO $\varepsilon = \infty$)

Atom	*x*	*y*	*z*
C	0.970464	-0.6548	-2.69344
N	0	0	-2.01964
C	-0.97046	0.654802	-2.69344
C	-0.99593	0.671375	-4.08306
C	0	0	-4.79279
C	0.995932	-0.67138	-4.08306
Pt	0	0	0.036394
N	-0.00954	-2.07737	0.053769
N	-1.04581	-2.62569	-0.26735
N	-1.98842	-3.23025	-0.55926
N	0	0	2.089845
C	-0.99565	-0.61554	2.762421
C	-1.02142	-0.63207	4.152114
C	0	0	4.861635
C	1.021421	0.632066	4.152114
C	0.995654	0.615536	2.762421
O	2.035052	-0.04157	0.025007
O	-2.03505	0.041574	0.025007
N	0.009538	2.077371	0.053769
N	1.045814	2.625686	-0.26735
N	1.988416	3.230248	-0.55926
H	1.776497	1.068187	2.153992
H	1.840426	1.139296	4.661134
H	0	0	5.952161
H	-1.84043	-1.1393	4.661134
H	-1.7765	-1.06819	2.153992
H	-2.27387	0.931921	0.34486
H	2.27387	-0.93192	0.34486

H	-1.72912	1.141874	-2.08501
H	-1.79498	1.209332	-4.59213
H	0	0	-5.88339
H	1.794985	-1.20933	-4.59213
H	1.729122	-1.14187	-2.08501

Table A17: Cartesian coordinates of converged structure of **D** after geometry optimisation with *Turbomole 7.3*, the basis set def2-TZVP and the functional B2-PLYP (COSMO $\varepsilon = \infty$)

Atom	*x*	*y*	*z*
C	0.978154	-1.30004	-2.94956
N	-0.08649	-0.67916	-2.43899
C	-1.19122	-0.53369	-3.1737
C	-1.26531	-1.01515	-4.46111
C	-0.17197	-1.67203	-4.99608
C	0.967382	-1.81517	-4.22537
Pt	-0.05314	0.009946	-0.50517
N	0.332245	-1.89231	0.156167
N	1.477652	-2.23649	0.263439
N	2.521206	-2.62633	0.3875
N	-0.04576	0.675347	1.441045
C	1.050087	0.542682	2.192992
C	1.079334	0.961032	3.503157
C	-0.0559	1.534194	4.049231
C	-1.18373	1.667719	3.261303
C	-1.14619	1.224337	1.957703
N	-0.31294	1.90135	-1.14523
O	1.860729	0.581827	-0.71487
O	-1.97029	-0.46478	-0.32392
H	1.848821	-1.36272	-2.32572
H	1.842168	-2.31411	-4.60024
H	-0.20616	-2.06342	-5.998
H	-2.17044	-0.87668	-5.02379
H	-2.01886	-0.03765	-2.70538
H	-2.01303	-1.37113	-0.02603
H	-1.99901	1.290665	1.310758
H	-2.08776	2.107489	3.641267

H	-0.05977	1.871073	5.071282
H	1.979895	0.83635	4.076202
H	1.912376	0.109286	1.723115
N	-1.3857	2.663853	-1.26426
N	-0.99773	3.854307	-1.56868
C	0.352767	3.877257	-1.65099
C	0.79812	2.593485	-1.38213
C	2.118569	1.85846	-1.22189
C	2.921106	1.722513	-2.5135
C	4.244151	1.303671	-2.42564
C	4.993572	1.094118	-3.56914
C	4.429122	1.296289	-4.82062
C	3.11223	1.708381	-4.91388
C	2.364031	1.920926	-3.76509
H	4.685821	1.140529	-1.45853
H	6.01836	0.771716	-3.48491
H	5.012138	1.133297	-5.71183
H	2.662335	1.869214	-5.8795
H	1.343651	2.248931	-3.86136
O	2.934817	2.561687	-0.3155
H	2.521995	2.539309	0.545919
C	1.122543	5.079468	-2.00657
C	0.493863	6.429431	-1.89695
C	0.906674	7.414041	-2.79138
C	0.396706	8.695783	-2.70612
C	-0.51338	9.013637	-1.70825
C	-0.91607	8.043941	-0.80448
C	-0.42456	6.752899	-0.90372
H	1.622419	7.165467	-3.55555
H	0.710211	9.446721	-3.41154
H	-0.90508	10.01445	-1.63498
H	-1.61445	8.290715	-0.02275
H	-0.74465	6.007983	-0.1991
O	2.263226	4.971842	-2.39479

Table A18: Cartesian coordinates of converged structure of **D** after geometry optimisation with *Turbomole 7.3*, the basis set def2-TZVP and the functional B3-LYP (COSMO $\varepsilon = \infty$)

Atom	*x*	*y*	*z*
C	0.866506	-1.29174	-3.01828
N	-0.19456	-0.69271	-2.4539
C	-1.33786	-0.54886	-3.14463
C	-1.45204	-1.01144	-4.44325
C	-0.36652	-1.64388	-5.03572
C	0.808947	-1.78441	-4.3092
Pt	-0.0936	-0.03195	-0.49949
N	0.260438	-1.9718	0.125166
N	1.40341	-2.3578	0.193687
N	2.450335	-2.80232	0.287058
N	-0.02212	0.600758	1.467951
C	1.091301	0.417233	2.198982
C	1.155587	0.813782	3.522016
C	0.045347	1.414405	4.103152
C	-1.09781	1.597754	3.33673
C	-1.10307	1.177427	2.018225
N	-0.3271	1.88521	-1.1076
O	1.852393	0.506304	-0.77629
O	-2.04357	-0.48094	-0.26704
H	1.765412	-1.34903	-2.42364
H	1.679857	-2.2667	-4.72982
H	-0.43452	-2.01935	-6.04823
H	-2.38549	-0.87605	-4.97114
H	-2.15705	-0.07496	-2.62657
H	-2.07192	-1.39824	0.037538
H	-1.97002	1.277844	1.383934
H	-1.98473	2.060701	3.745741
H	0.071718	1.734055	5.136478
H	2.067514	0.649782	4.078451
H	1.933681	-0.03744	1.700041
N	-1.40993	2.659518	-1.24181
N	-1.00211	3.859696	-1.55651
C	0.359723	3.87058	-1.62635
C	0.798072	2.575617	-1.34426

C	2.115844	1.838996	-1.16825
C	2.986518	1.791048	-2.42415
C	4.359384	1.575516	-2.30048
C	5.157493	1.439878	-3.43174
C	4.593205	1.514839	-4.70242
C	3.224239	1.72532	-4.83091
C	2.428189	1.861891	-3.69803
H	4.80601	1.516823	-1.31735
H	6.222679	1.27581	-3.31969
H	5.214814	1.410765	-5.5834
H	2.773224	1.788029	-5.81388
H	1.366083	2.034376	-3.81878
O	2.883595	2.493981	-0.16142
H	2.365714	2.508499	0.654372
C	1.147568	5.063084	-1.97944
C	0.514404	6.417908	-1.95985
C	0.993829	7.373785	-2.864
C	0.483056	8.664104	-2.86254
C	-0.49638	9.023984	-1.93852
C	-0.96601	8.085685	-1.02424
C	-0.47345	6.785076	-1.04005
H	1.763725	7.091747	-3.57044
H	0.849268	9.390861	-3.57703
H	-0.88975	10.03314	-1.93055
H	-1.71864	8.365296	-0.29752
H	-0.84544	6.063994	-0.32724
O	2.323487	4.94127	-2.29959

Table A19: Cartesian coordinates of converged structure of **D** after geometry optimisation with *Turbomole 7.3*, the basis set def2-TZVP and the functional BP-86 (COSMO $\varepsilon = \infty$)

Atom	*x*	*y*	*z*
C	0.881009	-1.25802	-3.03164
N	-0.20593	-0.70053	-2.45595
C	-1.37164	-0.61369	-3.13311
C	-1.48042	-1.09284	-4.43355
C	-0.3692	-1.67965	-5.04064

C	0.826264	-1.76303	-4.32553
Pt	-0.10619	-0.03163	-0.50905
N	0.224541	-1.97906	0.109064
N	1.369373	-2.3554	0.277918
N	2.417249	-2.8089	0.465662
N	-0.03207	0.605969	1.450423
C	1.097653	0.44677	2.176091
C	1.163844	0.8585	3.501924
C	0.04276	1.447257	4.089633
C	-1.116	1.602135	3.328184
C	-1.12652	1.169443	2.006633
N	-0.33335	1.882179	-1.1203
O	1.855786	0.494295	-0.78776
O	-2.07186	-0.47925	-0.27245
H	1.791732	-1.26613	-2.43633
H	1.718556	-2.21316	-4.75759
H	-0.43282	-2.06426	-6.05853
H	-2.43401	-1.00563	-4.95216
H	-2.2079	-0.17526	-2.59269
H	-2.0796	-1.40051	0.05307
H	-2.00504	1.240013	1.368934
H	-2.01511	2.054069	3.744264
H	0.072947	1.781583	5.12655
H	2.089909	0.714029	4.056133
H	1.947995	0.000991	1.663602
N	-1.42693	2.663571	-1.25454
N	-1.00983	3.872282	-1.57539
C	0.361596	3.877567	-1.64829
C	0.800631	2.574278	-1.36362
C	2.117552	1.838864	-1.18059
C	2.994351	1.783959	-2.43323
C	4.371578	1.557016	-2.30299
C	5.175265	1.413549	-3.43743
C	4.611945	1.491058	-4.71569
C	3.238044	1.712605	-4.84979
C	2.436043	1.857873	-3.7146
H	4.815466	1.495896	-1.30943

H	6.246979	1.241212	-3.32151
H	5.239874	1.380693	-5.60134
H	2.787559	1.777699	-5.84171
H	1.367214	2.042719	-3.83514
O	2.889266	2.500621	-0.16751
H	2.341523	2.53783	0.639532
C	1.152901	5.068079	-2.00776
C	0.524791	6.426904	-1.96322
C	1.019404	7.404956	-2.84639
C	0.511986	8.70286	-2.82142
C	-0.47915	9.04897	-1.89399
C	-0.96241	8.08943	-0.99861
C	-0.47371	6.781169	-1.0383
H	1.80092	7.128905	-3.55549
H	0.889951	9.448838	-3.52216
H	-0.87224	10.06662	-1.86894
H	-1.72368	8.360015	-0.26539
H	-0.85405	6.039534	-0.33813
O	2.334063	4.940875	-2.35345

Table A20: Cartesian coordinates of converged structure of **D** after geometry optimisation with *Turbomole 7.3*, the basis set def2-TZVP and the functional PBE (COSMO $\varepsilon = \infty$)

Atom	*x*	*y*	*z*
C	0.779487	-1.24535	-3.0516
N	-0.27277	-0.66452	-2.43846
C	-1.44151	-0.49935	-3.09354
C	-1.5898	-0.9225	-4.4089
C	-0.51523	-1.53488	-5.05432
C	0.684913	-1.69746	-4.36214
Pt	-0.11411	-0.0461	-0.48206
N	0.22194	-1.99887	0.106566
N	1.363534	-2.41745	0.095792
N	2.412668	-2.90434	0.119557
N	0.020601	0.551657	1.482173
C	1.155494	0.331965	2.181774
C	1.262847	0.713383	3.513489

C	0.177767	1.333866	4.134104
C	-0.98656	1.552612	3.398176
C	-1.03855	1.147821	2.069276
N	-0.33804	1.876114	-1.05687
O	1.842523	0.4608	-0.81109
O	-2.07555	-0.48007	-0.20034
H	1.701027	-1.3137	-2.47577
H	1.55161	-2.16774	-4.8251
H	-0.61107	-1.87935	-6.08455
H	-2.54519	-0.77064	-4.91002
H	-2.25017	-0.0428	-2.52577
H	-2.08203	-1.4104	0.096956
H	-1.92517	1.27097	1.450105
H	-1.85841	2.033977	3.839706
H	0.239793	1.642967	5.177962
H	2.193119	0.521232	4.0468
H	1.978598	-0.13606	1.644223
N	-1.42768	2.65939	-1.18698
N	-1.01005	3.86296	-1.51977
C	0.359886	3.863243	-1.6041
C	0.796287	2.560586	-1.31477
C	2.108651	1.817561	-1.14005
C	2.999263	1.802446	-2.38284
C	4.383873	1.64085	-2.24734
C	5.196462	1.527097	-3.37867
C	4.634639	1.570971	-4.65827
C	3.252432	1.728234	-4.79745
C	2.441918	1.841844	-3.666
H	4.827721	1.607271	-1.25192
H	6.274955	1.404134	-3.25853
H	5.269868	1.483845	-5.54182
H	2.802387	1.767613	-5.7915
H	1.364844	1.973242	-3.79024
O	2.863378	2.445666	-0.09433
H	2.291176	2.489132	0.694589
C	1.159116	5.044149	-1.97373
C	0.529932	6.402385	-1.99513

C	1.048353	7.345399	-2.90129
C	0.542896	8.643136	-2.93939
C	-0.47043	9.025083	-2.05195
C	-0.97829	8.100767	-1.13438
C	-0.49134	6.791991	-1.11134
H	1.847989	7.041335	-3.57896
H	0.940123	9.36151	-3.65883
H	-0.86134	10.04413	-2.07461
H	-1.75874	8.399494	-0.43215
H	-0.89187	6.077163	-0.39402
O	2.350708	4.908346	-2.27609

Table A21: Cartesian coordinates of converged structure of **F** after geometry optimisation with *Turbomole 7.3*, the basis set def2-TZVP and the functional B2-PLYP (COSMO $\varepsilon = \infty$)

Atom	*x*	*y*	*z*
Pt	1.015569	4.457886	3.863916
N	3.066412	4.240615	3.903162
N	-1.03526	4.675401	3.825652
N	1.008325	4.043552	1.851638
N	1.022953	4.872077	5.876123
N	3.801327	5.15415	3.711051
N	-1.77029	3.76108	4.013467
C	0.374955	2.966175	1.384251
C	1.634993	4.848916	0.991965
C	0.402481	4.062708	6.736493
C	1.650571	5.953134	6.342719
N	4.556069	5.977412	3.5376
N	-2.52517	2.937092	4.182866
H	-0.11553	2.339228	2.105797
C	0.347325	2.655679	0.042293
C	1.648092	4.606944	-0.36425
H	2.131588	5.707908	1.404014
H	-0.08954	3.200893	6.324817
C	0.390288	4.304112	8.092823
C	1.678353	6.263497	7.684711
H	2.136063	6.583115	5.62042

H	-0.17408	1.774745	-0.28571
C	0.993818	3.490123	-0.85109
H	2.16399	5.287096	-1.01747
H	-0.12031	3.620608	8.746716
C	1.038523	5.424784	8.578905
H	2.194819	7.147551	8.01214
H	0.987814	3.274494	-1.90552
H	1.045053	5.640145	9.633392

Table A22: Cartesian coordinates of converged structure of **G** after geometry optimisation with *Turbomole 7.3*, the basis set def2-TZVP and the functional B2-PLYP (COSMO $\varepsilon = \infty$)

Atom	*x*	*y*	*z*
P	0.733111	3.961367	1.486123
Pt	0.909145	4.570827	3.784811
N	-0.95529	5.46611	3.815019
N	-1.96222	4.947173	3.464934
N	-2.96102	4.516352	3.155507
N	2.750641	3.660727	3.843746
N	3.756792	4.280616	3.71584
N	4.751351	4.801419	3.603128
C	0.064323	2.280965	1.265219
C	0.214547	1.585097	0.066673
C	-0.32539	0.320997	-0.08285
C	-1.01954	-0.26758	0.963439
C	-1.169	0.411194	2.16024
C	-0.62768	1.677397	2.309495
H	0.757464	2.02261	-0.75312
H	-0.20185	-0.20508	-1.01427
H	-1.43641	-1.25373	0.846513
H	-1.70002	-0.0436	2.97914
H	-0.73647	2.190158	3.249051
C	-0.34074	5.093324	0.539649
C	-1.20557	4.651492	-0.45574
C	-1.97244	5.555898	-1.17161
C	-1.88165	6.911197	-0.90376
C	-1.02591	7.361154	0.089015

C	-0.26709	6.457617	0.810638
H	-1.29584	3.604026	-0.67855
H	-2.6405	5.19814	-1.93685
H	-2.4783	7.613464	-1.46147
H	-0.95417	8.413322	0.306928
H	0.378303	6.818855	1.592187
C	2.32303	3.947267	0.585083
C	3.208454	2.887431	0.774563
C	4.434641	2.874725	0.137127
C	4.798684	3.922195	-0.6957
C	3.92825	4.980021	-0.88734
C	2.696709	4.993463	-0.25071
H	2.94363	2.06761	1.418085
H	5.105634	2.046344	0.290091
H	5.754261	3.910531	-1.19264
H	4.200136	5.796512	-1.53487
H	2.033475	5.821944	-0.42115
P	1.070376	5.254906	6.063413
C	0.608416	7.011618	6.215506
C	-0.21351	7.49133	7.22755
C	-0.5258	8.840292	7.296996
C	-0.01626	9.722221	6.359932
C	0.802846	9.251501	5.344872
C	1.105843	7.904746	5.269446
H	-0.62245	6.82338	7.964048
H	-1.16768	9.197495	8.08455
H	-0.25898	10.77011	6.41566
H	1.19865	9.930478	4.60865
H	1.73037	7.550746	4.466297
C	2.724621	5.110233	6.820597
C	3.261889	3.836312	7.001215
C	4.512583	3.676137	7.564502
C	5.248943	4.786789	7.952264
C	4.72529	6.053962	7.775032
C	3.468219	6.216404	7.211451
H	2.703829	2.965441	6.703386
H	4.91394	2.686073	7.700995

H	6.224551	4.660967	8.391159
H	5.288393	6.921083	8.076608
H	3.076355	7.209856	7.089188
C	-0.00589	4.317927	7.200939
C	0.226537	4.331529	8.575128
C	-0.59933	3.630245	9.434949
C	-1.66601	2.900223	8.93406
C	-1.90286	2.874881	7.570468
C	-1.07704	3.579372	6.710009
H	1.054951	4.885277	8.9816
H	-0.40751	3.651863	10.49434
H	-2.30583	2.350696	9.60382
H	-2.72605	2.304787	7.174347
H	-1.26852	3.549826	5.653682

Table A23: Cartesian coordinates of converged structure of **H** after geometry optimisation with *Turbomole 7.3*, the basis set def2-TZVP and the functional B2-PLYP (COSMO $\varepsilon = \infty$)

Atom	*x*	*y*	*z*
C	-0.86732	5.812763	7.468594
C	0.152391	4.913339	7.16851
C	0.177957	3.689127	7.831323
C	-0.79078	3.372061	8.767655
C	-1.7966	4.276248	9.06118
C	-1.83099	5.497736	8.409402
P	1.434109	5.335663	5.930044
C	2.857346	4.300507	6.440124
C	3.020451	3.040342	5.87239
C	4.047722	2.207976	6.279637
C	4.935982	2.629516	7.255538
C	4.78929	3.885525	7.819229
C	3.755113	4.71504	7.41695
Pt	1.093676	5.006134	3.636264
N	1.167108	4.55531	1.598544
N	1.499749	5.368681	0.803764
N	1.809359	6.097706	-0.00381
P	-1.22697	4.884067	3.523687

C	-1.85411	4.946747	1.801828
C	-1.79415	3.797402	1.015745
C	-2.24878	3.812315	-0.2883
C	-2.76481	4.979498	-0.83333
C	-2.82186	6.126871	-0.06445
C	-2.36914	6.111188	1.247002
C	-1.96163	3.340308	4.152268
C	-3.30738	3.044092	3.929674
C	-3.84737	1.853977	4.376552
C	-3.04855	0.931823	5.037612
C	-1.70933	1.205179	5.244638
C	-1.17101	2.403302	4.803211
C	-2.03909	6.306224	4.328264
C	-3.25721	6.218531	4.992286
C	-3.84479	7.350153	5.531674
C	-3.22573	8.583131	5.412609
C	-2.01086	8.681431	4.75411
C	-1.42126	7.549863	4.219381
N	3.170868	5.321441	3.510657
N	3.8644	4.542425	2.945961
N	4.575329	3.837214	2.422785
C	1.879489	7.065231	6.310832
C	1.859485	7.545086	7.619714
C	2.227015	8.849061	7.897863
C	2.616394	9.695595	6.872141
C	2.637799	9.230815	5.568612
C	2.272428	7.924619	5.289177
H	-3.93651	3.731422	3.391595
H	-4.88818	1.641367	4.20056
H	-3.46935	0.001107	5.379187
H	-1.08005	0.488206	5.743787
H	-0.12552	2.597734	4.953773
H	-3.75141	5.272904	5.112713
H	-4.78497	7.264472	6.049607
H	-3.68464	9.461604	5.834007
H	-1.52043	9.635166	4.658819
H	-0.47461	7.641015	3.715106

H	-1.39366	2.884007	1.41918
H	-2.19979	2.913872	-0.88025
H	-3.12085	4.990083	-1.84987
H	-3.22287	7.037648	-0.4763
H	-2.43405	7.013868	1.82644
H	1.552619	6.908852	8.430542
H	2.206086	9.20242	8.914832
H	2.898178	10.71236	7.088791
H	2.936058	9.882915	4.765218
H	2.302403	7.578014	4.273295
H	2.351764	2.702295	5.099146
H	4.156395	1.235828	5.829488
H	5.740005	1.985575	7.569983
H	5.479028	4.224773	8.573631
H	3.66603	5.686009	7.868704
H	0.957231	2.976204	7.63379
H	-0.75198	2.420685	9.270564
H	-2.54634	4.033511	9.795354
H	-2.60704	6.209236	8.634266
H	-0.90814	6.770825	6.983422

Table A24: Cartesian coordinates of converged structure of **I** after geometry optimisation with *Turbomole 7.3*, the basis set def2-TZVP and the functional B2-PLYP (COSMO $\varepsilon = \infty$)

Atom	*x*	*y*	*z*
Pt	0	0	0
O	-0.23052	-1.98377	0
O	0.230517	1.983767	0
N	2.040478	-0.29797	0
N	-2.04048	0.297966	0
N	0	0	-2.06036
N	0	0	2.060356
H	0.640213	-2.37454	0
H	-0.64021	2.374541	0
N	2.752226	0.665879	0
N	-2.75223	-0.66588	0
C	-0.61598	-0.97604	-2.72972

C	0.615976	0.976045	-2.72972
C	-0.61598	-0.97604	2.729724
C	0.615976	0.976045	2.729724
N	3.475641	1.524084	0
N	-3.47564	-1.52408	0
H	-1.07366	-1.74511	-2.13899
C	-0.63997	-1.00392	-4.10627
C	0.63997	1.003924	-4.10627
H	1.073656	1.745105	-2.13899
H	-1.07366	-1.74511	2.138986
C	-0.63997	-1.00392	4.106271
C	0.63997	1.003924	4.106271
H	1.073656	1.745105	2.138986
H	-1.15076	-1.80569	-4.60776
C	0	0	-4.80959
H	1.150764	1.805687	-4.60776
H	-1.15076	-1.80569	4.607764
C	0	0	4.809586
H	1.150764	1.805687	4.607764
H	0	0	-5.88592
H	0	0	5.885919

Table A25: Cartesian coordinates of converged structure of **K** after geometry optimisation with *Turbomole 7.3*, the basis set def2-TZVP and the functional B2-PLYP (COSMO $\varepsilon = \infty$)

Atom	*x*	*y*	*z*
O	-0.66063	-2.1897	0.028184
Pt	-0.29008	-0.21506	-0.03003
P	-0.34464	-0.19815	2.427439
O	0.074655	1.763849	-0.08944
N	1.741158	-0.58714	0.116604
N	2.507549	0.321832	-0.01896
N	3.292255	1.116513	-0.13353
N	-2.3232	0.135502	-0.19799
N	-3.08432	-0.75063	0.05416
N	-3.86626	-1.52895	0.267702
P	-0.22584	-0.18305	-2.48663

H	-0.71243	-2.53586	-0.85649
H	0.261185	2.087849	0.785651
C	0.513125	-1.5707	3.259294
C	0.754983	-1.47042	4.630547
C	1.397484	-2.49112	5.303232
C	1.811697	-3.62213	4.614079
C	1.577739	-3.72549	3.254897
C	0.930319	-2.70443	2.574415
H	0.446442	-0.59648	5.178556
H	1.577276	-2.40309	6.361239
H	2.316074	-4.41673	5.138091
H	1.899695	-4.60095	2.716382
H	0.740887	-2.78828	1.521332
C	-2.04066	-0.16553	3.083425
C	-2.90463	0.871551	2.729333
C	-4.19545	0.906622	3.21982
C	-4.65006	-0.10032	4.057722
C	-3.80898	-1.14463	4.396668
C	-2.51197	-1.18002	3.91124
H	-2.58298	1.644096	2.054845
H	-4.84806	1.716874	2.942312
H	-5.65772	-0.07241	4.437002
H	-4.1566	-1.93591	5.038898
H	-1.87682	-2.00175	4.185622
C	0.520418	1.281521	3.069076
C	-0.13639	2.399905	3.573334
C	0.584777	3.490349	4.033746
C	1.967385	3.478801	3.997037
C	2.631769	2.368349	3.499833
C	1.915759	1.280316	3.039866
H	-1.20713	2.432546	3.632703
H	0.059111	4.344235	4.425994
H	2.52558	4.326421	4.357156
H	3.707741	2.346684	3.473184
H	2.448679	0.42181	2.672272
C	-1.28928	1.07463	-3.26223
C	-1.69964	0.893555	-4.58246

C	-2.46604	1.855477	-5.21415
C	-2.83137	3.007232	-4.53443
C	-2.42554	3.192544	-3.22405
C	-1.65727	2.231825	-2.58553
H	-1.42601	0.005488	-5.1249
H	-2.77762	1.704033	-6.23373
H	-3.43077	3.755336	-5.02578
H	-2.70839	4.085558	-2.69236
H	-1.34214	2.376058	-1.5692
C	1.446697	0.092909	-3.14102
C	2.458276	-0.83828	-2.9046
C	3.731402	-0.62901	-3.3977
C	4.018716	0.519061	-4.12017
C	3.026847	1.456399	-4.34552
C	1.746695	1.245945	-3.85973
H	2.260943	-1.72403	-2.32826
H	4.500178	-1.36008	-3.21335
H	5.012821	0.681595	-4.50143
H	3.242863	2.352977	-4.90133
H	0.989222	1.984177	-4.04926
C	-0.83448	-1.75923	-3.18318
C	-2.17067	-2.09364	-2.9548
C	-2.70346	-3.26089	-3.46668
C	-1.91084	-4.11603	-4.21695
C	-0.58813	-3.79081	-4.45678
C	-0.05145	-2.61923	-3.946
H	-2.80529	-1.43411	-2.39155
H	-3.73706	-3.49984	-3.28335
H	-2.32537	-5.02632	-4.61591
H	0.032455	-4.4428	-5.04759
H	0.972387	-2.38463	-4.16516

Table A26: Cartesian coordinates of converged structure of **O** after geometry optimisation with *Turbomole 7.3*, the basis set def2-TZVP and the functional B2-PLYP (COSMO $\varepsilon = \infty$)

Atom	*x*	*y*	*z*
C	0	0	-0.71704
C	-1.20369	0	-0.01328
C	-1.20057	0	1.369769
C	0	0	2.063738
C	1.200572	0	1.369769
C	1.203686	0	-0.01328
H	-2.13551	0	-0.55259
H	-2.13484	0	1.905337
H	0	0	3.140824
H	2.134838	0	1.905337
H	2.135512	0	-0.55259
C	0	0	-2.14973
C	0	0	-3.34382
H	0	0	-4.4043

Table A27: Cartesian coordinates of converged structure of **P** after geometry optimisation with *Turbomole 7.3*, the basis set def2-TZVP and the functional B2-PLYP (COSMO $\varepsilon = \infty$)

Atom	*x*	*y*	*z*
C	0.558686	1.052686	0
C	-0.65175	0.360198	0
C	-0.64797	-1.03252	0
C	0.545475	-1.7312	0
C	1.731276	-1.03479	0
C	1.734647	0.345599	0
C	-1.88758	1.082651	0
C	-2.91855	1.683652	0
H	-1.57887	-1.5707	0
H	0.563563	-2.807	0
F	2.894907	-1.68277	0
F	2.902438	0.988747	0
H	0.588702	2.127865	0
H	-3.83497	2.21759	0

Table A28: Cartesian coordinates of converged structure of **S** after geometry optimisation with *Turbomole 7.3*, the basis set def2-TZVP and the functional B2-PLYP (COSMO $\varepsilon = \infty$)

Atom	*x*	*y*	*z*
C	-1.91008	0.713512	0
C	-3.11206	1.392687	0
C	-4.3127	0.689933	0
C	-4.3127	-0.68993	0
C	-3.11206	-1.39269	0
C	-1.91008	-0.71351	0
H	-3.11889	2.468448	0
H	-5.24345	1.23095	0
H	-5.24345	-1.23095	0
H	-3.11889	-2.46845	0
C	-0.5994	-1.30798	0
C	-0.5994	1.307977	0
C	0.599399	1.307977	0
C	0.599399	-1.30798	0
C	1.910084	0.713512	0
C	3.112064	1.392687	0
C	4.312701	0.689933	0
C	4.312701	-0.68993	0
C	3.112064	-1.39269	0
C	1.910084	-0.71351	0
H	3.118891	2.468448	0
H	5.243446	1.23095	0
H	5.243446	-1.23095	0
H	3.118891	-2.46845	0

Table A29: Cartesian coordinates of converged structure of **T** after geometry optimisation with *Turbomole 7.3*, the basis set def2-TZVP and the functional B2-PLYP (COSMO $\varepsilon = \infty$)

Atom	*x*	*y*	*z*
C	0.289944	-1.77871	-3.51909
C	-0.72913	-0.80549	-3.53496
C	-1.67498	-0.86885	-4.54346
C	-1.61733	-1.85478	-5.51757

C	-0.60808	-2.8038	-5.49285
C	0.345478	-2.76895	-4.49165
C	-0.74657	0.342115	-2.53717
N	-0.84907	-0.0141	-1.10331
C	0.196479	0.351148	-0.20082
C	-0.00925	1.316615	0.767646
C	1.00049	1.642351	1.660657
C	2.234317	1.018557	1.579035
C	2.469063	0.075304	0.594586
C	1.46246	-0.26194	-0.30046
C	1.584781	-1.14836	-1.40577
C	1.186169	-1.642	-2.42164
H	-0.96231	1.813256	0.827716
H	0.821124	2.389464	2.414809
H	3.017244	1.275424	2.27189
H	3.432045	-0.39773	0.509517
H	-2.468	-0.14014	-4.56953
H	-2.36307	-1.88181	-6.29423
H	-0.56548	-3.56999	-6.24827
H	1.131717	-3.50362	-4.45871
C	-2.01865	-0.56942	-0.68651
C	-2.13172	-1.0402	0.74844
O	-2.94482	-0.70322	-1.46435
C	-3.18244	-2.12759	0.915734
N	-3.26399	-2.52391	2.319219
H	0.165649	0.916451	-2.64358
H	-1.57543	0.995031	-2.78248
H	-1.16841	-1.39516	1.101835
H	-2.3968	-0.18923	1.371908
H	-2.94556	-2.96308	0.254863
H	-4.15118	-1.74714	0.612056
H	-3.99613	-3.20444	2.439235
H	-2.41045	-2.97849	2.602399

Table A30: Cartesian coordinates of converged structure of **U** after geometry optimisation with *Turbomole 7.3*, the basis set def2-TZVP and the functional B2-PLYP (COSMO $\varepsilon = \infty$)

Atom	*x*	*y*	*z*
C	0.796502	0.217366	-0.71768
C	0.30976	0.084797	0.584689
C	1.223242	-0.06178	1.630949
C	2.583432	-0.07548	1.379045
C	3.056226	0.056514	0.082286
C	2.157742	0.20281	-0.96361
C	-1.09992	0.097885	0.842537
C	-2.29032	0.101964	1.058801
H	0.860673	-0.16458	2.639526
H	3.275138	-0.1893	2.196986
H	4.115647	0.045449	-0.11155
H	2.517308	0.305782	-1.9738
H	0.102487	0.331051	-1.53297
Au	-4.28162	0.102675	1.418696
P	-6.58937	0.109734	1.835413
C	-7.34647	1.747297	1.583322
C	-8.35176	2.238235	2.408727
C	-8.91139	3.482187	2.164992
C	-8.47501	4.243519	1.094123
C	-7.4719	3.761784	0.267003
C	-6.90694	2.52371	0.513457
H	-8.70283	1.659789	3.245067
H	-9.68765	3.853054	2.812746
H	-8.91069	5.210406	0.906217
H	-7.1247	4.351787	-0.56424
H	-6.12076	2.164672	-0.13002
C	-7.50139	-1.03828	0.754017
C	-8.74528	-0.72776	0.216419
C	-9.40663	-1.64072	-0.58956
C	-8.8338	-2.87145	-0.86138
C	-7.59339	-3.18896	-0.32913
C	-6.92847	-2.27573	0.468733
H	-9.20486	0.223902	0.417511
H	10.36816	-1.38741	-1.003

H	-9.34834	-3.57947	-1.48901
H	-7.14065	-4.14271	-0.54117
H	-5.96033	-2.52997	0.867527
C	-6.99718	-0.37539	3.543148
C	-6.18011	0.081315	4.575032
C	-6.46469	-0.24084	5.889622
C	-7.56317	-1.03288	6.18746
C	-8.3756	-1.49788	5.167266
C	-8.09607	-1.1698	3.85023
H	-5.31799	0.68906	4.35525
H	-5.82627	0.119305	6.67845
H	-7.7813	-1.28953	7.210452
H	-9.22809	-2.11598	5.392671
H	-8.73761	-1.53942	3.069871

Table A31: Cartesian coordinates of converged structure of **V** after geometry optimisation with *Turbomole 7.3*, the basis set def2-TZVP and the functional B2-PLYP (COSMO $\varepsilon = \infty$)

Atom	*x*	*y*	*z*
C	-0.088	-0.34044	-0.29517
C	-0.04596	-0.14778	1.080913
C	1.168487	0.169009	1.685851
C	2.320888	0.278199	0.929178
C	2.270732	0.083991	-0.44299
C	1.066313	-0.22258	-1.05307
P	-1.52232	-0.30913	2.135315
C	-2.95629	-0.23022	1.015353
C	-3.56199	-1.3708	0.500228
C	-4.6401	-1.26051	-0.36324
C	-5.11878	-0.01188	-0.72225
C	-4.52063	1.130465	-0.21257
C	-3.44949	1.022041	0.655694
Au	-1.60398	1.312661	3.828543
C	-1.66999	2.704533	5.297255
C	-1.70701	3.535233	6.175687
C	-1.74855	4.515175	7.213278
C	-2.78575	5.451451	7.264652

C	-2.82959	6.398501	8.264269
C	-1.82757	6.408487	9.218966
C	-0.78705	5.496101	9.19651
C	-0.75195	4.552606	8.193369
C	-1.48804	-2.00657	2.79455
C	-0.71367	-3.01086	2.224764
C	-0.733	-4.29241	2.75166
C	-1.5273	-4.58187	3.848133
C	-2.30227	-3.58571	4.422411
C	-2.27862	-2.3044	3.902269
H	0.050594	3.837282	8.164018
H	-0.02142	5.523696	9.948424
H	-3.62653	7.116696	8.302384
H	-3.5579	5.432549	6.516271
H	-0.09034	-2.80337	1.372928
H	-0.12683	-5.06143	2.303601
H	-1.53988	-5.57797	4.257547
H	-2.91797	-3.8036	5.278528
H	-2.87748	-1.53655	4.36342
H	-3.20277	-2.34868	0.768671
H	-5.10328	-2.1509	-0.75348
H	-5.95735	0.072113	-1.39282
H	-4.89187	2.104031	-0.48433
H	-2.99977	1.91662	1.05362
H	1.218221	0.332427	2.749631
H	3.253884	0.521893	1.408395
H	3.166647	0.176218	-1.03356
H	1.021185	-0.3709	-2.11867
H	-1.0153	-0.57945	-0.78518
N	-1.86928	7.406148	10.27615
O	-0.98473	7.40828	11.09737
O	-2.78603	8.190472	10.28891

Table A32: Cartesian coordinates of converged structure of **W** after geometry optimisation with *Turbomole 7.3*, the basis set def2-TZVP and the functional B2-PLYP (COSMO $\varepsilon = \infty$)

Atom	*x*	*y*	*z*
Au	-4.60588	0.063195	3.113438
C	-2.66994	0.039032	3.70175
C	-1.51488	0.032907	4.059708
C	-0.14572	0.027272	4.469255
C	0.872775	-0.13929	3.530544
C	2.192445	-0.14218	3.926344
C	2.538129	0.018892	5.254557
C	1.538327	0.184295	6.19434
C	0.205239	0.189659	5.81513
P	-6.84942	0.099734	2.431782
C	-8.00142	-0.36261	3.764631
C	-7.72595	0.068311	5.060317
C	-8.5877	-0.2362	6.098596
C	-9.72935	-0.9843	5.855519
C	-10.0065	-1.42348	4.571827
C	-9.14789	-1.11343	3.529551
C	-7.37889	1.744445	1.854663
C	-8.63796	2.263194	2.134648
C	-9.00043	3.513765	1.66009
C	-8.11109	4.254056	0.899892
C	-6.85303	3.744213	0.616912
C	-6.48701	2.499562	1.096156
C	-7.18402	-1.04909	1.058006
C	-8.01647	-0.71925	-0.00532
C	-8.25039	-1.63397	-1.02007
C	-7.65931	-2.88517	-0.97866
C	-6.82728	-3.22185	0.07852
C	-6.58603	-2.3073	1.087408
O	-0.7892	0.348959	6.712286
H	1.795311	0.310635	7.233364
H	3.569978	0.01628	5.55773
H	0.616159	-0.26519	2.494078
H	-9.34108	1.701787	2.724101
H	-9.97748	3.906163	1.885919

H	-8.39402	5.226247	0.532803
H	-6.15508	4.317536	0.030636
H	-5.50298	2.118812	0.878287
H	-8.48391	0.248368	-0.05301
H	-8.89445	-1.36589	-1.84038
H	-7.84146	-3.59449	-1.76834
H	-6.36088	-4.1918	0.113626
H	-5.92922	-2.57664	1.897897
H	-6.83655	0.641398	5.263253
H	-8.36418	0.103378	7.095713
H	-10.3971	-1.22739	6.664835
H	-10.8901	-2.00762	4.378075
H	-9.37791	-1.46292	2.538486
Cl	3.445999	-0.35248	2.728331
H	-0.43381	0.451174	7.594031

Good luck with this place,

- I'm out of here!

R. S., Part II Student 2021–22